



University of Sheffield

**Department of Electrical and Electronic Engineering
Communication Research Group**

**Reconfigurable Rectangular Dielectric Resonator
Antenna for X-band and Millimetre-Wave
Applications**

By:

Akrem Soltan

**Department of Electronic and Electrical Engineering
University of Sheffield**

A thesis submitted in partial fulfilment of the requirements for the degree
of Doctor of Philosophy

April 2023

COVID-19 statement impact.

The COVID-19 pandemic has had a significant impact on my research, which was theoretical and experimental. Due to the closure of the University premises to all but essential staff from March 2020 to July 2021, there was a substantial interruption to my work. This closure led to delays in my research, which is estimated to have set me back by approximately 12 months.

In addition, the pandemic led to an increase in the quotation price for fabrication, which affected our budget and thesis plan. Despite these challenges, we were able to adjust our research plan to complete the work within the funded period.

We had planned to investigate more designs for reconfigurable polarisation and radiation pattern using PIN diodes at mmWave. However, due to the impact of COVID-19, we were not able to fully explore these options.

Overall, the COVID-19 pandemic has had a profound effect on my research, but we were able to adapt and make progress despite the challenges.

Acknowledgements

First and foremost, I express my utmost gratitude and praise to the almighty ALLAH, who has showered me with countless blessings throughout my life. I humbly acknowledge that my achievements and breakthroughs would not have been possible without His divine guidance and support.

I also wish to express my sincere appreciation to those who have contributed to my academic success. I am deeply grateful for the support and guidance of my supervisor, Dr. Salam Khamas, whose patience and continuous assistance have been invaluable throughout my research journey. In addition, I extend my thanks to the communication group at the University of Sheffield and my colleagues, whose helpful discussions and valuable experience have helped me overcome technical challenges.

My family and friends have been a constant source of moral support and encouragement, and I extend my heartfelt gratitude to them for their unwavering belief in me. I am also grateful for the financial support I received from the Ministry of Higher Education in Libya, particularly from my academic advisor, Dr. Atef Saeeh, at Libyan Cultural Affairs in London, UK

Lastly, I would like to recognize the staff and colleagues at the Electronic and Electrical Department who have provided me with timely and friendly assistance in managing my deadlines and submissions. Their professionalism and dedication to their work are deeply appreciated.

Publications

Journal articles

[3] Soltan, A.A., Khamas, S.K. and Salman, S.M., A Polarisation Reconfigurable Rectangular Dielectric Resonator Antenna Using PIN Diode for X-Band Applications. Progress In Electromagnetics Research M, Vol. 116, 1-10, 2023.

Conference papers

[1] Soltan, A.A., Abdulmajid, A.A. and Khamas, S.K., 2021, May. Optically Controlled Frequency-Reconfigurable Rectangular Dielectric Resonator Antenna with Photoconductive Switches. In 2021 IEEE Texas Symposium on Wireless and Microwave Circuits and Systems (WMCS) (pp. 1-4). IEEE.

[2] Soltan, A.A., Abdulmajid, A.A. and Khamas, S.K., 2022, March. Optically Controlled Circularly Polarised-Reconfigurable Millimeter-Wave Rectangular Dielectric Resonator Antenna using Photoconductive Switches. In 2022 16th European Conference on Antennas and Propagation (EuCAP) (pp. 1-5). IEEE.

Abstract

Reconfigurable antennas are in high demand for use in modern wireless communication systems, since their frequency, polarisation, and pattern, can be dynamically changed. Recently, dielectric resonator antennas (DRAs) have been extensively studied owing to their high efficiency, low cost, ease of excitation, and high degree of design flexibility. Additionally, various types of reconfiguration techniques have been identified and thoroughly investigated to meet the ever-increasing demand for new and advanced technologies. This research explores the feasibility of designing reconfigurable DRAs with various types of reconfigurability directions, particularly in response to the growing interest in the field of DRAs over the past thirty years.

The primary objective of this research is to investigate a range of designs for frequency, polarization, and pattern reconfigurable DRAs.

Frequency-reconfigurable antennas utilizing PIN diodes as switches face notable challenges in achieving reconfigurability, primarily related to complexities such as the utilization of multiple DRA elements, incorporation of multiple slots, low gain, and a limited degree of experimental validation. Future research opportunities lie in its simplicity, single-slot reconfigurability, dual-scenario operation, wide tuning range, high radiation efficiency, and gain, as well as the antenna operating in lower and higher order modes.

Furthermore, the current literature lacks antenna element designs that encompass multiple reconfiguration aspects, including frequency and pattern reconfigurability. This gap is significant because such multifaceted designs play a pivotal role in augmenting the adaptability, functionality, and overall performance of intelligent wireless systems. The reconfigurable rectangular DRA can steer the main beam direction to both $+45^\circ$ and -45° at 9.5 GHz, offering exceptional adaptability. It boasts an impressive 14.6% frequency tuning range, from 8.2 to 9.5 GHz. It is worth noting that the majority of designs in existing literature resort to optical switches to achieve reconfigurable antennas, primarily patch antennas and dipole antennas. This research marks a pioneering endeavour as it seeks to attain reconfigurable antennas using DRAs. In particular, achieving a reconfigurable rectangular DRA using a PIN diode at mmWave represents a ground breaking development in this research.

Several prototypes have been fabricated and measured at the x-band and mm-wave frequency range with good agreement between simulated and measured results.

Contents

COVID-19 statement impact.	i
Acknowledgements.....	ii
Publications	iii
Abstract.....	iv
Contents	v
List of Figures	viii
List of tables.....	xii
List of Abbreviations	xiii
Chapter 1	1
1.1 Introduction	1
2. Dielectric Resonator Antenna	2
3. Reconfigurable Antennas	4
3.1 Electrical switching techniques	4
3.2 Optical switching techniques.....	4
3.3 Mechanical switching techniques	5
3.4 Material change switching technique	5
4. Motivation and Contributions	5
Chapter 2	7
2.1 Frequency reconfigurable antenna.....	7
2.2 Radiation pattern reconfigurable antenna.....	12
2.3 Polarisation reconfigurable antennas.....	13
3. mmWave frequency reconfigurable antennas	14
4. Rectangular Dielectric Resonator Antenna	15
Chapter 3	20
Frequency and Pattern Reconfigurable DRAs	20
3.1 Introduction	20
3.2 PIN Diode Operation.....	20
3.3 Linear-Slot FED Frequency Reconfigurable Rectangular DRA Configuration	21
3.3.1 Parametric Analysis.....	24
3.3.2 Experimental Results.....	27

3.3.3 DRA with PIN Diodes in the OFF States	29
3.3.4 Rectangular DRA with PIN Diodes in the ON States	33
3.4 Reconfigurable Frequency and Radiation Pattern Rectangular DRA.....	39
3.4.1 Antenna Configuration	39
3.4.2 Experimental Results.....	45
3.5 Conclusion.....	57
Chapter 4.....	58
Polarisation Reconfigurable Rectangular DRAs.....	58
4.1 Introduction	58
4.2 Cross Slot-Fed Rectangular DRA with Polarisation Reconfigurability.....	58
4.2.1 Antenna Configuration	58
4.2.2 Left-hand Circular Polarisation	62
4.2.3 Right-hand Circular Polarisation	66
4.2.4 Linear Polarisation.....	69
4.3 Square Slot-fed Polarisation Reconfigurable Rectangular DRA	72
4.3.1 Antenna Configuration.	72
4.3.2 Experimental Results.....	76
4.3.3 Left-hand Circular Polarisation	78
4.3.4 Right-hand Circular Polarisation	83
4.3.5 Linear Polarisation.....	87
4.4 Conclusion.....	89
Chapter 5.....	90
Reconfigurable DRA using Photoconductive Switches.....	90
5.1 Introduction	90
5.2 Optically Controlled Frequency-Reconfigurable Rectangular DRA	91
5.2.1 Antenna Configuration	91
5.2.2 Results and Discussion	92
5.3 Optically Controlled Polarisation Reconfigurable Millimetre-Wave DRA using Photoconductive Switches.....	101
5.3.1 Antenna Configuration	101
5.3.2 Left-hand Circular Polarisation	103
5.3.3 Right-hand Circular Polarisation	106
5.3.4 Linear Polarisation.....	108

5.4 Conclusion.....	114
Chapter 6.....	115
Frequency Reconfigurable mmWave Rectangular DRAs	115
6.1 Introduction	115
6.2 Frequency reconfigurable single rectangular DRA.....	116
6.2.1 Antenna Configuration	116
6.2.2 Parametric study	117
6.2.3 Experimental Results.....	121
6.2.4 OFF state Scenario.....	123
6.2.5 ON State Scenario.	125
6.3 Frequency Reconfigurable DRA Array.....	128
6.3.1 Antenna Configuration.	128
6.3.2 Parametric study	128
6.3.3 Experimental results	134
6.3.4 OFF state scenario	135
6.3.5 ON state scenario.....	137
6.4 Conclusion.....	141
Chapter 7.....	142
Conclusions and Future Work.....	142
Future Work	144
Reference.....	145

List of Figures

Figure 1.1: The basic geometries of DRA: (a) rectangular, (b) cylindrical, and (c) hemispherical.....	3
Figure 2.1: (a) The antenna top layer. (b) The antenna bottom part [69].....	10
Figure 2.2 Photographs of antenna prototype and measurement setup [70].	10
Figure 2.3: Geometry of a rectangular DRA mounted on the ground plane.....	16
Figure 2.4: Simulated Magnetic field distribution TE ₁₁₁ inside the RDRA for Antenna 1at 8.6 GHz.	19
Figure 2.5: Simulated Magnetic field distribution TE ₁₁₃ inside the RDRA for Antenna 2at 17.7 GHz.	19
Figure 2.6: Simulated Magnetic field distribution TE ₁₁₅ inside the RDRA for Antenna 3at 10.6 GHz.	19
Figure 3.1: The construction of the PIN diode.....	20
Figure 3.2: Equivalent circuit of a PIN diode (a) Forward bias (ONstate). (b) Reversed bias (OFFstate).	21
Figure 3.3: Configuration of the proposed DRA with reconfigurable frequency.	21
Figure 3.4: Configuration of proposed feed network of RDRA (a) top view (b) bottom view.	22
Figure 3.5: The dimensions of a rectangular DRA and a groove.....	23
Figure 3.6: Reflection coefficient of slot 6 mm with and without reversed biased PIN diode.	25
Figure 3.7: Different positions of the switches at the ON state.	25
Figure 3.8: Reflection coefficient of different switch positions at ON State.	26
Figure 3.9: Photograph of the Rectangular DRA feed network with PIN diodes.	28
Figure 3.10: Photograph of the Rectangular DRA with a groove.	28
Figure 3.11: Rectangular DRA inside the anechoic chamber.	29
Figure 3.12: Simulated and measured return losses of RDRA when two PIN diodes are OFF.....	30
Figure 3.13: Simulated and measured realised gain for the rectangular DRA in the scenario I.	30
Figure 3.14: Radiation patterns of RDRA at 10.8 GHz. (a) $\Phi=0^0$. (b) $\Phi=90^0$	31
Figure 3.15: Radiation patterns of RDRA operating at the TE ₁₁₃ at 12 GHz. (a) $\Phi=0^0$. (b) $\Phi=90^0$	32
Figure 3.16: Simulated magnetic fields: (a) TE ₁₁₃ resonance modes at 10.8GHz and (b) TE ₁₁₃ at 12 GHz.	33
Figure 3.17: Simulated and measured return losses of rectangular DRA operating in scenario II.	35
Figure 3.18: Simulated and measured gain for the rectangular DRA in scenario II.	35
Figure 3.19: Radiation patterns of RDRA operating at the TE ₁₁₁ at 9 GHz. (a) $\Phi=0^0$. (b) $\Phi=90^0$	36
Figure 3.20: Radiation patterns of RDRA operating at the TE ₁₁₅ at 13 GHz. (a) $\Phi=0^0$. (b) $\Phi=90^0$	37
Figure 3.21: Simulated magnetic fields TE ₁₁₁ resonance modes at 9 GHz.	38
Figure 3.22: Simulated magnetic fields TE ₁₁₅ resonance modes at 13 GHz.	38
Figure 3.23: The proposed ring slot-feed network of RDRA (a) top view (b) bottom view.	40
Figure 3.24: Rectangular DRA with a Groove.	41
Figure 3.25: Simulated reflection coefficient for scenarios I and II with different x_1 and x_2 values. ...	41
Figure 3.26: Simulated radiation pattern for scenarios I and II with different x_1 and x_2 values. a) E-Plane and b) H- Plane.	42
Figure 3.27: Simulated reflection coefficients for scenario III with different x_1 and x_2 values.....	43
Figure 3.28: Simulated radiation pattern for scenario III with different x_1 and x_2 values. a) E- Plane and b) H- Plane.	44
Figure 3.29: a) The RDRA feed network with PIN diodes, b) bottom view c) Photographs of RDRA with a groove.....	45
Figure 3.30: The proposed antenna inside the anechoic chamber.	46

Figure 3.31: PIN diode connections.....	47
Figure 3.32: Simulated and measured reflection coefficients for scenario I.....	48
Figure 3.33: Simulated and measured gain for scenario I.....	48
Figure 3.34: Simulated and measured radiation pattern for scenario I at 9.5 GHz. a) E-Plane and b) H-Plane.....	49
Figure 3.35: The magnetic field distributions of the TE ₁₁₁ modes inside the RDRA. a) xz-plane, b) yz-plane.....	50
Figure 3.36: Simulated and measured reflection coefficients for scenario II.	51
Figure 3.37: Simulated and measured gain for scenario II.	51
Figure 3.38: Simulated and measured radiation patterns for scenario II at 9.5 GHz. a) E- Plane and b) H- Plane.	52
Figure 3.39: Simulated and measured reflection coefficients for scenario III.	53
Figure 3.40: Simulated and measured gain for scenario III.	54
Figure 3.41: The magnetic field distributions of the TE ₁₁₁ modes inside the RDRA. a) xz-direction, b) yz-direction.	54
Figure 3.42: Simulated and measured radiation pattern for scenario III at 8.2 GHz. a) E- Plane and b) H- Plane.	55
Figure 4.1: The geometry of the cross slot-fed reconfigurable DRA with ground plane divided into four identical sectors.....	59
Figure 4.2: The connections of PIN diodes for simple switching.....	60
Figure 4.3: Return losses with different values of Δ	61
Figure 4.4: Axial ratio with different values of Δ	61
Figure 4.5: Return losses of the left hand circularly polarised rectangular DRA.	62
Figure 4.6: Axial ratio for rectangular DRA with LHCP radiation.	63
Figure 4.7: Gain of a rectangular DRA with LHCP radiation.	63
Figure 4.8: Radiation patterns of RDRA excited in the TE ₁₁₃ mode at 10.8 GHz. a) E- Plane and b) H-Plane.....	64
Figure 4.9: The magnetic field for the TE ₁₁₃ mode at 10.8 GHz. (a) xz plane (b) yz plane.....	65
Figure 4.10: The magnetic field for the TE ₃₂₁ mode at 13.4 GHz. (a) xz plane (b) yz plane.....	65
Figure 4.11: Return losses of the circularly polarised rectangular DRA.	66
Figure 4.12: Axial ratio for rectangular DRA with LHCP radiation.	67
Figure 4.13: Gain for rectangular DRA with RHCP radiation.....	67
Figure 4.14: Radiation patterns of RDRA excited in the TE ₁₁₃ mode at 10.8 GHz. (a) $\phi= 0^0$ (b) $\phi= 90^0$	68
Figure 4.15: The return loss of linearly polarised rectangular DRA.....	69
Figure 4.16: Gain of the linearly polarised rectangular DRA.	70
Figure 4.17: Radiation patterns of the linear polarisation rectangular DRA excited in the TE ₁₁₃ mode at 11.2 GHz.	70
Figure 4.18: The magnetic field for the TE ₁₁₃ mode at 11.2 GHz. (a) xz plane (b) yz plane.....	71
Figure 4.19: Configuration of proposed Rectangular DRA.	72
Figure 4.20: The geometry of the slot-fed reconfigurable RDRA, (a) Top View, (b) Bottom View. ...	73
Figure 4.21: Simulated return losses of rectangular DRA for different switch positions.	75
Figure 4.22: Simulated axial ratio for different switch positions.....	75
Figure 4.23: Prototype of the proposed antenna: (a) Top View, (b) Bottom View, (c) Rectangular DRA with a groove.....	76
Figure 4.24: Simulated and measured return loss of RDRA.....	79
Figure 4.25: Simulated and measured Axial ratio rectangular DRA.	80
Figure 4.26: Simulated and measured gain for the rectangular DRA.	80

Figure 4.27: Simulated and measured normalized radiation patterns for TE ₁₁₃ at 10.6 GHz (a) E-plane, (b) H-plane.....	81
Figure 4.28: The magnetic field for the TE ₁₁₃ mode at 10.6 GHz. (a) xz, plane (b) yz plane.....	82
Figure 4.29: Simulated and measured return losses of the rectangular RHCP DRA.....	83
Figure 4.30: Simulated and measured axial ratio for the RHCP RDRA.....	84
Figure 4.31: Simulated and measured gain for the RHCP RDRA.....	84
Figure 4.32: Simulated and measured normalized radiation patterns for TE ₁₁₃ at 10.8 GHz (a) E-plane, (b) H-plane.....	85
Figure 4.33: The magnetic field for the TE ₁₁₃ mode at 10.6 GHz (a) xz plane (b) yz plane.....	86
Figure 4.34: Simulated and measured reflection coefficients of linearly polarised RDRA.....	87
Figure 4.35: Simulated and measured Gain of linearly polarised RDRA.....	87
Figure 4.36: Simulated and measured normalized radiation patterns for TE ₁₁₃ at 10.4GHz (a) E-plane, (b) H-plane.....	88
Figure 5.1: Geometry of the optically controlled frequency reconfigurable DRA.....	91
Figure 5.2: Simulated reflection coefficients of RDRA under different illuminating power levels.....	93
Figure 5.3: Simulated gain as a function of frequency for an incident optical power of 212 mW.....	93
Figure 5.4: The H-plane and E-plane radiation patterns for frequency reconfigurable RDRA at 12.7 GHz with mode TE ₁₁₃ When the switches are ON.....	94
Figure 5.5: Magnetic field distribution inside the DRA for the TE ₁₁₃ mode at 12.7 GHz.....	94
Figure 5.6: Simulated reflection coefficient of frequency reconfigurable RDRA for both 0 mw.....	95
Figure 5.7: Simulated gain as a function of frequency in the absence of the illuminating laser beam.....	95
Figure 5.8: The H-plane and E-plane radiation patterns for frequency reconfigurable RDRA for the following modes (a) TE ₁₁₁ at 11 GHz and (b) TE ₁₁₃ at 13.7 GHz.....	96
Figure 5.9: Simulated magnetic field for the (a) TE ₁₁₁ mode at 11 GHz. (b) TE ₁₁₃ at 13.7 GHz.....	97
Figure 5.10: Simulated reflection coefficient of frequency reconfigurable RDRA.....	98
Figure 5.11: Simulated gain as a function of frequency reconfigurable RDRA.....	98
Figure 5.12: The H-plane and E-plane radiation patterns for frequency reconfigurable RDRA for modes (a) TE ₁₁₁ at 10 GHz, (b) TE ₁₁₃ at 13.8 GHz.....	99
Figure 5.13: Simulated magnetic field for the (a) TE ₁₁₁ mode at 10 GHz, (b) TE ₁₁₃ at 13.8 GHz.....	100
Figure 5.14: The geometry of the polarisation reconfigurable DRA, (a) proposed rectangular DRA, (b) slot feeding (c) complete antenna configuration.....	102
Figure 5.15: Reflection coefficient of the left hand circularly polarised rectangular DRA.....	103
Figure 5.16: Broadside gain and axial ratio for the LHCP RDRA.....	103
Figure 5.17: Radiation patterns of RDRA excited at TE ₁₁₃ mode at 27.5 GHz. (a) $\phi = 0^{\circ}$. (b) $\phi = 90^{\circ}$	104
Figure 5.18: Radiation patterns of RDRA excited at TE ₁₃₁ mode at 33.5 GHz.....	105
Figure 5.19: The magnetic field distribution for the excited modes (a) TE ₁₁₃ at 27.5 GHz. (b) TE ₁₃₁ at 33.5 GHz.....	105
Figure 5.20: Broadside gain and axial ratio for the RHCP RDRA.....	106
Figure 5.21: Radiation patterns of RDRA excited (a) $\phi = 90^{\circ}$. (b) $\phi = 0^{\circ}$ for mode TE ₁₁₃ at 27.5 GHz.	107
Figure 5.22: Radiation patterns of RDRA excited for mode TE ₁₃₁ at 33.5 GHz.....	108
Figure 5.23: Reflection coefficients of linearly polarised rectangular DRA.....	109
Figure 5.24: Gain of the linearly polarised Rectangular DRA.....	109
Figure 5.25: Radiation patterns of the LP RDRA antenna excited TE ₁₁₃ at 30.6 GHz.....	110
Figure 5.26: The magnetic field distribution inside a rectangular DRA excited TE ₁₁₃ mode at 30.6 GHz.	110
Figure 5.27: Reflection coefficients of linearly polarised rectangular DRA.....	111

Figure 5.28: Gain of the linearly polarised rectangular DRA operation.....	111
Figure 5.29: Radiation patterns of LP RDRA antenna: (a) Excited TE_{113} at 28 GHz. (b) Excited TE_{131} at 34 GHz.....	112
Figure 6.1: Geometry of rectangular DRA.....	116
Figure 6.2: A bottom view of the proposed antenna feed network.....	117
Figure 6.3: Simulated reflection coefficient with different stub lengths.....	118
Figure 6.4: A bottom view of the proposed antenna feed network and bias lines.....	119
Figure 6.5: Simulated reflection coefficient with different l_{s2} lengths.....	120
Figure 6.6: Radiation pattern of rectangular DRA at 22 and 26.7 GHz. (a) E-plane. (b) H-plane.....	120
Figure 6.7: Prototype of mmWave frequency reconfigurable DRA. (a) Feed network with outlined DRA position. (b) Assembled rectangular DRA and feed network. (c) DC bias network.....	122
Figure 6.8: Photographs of RDRA. (a) Alignment RDRA. (b) RDRA inside the mmWave Chamber.....	122
Figure 6.9: Reflection Coefficient of the reconfigurable DRA when a PIN diode is OFF.....	123
Figure 6.10: Gain of the reconfigurable rectangular DRA for OFF state.....	123
Figure 6.11: Radiation pattern of rectangular DRA at 22 GHz. (a) E-plane. (b) H-plane.....	124
Figure 6.12: Magnetic field of the TE_{131} resonance mode at 22GHz for ON scenario. (a) xz plane (b) xy plane.....	125
Figure 6.13: Reflection coefficient of the reconfigurable RDRA when a PIN diode is ON.....	126
Figure 6.14: The gain of the reconfigurable RDRA when a PIN diode is ON.....	126
Figure 6.15: Radiation pattern of the reconfigurable RDRA with ON state. (a) E-plane. (b) H-plane.....	127
Figure 6.16: Magnetic field of the TE_{133} resonance mode for ON scenario. (a) xz plane (b) yz plane.....	127
Figure 6.17: Geometry of the reconfigurable DRA.....	129
Figure 6.18: Simulated reflection coefficient for the first rectangular DRA with different stub lengths.....	129
Figure 6.19: Geometry of feed network and biasing lines.....	130
Figure 6.20: Geometry of the reconfigurable DRA array.....	131
Figure 6.21: Simulated reflection coefficient of rectangular DRAs with different separation distances.....	132
Figure 6.22: Simulated gain of two rectangular DRAs with different separation distances.....	132
Figure 6.23: Simulated radiation pattern of the two DRAs configuration when the PIN diode in the ON state for $d= 9.5$ mm. a) E- Plane, b) H- Plane.....	133
Figure 6.24: Simulated reflection coefficient for the second rectangular DRA with different stub lengths.....	134
Figure 6.25: Prototype and feed network a) Assembled antenna b) Bottom view.....	134
Figure 6.26: Reflection coefficient of two DRAs configurations when a diode is OFF.....	135
Figure 6.27: Gain of the two DRAs configurations when the diode is in the OFF state.....	136
Figure 6.28: Radiation patterns at 24.3 GHz when a PIN diode is OFF. a) E- Plane, b) H- Plane.....	136
Figure 6.29: Magnetic fields of the TE_{311} resonance modes at 24.3 GHz. (a) xy plane (b) yz plane.....	137
Figure 6.30: Reflection coefficient of the two DRAs configurations when the diode is in the ON state.....	138
Figure 6.31: Gain of the two DRAs configurations when the diode is in the ON state.....	138
Figure 6.32: Radiation patterns of the two DRAs configurations when the diode is in the ON state at 29.3 GHz. a) E- Plane, b) H- Plane.....	139
Figure 6.33: Magnetic field distribution of the TE_{513} resonance modes at 29.3 GHz. (a) xy plane (b) yz plane.....	139

List of tables

Table 2-1: Impact of Rectangular Dielectric Resonator Antenna Dimensions on the Supported Modes when $\epsilon_r = 10$	18
Table 3-1: Calculated (DWM) and Simulated (CST) Resonance Frequency of Various Rectangular DRA Modes.....	26
Table 3-2: Comparison of the performance of the proposed design with those reported in the literature for antennas with combined reconfigurable frequency and radiation pattern.	56
Table 3-3: The proposed combined rectangular DRA design with other DRAs designs.	56
Table 4-1: Performance comparison proposes a design with another reconfigurable polarisation antenna.	71
Table 4-2: Different switches positions when D1 is ON and D2 is OFF.	74
Table 5-1: Physical Properties of Silicon at 12 GHz [69].	91
Table 5-2: Comparison of Reconfigurable Antennas using Photoconductive Switched to Tune the Frequency and Polarisation.	113
Table 5-3: Comparison of Polarisation Reconfigurable DRAs.	113
Table 6-1: Comparison of the proposed reconfigurable DRA with previously reported reconfigurable mmWave antenna designs	140

List of Abbreviations

Electromagnetic Interference	EMI
Dielectric resonator antennas	DRA
Millimetre wave	mmWave
Ultra High Frequency	UHF
Dielectric Waveguide Model	DWM
Linear Polarisation	LP
Left Hand Circular Polarisation	LHCP
Right Hand Circular Polarisation	RHCP
wireless local area network	WLAN
Computer Simulation Technology	CST
Positive Intrinsic Negative	PIN
Radiation Absorbing Material	RAM
Bandwidth	BW
Axial Ratio	AR

Chapter 1

1.1 Introduction

Wireless technology has been rapidly evolving since the invention of the telegraph by Guglielmo Marconi in the 20th century. The recently launched wireless systems, such as the fifth-generation (5G) wireless communication [1], Starlink satellite internet constellation [2], and vehicle-to-everything communications [3], can provide much higher data rates, larger signal coverage, and lower latency to users and terminals. Given these attractive properties, these wireless systems may revolutionize the global industry and our daily lives. Owing to the explosive development of wireless technology, the number of wireless devices has grown significantly. Consequently, the available electromagnetic (EM) spectrum is extremely congested, therefore, wireless systems are prone to severe electromagnetic interference (EMI) and latency, which greatly lowers the channel capacity and spectral efficiency. In these systems, antennas represent key components that significantly affect the overall performance.

Reconfigurable antennas can dynamically adapt their radiation features to meet different application scenarios, hence they are promising candidates to overcome the above-mentioned problems. Reconfigurable antennas can adapt their radiation characteristics, enabling them to optimize the system's performance. This can lead to better communication range, improved data throughput, and reduced interference. Reconfigurable antennas can be used in a wide range of applications, from wireless communication systems to radar and sensing systems. They can be designed to operate over different frequency bands and have different radiation patterns. Reconfigurable antennas can reduce system complexity, reconfigurable antennas can replace the need for multiple fixed antennas, reducing the system's complexity and cost. By dynamically adjusting their radiation characteristics, reconfigurable antennas can provide the same functionality as multiple fixed antennas [4].

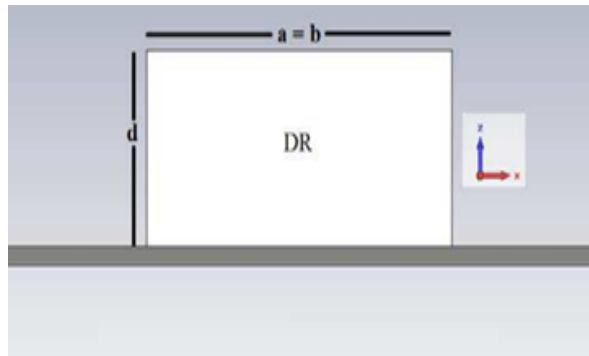
The reconfigurable operation can be achieved by utilizing frequency, polarisation or pattern reconfigurable antennas that offer tuneable frequency, polarisation, and radiation patterns,

respectively. The reported reconfigurable antennas have mostly focused on dipole [5, 6], slot [7, 8], and microstrip [9, 10].

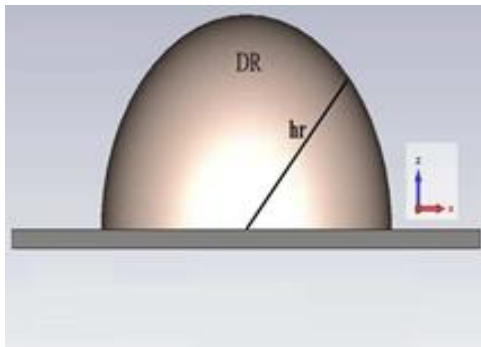
Dielectric resonator antennas (DRA) are three-dimensional radiators that offer high radiation efficiencies, and wide bandwidths with wide options of feeding mechanisms. Moreover, they have more usable operating modes than conventional dipole or patch antennas. These advantages make them promising as reconfigurable antennas. Recently, several reconfigurable DRAs have been presented [11-13]. To realize reconfigurability, switchable feeding networks [14], integrated polarisers [15], liquid ethyl acetate [16], and liquid metal [17] have been deployed in the designed reconfigurable DRAs. In this study, DRA designs with frequency, polarisation, and pattern reconfigurability are investigated for the x-band as well as the millimetre wave (mmWave) frequency range.

2. Dielectric Resonator Antenna

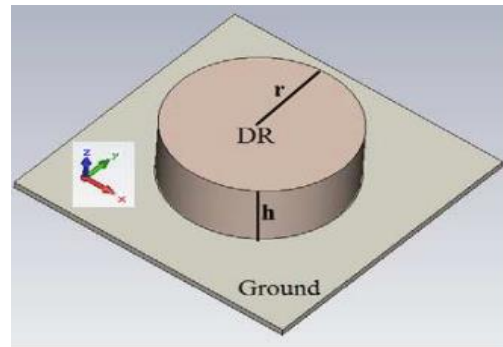
The dielectric resonator antenna has been available for nearly a quarter of a century, and during this period, numerous research studies have been conducted that confirm its advantageous features as a highly efficient and broad-spectrum radiator. These characteristics make it particularly promising for high-frequency applications. In 1983, Long et al discovered that, by removing the metallic shielding and providing proper feeding to excite the desired mode, dielectric resonators could function as efficient radiators [18]. A compact DRA can be designed to radiate with high efficiency, more than 95%, because of its extremely low losses [19]. An additional appealing feature is a fact that varying the dielectric constant and dimensions allows DRAs to operate over a wide range of frequencies [20]. In addition, DRAs are three-dimensional components, which gives a higher degree of design flexibility in terms of the antenna shape compared to conventional antennas such as dipole or microstrip. For ease of analysis, three basic DRA geometries, namely hemispherical, cylindrical, and rectangular DRAs, are most frequently studied when placed above a ground plane as illustrated in Figure 1.1.



(a)



(b)



(c)

Figure 1.1: The basic geometries of DRA: (a) rectangular, (b) cylindrical, and (c) hemispherical.

It should be noted that the rectangular and cylindrical DRAs are more commonly used since they offer extra degrees of freedom. Moreover, their structures are much simpler and easier to fabricate [21]. On the other hand, a hemispherical DRA offers zero degrees of freedom because it has only one parameter that can be adjusted, which is the radius r , compared to the cylindrical DRA, which has two independent structural parameters; radius r and height h [22]. The resonance frequency and bandwidth of different operating modes of a cylindrical DRA can be tuned by controlling the radius-to-height aspect ratio, which is not possible in hemispherical DRAs. Among the three basic DRA geometries, the rectangular DRA offers the most degrees of freedom due to the three independent structural parameters of length, a , width, b , and height h . Therefore, it is much easier to tune the operating frequencies of the different resonance modes to achieve wideband and multiband rectangular DRAs operations [23].

Other DRA geometries have been proposed and used in the literature including triangular [24], conical [25], pyramid [26], and bowtie [27] DRAs with wide bandwidth, high gain, and other desirable performances. Recently, with the rapid development of three-dimensional dielectric

printing technology, some DRAs with more complicated structures have been produced [28-32], which cannot be fabricated with traditional mechanical methods.

3. Reconfigurable Antennas

Wireless communication systems have developed and are developing rapidly and this requires new equipment to meet new multimedia applications' requirements, [33] particularly in improving performance in harsh environments where data rates are significantly limited by interference from multipath wave propagation. Antennas in which polarisation, radiation patterns or frequency can be reconfigured have the potential to meet requirements with low clutter and complexity [34]. Their main advantage over conventional non-reconfigurable counterparts is the extended capability and improved performance provided by applying electrical, mechanical or optical switching technology with minimal impact on system performance and cost. The reconfiguration technique used is usually chosen to satisfy existing constraints in the most efficient way. Reconfigurable antenna operation can be achieved through various techniques such as electrical switching, optical switching, or mechanical adjustments as well as a material change. Electrical switching makes use of devices like PIN diodes, Field-Effect-Transistors (FETs), and Micro-ElectroMechanical-System (MEMS) switches. On the other hand, optical switching employs photodiodes. In contrast, mechanical alteration techniques rely on physical changes to the antenna structure without biasing requirements [35].

3.1 Electrical switching techniques

Electrical switching techniques involve the use of switches to alter various antenna parameters. This leads to the redistribution of antenna currents, resulting in the required reconfiguration. The most commonly used elements in electrical switching are PIN diodes [36, 37], FET switches [38] and RF MEMS switches [39]. The aforementioned techniques often necessitate the use of biasing circuitry and regional separation for DC isolation.

3.2 Optical switching techniques

Optical control has been employed to switch reconfigurable antennas, and its fundamental design involves the transfer of electrons from the valence band to the conduction band upon exposure to a specific wavelength of light from a laser diode. This activation eliminates the

need for a metallic biasing line, which can disrupt the antenna radiation [40]. The primary benefit of using optically-driven switches is the absence of interference in the radiation pattern [41-43].

3.3 Mechanical switching techniques

Mechanical reconfiguration involves the alteration of the main radiator of the antenna through physical movement to achieve different characteristics [44, 45]. Unlike other reconfiguration techniques that use switches, this type of reconfigurable antenna does not require active element integration, biasing systems, or switching mechanisms. However, the performance flexibility is limited, and it is challenging to achieve multi-functional reconfigurable characteristics. Additionally, the response time is relatively slow and the integration of the reconfiguration element into the antenna structure can be complex [46-48].

3.4 Material change switching technique

The reconfiguration technique described in this context involves the alteration of the radiation characteristics by introducing a fluid into a cavity located behind the antenna. This changes the relative electric permittivity, or magnetic permeability, of the DRA or substrate resulting in a reconfiguration of the antenna's properties [49, 50]. The disadvantages of this technique include the tendency of liquid metals to either have too high toxicity or to rapid oxidisation in air. In addition, few designs are rather complex and bulky [51]. The reconfigurability can be achieved through the use of liquid materials albeit at the expense of increased antenna complexity and slower switching speed [52].

4. Motivation and Contributions

The electromagnetic environment has become more complex due to the presence of various wireless devices, leading to problems such as spectrum congestion, Electromagnetic Interference and unreliable connections. The reconfigurable antenna, with its ability to modify its radiating characteristics such as frequency, polarisation, and pattern, is a suitable solution to address these issues. The reconfigurable DRA has been the focus of numerous studies recently. Although the reconfigurable DRA is typically easier to excite and more efficient than other reconfigurable antennas such as slot, patch, or leaky-wave antennas, most reported

reconfigurable DRAs use liquid materials, which slows the switching speed as well as increasing the size and complexity. At mm-wave frequencies, precise alignment and assembly of DRAs can represent significant challenges, which can be addressed by outlining the DRA positions on the ground plane. The dimensions of the PIN diodes used for reconfigurability are often small, making soldering more challenging.

This thesis examines six electrically controlled reconfigurable DRA designs and two simulated optical reconfigurable rectangular DRA. The main contributions are as follows:

Chapter 3 is focused on the reconfigurable frequency and radiation pattern rectangular DRA at X-band. The first proposed design in Chapter 3 is a reconfigurable frequency rectangular DRA using a single linear slot and two PIN diode switches. The second proposed antenna is a combined reconfigurable frequency and radiation pattern rectangular DRA using a rectangular ring slot and two PIN diodes. To the best of the authors' knowledge, this is the first proposed combined frequency and radiation pattern design for DRAs. On the other hand, Chapter 4 focuses on polarisation reconfigurable rectangular DRAs. The first proposal utilizes a cross slot and four PIN diodes to switch between linear and circular polarisations. The second proposed antenna utilises a ring rectangular slot and two PIN diodes to switch between linear and circular polarisations.

Chapter 5 is focused on reconfigurable DRAs for x-band and mmWave communications. The two designs in Chapter 5 photoconductive switches to create a frequency-reconfigurable rectangular DRA a wideband circularly polarised reconfigurable rectangular DRA at X-band and mm-wave. The first proposed design uses a single linear slot and a pair of photoconductive switches to tune the frequency while in the second proposed design, A pair of photoconductive switches are used in conjunction with a rectangular ring slot to achieve LP, LHCP and RHCP.

Chapter 6 focuses on the design and measurements of a frequency-reconfigurable rectangular DRA. The first proposed design utilizes a linear slot that incorporates a PIN diode located in a microstrip line to change the length of the stub, achieving reconfigurability. The second proposed design uses two rectangular DRAs, two linear slots and a PIN diode located on the transmission line to achieve reconfigurability

The design of the antennas was accomplished using CST Microwave Studio. Following this, multiple prototypes were produced and tested, and the experimental results were found to closely match the simulated outcomes.

Chapter 2

There are three main types of reconfigurable antennas: frequency reconfigurable, polarisation reconfigurable, and pattern reconfigurable antennas. With the continuous development of communication technology, it is now feasible to design an antenna that exhibits a combination of two or more reconfiguration capabilities within a single structure [53].

2.1 Frequency reconfigurable antenna

The frequency reconfigurable antennas allow limited control over the antenna's operating frequencies from a single terminal. This capability is aimed at enhancing performance, specifically reducing interference with other wireless systems and maximizing throughput [54]. A frequency-reconfigurable antenna can alter its operating frequency while retaining its radiation pattern and polarisation characteristics. Numerous frequency reconfigurable antenna designs have been reported in the literature, either operating across multiple frequency bands or covering a wide frequency band [55]. To put it simply, a frequency reconfigurable antenna serves as a replacement for multiple antennas switched between multiple transceivers, thereby significantly reducing the product size and complexity. The main benefit of a frequency reconfigurable antenna is its efficiency in using the frequency spectrum, which leads to improved noise rejection in unused bands [56]. In addition, a frequency reconfigurable antenna helps reduce negative effects such as co-site interference and jamming. The frequency reconfiguration can be achieved through a variety of methods, as described in the literature. The fundamental approach to achieve frequency reconfiguration is by modifying the current distribution across the antenna's geometry. One way to create a frequency reconfigurable antenna is by regulating the effective length of the radiator, which ultimately determines the operating frequency [57, 58]. The integration of switching systems, such as RF MEMS, PIN diodes, Photoconductive Switches, and Varactor diodes, facilitates the control over the antenna's operating frequency.

Two frequency reconfiguration approaches that are based on utilising PIN diodes and optical switches are employed in the thesis.

i. PIN Diode

The PIN diode is the most commonly utilised method for reconfigurable antennas. This is due to its numerous benefits, including low cost, low loss, reliability, and simplicity. The standout attribute of PIN diodes is their quick switching speed, which ranges from 1 to 100 nanoseconds [33]. Compared to other technologies such as FETs and MEMS, PIN diode switched antennas exhibit superior radiation efficiency [59]. The relatively uncomplicated requirement for a DC biasing network, as well as the availability of a range of package sizes, makes PIN diodes a viable option. However, it is worth noting that PIN diodes consume more power than FETs or MEMS, as they are current-controlled devices. Despite this drawback, their numerous benefits have made them a desirable choice for use in reconfigurable antennas and large tuning ranges have been reported for PIN diode switched antennas.

A frequency-tuneable rectangular DRA has been proposed, where the antenna has been excited using a microstrip feedline with a length that is controlled by two PIN diodes [60]. The proposed antenna is capable of operating in five separate, narrow frequency bands at 2.4, 2.5, 3.5, 5, 5.2, and 5.8 GHz, supporting LTE, WWAN, and WLAN applications, with a maximum antenna gain of 2.14 dBi. A frequency reconfigurable multi-slot fed rectangular DRA has been proposed. Upon the activation of the first slot, the proposed antenna operates at a frequency of 5.64 GHz, exhibiting a gain of 4.27 dBi and a radiation efficiency of 91.3% [61]. The activation of the second slot results in the excitation of additional modes at 7.68 GHz, 9.48 GHz, and 10.11 GHz, with respective gains of 3.63 dBi, 6.94 dBi, and 6.96 dBi. A coplanar waveguide fed rectangular DRA with two PIN diode switches that are positioned on the feed network lines have been presented with frequency tuning over three frequency bands spanning a range of 3.45 to 6.77 GHz [62]. Setting one of the switches to be ON results in bandwidths of 8% and 16%, while activating both switches result in a wideband impedance of 65%. The measured gain values range from 3.52 to 4.86 dBi across the three switching states. In another study, a reconfigurable rectangular DRA has been proposed for use in wireless local area network (WLAN) applications. The antenna design consists of four identical RDRAs and three PIN diodes, providing four impedance bandwidths ranging from 6% to 17% with a maximum gain of 1.69 dBi [63].

A double-slot, frequency reconfigurable patch antenna, which comprises two rectangular slots has been reported [64]. Each slot includes three symmetrically placed PIN diodes to achieve operating frequencies of 2.2 GHz, 4.3 GHz, 5.2 GHz, and 5.8 GHz. In another study, the

utilization of PIN diodes as switches reconfigures the patch antenna to provide multi-band operation, enabling the generation of specific frequencies for WiMAX and WLAN applications. The antenna is capable of producing up to ten different frequency bands between 2 and 6 GHz, with relative impedance bandwidths ranging from 2.5 to 8% [65]. A wideband Koch snowflake fractal antenna with reconfigurable frequency for the Ultra High Frequency (UHF) band was designed using PIN diodes [66]. The antenna achieved three frequency bands with the following frequencies and bandwidths: 3.34–4.52 GHz (30%), 2.2–3.4 GHz (43%), and 1.45–4.1 GHz (95.49%).

Various designs of frequency reconfigurable antennas using PIN diodes as switches have been presented. , there were some limitations and areas for improvement. For instance, some of the designs involved using multiple elements of DRAs to achieve frequency reconfigurability [60] and [63], adding complexity to the structure and biasing and feed network of the antenna. Achieving the same level of reconfigurability using a single element of DRA could simplify the antenna design. In [62] a complex biased network and low gain which could limit their practical applications. Furthermore, some of the designs use two slots to achieve reconfigurability, whereas achieving the same level of reconfigurability with one slot could reduce the complexity of the antenna and lacked experimental measurements, and the results were only simulated [61] and [64]. Both [65] and [66] designs suffer from low gain, with [66] using fractal antenna resulting in a complicated design and manufacturing process.

ii. Optical Switch

Photoconductive switches offer higher isolation compared to electrical switches, which results in reduced interference due to the absence of a biasing network. Furthermore, photoconductive switches exhibit faster switching speeds of nanoseconds, which are much faster than that of electrical switches. This leads to a more efficient and quicker reconfiguration of the antenna.[67, 68]. In addition, photoconductive switches have been suggested as the basis for optical reconfiguration [69-76]. Incorporated into an antenna structure, these switches become conductive when subjected to a laser beam emitted by integrated laser diodes. A frequency reconfigurable antenna has been proposed with the capability to switch from single to dual-band operation that uses photoconductive silicon elements as optical switches [69]. Figure 2.1 Shows that the antenna consists of an outer and inner annular ring patch. The resonance of the antenna falls between 18 and 19 GHz when the silicon switches are not activated by laser light. However, when the switches are turned ON, the resonance frequency is shifted to 12 GHz.

are not illuminated by light, the antenna covers frequency bands of 3.84 to 4.8 GHz and 6.2 to 7.4 GHz. If switch S_1 is activated while S_2 is OFF, the frequency is shifted from 4.6 to 5.92 GHz and 7.35 to 8.6 GHz. If S_1 is OFF and S_2 is ON, the antenna covers the frequency bands of 3.2 to 4.1 GHz and 7.0 to 7.5 GHz. However, this design does not simulate or measure the gain, efficiency, or operating modes of the antenna. An alternative study investigated an optically-controlled reconfigurable antenna array that utilized two patch elements with E-shaped slots, a printed probe, and a photoconductive switch. The proposed antenna operates at two frequencies, 2.4 and 5GHz with a measured gain of 12.5 dBi [72]. A frequency reconfigurable dipole antenna has been proposed using two photodiode switches placed in the gaps of both dipole arms with respective resonance frequencies of 2720 MHz and 800 MHz in the OFF and ON states [73]. An optically reconfigurable printed dipole antenna that can switch between different frequencies and radiation patterns using two photoconductive switches that can reduce the length of the antenna from 62.3 to 33.5 mm. In different switch configurations, the antenna's resonant frequency can be varied from 2.26 GHz to 2.7 GHz and 3.15 GHz, with a maximum gain of 3.1 dBi [74]. A patch antenna that can reconfigure frequency through integrated laser diodes into the antenna has been proposed [75]. Despite achieving narrow bandwidth, when the two silicon switches are not illuminated by laser light, the antenna resonates between 4.15 and 5.1 GHz. If one switch is activated, the antenna's resonance shifts to the 4.8-5.7 GHz band. Activating the second switch shifts the operating frequency to the 3.2-4.3 GHz band. A slot E antenna shape that can switch from 2.5 GHz to 5.1 GHz has been proposed through the use of a silicon switch. The antenna has a maximum gain of less than 5 dBi [76]. In [77], a cognitive radio application was proposed, which uses an optically reconfigurable antenna. The design's prototype consists of a U-shaped monopole antenna with ultra-wideband (UWB) characteristics, and an open-annulus antenna equipped with four switches. The antenna has four frequency bands around 6, 7, 8, and 9 GHz with varying bandwidths, which are achieved by different combinations of the four switch states.

Previous research has explored the use of photoconductive switches for achieving reconfigurable frequency in antennas, but these studies have primarily utilized different types of antennas, such as dipole, patch, and slot antennas. To the best of our knowledge, our proposed design is the first to use Rectangular DRA in conjunction with photoconductive switches for achieving reconfigurable frequency. Our design presents a unique approach that has not been previously explored in the literature.

2.2 Radiation pattern reconfigurable antenna

Radiation pattern reconfigurable antennas have the ability to alter their far field pattern while keeping the frequency and polarisation constant. By providing diversity in the radiation pattern reconfigurable antennas can increase the number of users in wireless communication systems without requiring more array elements [78, 79]. Moreover, these antennas can improve the overall performance of modern wireless communication systems by reducing inter-user interference, enhancing security, and conserving energy through the directed signal to the appropriate direction [80-82]. Several references describe the use of PIN diodes to achieve reconfigurable radiation patterns, including [83-87].

In [83], a cylindrical DRA with a reconfigurable radiation pattern in eight directions was proposed. The pattern reconfigurability was achieved through the use of an annular ring slot in conjunction with eight PIN diode switches placed symmetrically to cover the entire azimuth plane. The proposed prototype had an impedance bandwidth of 5.66-5.88 GHz and a maximum gain of 7.27 dBi. In another study [84], four parasitic strips were utilized to shift the main beam of a rectangular DRA. These strips were located at each corner of the DRA and connected to the ground plane via switches to steer the main beam to $\theta = \pm 45^\circ$. The proposed design had an impedance bandwidth of 41.4% and a gain of approximately 4dBi. A design for a single feed, four-element rectangular DRA array and four PIN diodes with the ability to steer its beam were proposed in [85]. The main beam could be steered to $\theta = +45^\circ$ at $\phi = 0^\circ, 60^\circ, 120^\circ, 180^\circ, 240^\circ,$ and 300° , resulting in a maximum gain of 7dB. The proposed design achieved an impedance bandwidth of greater than 25% at a centre frequency of 1.95 GHz.

An alternative study demonstrated a pattern-reconfigurable cylindrical DRA using a feeding probe with four parasitic elements and four PIN diode switches to change the electric field distribution [86]. A recent study reported a pattern-reconfigurable cylindrical DRA with an endfire beam and the ability to scan the beam using ten PIN diodes to achieve nine different main beam directions[87]. The achieved impedance bandwidth was 2.38 GHz to 2.43 GHz with a maximum gain of 5.3 dBi.

While the studies demonstrate the potential of using PIN diode switches to achieve reconfigurable radiation patterns, some of the designs rely on a high number of switches which may increase the complexity of the antenna system. For example, [84] utilized eight PIN diode switches, [85] used four parasitic elements and four PIN diode switches, [86] used four PIN

diode switches, [87] used four parasitic elements and four PIN diode switches, while [88] required ten PIN diodes to achieve nine different main beam directions.

2.3 Polarisation reconfigurable antennas

A polarisation reconfigurable antenna has the ability to alter the polarisation of the radiated wave while preserving the frequency and pattern attributes. Polarisation refers to the orientation of the electric field vector over time and it can be classified as linear, circular, and elliptical polarisation. It is crucial to establish a polarisation match between the transmitting and receiving antennas to minimise signal losses. Reconfigurable antennas are a valuable tool for improving the performance of communication systems. They can provide diverse reception, minimize fading loss, and improve the overall quality of the received signal [88].

In [89] effort, a PIN diode-based polariser was integrated with a Multi-Input Multi-Output DRA to realize polarisation reconfigurability [89]. The proposed design used four single DRAs four PIN diodes and four input ports to achieve both circular and linear polarisation at 4.35 GHz. The -10 dB $|S_{11}|$ bandwidths were recorded as 11.26% for all states. Furthermore, the axial ratio bandwidth and gain of the antenna were 8.7% and 6.4 dBi, respectively. In another research, a circularly polarised DRA with a lattice design has been proposed using a cross-slot excitation and can switch between LHCP, RHCP, and LP polarisations with the help of five PIN diodes. The LP state exhibits an impedance bandwidth of 29.6%, while the CP states boast a bandwidth of over 26.8%. The 3-dB axial ratio bandwidths for the two CP states range are approximately 20.7% with a peak gain of 7.4 dBi [90].

A polarisation reconfigurable cylindrical DRA that operates at 2.5 GHz, utilizing a feed network of tunable dual-port probes that involves eight PIN diodes, allowing for achieving LHCP, RHCP, and LP states. The reflection coefficients for LHCP and RHCP are 34.3% and 36.6% compared to 9.5% and 6.3% for the two LP states. The 3 dB axial ratio bandwidths for LHCP and RHCP are 30.4% and 32.9% respectively, with a maximum gain of 6.58 dBic [91]. In [92], a circular polarisation reconfigurable cylindrical DRA was proposed for the S-band and linear polarisation at the C-band. In that study, the circular polarisation had -10 dB bandwidths of 14.56% for RHCP and 12.54% for LHCP compared to 3.42% for linear polarisation. The axial ratio bandwidths were 8.54% for RHCP and 9.73% for LHCP with a maximum gain of 5.67 dBi. In a recent study, a cylindrical DRA has been proposed with switchable LP, RHCP and LHCP radiations [93], which has been achieved by altering the states

of four PIN diodes located beneath the antenna. The impedance bandwidth and 3-dB RHCP axial ratio bandwidths are 27.2% and 27.3%, respectively, compared to respective counterparts of 22.2% and 21.4% for the LHCP sense. Furthermore, the impedance bandwidth for LP was 21.6%. Across all operating modes, the antenna achieves a maximum gain of 5.25dBi at 3.5 GHz.

In another study, a circularly polarised reconfigurable single-layer metasurface antenna has been reported using four PIN diodes [94]. The simulated results demonstrated impedance and axial ratio bandwidths of 16% and 13% for both RHCP and LHCP radiations with a gain of 6 dBic. Furthermore, electronically reconfigurable rectangular DRA using eight PIN diodes has been proposed to achieve linear and circular polarisation [95]. The antenna achieved wider impedance bandwidth of 27%, 21%, 22% and 28% for all states LP, LP, LHCP and RHCP with a narrow axial ratio bandwidth of ~1% with a maximum gain of 5 dBic.

While all of the antennas discussed in this literature show promising results in terms of polarization and bandwidth, some of them have complex structures [89],[90] or use a large number of PIN diodes [91] or have low gain [92], [93] or narrow CP.

3. mmWave frequency reconfigurable antennas

MmWave frequencies have recently gained significant attention in academic research due to their potential use in 5G communication systems and radar. As the demand for wireless mobile devices and services continues to grow, the new applications demand high data rates of up to 1 Gbit/s [96]. Reconfigurable mmWave antennas are crucial because they provide several benefits compared to conventional antennas. For instance, reconfigurable frequency antennas have the capability to dynamically switch frequency bands, which increases network capacity, reduces interference, and enhances overall system performance. Overall, reconfigurable antennas provide greater flexibility, improved performance, and increased reliability for wireless communication systems [97]. The development of a reconfigurable antenna for mmWave applications was achieved by utilizing a slotted-waveguide antenna array and incorporating two photoconductive switches. These switches were utilized to modify the electrical length of the slots in the antenna, enabling reconfiguration [98]. This facilitated frequency tuning and radiation pattern reconfiguration over the 28 and 38 GHz frequency bands with respective broadside gains of 8.0 and 9.0 dBi. The achieved impedance bandwidths are 10.95% and 4.25% in the 1st and 2nd bands, respectively. In addition, a Flexible frequency reconfigurable mmWave antenna has been investigated theoretically using a radiating patch

with a liquid crystal polymer substrate and PIN diode as well as a maximum gain of 5 dBi at 31.7 GHz [99].

Furthermore, a low-profile mmWave folded slot antenna was proposed that utilises a PIN diode to operate in two bands with a tuning range is 2.47%, i.e. 27.95–28.65 GHz and a maximum gain of 6.4 dBi [100]. In addition, a mmWave frequency-reconfigurable meta-surface antenna has been investigated by utilising vanadium dioxide (VO₂) for electrical control [101]. The antenna operates in dual bands with a tuning range of 30.3%, covering frequencies from (28.5–29.6 GHz) and (36.7–38.3 GHz) while exhibiting a maximum gain of 7.9 dBi. It should be noted that a reconfigurable mm wave DRA has not been reported in any earlier study.

4. Rectangular Dielectric Resonator Antenna

During the 1960s, a couple of studies were conducted that centred around the examination of rectangular dielectric resonators, particularly those with high dielectric constants. Using a material with a lower dielectric constant allows a dielectric resonator antenna to resonate at a higher frequency, enabling it to be smaller and more efficient in radiating and receiving electromagnetic waves. [102, 103]. Figure 2.3 illustrates a rectangular DRA on top of a metal ground plane. It should be noted that such configuration supports the transverse electric, TE, modes only. However, transverse magnetic (TM) modes cannot be excited in the presence of a ground plane because these modes require the electric field to be maximum at $z=0$, which doesn't meet the boundary conditions [104]. Moreover, the resonance frequency of each TE and TM resonance mode depends on the DRA's dimensions and permittivity [105]. The Dielectric Waveguide Model (DWM) can predict these resonance frequencies, which expresses the magnetic fields inside a rectangular DRA with width, length, and height of a , b , and h , respectively [106].

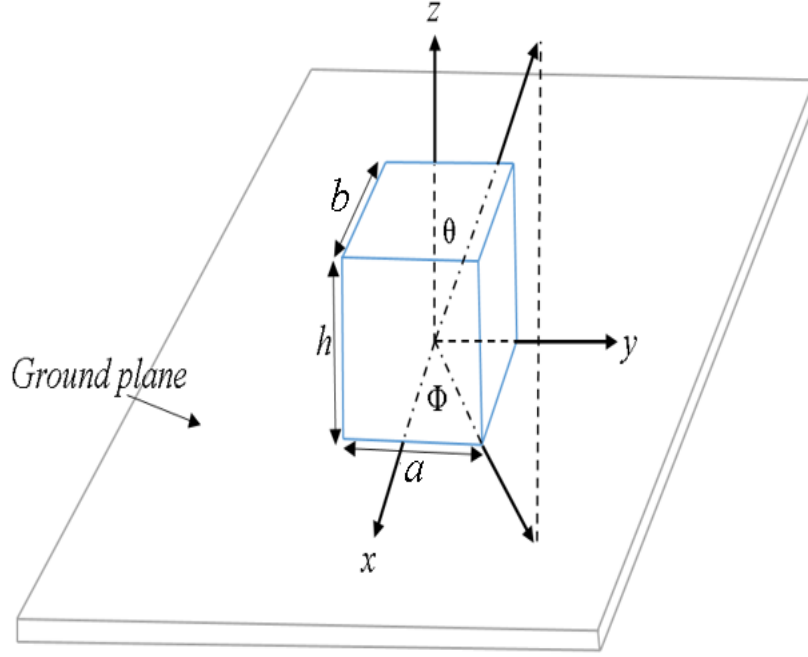


Figure 2.3: Geometry of a rectangular DRA mounted on the ground plane.

$$H_x = \frac{(k_y^2 + k_z^2)}{(j\omega\mu_0)} \cos(k_x x) \cos(k_y y) \cos(k_z z) \quad (2.1)$$

$$H_y = \frac{(k_y k_x)}{(j\omega\mu_0)} \sin(k_x x) \sin(k_y y) \cos(k_z z) \quad (2.2)$$

$$H_z = \frac{(k_z k_x)}{(j\omega\mu_0)} \sin(k_x x) \cos(k_y y) \sin(k_z z) \quad (2.3)$$

$$E_x = 0 \quad (2.4)$$

$$E_y = k_z \cos(k_x x) \cos(k_y y) \sin(k_z z) \quad (2.5)$$

$$E_z = -k_y \cos(k_x x) \sin(k_y y) \sin(k_z z) \quad (2.6)$$

where,

$$k_x = \frac{m\pi}{a}, k_y = \frac{n\pi}{b}$$

$$k_z \tan\left(\frac{k_z h}{2}\right) = \sqrt{(\epsilon_r - 1) k_0^2 - k_x^2}$$

k_0 represents the free-space wavenumber, which is defined as

$$k_0 = \frac{2\pi}{\lambda_0} = \frac{2\pi f_0}{c}$$

where m and n are the half-wave field variations along x and y directions.

The relationship between the wavenumbers in all directions and free space wave number is

$$k_x^2 + k_y^2 + k_z^2 = \epsilon_r k_0^2 \quad (2.7)$$

$$k_0 = \frac{2\pi}{\lambda_0} = \frac{2\pi f_0}{c} \quad (2.8)$$

where c is the speed of light. Equation (1.8) can be substituted in equation (1.7) to obtain the modes' resonance frequencies as:

$$f_0 = \frac{c}{2\pi\epsilon_r} \sqrt{k_x^2 + k_y^2 + k_z^2} \quad (2.9)$$

The amount of couple power that is transmitted to a dielectric resonator antenna (DRA) is affected by various factors, including the type, location, and size of the feeding element used. Examples of feeding elements include a slot aperture [107], coplanar waveguide [108], probe [109] and microstrip line [110]. However, each feeding mechanism has its limitations, and the slot aperture is typically the most popular choice for higher frequencies. For example, a feeding probe requires drilling a hole in a hard ceramic, which can negatively impact DRA performance if not done accurately. This becomes particularly challenging for smaller DRAs at higher frequencies. In contrast, a microstrip line feed can affect the antenna's radiation characteristics because the line is not isolated from the DRA. This study chose slot coupling because it is easy to fabricate and provides better isolation between the antenna and the feed network, resulting in reduced spurious radiation. Linear rectangular feeding slot length can be calculated using the following equations [111]:

$$l_s = \frac{0.4\lambda_0}{\sqrt{\epsilon_e}} \quad (2.10)$$

$$\text{where } \epsilon_e = \frac{\epsilon_r + \epsilon_s}{2} \quad (2.11)$$

ϵ_r and ϵ_s represent the dielectric constants of the DRA and substrate, respectively. The width of the feeding slot can be determined as

$$w_s = 0.2l_s \quad (2.12)$$

In addition, a quarter wavelength stub section can be utilized to improve coupling to the DRA significantly as it optimizes the matching by cancelling out the reactance at the feeding point [106]. Usually, the length is optimised for optimum matching.

A MATLAB code was created to solve equations (1-9). This code was employed to calculate the influence of changing the dimensions of the RDRA and its relative permittivity on the resonance frequencies of the DRA modes. These calculations were then compared to the results obtained from CST simulations and recorded in Table 2-1. It is worth mentioning that the absence of the feed network in the calculations can account for the discrepancy between the calculated and simulated resonance frequencies. Figures 2.4, 2.5 and 2.6 depicts the distribution of magnetic fields TE_{111} , TE_{113} and TE_{115} at 8.6, 17.7 and 10.5 GHz which indicates that the expected modes have been excited.

Table 2-1: Impact of Rectangular Dielectric Resonator Antenna Dimensions on the Supported Modes when $\epsilon_r = 10$.

No	Rectangular DRA dimensions (mm)			Simulated f_o (GHz)	Calculated f_o (GHz)	Resonance mode
	a	b	h			
1	8	6	10	8.6	8.8	TE_{111}
2	7	3.5	6.15	17.7	18.1	TE_{113}
3	5	5	30	10.6	10.3	TE_{115}

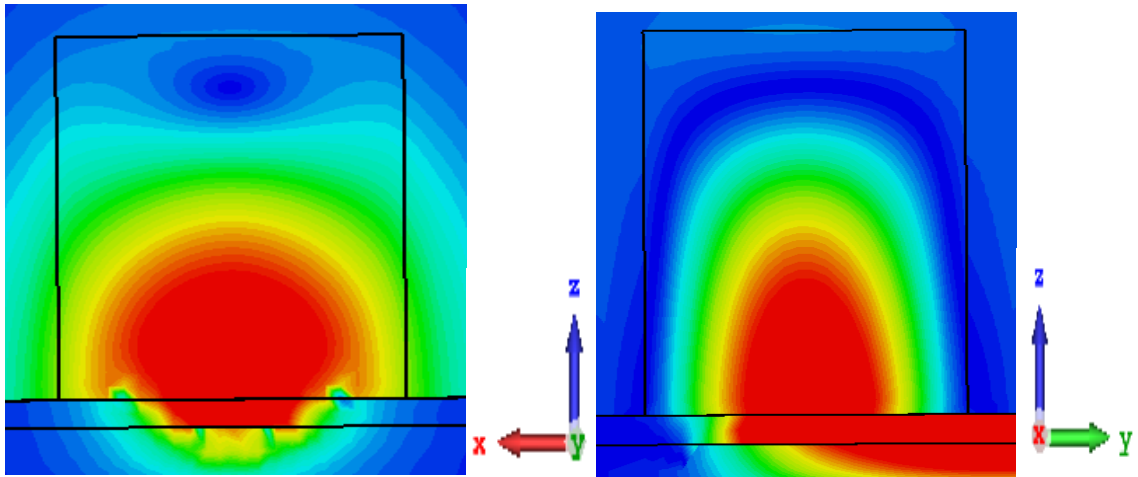


Figure 2.4: Simulated Magnetic field distribution TE111 inside the RDRA for Antenna 1at 8.6 GHz.

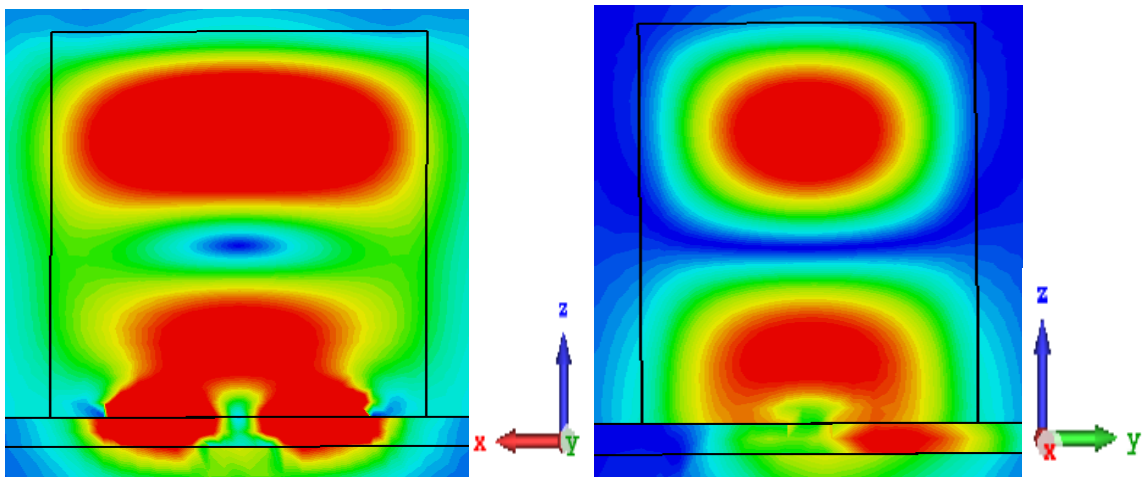


Figure 2.5: Simulated Magnetic field distribution TE113 inside the RDRA for Antenna 2at 17.7 GHz.

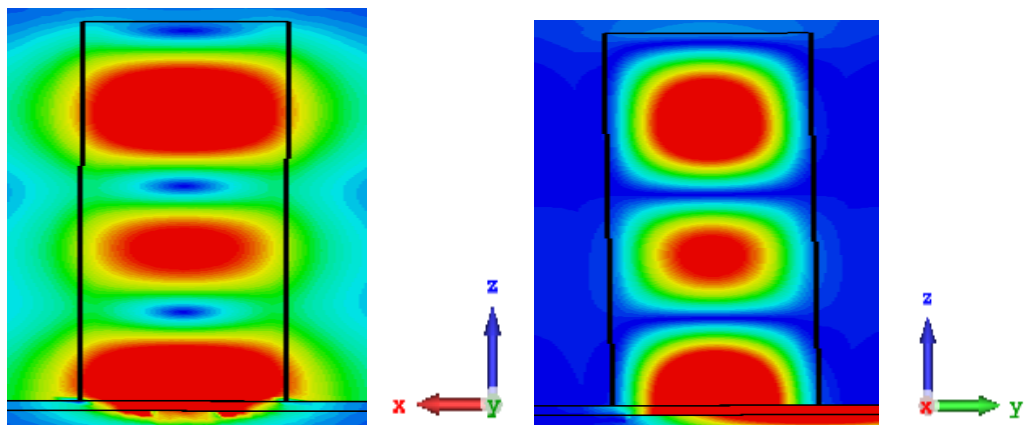


Figure 2.6: Simulated Magnetic field distribution TE115 inside the RDRA for Antenna 3at 10.6 GHz.

Chapter 3

Frequency and Pattern Reconfigurable DRAs

3.1 Introduction

With the fast pace of development in wireless and mobile communication systems, reconfigurable antennas have gained significant attention in the field of wireless communications as they can improve performance compared to traditional antennas [112]. For instance, a single frequency reconfigurable antenna can cover multiple frequency bands in an integrated system[113]. This used to require a separate antenna for each band or a multi-band antenna with an expensive RF-front end. As discussed in Chapter 1, there are various types of DRA shapes, including rectangular, cylindrical, hemispherical, triangular, and more. Compared to cylindrical and hemispherical configurations, a rectangular DRA geometry is easier to fabricate and provides two aspect ratios that can be changed to stimulate different modes.

3.2 PIN Diode Operation

Controlling an antenna's frequency, pattern, and polarisation can be achieved by manipulating switches. PIN diodes have become popular in reconfigurable antenna research due to their fast response times and low resistance at high frequencies [114]. These diodes consist of p-type and n-type regions separated by an intrinsic region, as shown in Figure 3.1.

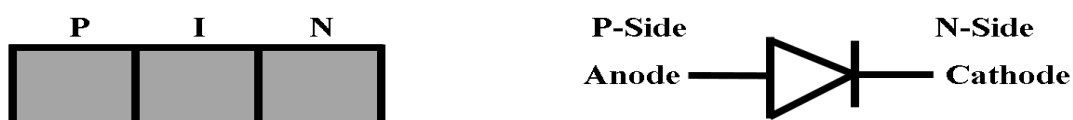


Figure 3.1: The construction of the PIN diode.

When a PIN diode is forward-biased, it has very low resistance and is in the ON state, while reverse-biasing creates an open circuit or OFF mode. The equivalent circuit of the PIN diode during the ON and OFF states is illustrated in Figure 3.2. The PIN diode

(MA4SPS402) has a 5.2Ω resistance and 0.45 nH inductance in the ON state compared to $20 \text{ k}\Omega$ resistance in parallel with a 0.045 pF capacitance in the OFF state [115].

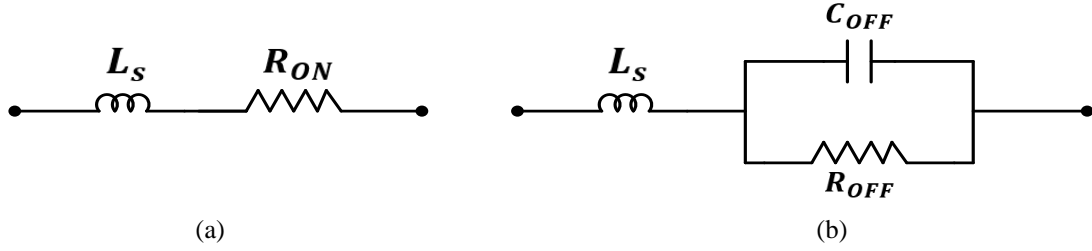


Figure 3.2: Equivalent circuit of a PIN diode (a) Forward bias (ONstate). (b) Reversed bias (OFFstate).

3.3 Linear-Slot FED Frequency Reconfigurable Rectangular DRA Configuration

The proposed antenna is illustrated in Figure 3.3. The antenna feed network has a square cross-section of $50 \times 50 \text{ mm}^2$ as shown in Figure 3.4a. The substrate is a 0.8 mm thick Rogers 4005C with a dielectric constant of $\epsilon_{rs} = 3.38$ and loss tangent of $\tan\delta = 0.0027$. The feed network consists of a single slot with dimensions of $l_s = 6 \text{ mm}$ and $w_s = 1 \text{ mm}$ as shown in figure 3.4b and it is driven by a 50Ω microstrip line, which is printed on the back of the PCB as shown in Figure 3.4b.

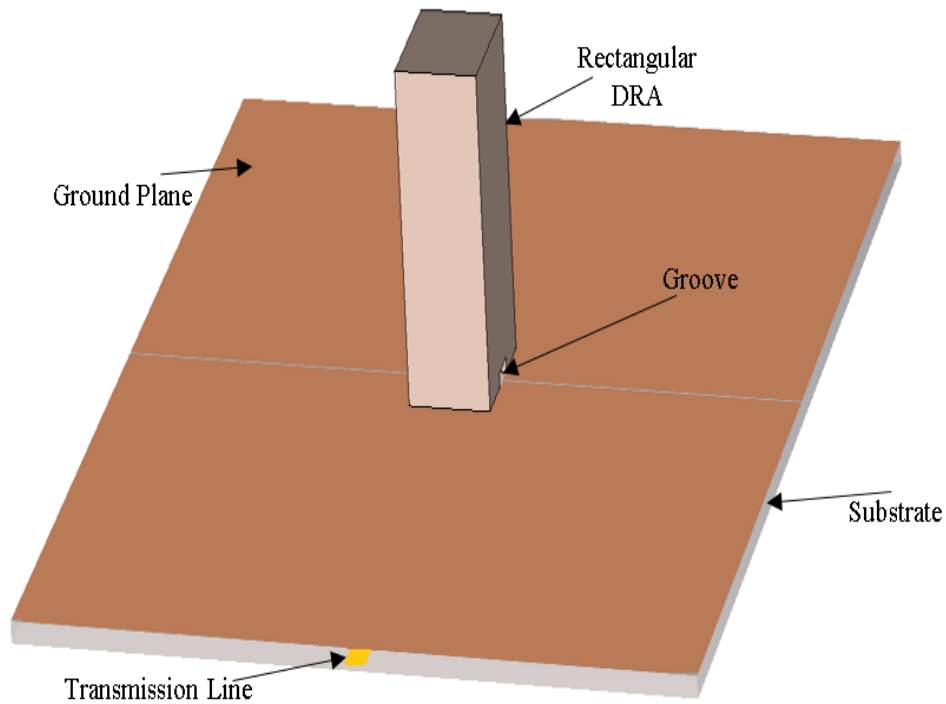
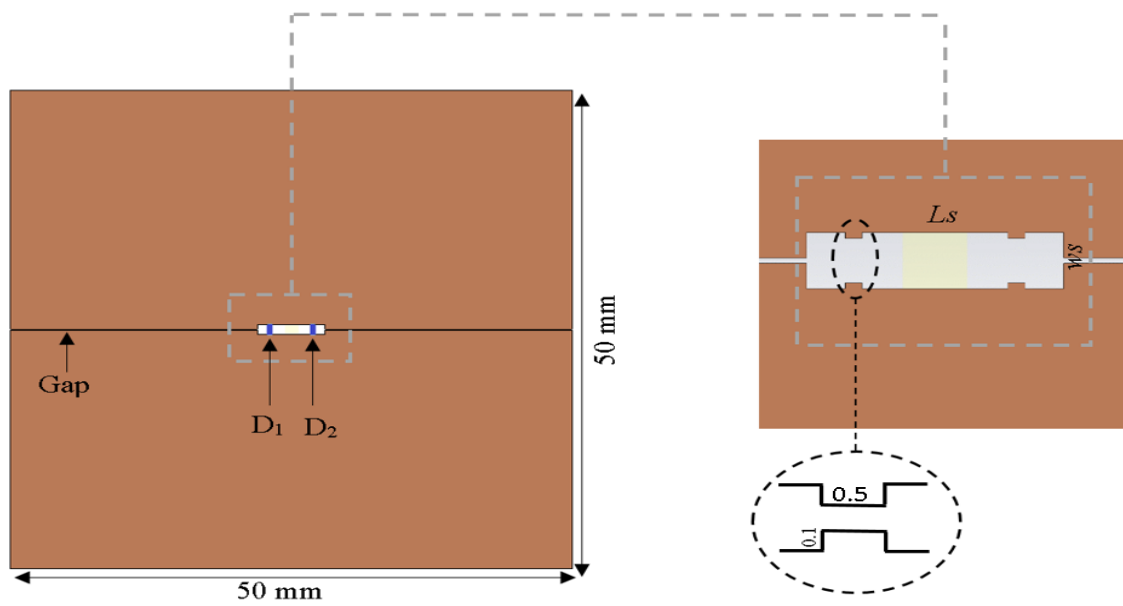
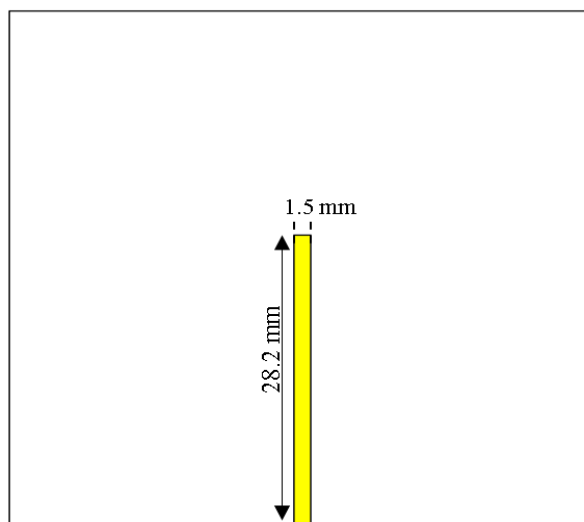


Figure 3.3: Configuration of the proposed DRA with reconfigurable frequency.

The DRA has a square cross-section, with dimensions $a=b=6$ mm and height of $h=12$ mm as illustrated in Figure 3.5. The antenna's dimensions have been selected to operate in a single order mode [116]. Single higher order mode operation can be achieved when the DRA's width-to-height aspect, i.e. aspect ratio has a range of approximately 0.25 to 1.5, and this work has been maintained as 0.5. A groove was etched on the bottom of the rectangular DRA to provide space for the PIN diode, which will be soldered on the top of the ground plane. The groove dimensions are $l \times w \times h_g$ of $6 \times 1.5 \times 0.5$ mm, respectively, as illustrated in Figure 3.5.



(a)



(b)

Figure 3.4: Configuration of proposed feed network of RDRA (a) top view (b) bottom view.

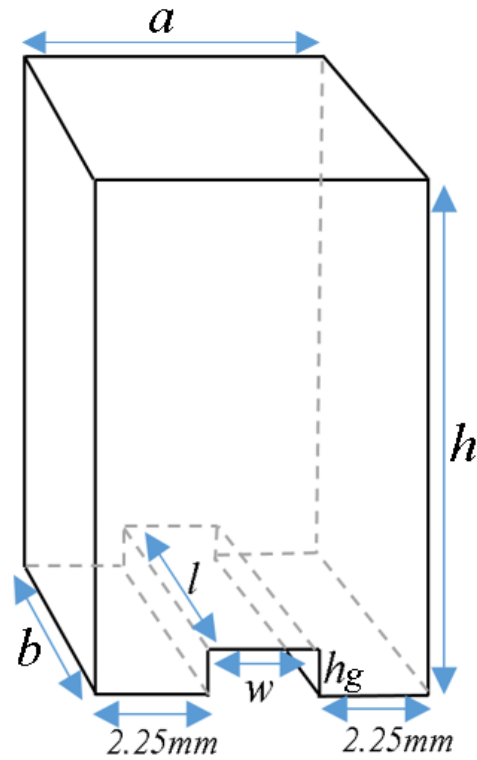


Figure 3.5: The dimensions of a rectangular DRA and a groove.

The proposed design incorporates a rectangular DRA on top of the ground plane, and two PIN diodes positioned above a slot located beneath the centre of the rectangular DRA. A groove has been etched on the bottom of a rectangular DRA to accommodate the height of the PIN diodes, allowing the DRA to be placed firmly on the ground plane without any air gaps in between. The Touchstone lumped element in CST can be used to import a file for the ON and OFF state which contains the values of resistance, inductance, and capacitance for a PIN diode circuit. This allows for the accurate simulation and analysis of the circuit's performance, based on the specific values of the passive elements. Importing the file (provided by Macom) can make it easier to change or update the values of the elements in the circuit, without having to manually input them into the simulation software [117]. Additionally, a surface-mount PIN diode has been employed, which is easier to solder as it can be connected to the ground plane from the bottom of the diode. Conductive silver paint has been used for soldering and the PIN diodes' position has been marked by four edges to be soldered at the precise location as shown in Figure 3.4a.

3.3.1 Parametric Analysis

For the X-band frequency range, it is recommended to utilize a 6 mm long and 1 mm wide slot to ensure efficient coupling between the DRA and the feeding microstrip line. The microstrip line should be placed in the substrate's centre and possess a width of 1.5 mm, while a 3.4 mm stub length is advised to achieve optimal matching. The slot's width should be suitable to accommodate the PIN diodes. The PIN diode has dimensions of 1.2mm × 0.5mm × 0.2mm in length, width, and height as shown in figure 3.7. The configuration of Figure 3.4 has been simulated using CST, where the built-in diode modes have been utilized in two cases; the first is when the switches are in the OFF state and the second is when they are in the ON state. Each PIN diode has been located at a distance of 0.75 mm from the slot ends, which means the slot length will vary between 6 mm when the PIN diodes are in the OFF state and a shorter length when they are in the ON state. This is due to the fact that each diode has a width of 0.5mm. As illustrated in Figure 3.6, the same reflection coefficients have been achieved in the absence of the PIN diodes and when reversed biased PIN diodes are incorporated along the slots. In both cases, the TE_{113} resonance mode has been excited at 10.8 and 12 GHz, respectively. It should be noted the achieved impedance bandwidths are 1.85% and 3.1%. Figure 3.7 shows the possible different positions of the PIN diodes and how they can impact the useful slot length when they are forward biased. The impact of the different PIN diode positions, when they are in the ON state is illustrated in Figure 3.8, where it can be noted that the respective TE_{111} and TE_{115} modes are excited at 9 GHz and 13 GHz in all cases albeit with different strengths that depend on the effective slot length. Table 3.1 presents the resonance frequencies that have been calculated and simulated for different modes. It is worth mentioning that the slight difference between simulated CST and calculated dielectric waveguide model resonance modes is attributed to the fact that the feed network has not been considered in MATLAB calculations. It should be noted that the stub length has been fixed at 3.6 mm during these simulations, which also impacts the strength of the coupling and hence the achieved depth of S_{11} . Therefore, the positions of the PIN diodes have been chosen to give an effective feeding slot length of 4.5 mm as this corresponds to the strongest coupling between the DRA and feed for the given stub length. It is important to note that frequency reconfigurability has been achieved with dual bands in each state.

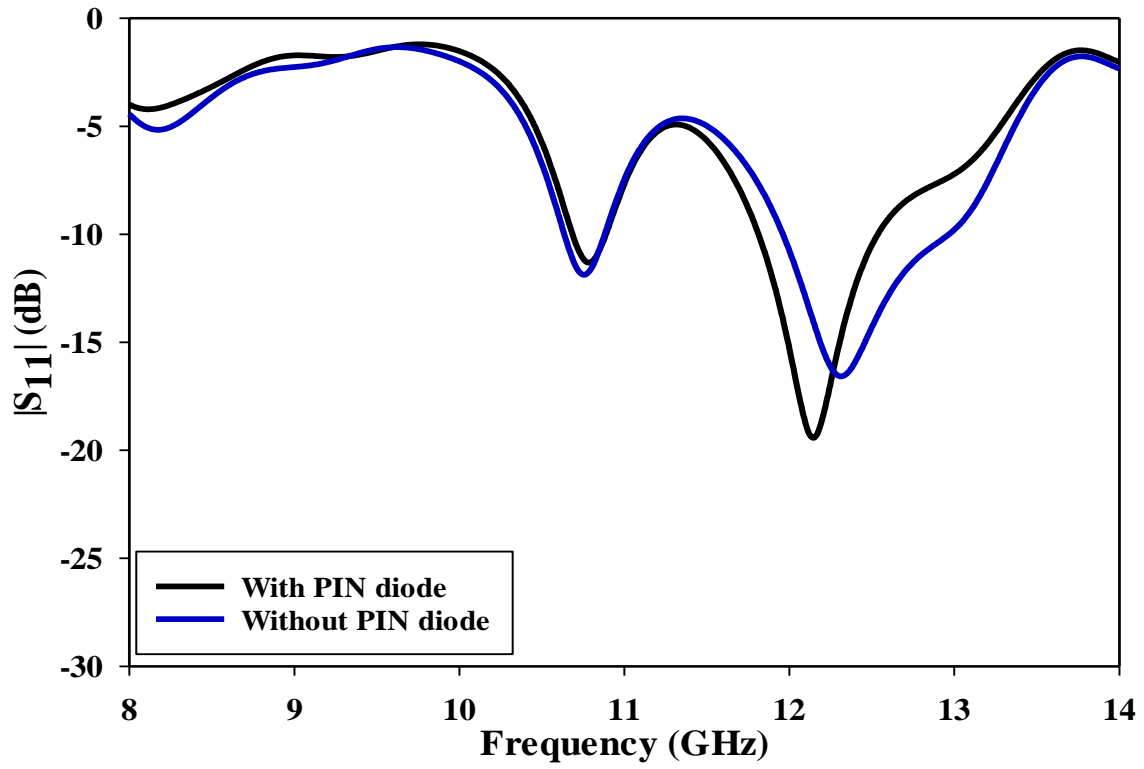


Figure 3.6: Reflection coefficient of slot 6 mm with and without reversed biased PIN diode.

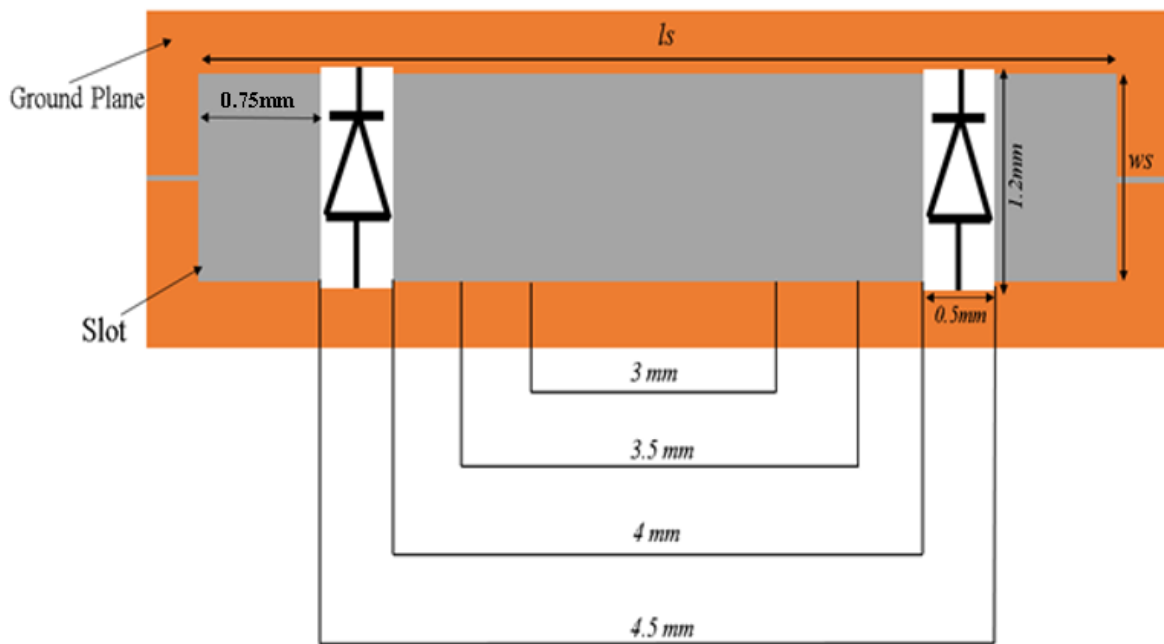


Figure 3.7: Different positions of the switches at the ON state.

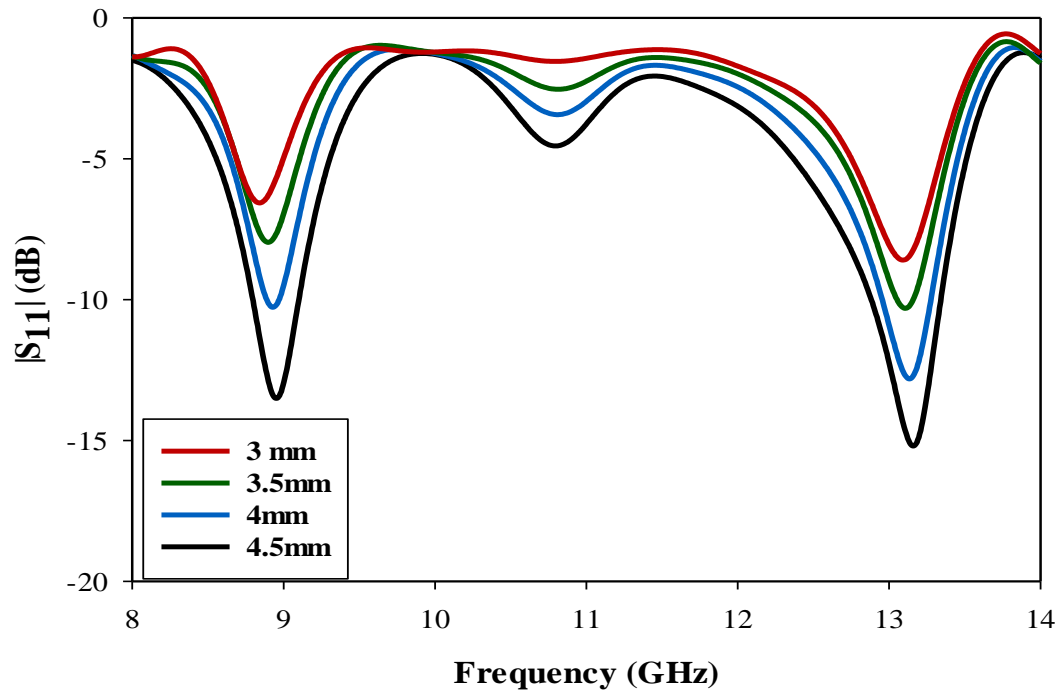


Figure 3.8: Reflection coefficient of different switch positions at ON State.

Table 3-1: Calculated (DWM) and Simulated (CST) Resonance Frequency of Various Rectangular DRA Modes.

Resonance mode	TE ₁₁₁	TE ₁₁₃	TE ₁₁₅
Simulated resonance frequency (CST) GHz	9	10.8	13
Calculated resonance frequency (MATLAB) GHz	8.5	10.3	12.9

3.3.2 Experimental Results

As demonstrated in Figure 3.4a, the ground plane has been cut into two halves by a gap of 0.1mm. It is important to keep the space between the two halves of the ground plane as minimal as possible, the recommendation to keep the gap size typically below 0.3 mm is based on maintaining it below 1/10th of the operating wavelength (λ) for the antenna. In this specific design context, where the operating frequency is 10 GHz, the corresponding wavelength (λ) is 30 mm ($1/30 * 10$). Staying below 1/10th of the wavelength helps to minimize the impact of the gap on the antenna's performance, ensuring that it remains an effective radiating element for the given frequency range. The gap facilitates the DC biasing of the PIN diodes without impact on the antenna performance. One half of the ground plane has been connected to the common ground, while the other half is connected to the positive DC. In addition, the diodes have been placed at the edge sides of the linear slot, as illustrated in Figure 3.4a, and were attached to the ground plane using conductive silver paint. A groove has also been etched into the lower DRA side with respective depth, length, and width of 0.5mm, 6mm, and 1.5mm, as shown in Figure 3.5. The purpose of this groove is to accommodate the height of the PIN diodes so that the DRA can be positioned steadily on the ground plane without creating any air gaps in between. Figure 3.9 illustrates the utilised feed network of the rectangular DRA incorporating the two PIN diodes, a 50 x 50 mm² ground plane and excited using a 50 Ω microstrip-feed line through a 6 x 1 mm² slot aperture. The aperture has been etched on a Rogers 4005C substrate with a thickness of 0.8, a dielectric constant of $\epsilon_r = 3.48$ and a loss tangent of $\tan\delta = 0.0027$. Figure 3.10 illustrates the proposed rectangular DRA with a groove that was fabricated using Alumina as the dielectric material. With a dielectric constant of $\epsilon_r=9.9$ and a low loss tangent of $\tan \delta 0.0001$, the fabrication was carried out by Almath Crucibles Ltd. It should be noted that a double-sided self-adhesive copper tape has been utilized to attach the DRA to the ground plane. In addition, it is important to note that when designing a circuit to prevent RF signal leakage to the DC bias lines, inductors with larger values should be used. This is because the impedance of an inductor is given by $Z_L = (j \times 2\pi \times f \times L) \Omega$, where f is the frequency and L is the inductance. Thus, to effectively choke the RF signal, the inductor should have a high impedance value. For instance, if an inductor with a value of 1 nH is used, its impedance at 10 GHz will only be 75.3Ω , which is not enough to effectively block the RF signal. Therefore, a higher value inductor such as 68 nH, which has an impedance of 5124.5Ω at 12 GHz, should be used instead [118] from coilcraft served as RF chokes. In addition, to prevent any DC signal from reaching the Network Analyzer, an External DC block has been

implemented. Figure 3.11 depicts the proposed antenna inside an anechoic chamber. The power supply is located outside of the chamber and the PIN diodes are controlled through the use of wires. A comparison method has been utilized to determine the gain of the antenna. In this method, a horn antenna is used at the receiving end and the gain of the directive radiation antenna (DRA) is determined by comparing it to the known gain of a reference horn antenna using the equation stated in [119].

$$G_{DRA \text{ in } dB} = G_{Horn \text{ in } dB} + 10 \log_{10} \left(\frac{P_{DRA}}{P_{Horn}} \right) \quad 2.1$$

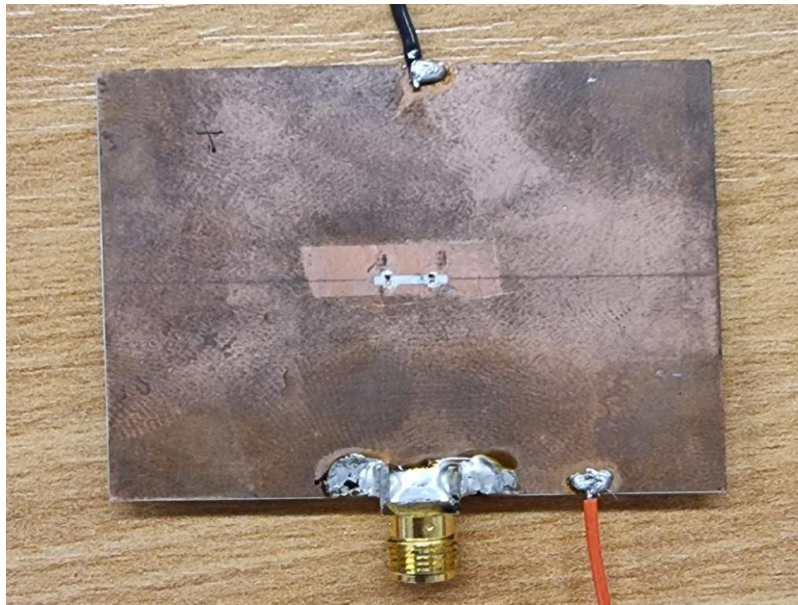


Figure 3.9: Photograph of the Rectangular DRA feed network with PIN diodes.



Figure 3.10: Photograph of the Rectangular DRA with a groove.



Figure 3.11: Rectangular DRA inside the anechoic chamber.

The return losses and radiation performance of the rectangular DRA have been measured using an E5071C vector network analyser. The proposed design offers two operating scenarios by altering the states of the two PIN diode switches: Scenario I: OFF states, and Scenario II: ON states.

3.3.3 DRA with PIN Diodes in the OFF States

In this scenario, both switches D1 and D2 are OFF. The simulated and measured return losses are illustrated in Figure 3.12, where it can be noted that the simulated impedance bandwidths are 1.85% (10.68-10.88 GHz) and 5.5% (11.81-12.53 GHz), while the measured counterparts are ~1.85% (10.705-10.90 GHz) and 5.3% (11.87-12.52 GHz). From the measurement, it can be seen that the depth of the return losses is reduced compared to the simulated data, which may be due to loss in the cable and solder SMA which has been utilized between the coaxial cable and the feeding strip line and fabrication error. The simulated realised gain is ~ 8 dBi at 10.8 and 12 GHz, while the measured gain is ~7.5 dBi at 10.8 and 12 GHz as illustrated in Figure 3.13. Figures 3.14 and 3.15 illustrates the normalized simulated and measured radiation patterns of the TE₁₁₃ mode at both 10.8 and 12 GHz bands, where it can be observed a good agreement has been achieved between the measured and simulated radiation patterns. Figure 3.16 presents the magnetic field distributions within the rectangular DRA, where it can be observed that the same TE₁₁₃ mode has been excited at 10.8 and 12 GHz.

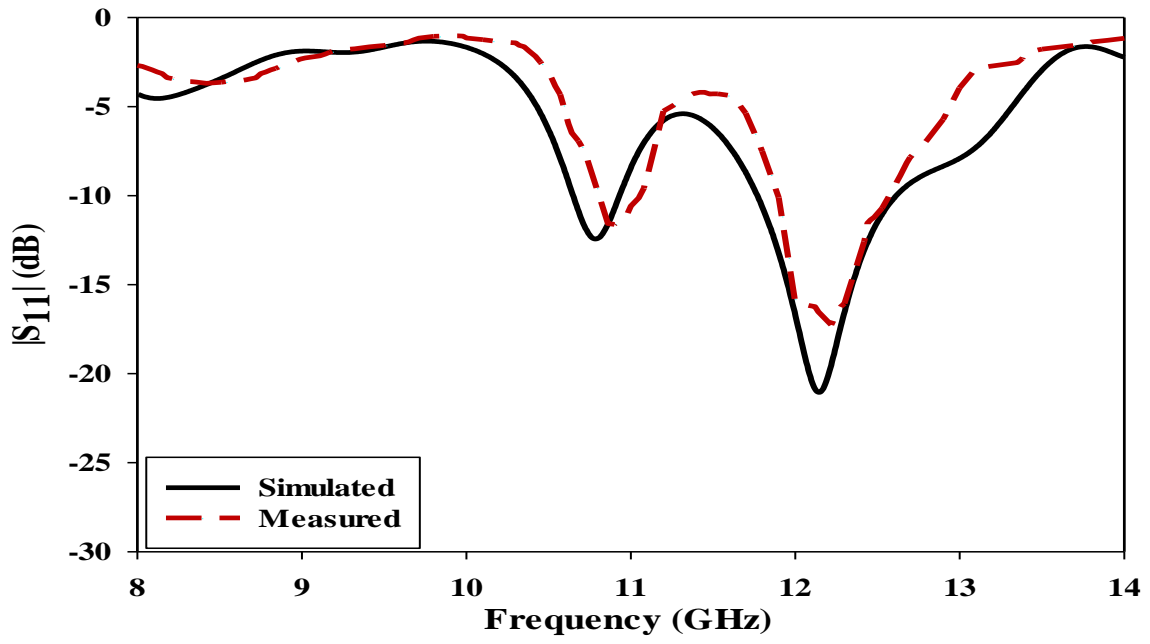


Figure 3.12: Simulated and measured return losses of RDRA when two PIN diodes are OFF.

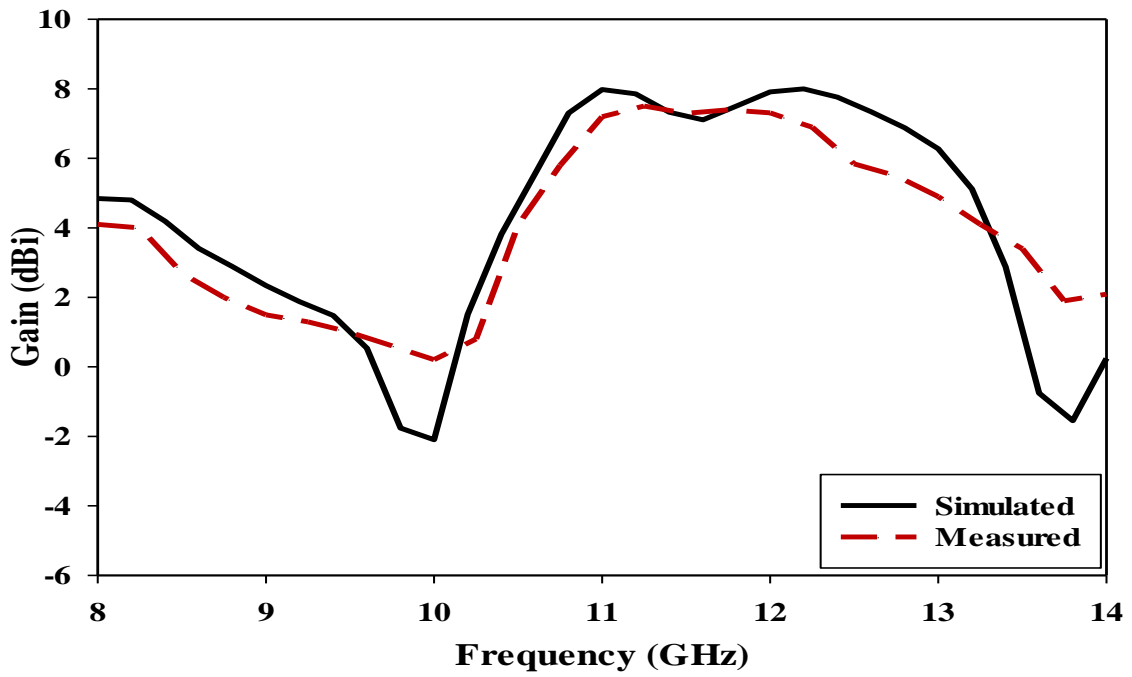
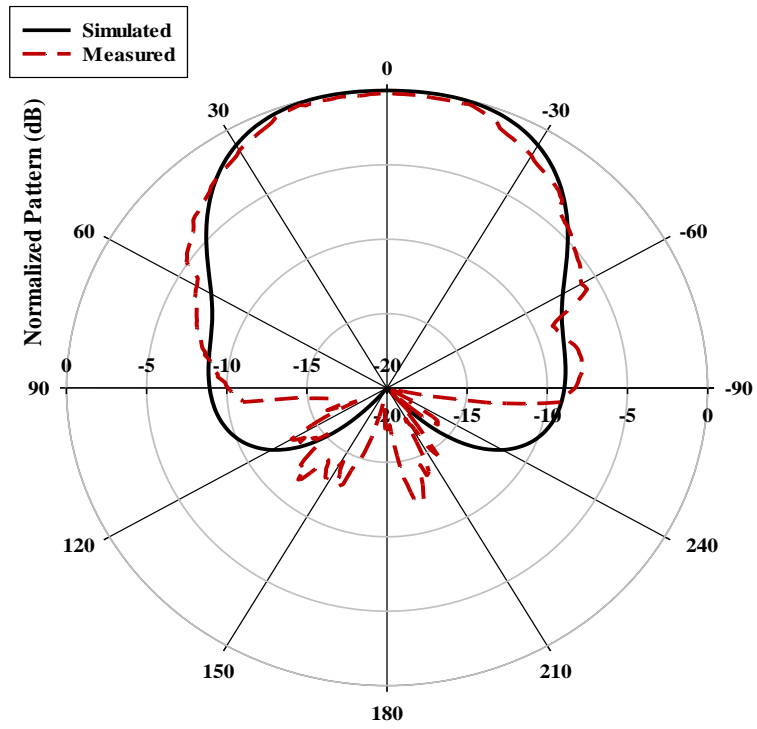
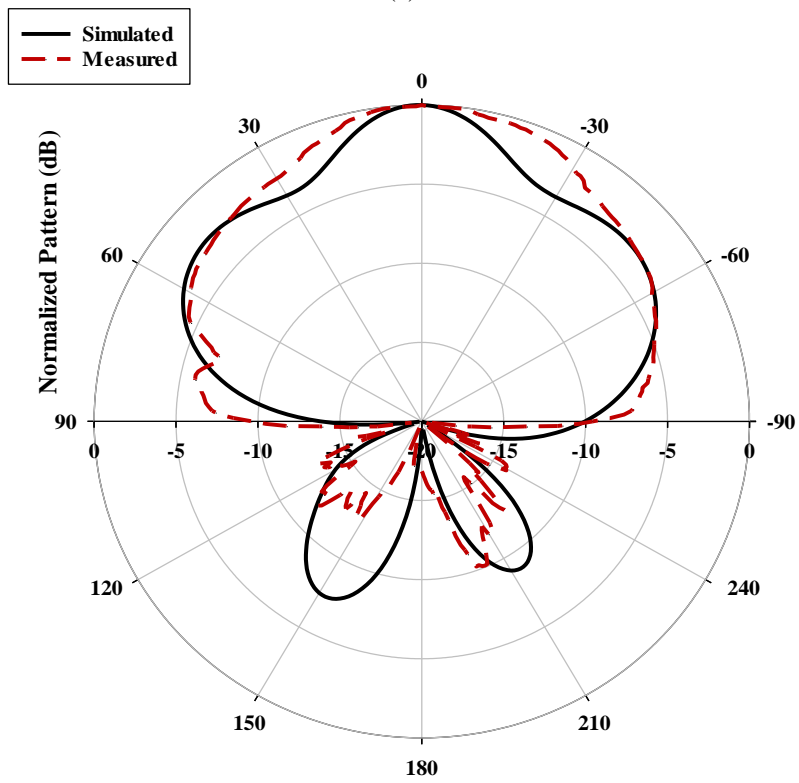


Figure 3.13: Simulated and measured realised gain for the rectangular DRA in the scenario I.



(a)



(b)

Figure 3.14: Radiation patterns of RDRA at 10.8 GHz. (a) $\Phi=0^\circ$. (b) $\Phi=90^\circ$.

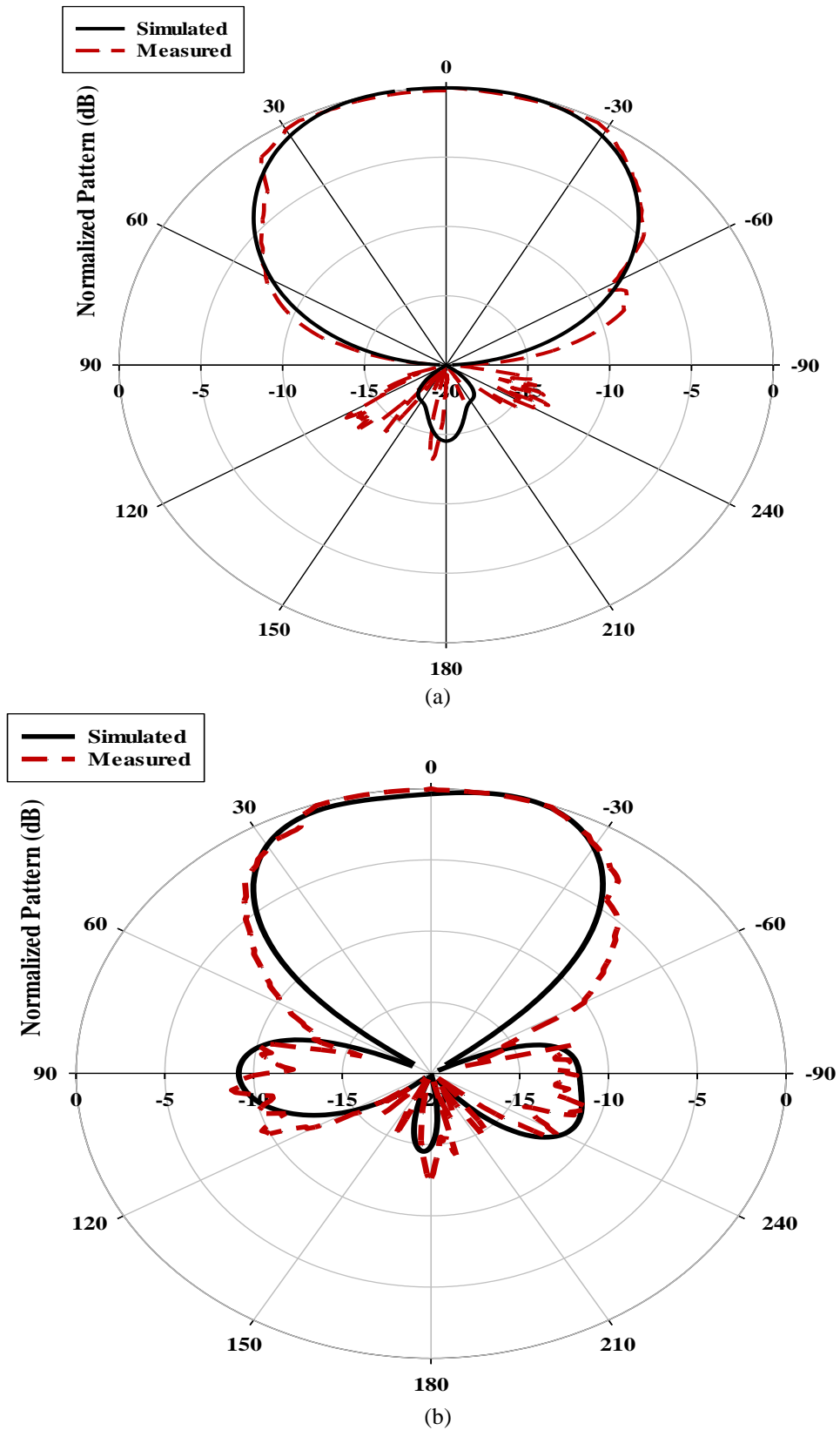


Figure 3.15: Radiation patterns of RDRA operating at the TE_{113} at 12 GHz. (a) $\Phi=0^\circ$. (b) $\Phi=90^\circ$.

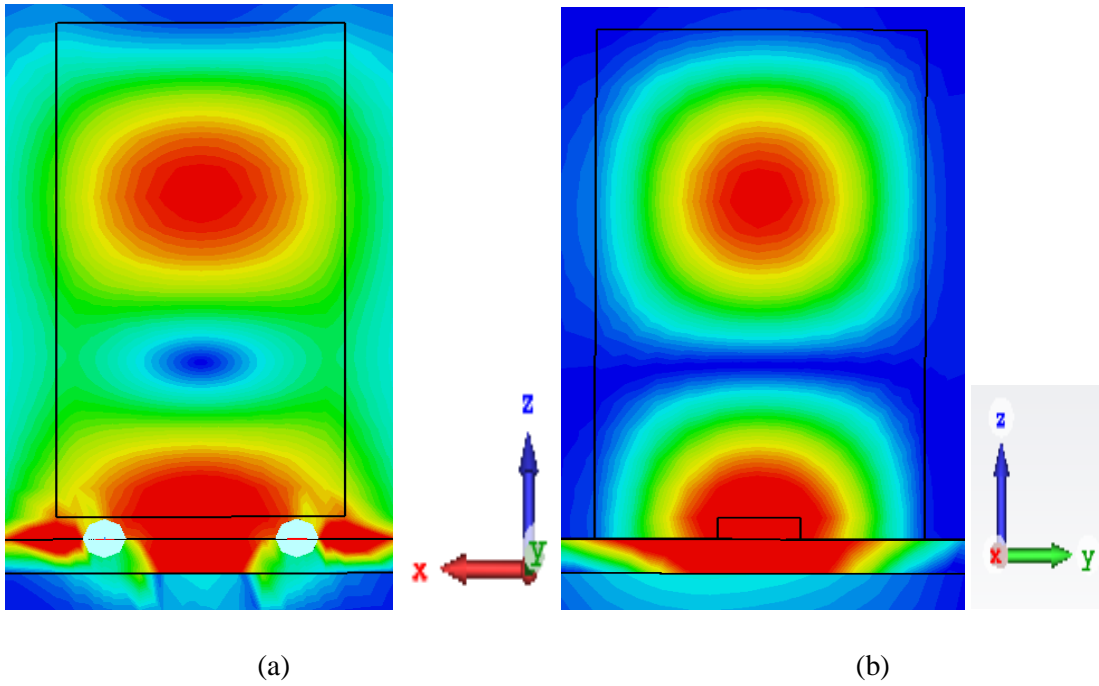


Figure 3.16: Simulated magnetic fields: (a) TE_{113} resonance modes at 10.8GHz and (b) TE_{113} at 12 GHz.

3.3.4 Rectangular DRA with PIN Diodes in the ON States

The second scenario is when both PIN diodes are ON, i.e. they are short circuited and hence leaving a feeding slot length of 4.5 mm, as shown in Figure 3.9. As mentioned earlier, the rectangular DRA operates in dual bands at 9 and 13 GHz. The simulated impedance bandwidths at 9GHz are 3.47 % (8.79–9.10 GHz) and 3.5% (12.88–13.34 GHz) compared to measured bandwidths of ~3.45% and 3% at the lower and upper frequency bands). The comparison is illustrated in Figure 3.17, where it can be observed that a good agreement has been achieved between the simulated and measured results. Figure 3.18 presents the simulated antenna realised gains of 6.4 dBi at 9 GHz and ~7.2 dBi at 13 GHz while the measured gain is ~5.8 dBi at 9 GHz and 6.8 dBi at 13 GHz. Figure 3.19 shows the normalized simulated and measured radiation patterns of the TE_{111} mode at 9 GHz. The normalized simulated and measured radiation patterns of the TE_{115} mode at 13 GHz as illustrated in Figure 3.20. It can be noted from these results that a good agreement has been achieved between the measured and simulated radiation patterns. The magnetic field distributions inside the DRAs are illustrated in Figures 3.21 and 3.22, where it can be noticed that the lower mode TE_{111} has been excited at 9GHz and higher order mode TE_{115} excited at 13 GHz.

In the case where the switches are OFF, the slot length is 6 mm, which corresponds to a resonant frequency in the TE_{113} mode. On the other hand, when the switches are ON and the slot length is reduced to 4.5 mm, the resonant frequency shifts to the TE_{111} mode at 9 GHz and to the TE_{115} mode at 13 GHz. The change in the resonant modes is due to the fact that the change in the slot length alters the effective electrical length of the resonator and hence the resonant frequencies and modes. The resonant frequencies and modes are further influenced by the material properties of the dielectric, which determine the dispersive behaviour of the resonator. By changing the slot length, you are effectively changing the electric length of the resonator and its interaction with the incoming electromagnetic waves, which leads to changes in the resonant modes and frequencies.

Achieving a reconfigurable antenna with dual bands is a desirable property in many communication and sensing applications, as it allows for greater flexibility in tuning the antenna to specific frequency bands and accommodating changing communication requirements. By incorporating two pin diodes into the design of the dielectric resonator antenna, you have created a reconfigurable antenna that can operate in two different frequency bands depending on the state of the switches. When the switches are OFF, the antenna operates in the TE_{113} mode with resonant frequencies at 10.8 GHz and 12 GHz, providing dual-band coverage in these frequency ranges. Conversely, when the switches are ON, the antenna operates in the TE_{111} and TE_{115} modes with resonant frequencies at 9 GHz and 13 GHz, respectively, allowing for reconfiguration to different frequency bands. This reconfigurable design allows for greater flexibility in tuning the antenna to specific frequency bands, which is particularly useful in situations where the communication requirements change dynamically. By switching the pin diodes, the antenna can be quickly reconfigured to operate in the desired frequency band, which is not possible with a fixed antenna design. This is the main advantage of the reconfigurable dielectric resonator antenna design, as it provides greater flexibility in accommodating changing communication requirements.

In the ON state, the slot length is $0.19\lambda_0$, where λ_0 is the wavelength of the electromagnetic wave in free space at the resonant frequency. In the OFF state, the slot length is $0.24\lambda_0$. The reason why the slot length is different in the ON and OFF states is that the two pin diodes, when ON, change the length of the slot from 6mm to 4.5mm. This change in length affects the resonant behaviour of the antenna, leading to different resonant frequencies and modes in each state. By controlling the state of the two PIN diodes, the antenna can be reconfigured to operate

at different frequencies and with different resonant modes, which is useful for many applications.

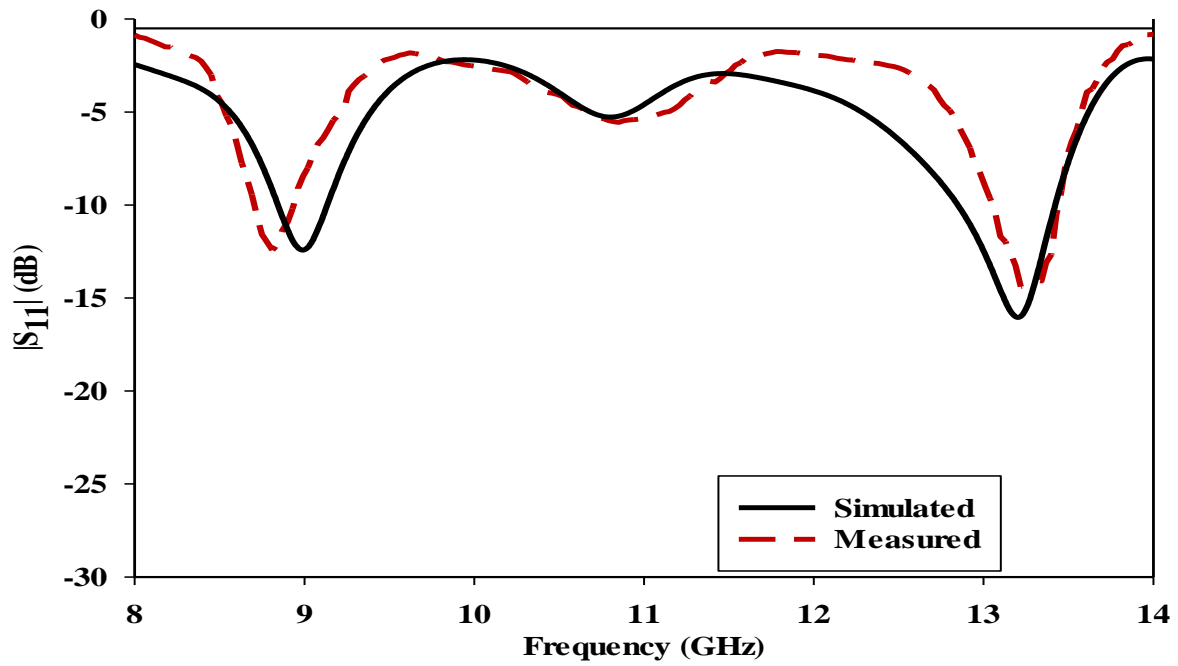


Figure 3.17: Simulated and measured return losses of rectangular DRA operating in scenario II.

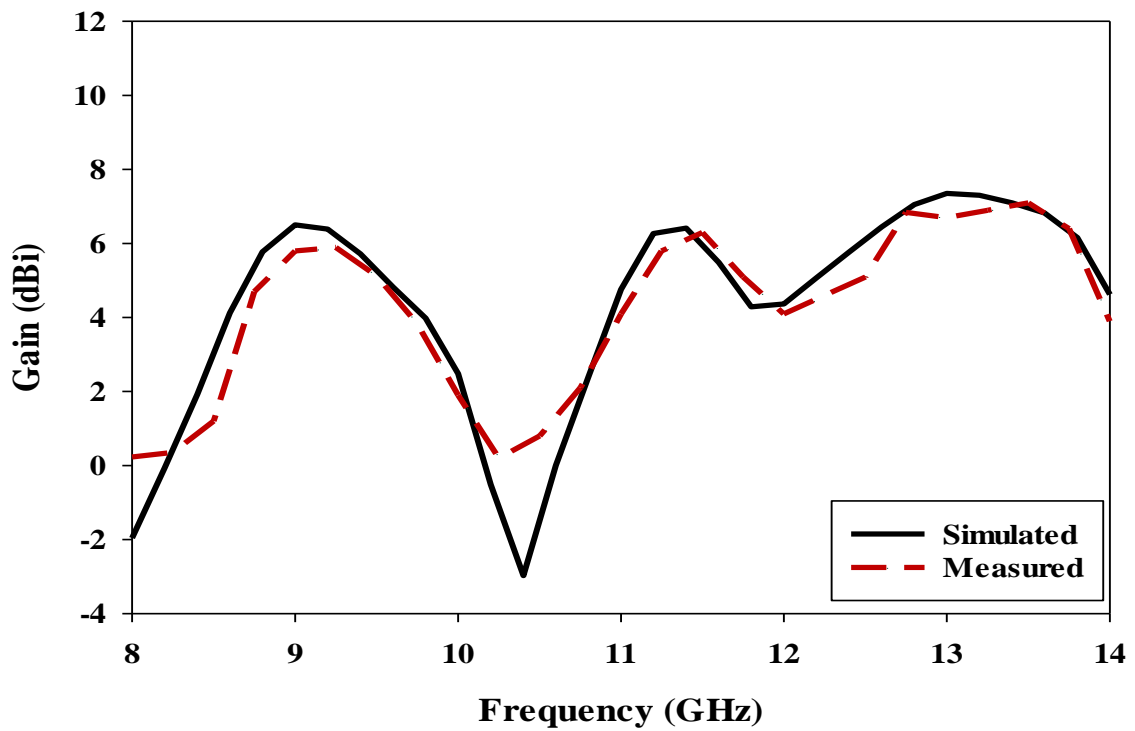
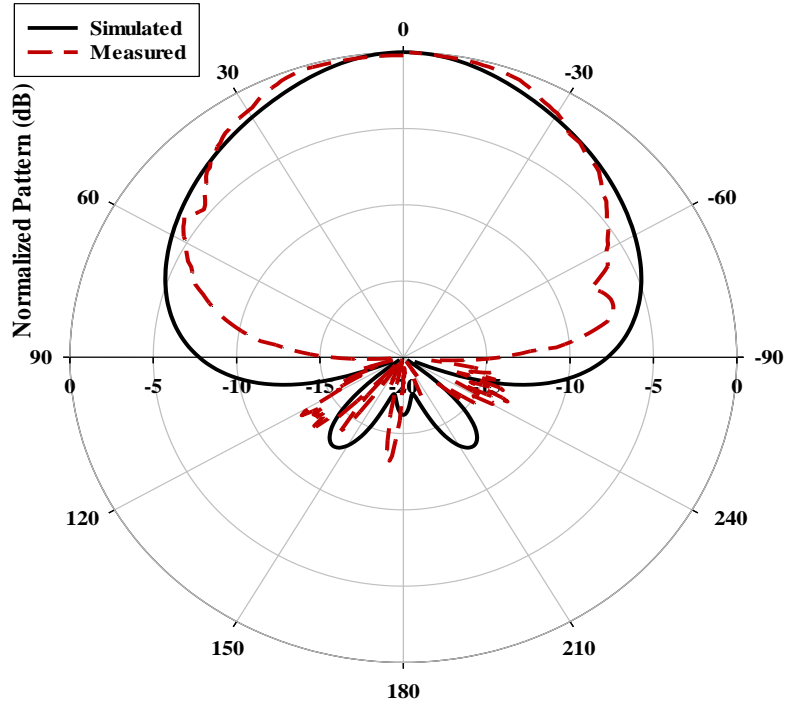
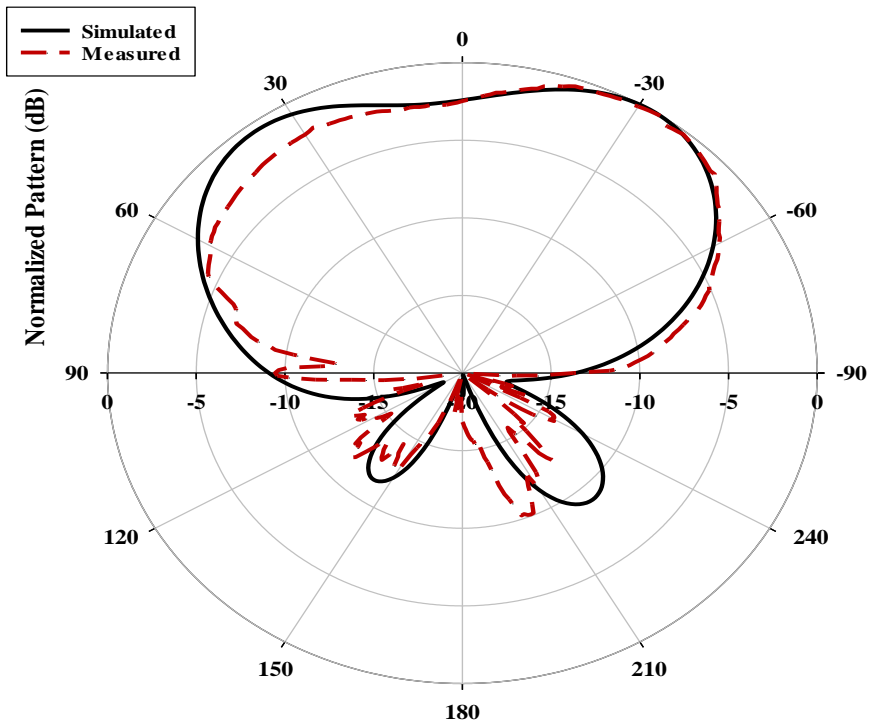


Figure 3.18: Simulated and measured gain for the rectangular DRA in scenario II.

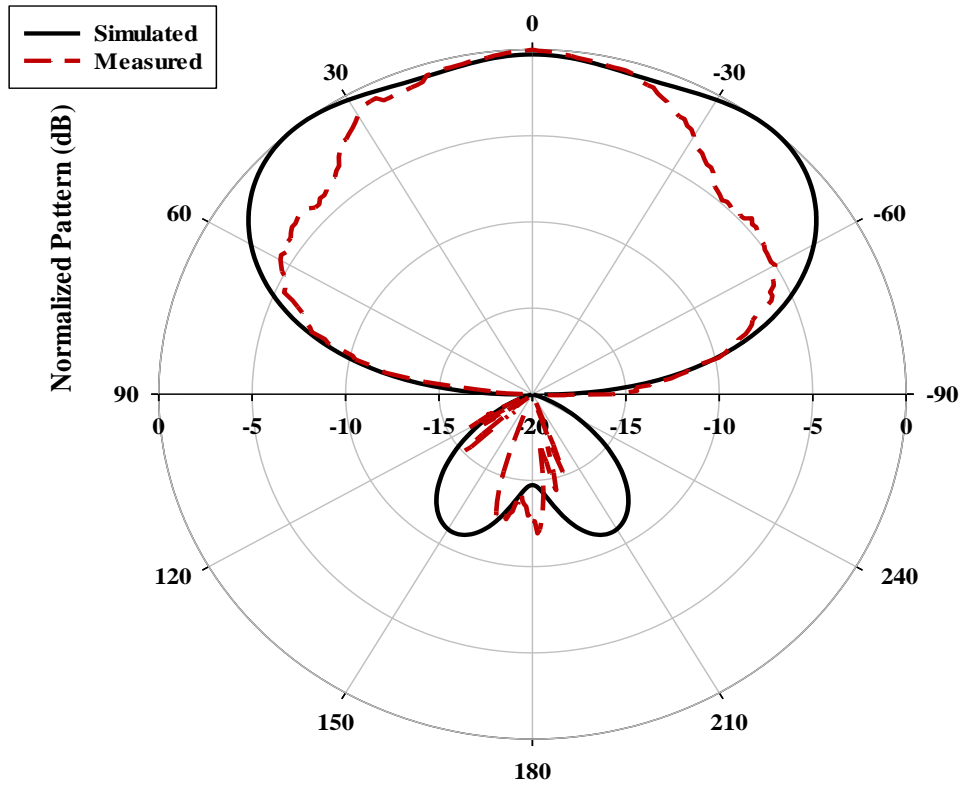


(a)

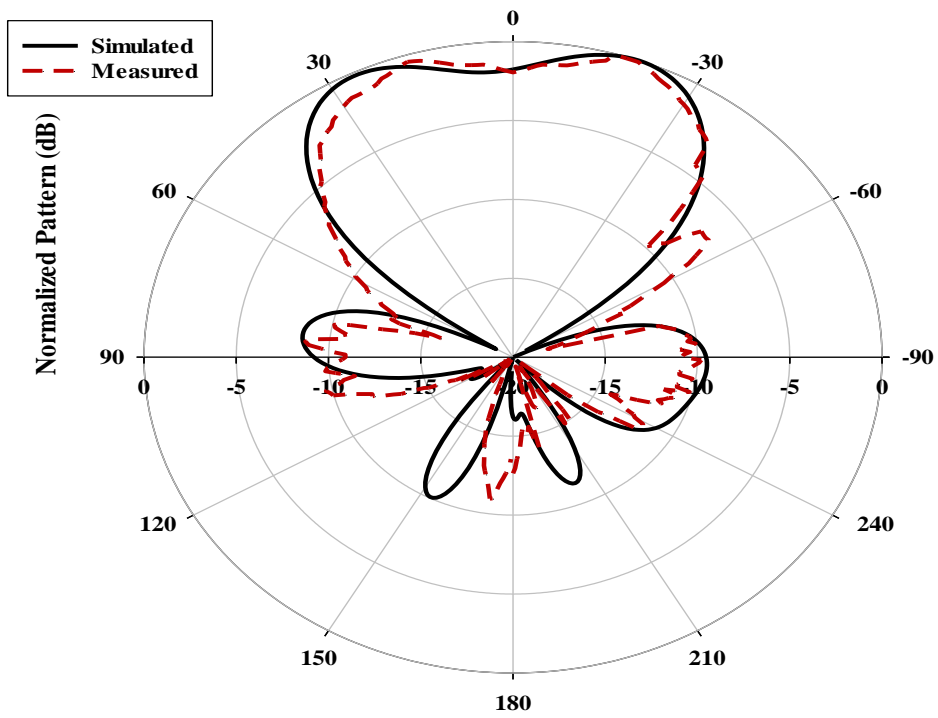


(b)

Figure 3.19: Radiation patterns of RDR operating at the TE_{111} at 9 GHz. (a) $\Phi = 0^\circ$. (b) $\Phi = 90^\circ$.



(a)



(b)

Figure 3.20: Radiation patterns of RDRA operating at the TE_{115} at 13 GHz. (a) $\Phi = 0^\circ$. (b) $\Phi = 90^\circ$.

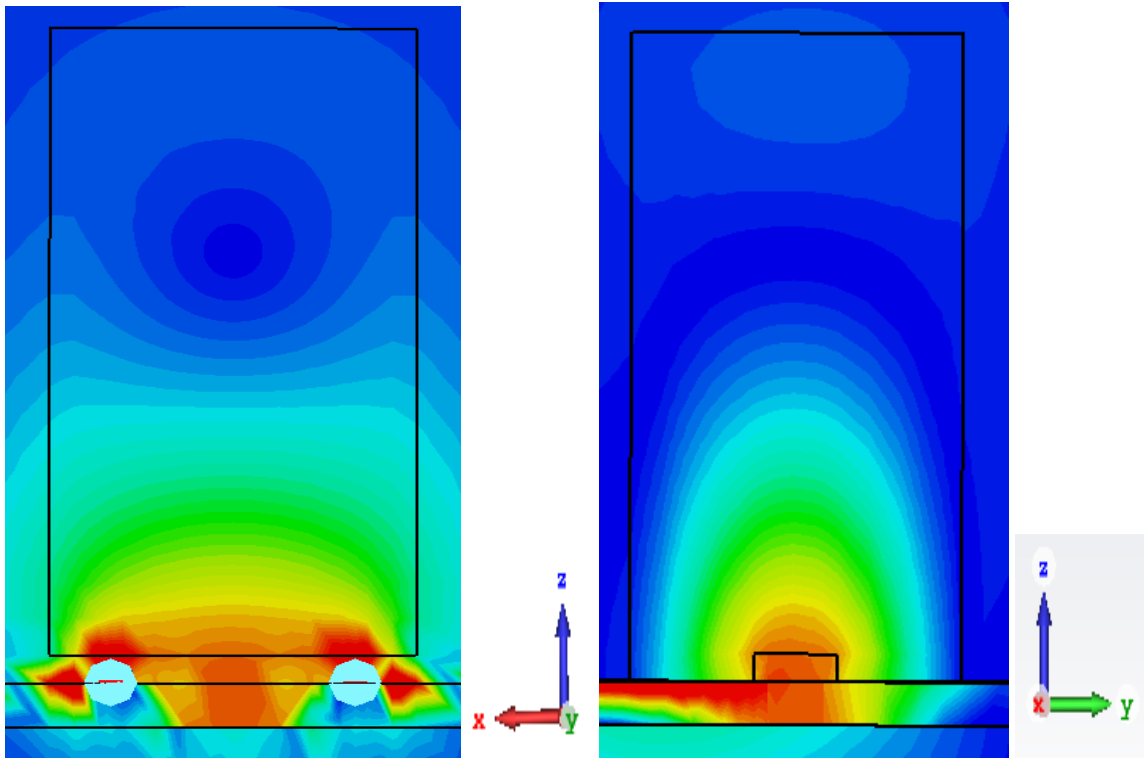


Figure 3.21: Simulated magnetic fields TE_{111} resonance modes at 9 GHz.

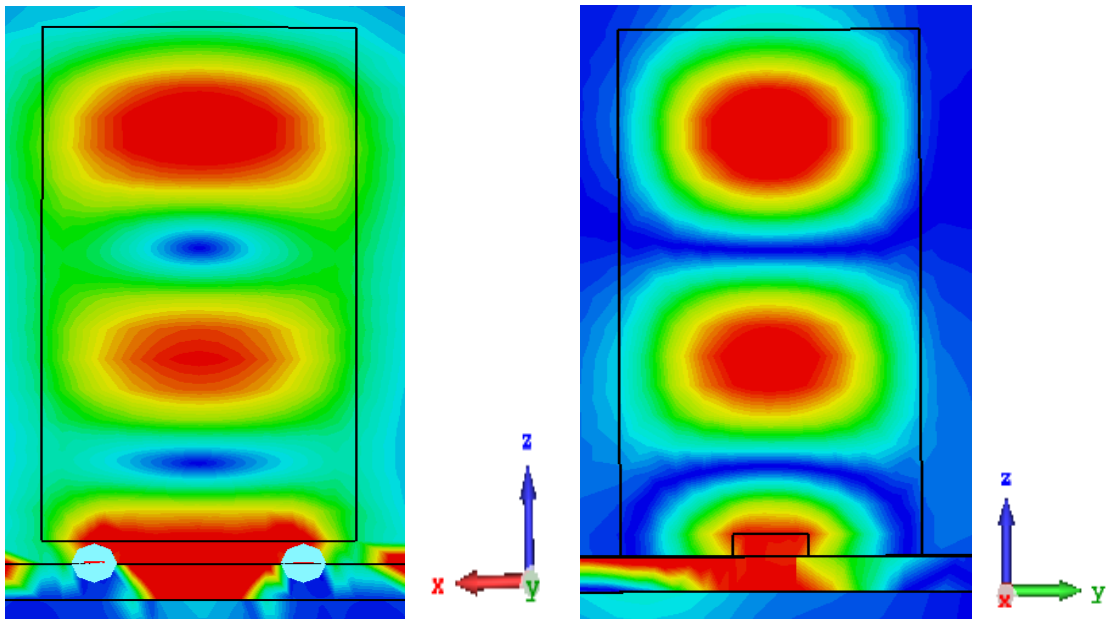


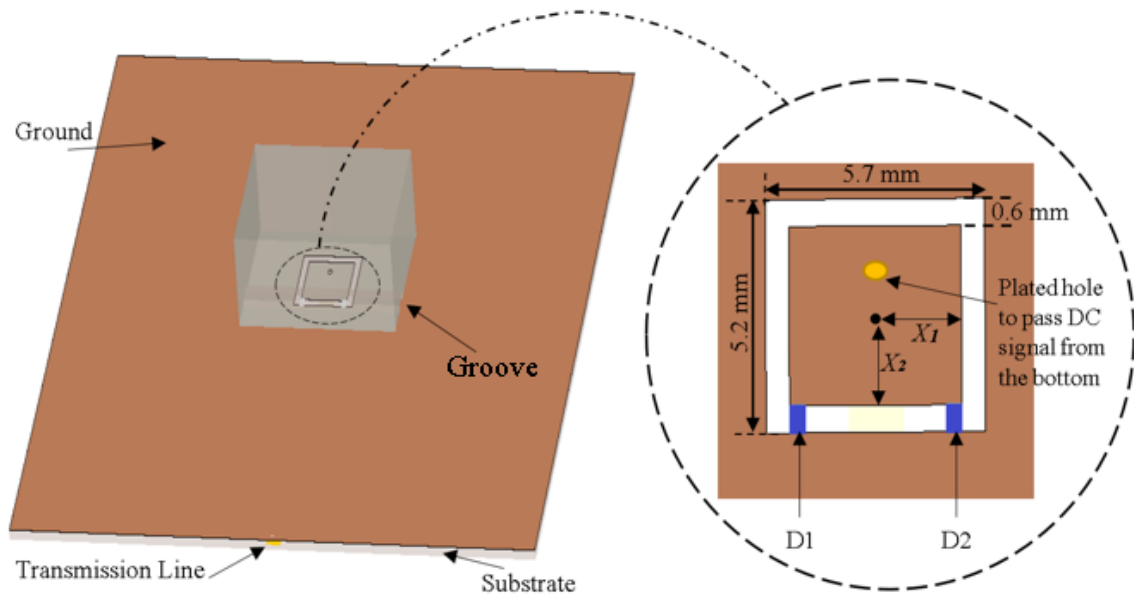
Figure 3.22: Simulated magnetic fields TE_{115} resonance modes at 13 GHz.

3.4 Reconfigurable Frequency and Radiation Pattern Rectangular DRA

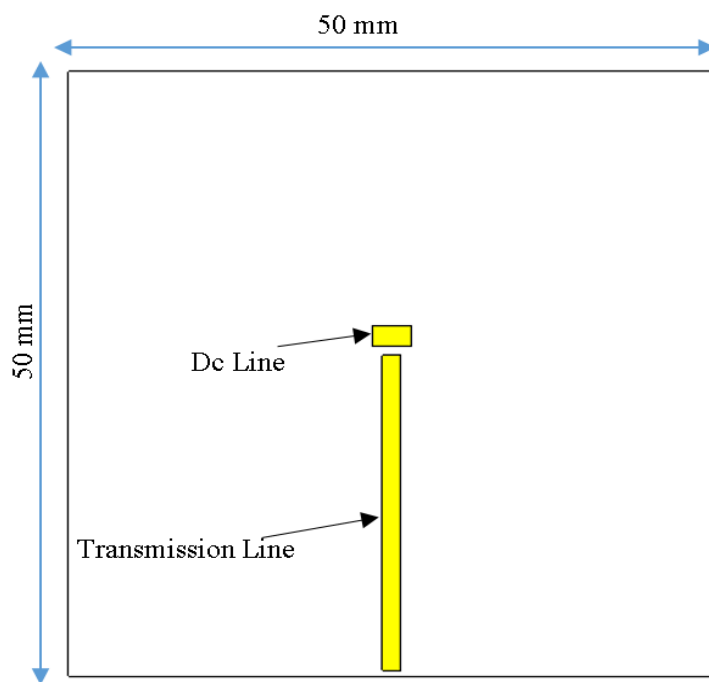
Many antennas have been designed to operate either as frequency-reconfigurable, polarisation-reconfigurable, or pattern-reconfigurable [120]. Other designs combine two types of reconfigurability, e.g., frequency and radiation pattern as reported in [121-124].

3.4.1 Antenna Configuration

A rectangular DRA was simulated using low-loss Alumina, which has a dielectric constant of $\epsilon_r=9.9$ and a loss tangent of $\tan \delta < 0.0001$ as illustrated in figure 3.23 (a). The rectangular DRA was placed on a $50 \times 50 \text{ mm}^2$ ground plane and excited using a 50Ω microstrip-feed line through a slot aperture etched on the ground plane. Additionally, a microstrip line was printed on the substrate's bottom and had an open stub length of $l_{stub}=1.5\text{mm}$ to achieve optimal matching as illustrated in Figure 3.23 (b). Figure 3.24 illustrates the dimensions of a rectangular DRA as $a=15\text{mm}$, $b=10 \text{ mm}$, and $h=5.6\text{mm}$ [116] with a groove that has been etched at the lower DRA side with respective depth, length and width of 0.5 mm, 8.6 mm and 1.5 mm. The groove has been incorporated to accommodate the height of the PIN diodes and hence allowing the DRA to sit securely on the ground plane without any gaps between them. A rectangular ring slot has been utilised to excite the DRA with optimized dimensions of $5.7 \text{ mm} \times 5.2 \text{ mm}$ and a slot width of 0.6 mm. The feeding microstrip transmission line has a length and width of 25mm and 1.5mm, respectively. The ground plane has two parts: an inner ring rectangular ground plane and an outer rectangular ground plane, where x_1 and x_2 indicate the dimensions of the inner ring rectangular ground plane from the centre of the ground plane.



(a)



(b)

Figure 3.23: The proposed ring slot-feed network of RDRA (a) top view (b) bottom view.

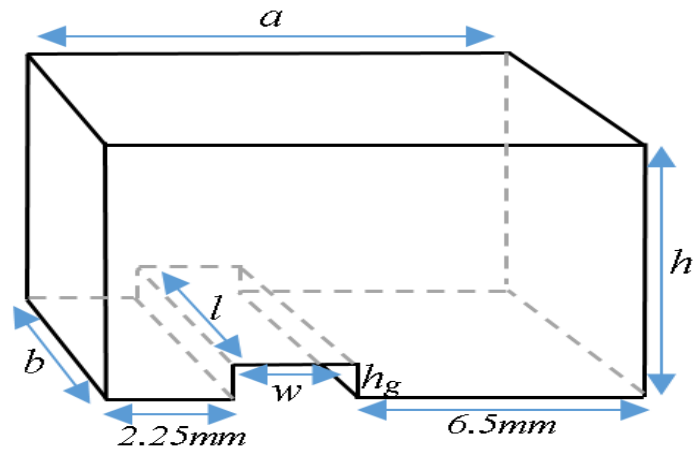


Figure 3.24: Rectangular DRA with a Groove.

In this research, two PIN diodes are used with a rectangular ring slot to achieve the required reconfigurability. Figure 3.23a reversed biased illustrates that the two PIN diodes, D1 and D2, are placed on the lower side of the rectangular ring slot to achieve three different scenarios. Scenario I: D1 is ON and D2 is OFF, scenario II: D1 is OFF and D2 is ON, scenario III: D1 and D2 are OFF. A forward-biased PIN diode was used to create a short circuit for the purpose of enabling reconfigurability of the frequency and radiation pattern. The dimensions of the diode were determined based on the datasheet and the position was optimized using CST software.

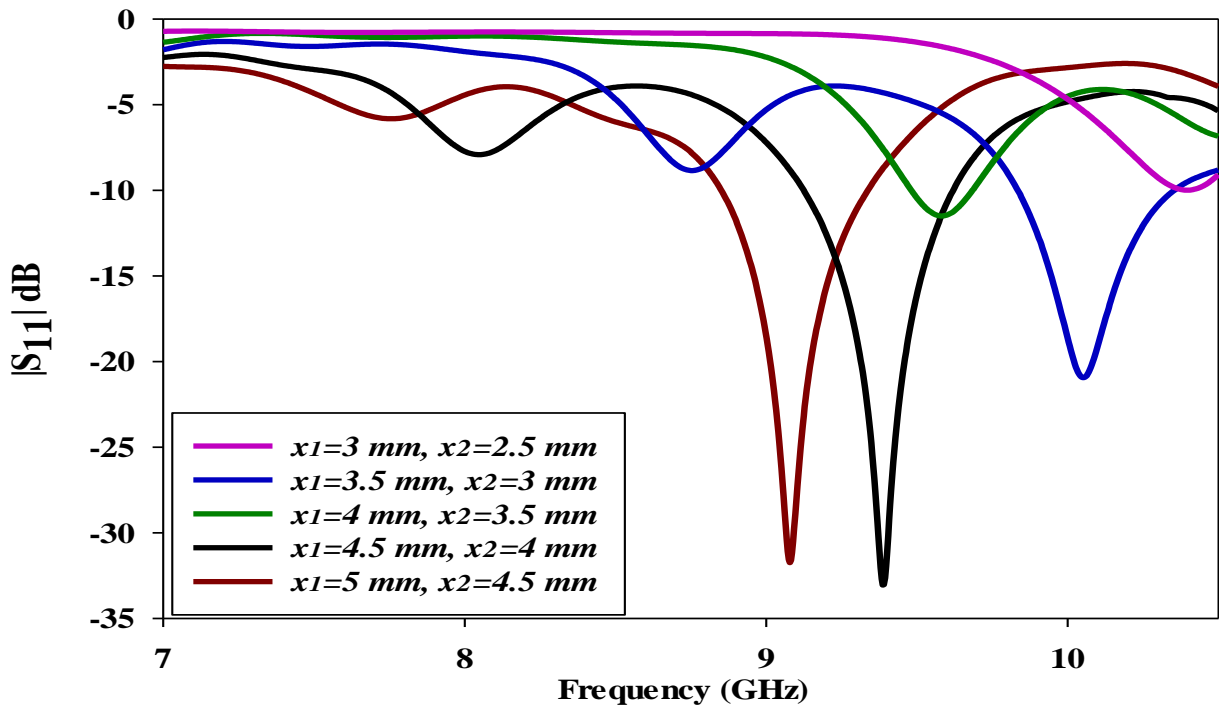
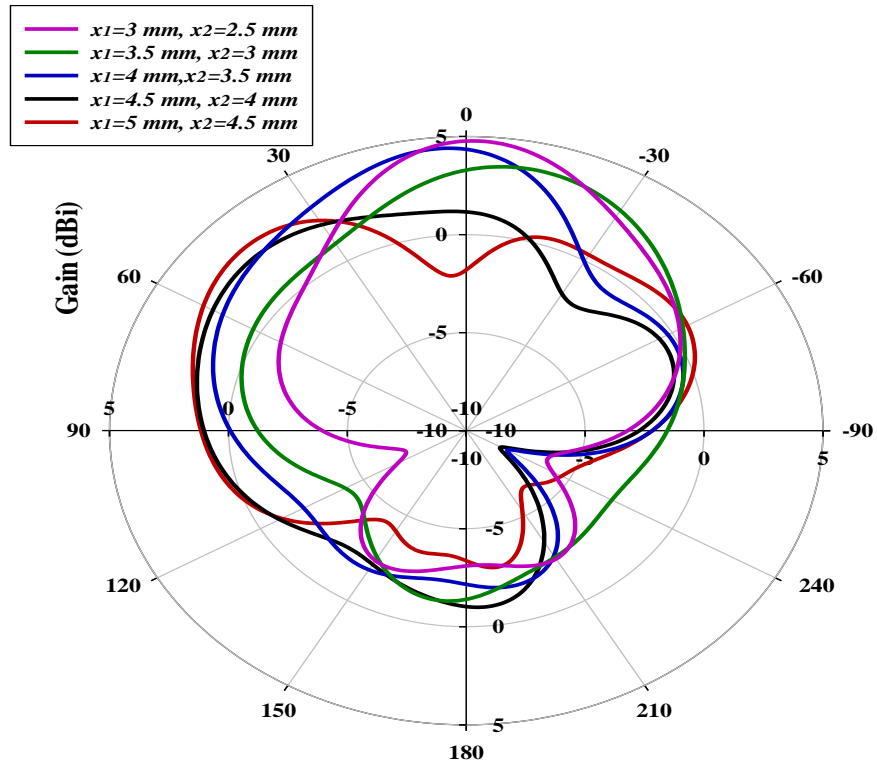
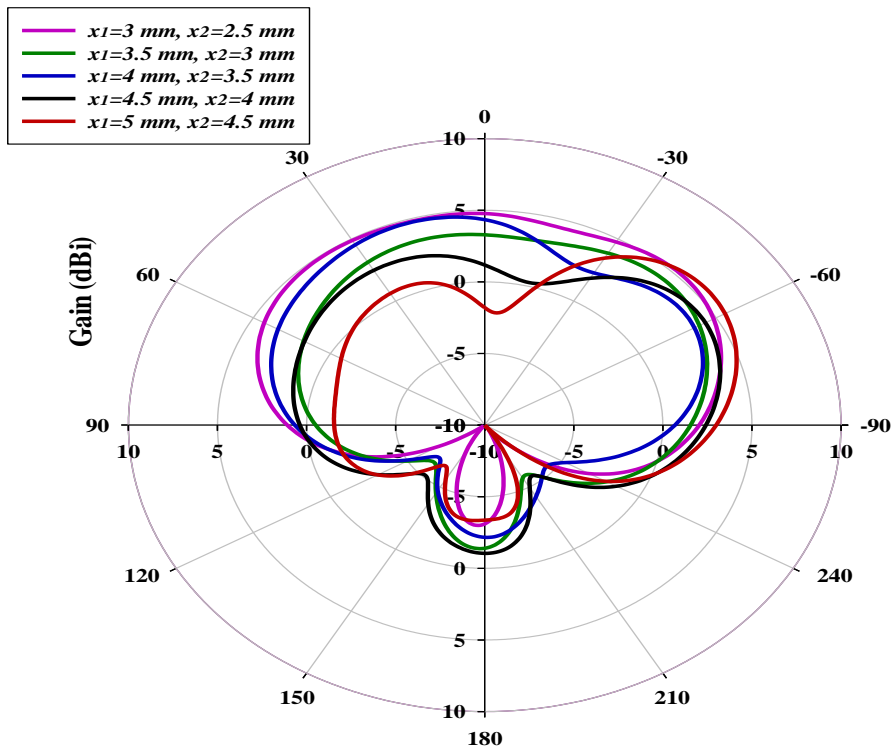


Figure 3.25: Simulated reflection coefficient for scenarios I and II with different x_1 and x_2 values.



(a)



(b)

Figure 3.26: Simulated radiation pattern for scenarios I and II with different x_1 and x_2 values. a) E- Plane and b) H- Plane.

Figures 3.25 and 3.26 present the reflection coefficient and radiation pattern for scenarios I and II, with different values of x_1 and x_2 . From Figure 3.25, it can be observed that the resonance frequency strongly depends on the choice of x_1 and x_2 and PIN diodes. For instance, when $x_1 = 4.5$ and $x_2 = 4$ mm, the rectangular DRA resonance mode of TE_{111} is excited at 9.5 GHz. Additionally, Figure 3.26 demonstrates that a 45° shift in the main beam can be achieved at two values of x_1 and x_2 , namely, $x_1 = 4.5$ and $x_2 = 4$ mm, and $x_1 = 5$ and $x_2 = 4.5$ mm. It is noteworthy that the best values are $x_1 = 4.5$ and $x_2 = 4$ mm. The beam shift in the reconfigurable radiation antenna design is achieved due to the presence of the two PIN diodes. When one of the switches is ON, causing a low impedance, the short in the slot changes the electric field distribution of the antenna.

The reflection coefficient for scenario III with different values of x_1 and x_2 is illustrated in Figure 3.27. It can be noted that the achieved resonance is at 8 GHz when $x_1 = 4.5$ and $x_2 = 4$ mm, which agrees with the x_1 and x_2 values of scenarios I and II. Figure 3.28 shows different radiation patterns for various values of x_1 and x_2 . It can be noticed that for all x_1 and x_2 values, the proposed antenna radiation pattern is broadside when both switches are open circuits.

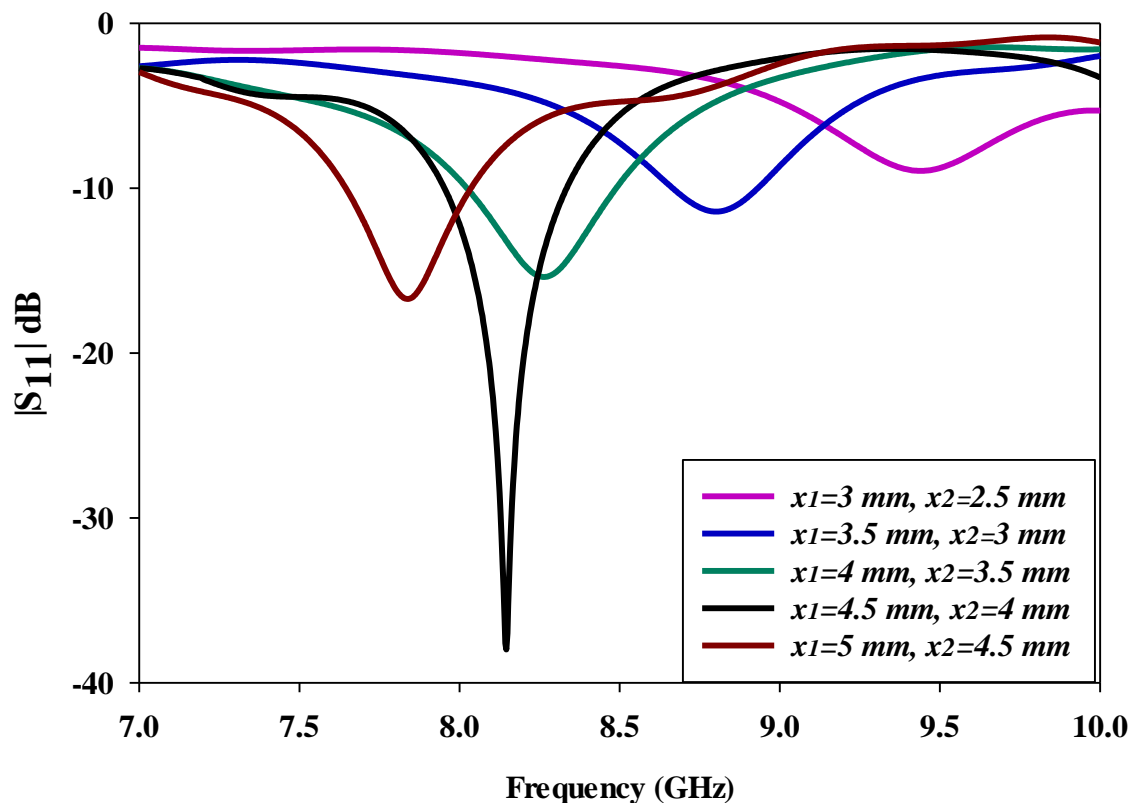
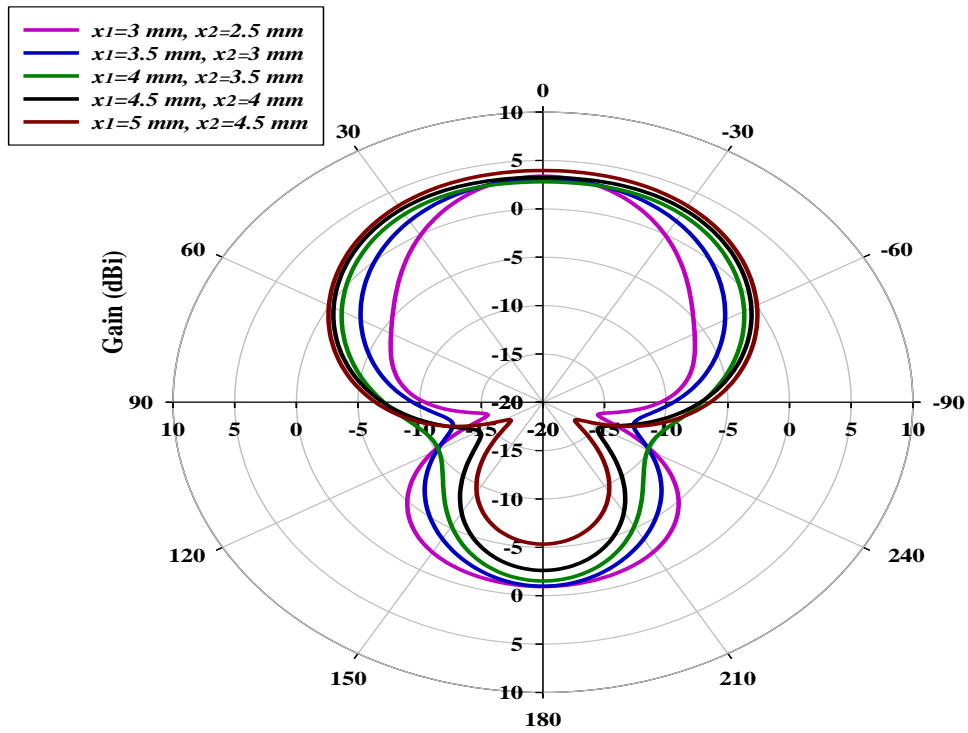
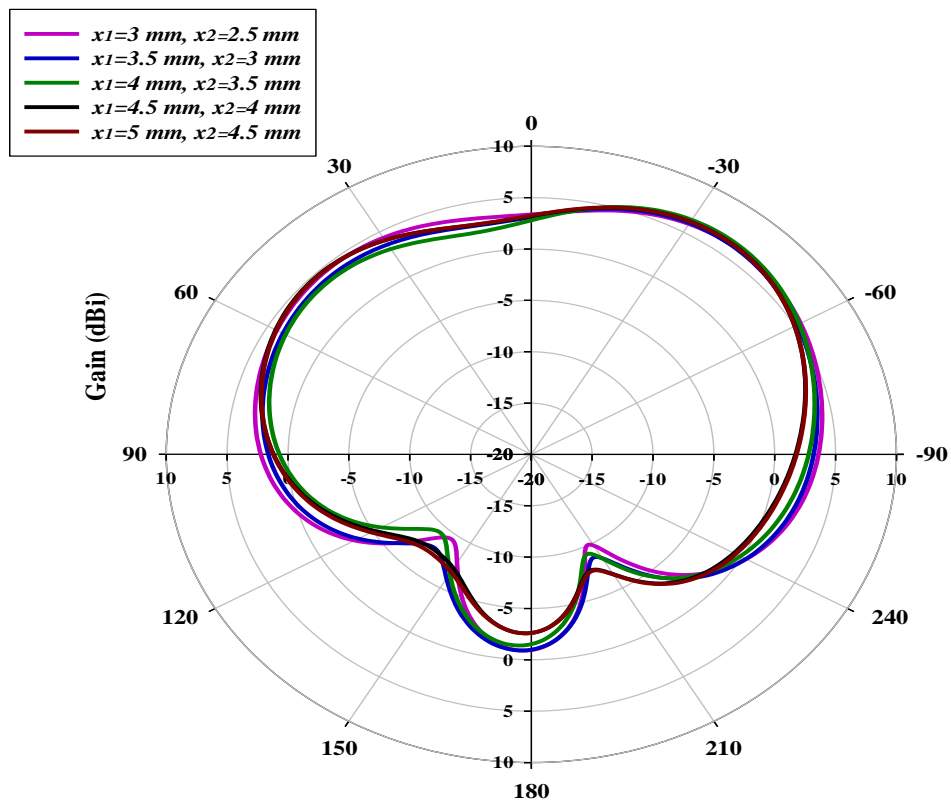


Figure 3.27: Simulated reflection coefficients for scenario III with different x_1 and x_2 values.



(a)

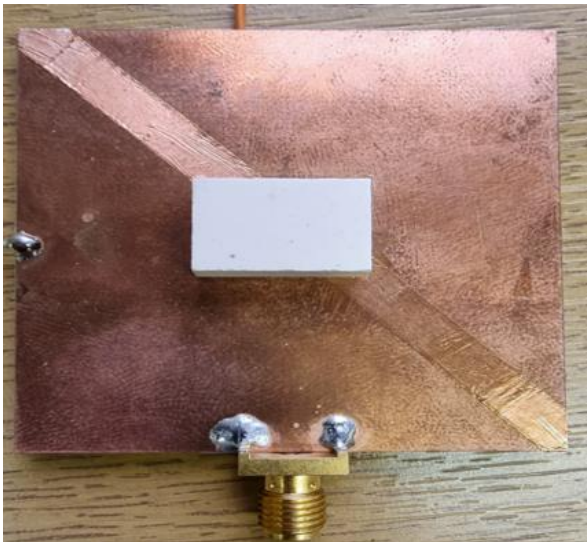


(b)

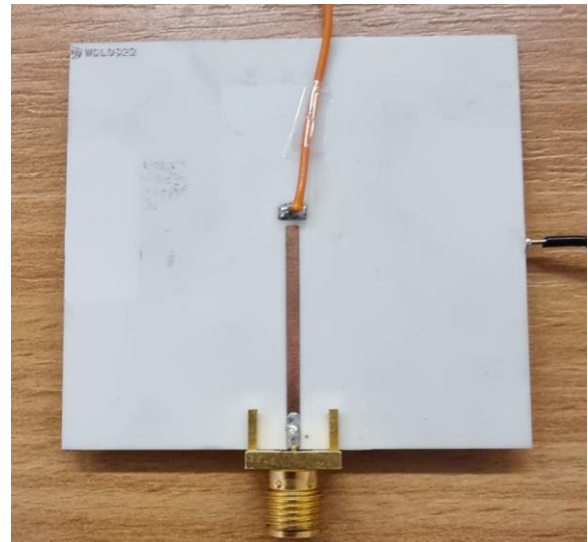
Figure 3.28: Simulated radiation pattern for scenario III with different x_1 and x_2 values. a) E-Plane and b) H-Plane.

3.4.2 Experimental Results.

Figure 3.29a presents the front view of the fabricated feed network configuration and PIN diode. A microstrip line has been printed on the bottom of the substrate as shown in Figure 3.29b. The commercially available substrate is Rogers RO4535 with an equal length and width of 50 mm^2 and thickness of 0.8 mm , dielectric constant of 3.38 , and loss tangent of 0.0027 . The DRA has been attached to the metallic ground plane using a thin (0.036 mm) double-sided adhesive copper tape. Each PIN diode has respective dimensions of $1.2 \text{ mm} \times 0.5 \text{ mm} \times 0.2 \text{ mm}$ for the length, width, and height. The diodes are located closer to the lower end of the feeding slot as demonstrated in Figure 3.23a and have been attached to the ground plane using conductive silver paint. Two biasing wires are connected to the two sections of the ground plane.



(a)



(b)



(c)

Figure 3.29: a) The RDRA feed network with PIN diodes, b) bottom view c) Photographs of RDRA with a groove

One of the biasing wires is connected to an outer section of the ground plane, as shown in Figure 3.29a. The inner, smaller section of the ground plane is connected to a DC transmission line through a plated hole that passes through the substrate, as illustrated in Figure 3.29b. The rectangular DRA featuring a groove was fabricated by Almath Crucibles Ltd utilizing Alumina. The fabrication was carried out with precision, achieving an accuracy of 0.05mm. This is illustrated in Figure 3.29c. The reflection coefficient, S_{11} , has been measured using a network analyser through a calibrated cable and the radiation patterns have been measured using an anechoic chamber as demonstrated in Figure 3.30. As mentioned earlier, three scenarios have been achieved from the proposed antenna as scenarios I, II and III.

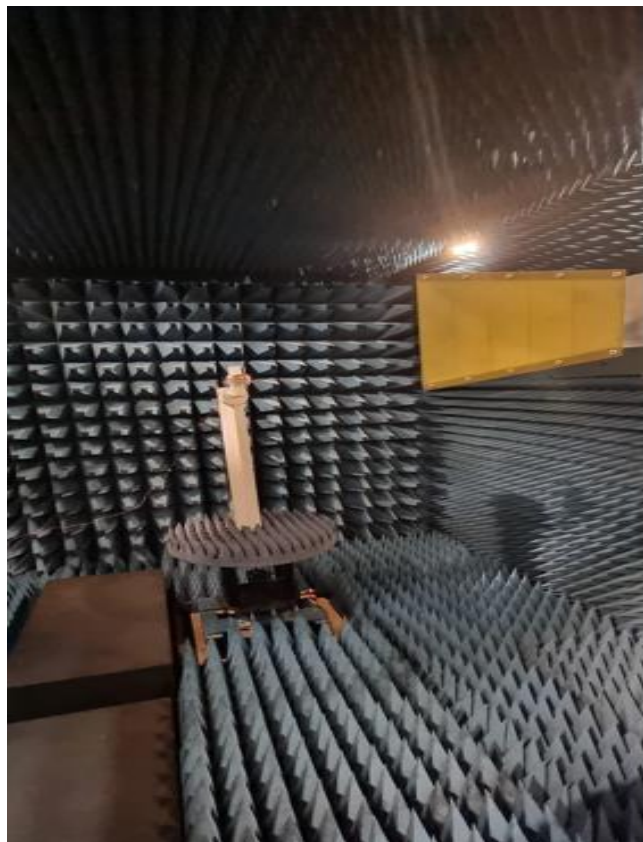


Figure 3.30: The proposed antenna inside the anechoic chamber.

3.4.2.1 Scenario I.

In the first scenario, the first PIN diode, i.e. D_1 in Figure 3.31, is reverse biased while the other diode, D_2 , has been biased to be in the ON state. Figure 3.31 shows the positive DC signal is connected to the positive terminal, P, of D_2 via the inner rectangular ground plane section and the negative terminal N is connected to the outer ground plane. The negative, N, terminal of D_1 was connected to the positive DC via the inner rectangular ground plane section and the

positive terminal P was connected to the negative DC via the outer rectangular ground plane section to be in the OFF State.

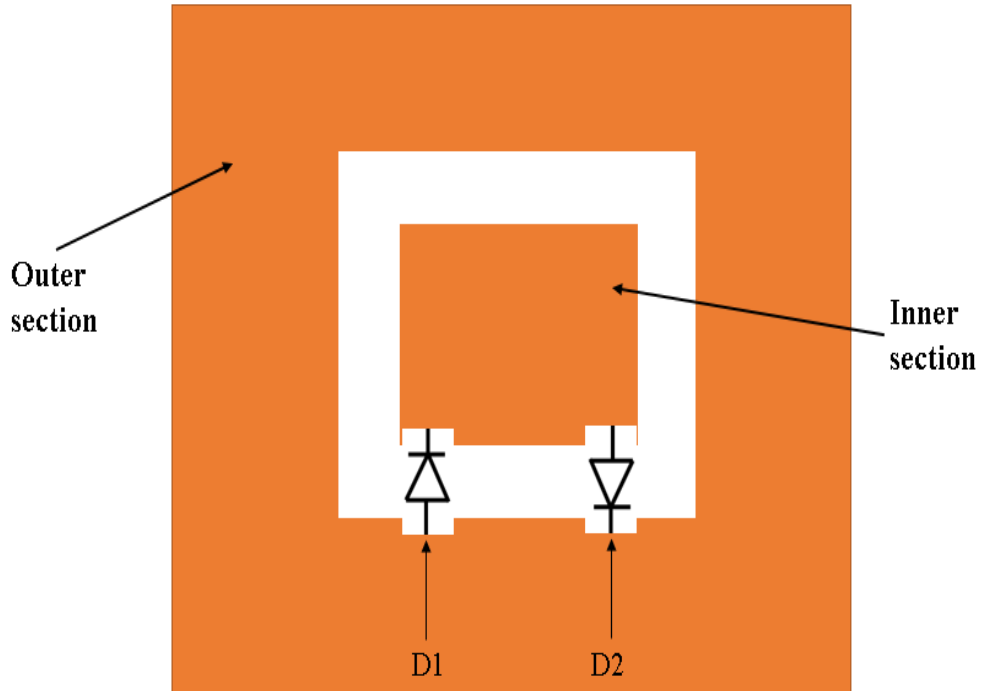


Figure 3.31: PIN diode connections.

The measured and simulated reflection coefficients are presented in Figure 3.32, where it can be noted that the simulated bandwidth of $\sim 5\%$ has been achieved over a frequency range of 9.27 to 9.75 GHz. However, a measured bandwidth is 4.7% with a small shift compared to simulations. The lower order TE_{111} mode has been excited at 9.5 GHz. The measurements demonstrate that the return loss is lower than with the simulated counterpart due to the experiment's noise and multipath impact. As can be noted from Figure 3.33, the measured gain at 9.5GHz is 4.8 dBi compared to a simulated counterpart of ~ 5.2 dBi. A good agreement has been achieved between the simulated and measured radiation patterns of the TE_{111} mode. The radiation beam is deflected by angles of $+45^\circ$ in the E-plane at 9.5 GHz as illustrated in Figure 3.34. The magnetic field distribution inside the rectangular DRA is demonstrated in Figure 3.35, where it is evident that the mode TE_{111} is excited at 9.5 GHz.

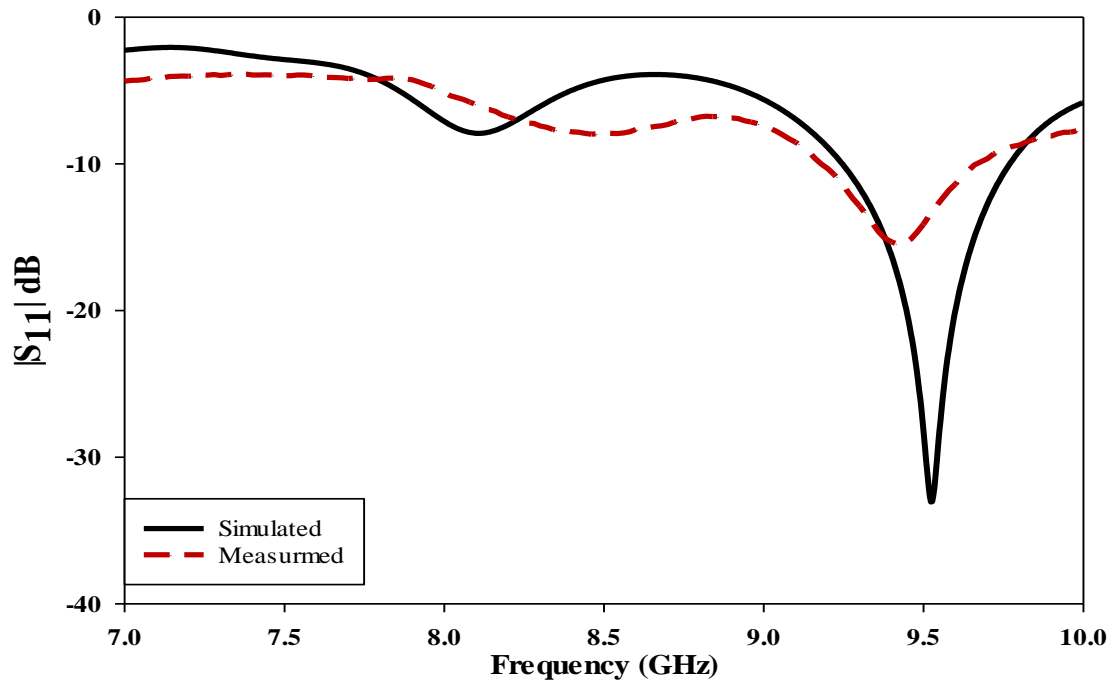


Figure 3.32: Simulated and measured reflection coefficients for scenario I.

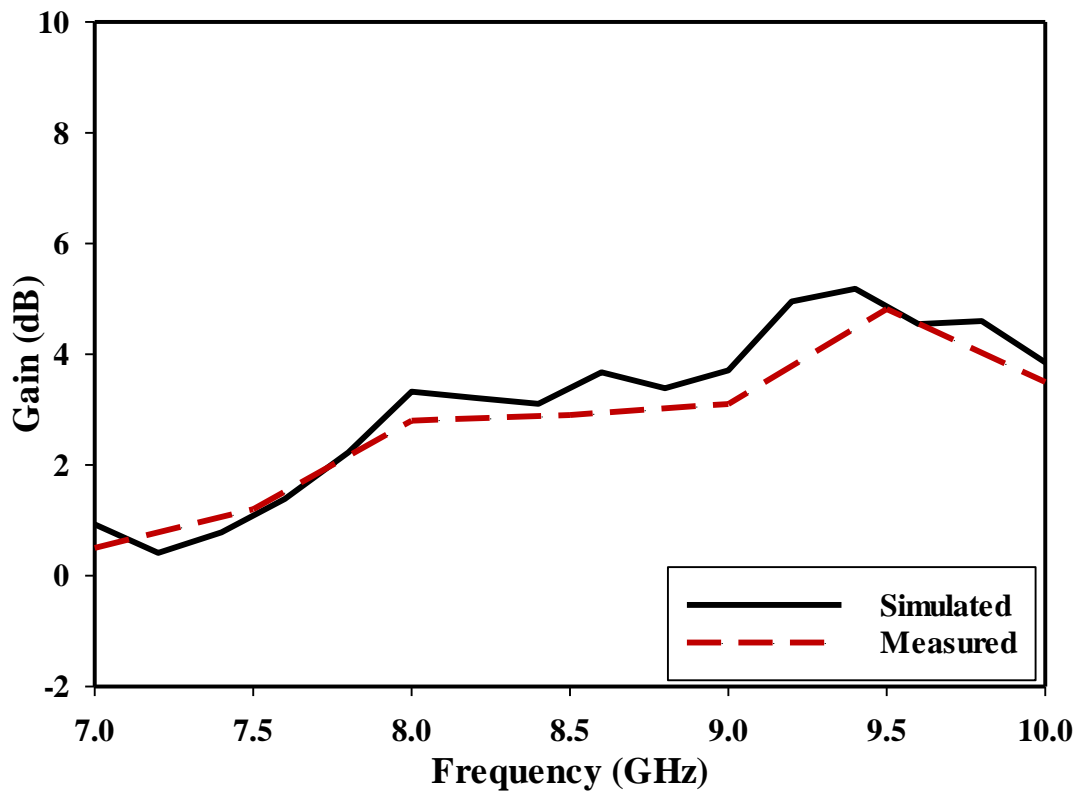
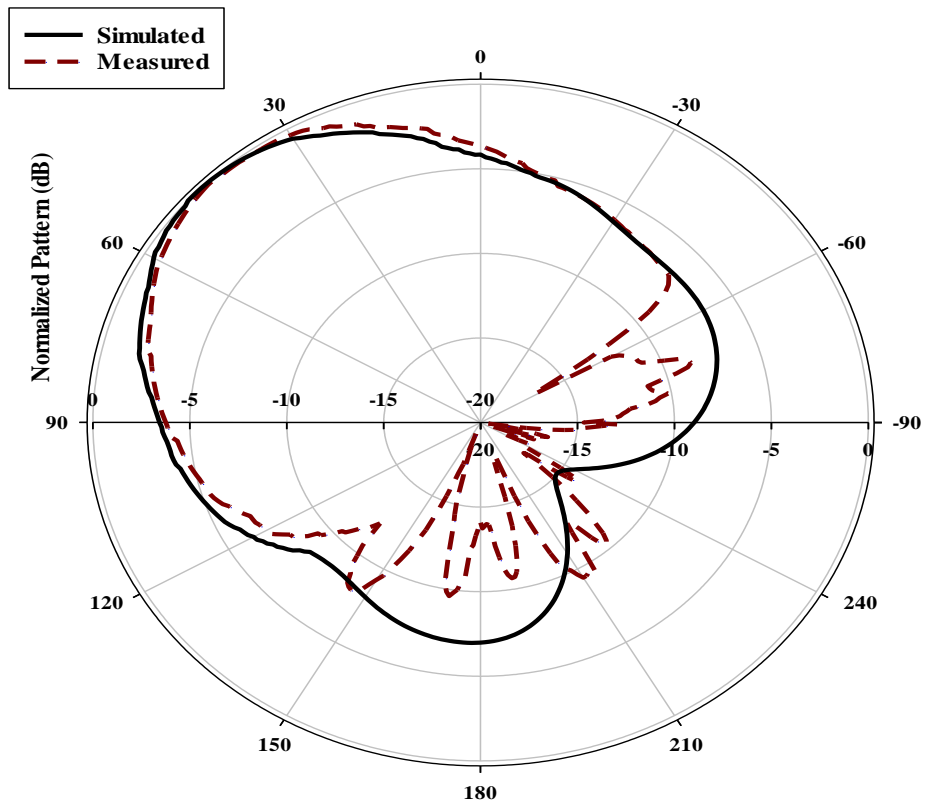
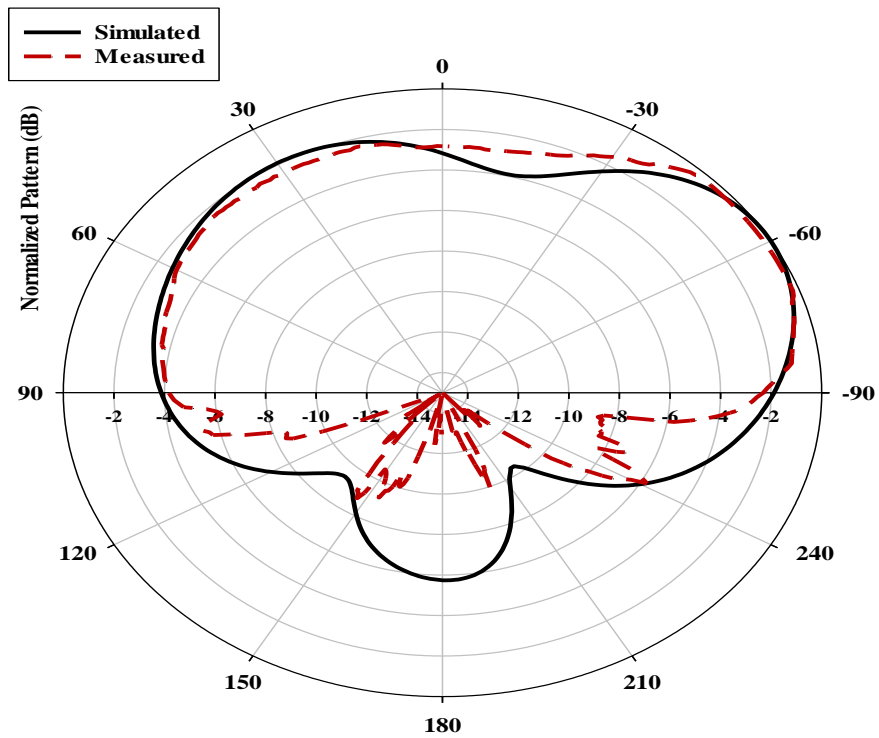


Figure 3.33: Simulated and measured gain for scenario I.



(a)



(b)

Figure 3.34: Simulated and measured radiation pattern for scenario I at 9.5 GHz. a) E-Plane and b) H-Plane.

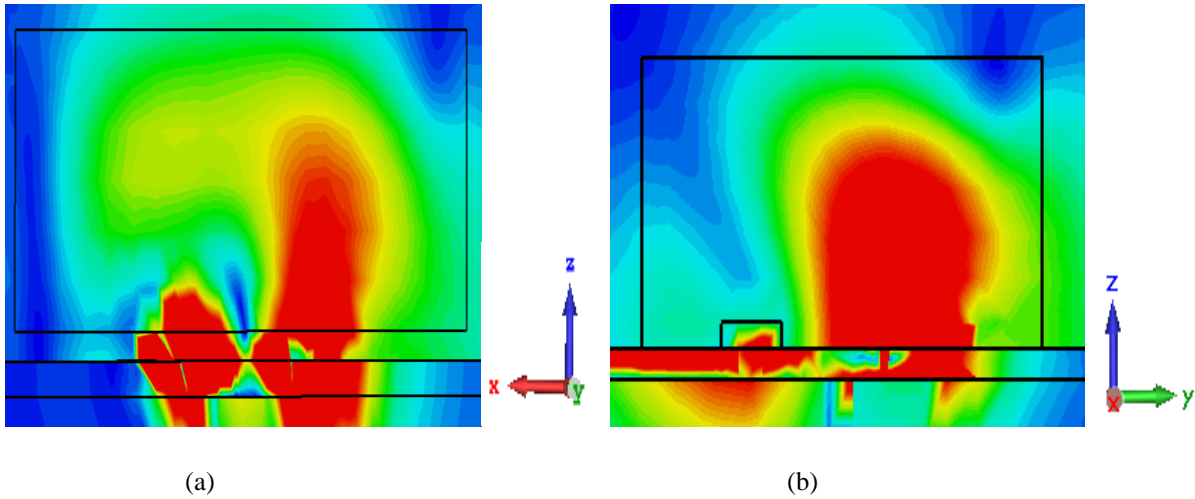


Figure 3.35: The magnetic field distributions of the TE_{111} modes inside the RDRA. a) xz-plane, b) yz-plane.

3.4.2.2 Scenario II.

In the second scenario, the first PIN diode, D_1 , is biased to be in the ON state, while the other PIN diode, D_2 , is biased to be in the OFF state. In this scenario, the bias wires will be exchanged. The positive DC signal will be connected to the outer ground plane section, and the inner rectangular ground plane section will be connected via negative DC. The simulated impedance bandwidth is $\sim 5\%$ over a frequency range of 9.27 to 9.75 GHz, as demonstrated in Figure 3.36. However, the actual measured bandwidth is $\sim 4.7\%$, with a small shift compared to the simulated result. As illustrated in Figure 3.37, the measured gain at 9.5 GHz is 4.8 dBi, while the simulated antenna shows a gain of 5.2 dBi. For the TE_{111} mode, the simulated and measured radiation patterns agree closely with each other as illustrated in Figure 3.38. The main beam is steered by angles of -45° in the E-plane. The magnetic field distributions inside the rectangular DRAs demonstrate the excitation of the TE_{111} resonance mode at 9.5 GHz as shown in Figure 3.35.

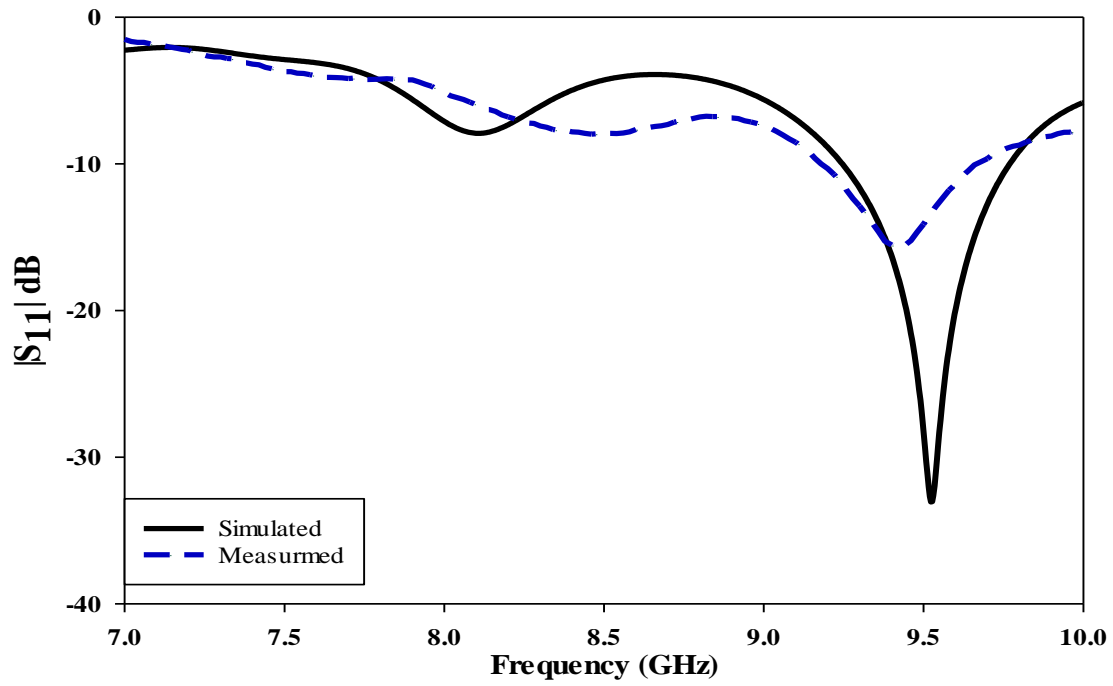


Figure 3.36: Simulated and measured reflection coefficients for scenario II.

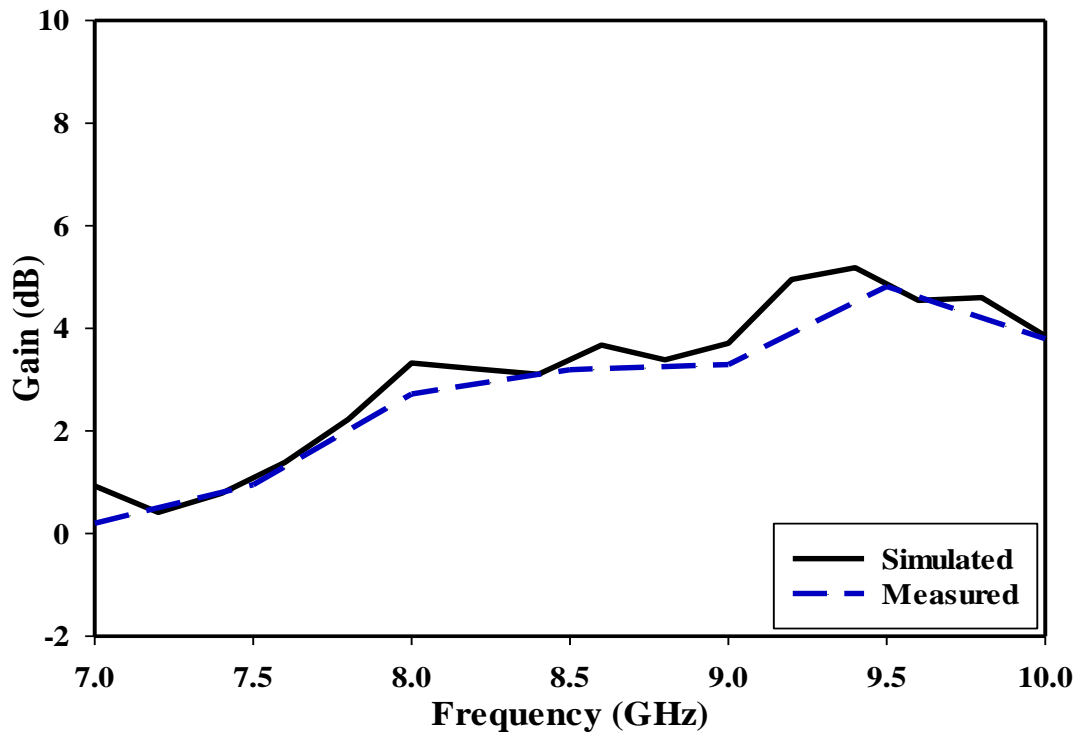
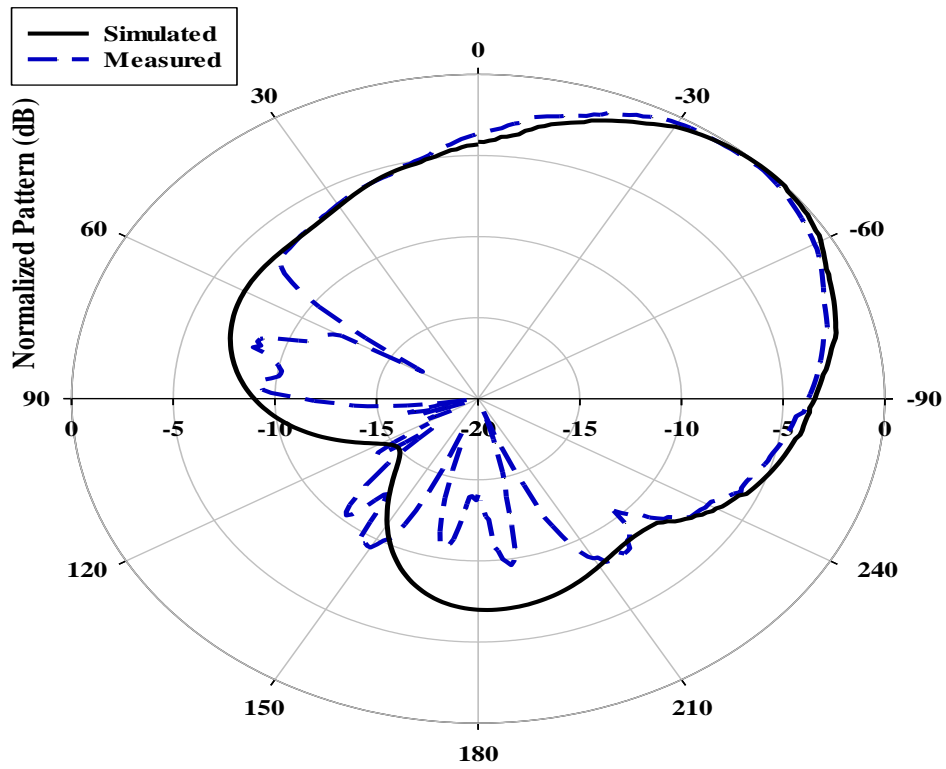
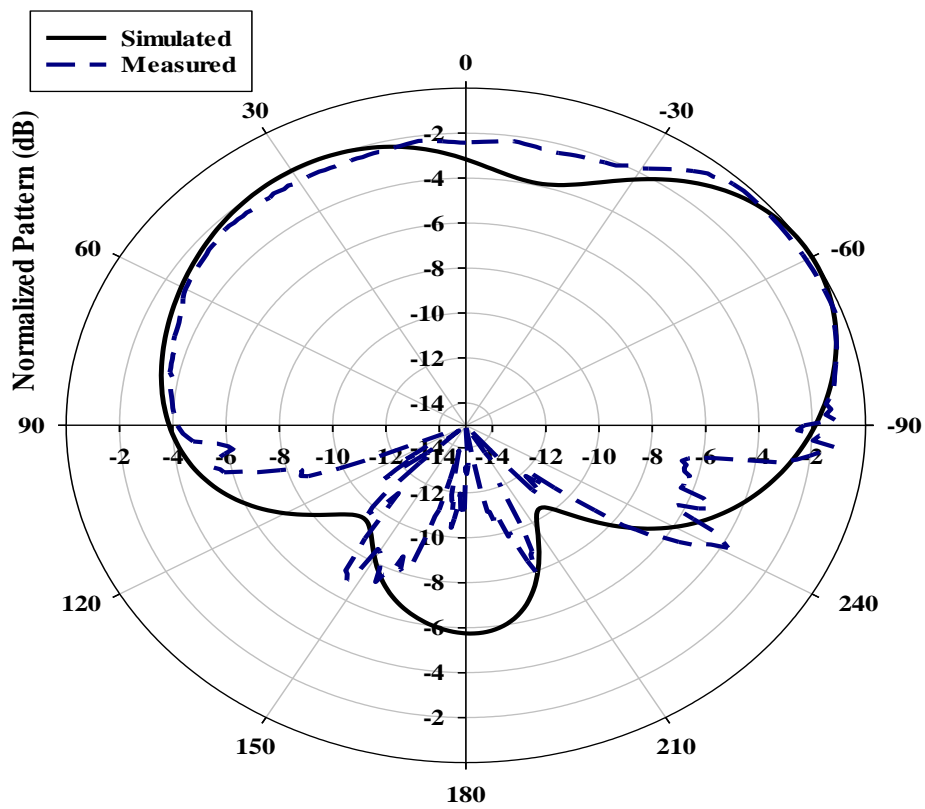


Figure 3.37: Simulated and measured gain for scenario II.



(a)



(b)

Figure 3.38: Simulated and measured radiation patterns for scenario II at 9.5 GHz. a) E- Plane and b) H- Plane.

3.4.2.3 Scenario III.

In the third scenario, both of the PIN diodes are in the OFF state. The reflection coefficient is presented in Figure 3.39, where it can be noted that the proposed antenna has a resonance frequency of 8.2 GHz, with simulated and measured impedance bandwidths of 6% (7.9-8.48GHz) and 4.5% (7.95-8.32 GHz), respectively. As demonstrated in Figure 3.40, the measured gain at 8.2 GHz is 5.6 dBi compared to a simulated counterpart of 6.1 dBi. The magnetic field distributions inside rectangular DRAs excited at 8.2 GHz as shown in figure 3.41. The simulated and measured radiation pattern at 8.2 GHz are in close agreement as shown in Figure 3.42.

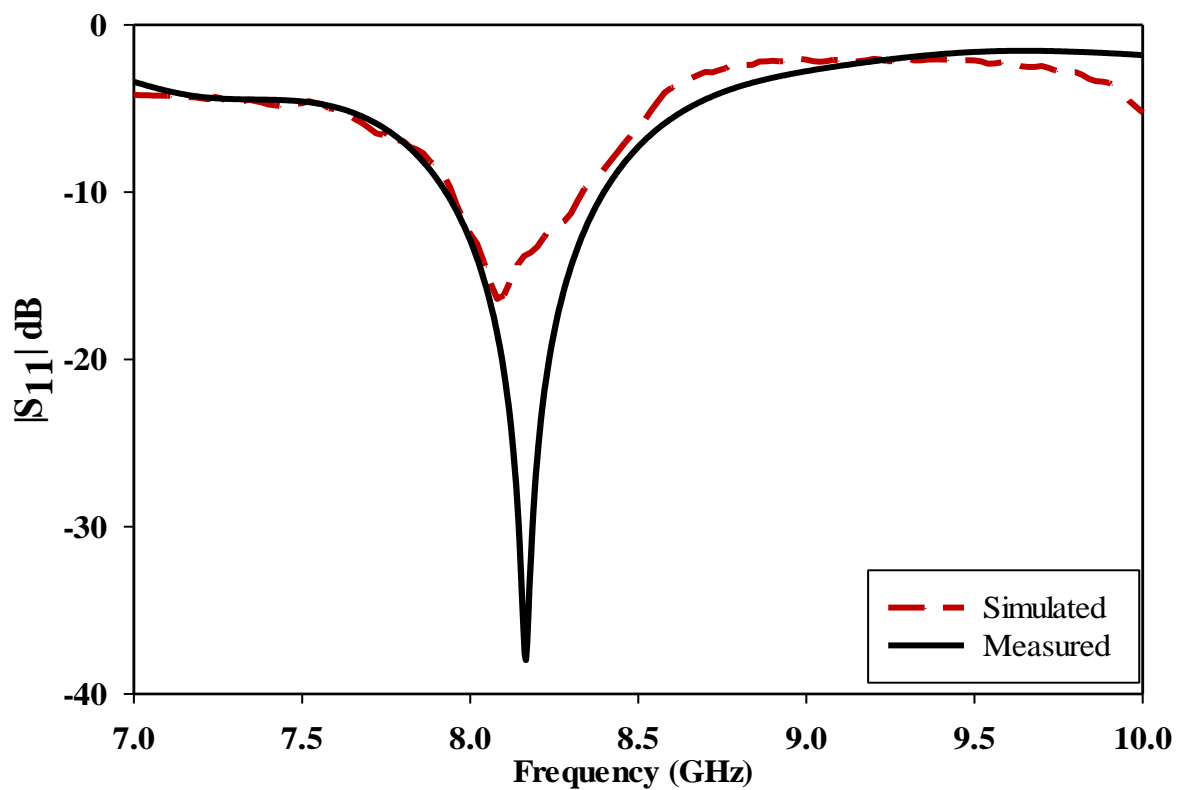


Figure 3.39: Simulated and measured reflection coefficients for scenario III.

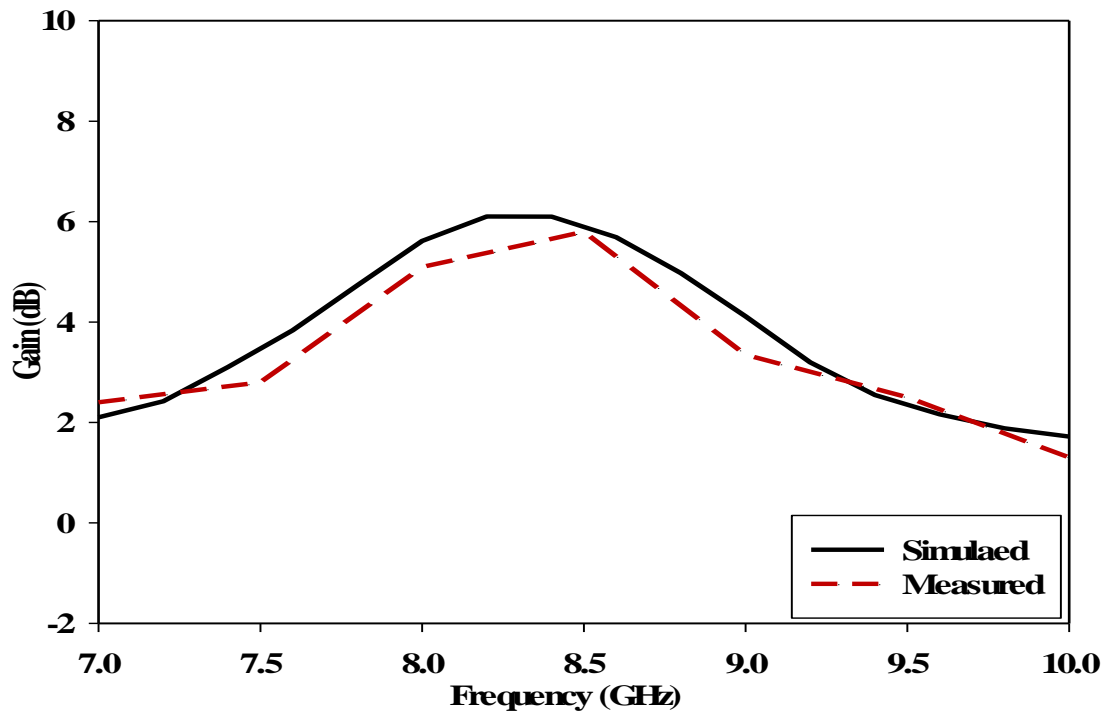


Figure 3.40: Simulated and measured gain for scenario III.

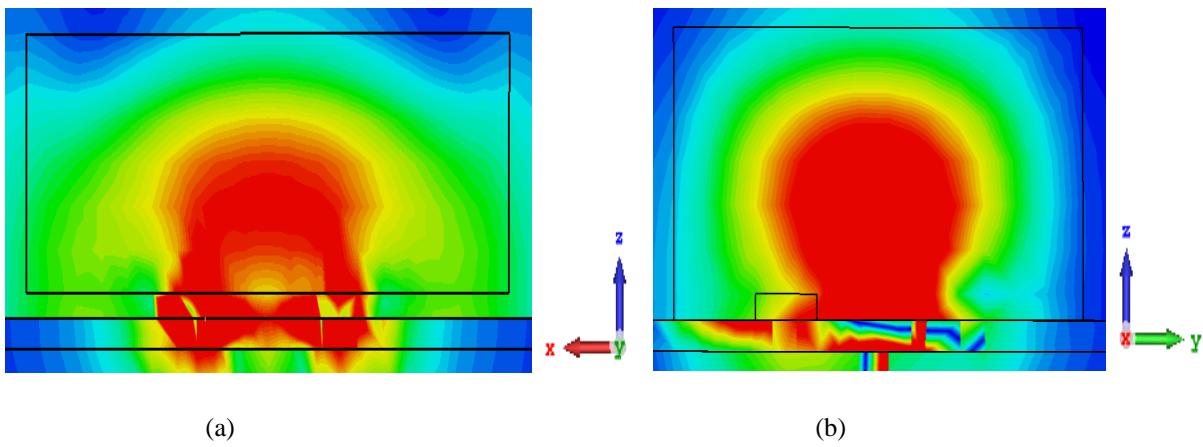
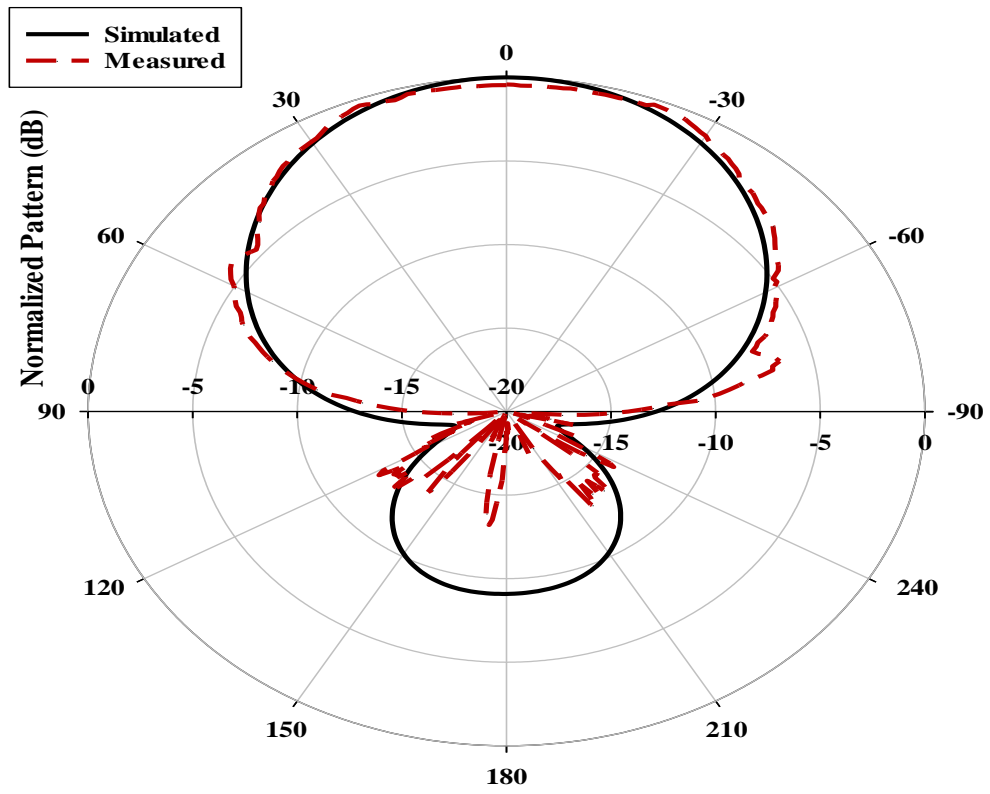
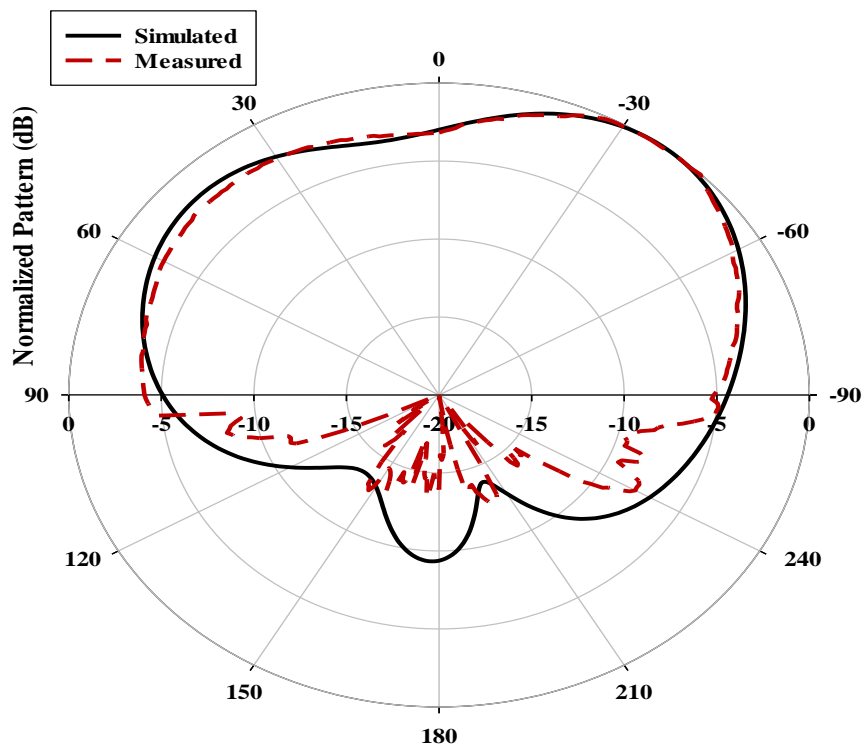


Figure 3.41: The magnetic field distributions of the TE_{111} modes inside the RDRA. a) xz -direction, b) yz -direction.



(a)



(b)

Figure 3.42: Simulated and measured radiation pattern for scenario III at 8.2 GHz. a) E- Plane and b) H- Plane.

Table 3.2 summarises the performances of different designs that offer combined reconfigurability in frequency and radiation patterns. From this comparison, it can be observed that the proposed rectangular DRA achieved reconfigurability with high efficiency and a simple design.

Table 3-2: Comparison of the performance of the proposed design with those reported in the literature for antennas with combined reconfigurable frequency and radiation pattern.

Ref	Antenna Type	No. of electronic Devices	Main beam directions	Frequency Bands (GHz)	Frequency Tuning Range	Efficiency	Complexity
[121]	Slot	14 PIN diodes	-15°,0°,15°	1.79, 1.89,2.07	14.5%	85%	High
[122]	Pixel	12 PIN diodes	-60°, -30°,0° ,30°, 60°	1.5,2.5 ,5	76%	50%	High
[123]	Patch array	4 PIN diodes	-30°,0°,30°	4.5, 4.8,5.2,5.8	25.2%	84%	High
[124]	Patch array	2 Varactors	-23°,0°,23°	2.15,2.27,2.38	10%	87%	Medium
Our work	DRA	2 PIN diodes	-45°,0°,45°	8.2,9.5	14.6%	94%	Low

Table 3.3 presents different DRA designs that achieved either frequency or radiation pattern reconfigurability. The combined frequency and radiation pattern reconfigurability has not been reported earlier for a DRA.

Table 3-3: The proposed combined rectangular DRA design with other DRAs designs.

Reference	DRA Type	Reconfigurable Techniques	No. of Ports	Reconfigurable Frequency	Reconfigurable Pattern
[50]	Cylindrical	Different permittivity	Two	No	Yes
[51]	Cylindrical	Smart materials	One	No	Yes
[56]	Rectangular	3 Varactors	One	Yes	No
[79]	Cylindrical	2 PIN diodes	One	No	Yes
[82]	Spherical	2 SPDT switches	Two	No	Yes
Our work	Rectangular	Electric	One	Yes	Yes

3.5 Conclusion

In this Chapter, two designs of reconfigurable rectangular dielectric resonator antennas have been studied both theoretically and experimentally. The first design presents a frequency reconfigurable antenna that achieved reconfigurability through the use of a single linear slot with two PIN diodes that are soldered to the sides of the slot. Two scenarios were achieved; when both switches are ON and OFF, the antenna operates in four bands: two bands when the switches are OFF at 10.8 and 12 GHz, and another two bands at 9 and 13 GHz when both switches are ON. Measured results show that the antenna has a tuning range from 8.78 to 13.34 GHz, i.e. 41.2%, with respective radiation efficiency and a peak realized gain of more than 86% and 7.5 dBi. For instance, the proposed rectangular DRA operates in the TE_{111} mode at 9 GHz, TE_{113} mode at 10.8 and 12 GHz and TE_{115} mode at 13 GHz.

The second design introduces a simple, yet compact reconfigurable rectangular DRA that can generate radiation patterns with main beams in three directional combined with frequency tuning through the utilisation of two PIN diodes and a rectangular ring slot, resulting in good impedance matching and gain. By switching diode D_1 to the OFF state and diode D_2 to the ON state, the proposed DRA can steer the maximum beam direction to $+45^\circ$ at 9.5 GHz. On the other hand, when D_1 is ON and D_2 is OFF, the main beam direction is steered to -45° at 9.5 GHz. When both D_1 and D_2 are OFF, broadside radiation is achieved at 8.2 GHz. The antenna frequency tuning range is 14.6% over a frequency range of 8.2 -9.5 GHz. The process of controlling the PIN diodes using a dc bias network is uncomplicated as it only involves the utilization of RF choke inductors and eliminates the need for dc blocking capacitors.

Chapter 4

Polarisation Reconfigurable Rectangular DRAs

4.1 Introduction

Reconfigurable DRAs that can switch between linear polarisation and circular polarisation would have greater potential in modern wireless systems. In this Chapter, two designs of rectangular DRAs are proposed to achieve LP and CP in two polarisation senses; left-hand CP and right hand CP. The proposed antenna configurations have been considered theoretically and experimentally.

4.2 Cross Slot-Fed Rectangular DRA with Polarisation Reconfigurability

This section proposes a wideband polarisation reconfigurable rectangular DRA using four PIN diodes and a cross-slot feeding as demonstrated in Figure 4.1. Each PIN diode has been placed near the edge of one of the feeding slot arms to facilitate polarisation reconfigurability. To overcome any undesired interference from bias lines, the ground plane has been divided into four individual sectors to achieve the biasing. Each PIN diode has been placed between two adjacent sectors. The proposed structure is simple and easy to fabricate and needs only four PIN diodes to achieve three polarisation states; LP, LHCP and RHCP. The antenna demonstrates a wider impedance and AR bandwidths compared to those in the literature. The simulations have been conducted using CST microwave studio [125].

4.2.1 Antenna Configuration

The configuration of a cross-slot fed for a Rectangular DRA is shown in Figure 4.1. This configuration can generate both linearly and circularly polarised electric field radiation. Simulations have been conducted to investigate the effects of using a pin diode in different positions to achieve wider impedance bandwidth and axial ratio. The rectangular DRA operates in the frequency range of 10 to 14GHz and has a permittivity of $\epsilon_r = 9.9$ and a loss tangent of $\tan \delta = 0.0001$. The length, width, and height of the DRA are 10.6, 9, and 8mm, respectively.

The proposed antenna is placed on a Rogers RO4003C substrate with a length, width, and thickness of 50mm, 50mm, and 0.8mm, respectively. The substrate has a dielectric constant of 3.38 with a loss tangent of 0.0027. A copper ground plane is positioned on the upper side of the substrate, and a microstrip transmission line is applied to the bottom side. A cross slot has been created in the ground plane with dimensions of $0.8 \times 6 \text{ mm}^2$ for each slot, which has been used to excite the DRA. In addition, an open stub length of $l_{stub} = 2.2 \text{ mm}$ has been utilized for optimum matching.

To achieve polarisation reconfigurability, a design for a CP Rectangular DRA has been proposed, which involves using a forward-biased PIN diode to create the desired short-circuit on the cross slot. An additional PIN diode has been added at an angular distance of 180° from the first diode, as shown in Figure 4.1. The PIN diode (MA4SPS402) has $R_{ON} 5.2 \Omega$ resistance and $L_s 0.45 \text{ nH}$ inductance in the ON-state and $R_{OFF} 20\text{-k}\Omega$ resistance parallel with $C_{OFF} 0.045\text{-pF}$ capacitance in the OFF-state.

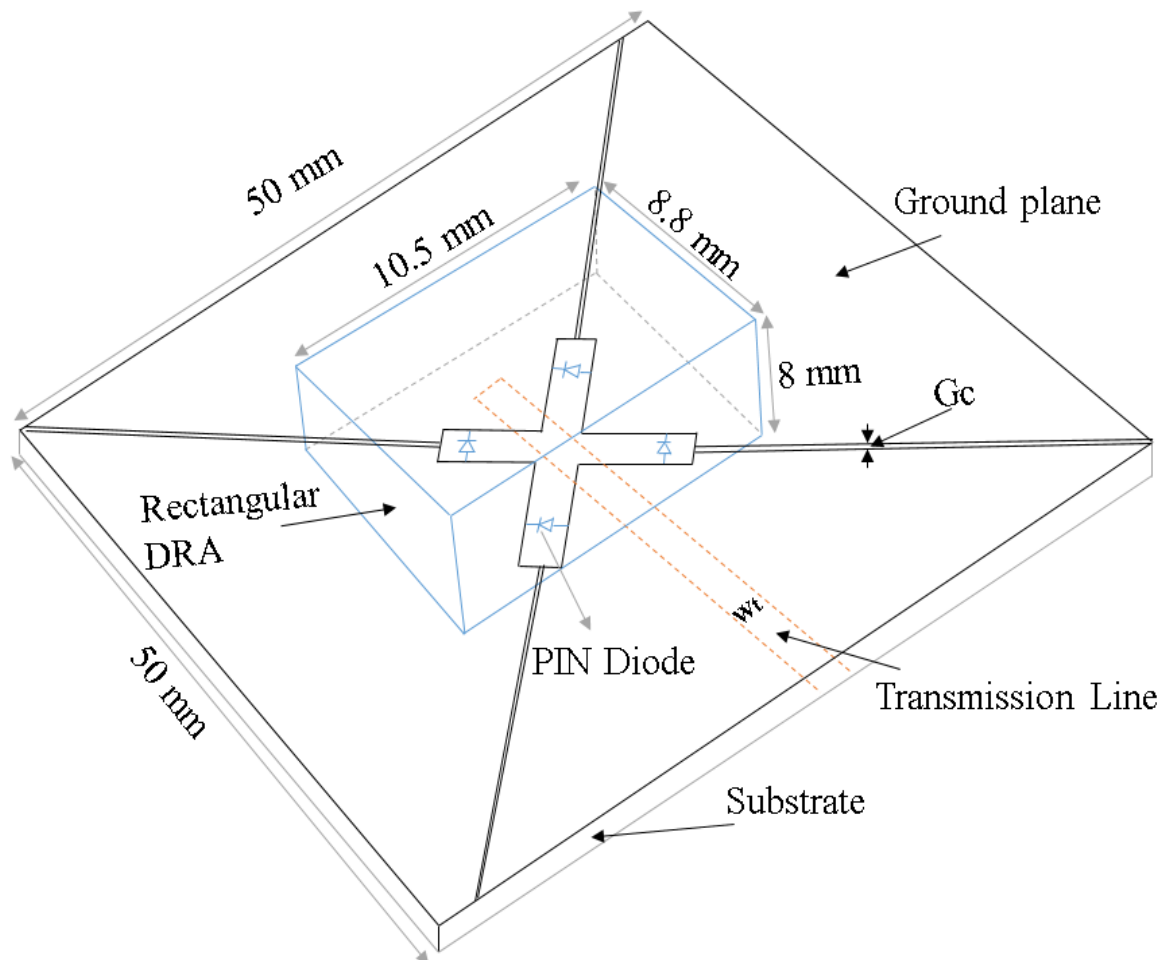


Figure 4.1: The geometry of the cross slot-fed reconfigurable DRA with ground plane divided into four identical sectors.

The polarisation can be controlled by changing the four PIN diode states to achieve different polarisations. Figure 4.2 illustrates the utilized diodes arrangement that facilitates a simple switching. The four ground plane sectors have been isolated by a gap with a width of $G_c = 0.1$ mm. As a result, different biasing polarities can be achieved for any two adjacent sectors, which is essential for the diodes' biasing. For example, diodes D1 and D2 are connected in a way that ensures they are always in the same state to increase or decrease the length of the first cross-slot's arm (S1). Similarly, D3 and D4 will be in the ON or OFF states at the same time, hence controlling the length of the second cross-slot's arm (S2). The TE_{113} and TE_{321} resonance modes are supported by the rectangular DRA dimensions illustrated in Figure 4.1 at 10.8 GHz and 13.4 GHz, respectively. The CP radiation can be achieved by exciting two orthogonal degenerate modes... These modes can be obtained by allowing the two arms of the slots to resonate at two closely spaced frequencies. Each arm of the cross slot is designed to be a different length from the other by 2Δ where Δ is the distance between the PIN diode position and the end of slot edge as shown in figure 4.2. Figure 4.3 illustrates the variation of the return losses as a function of Δ when the arm length of one slot was fixed at 6 mm. From these results, it can be observed that the widest impedance bandwidth of 30% has been achieved when $\Delta = 1.1$ mm. The impact of Δ on the axial ratio is presented in Figure 4.4, where again the widest AR bandwidth of 15% has been achieved when $\Delta = 1.1$ mm.

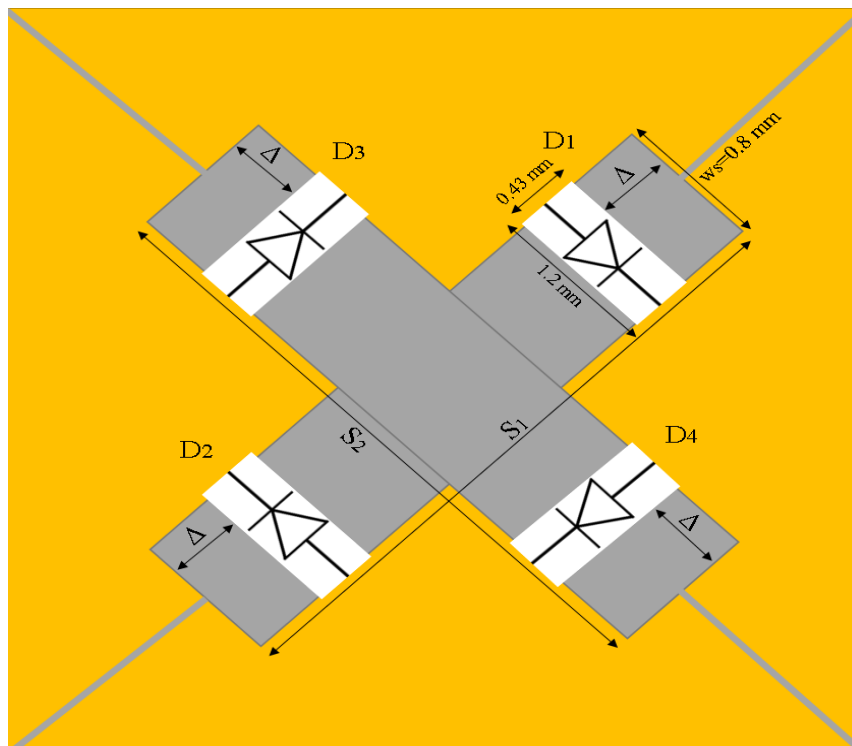


Figure 4.2: The connections of PIN diodes for simple switching.

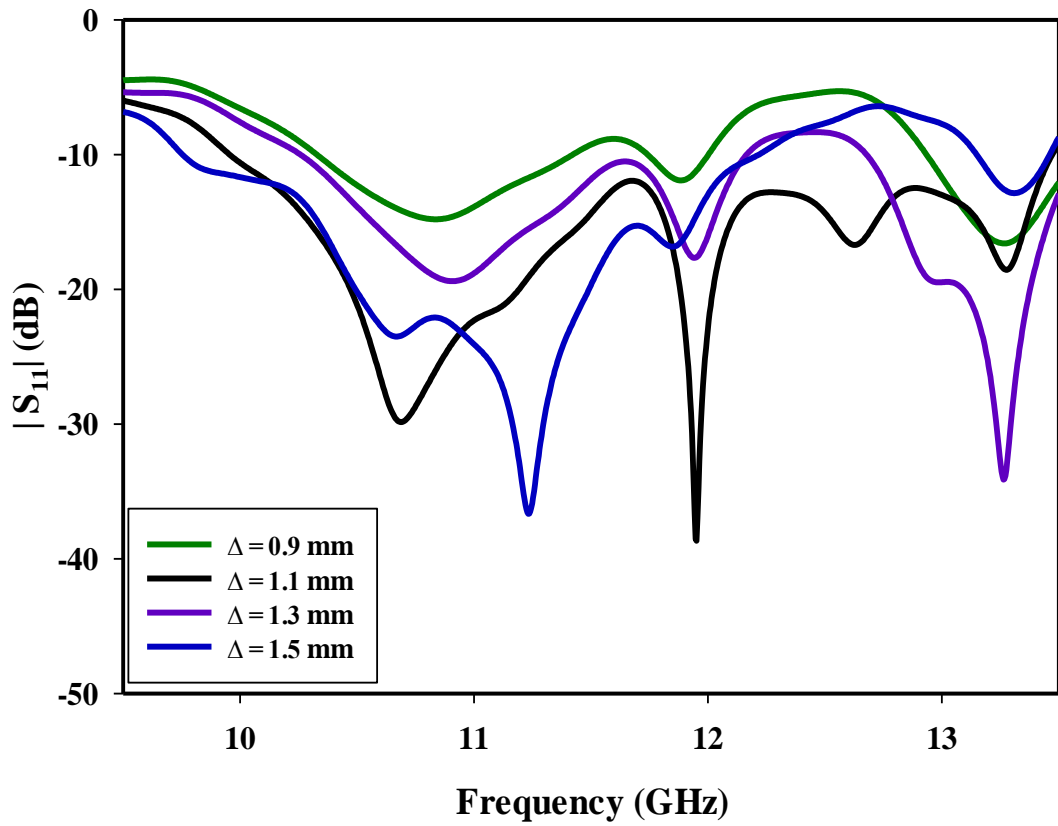


Figure 4.3: Return losses with different values of Δ .

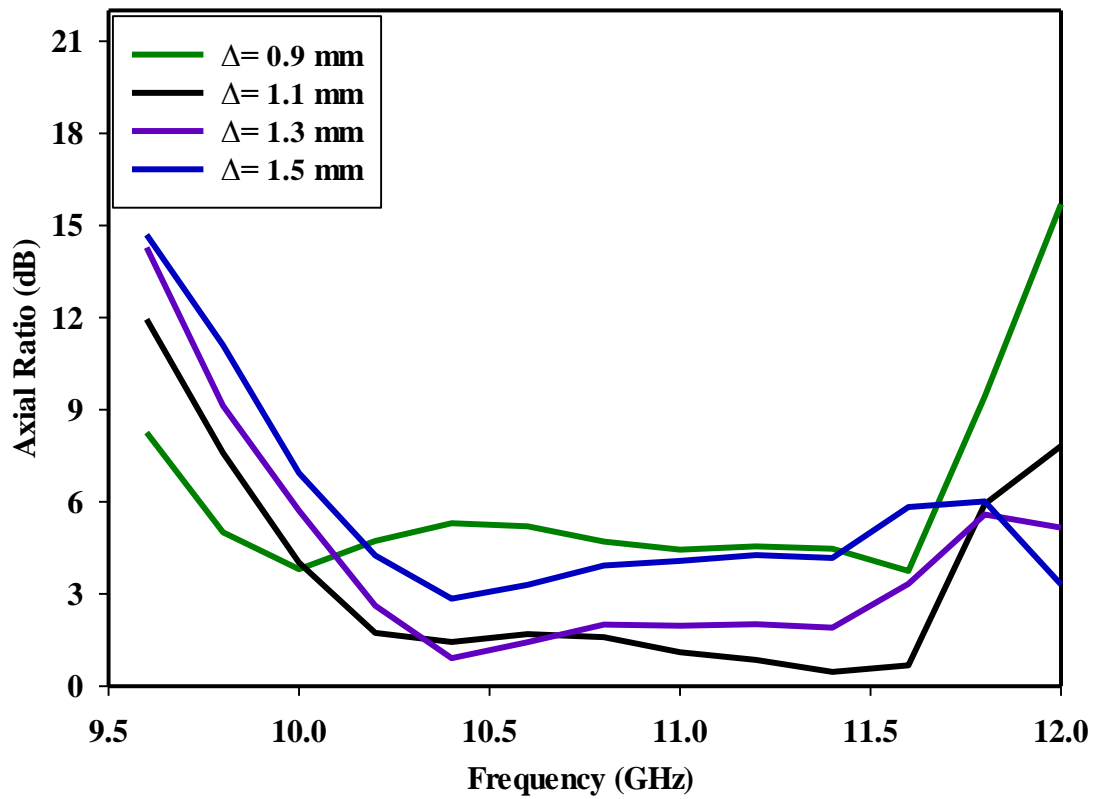


Figure 4.4: Axial ratio with different values of Δ .

4.2.2 Left-hand Circular Polarisation

In the first scenario, the states of D_1 and D_2 have been chosen to be ON while those of D_3 and D_4 are OFF. As a result, the first cross-slot arm, S_1 , has a length of 4.9 mm compared to 6 mm for the second arm, S_2 . As a result, LHCP wave is expected. Figure 4.5 demonstrates that the antenna has achieved a wide impedance bandwidth that extends from 10.15 to 13.67 GHz, which corresponds to $\sim 30\%$. In addition, a wide axial ratio bandwidth of 15% (10.09-11.68 GHz) has been achieved with a maximum gain of 8.2 dBic as presented in Figures 4.6 and 4.7. Furthermore, Figure 4.8 illustrates the far-field pattern, where it can be noted that LHCP radiation has been achieved since where E_L is greater than E_R by 20 dB at 10.8 GHz. Figures 4.9 and 4.10 show the DRA excited mode TE_{113} at 10.8 GHz and mode TE_{321} at 13.4 GHz.

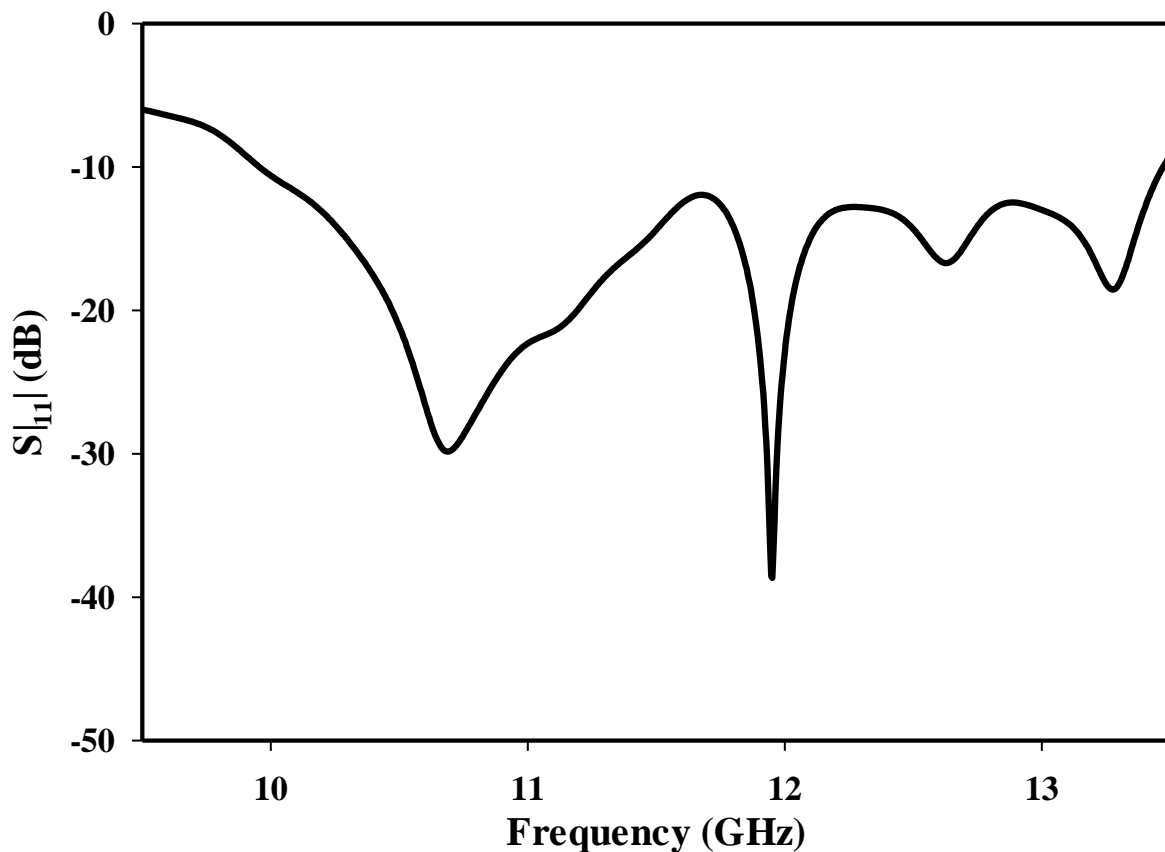


Figure 4.5: Return losses of the left hand circularly polarised rectangular DRA.

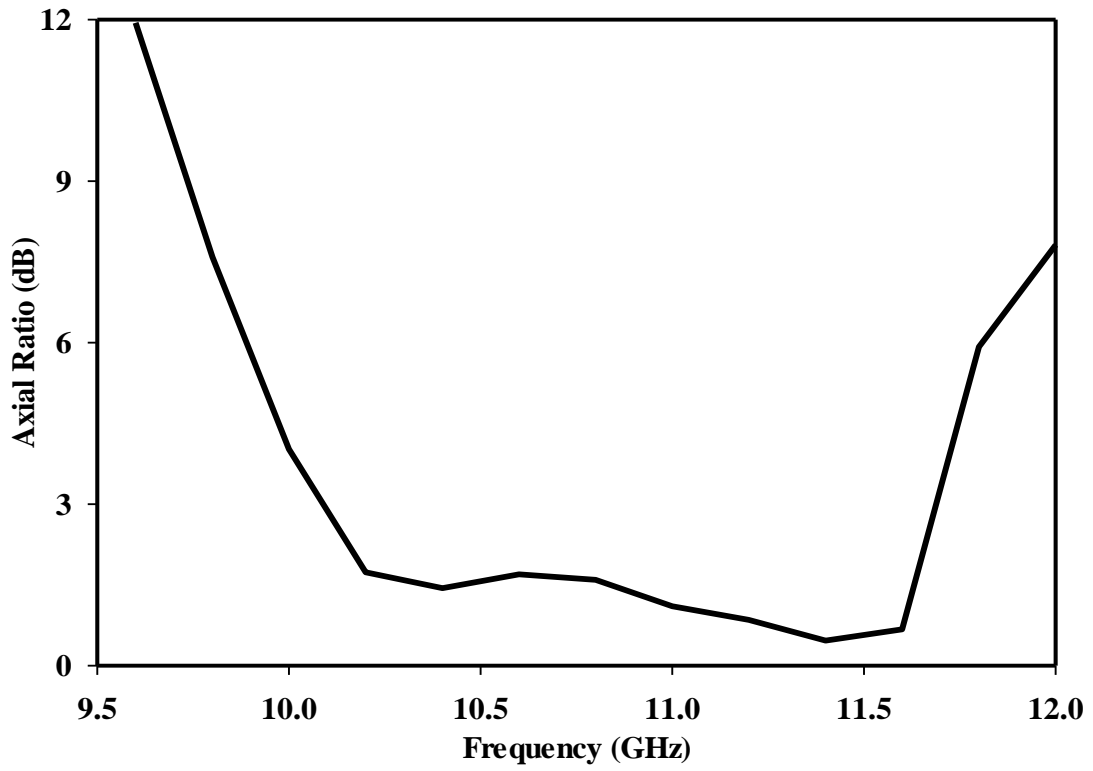


Figure 4.6: Axial ratio for rectangular DRA with LHCP radiation.

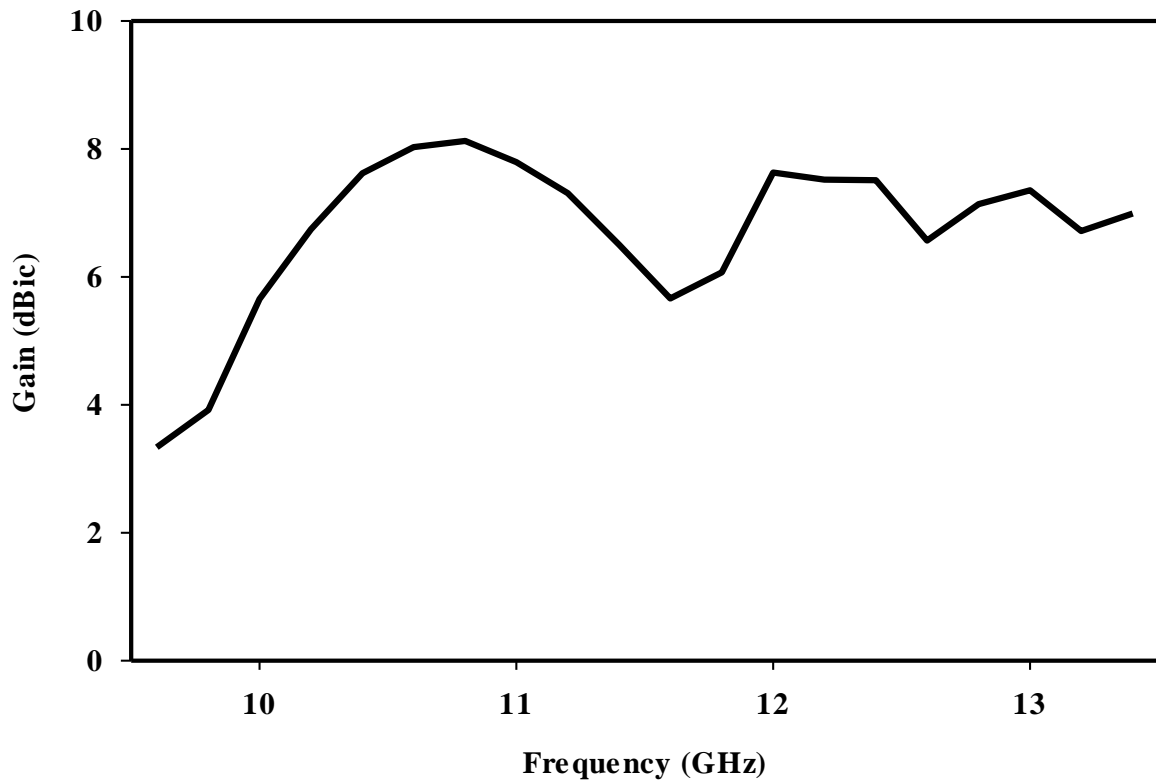
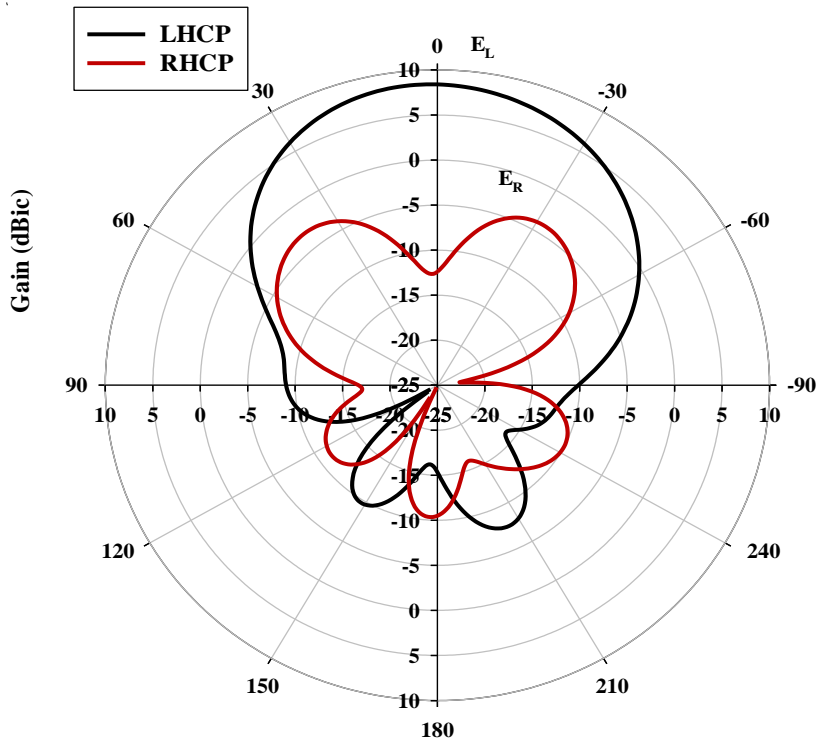
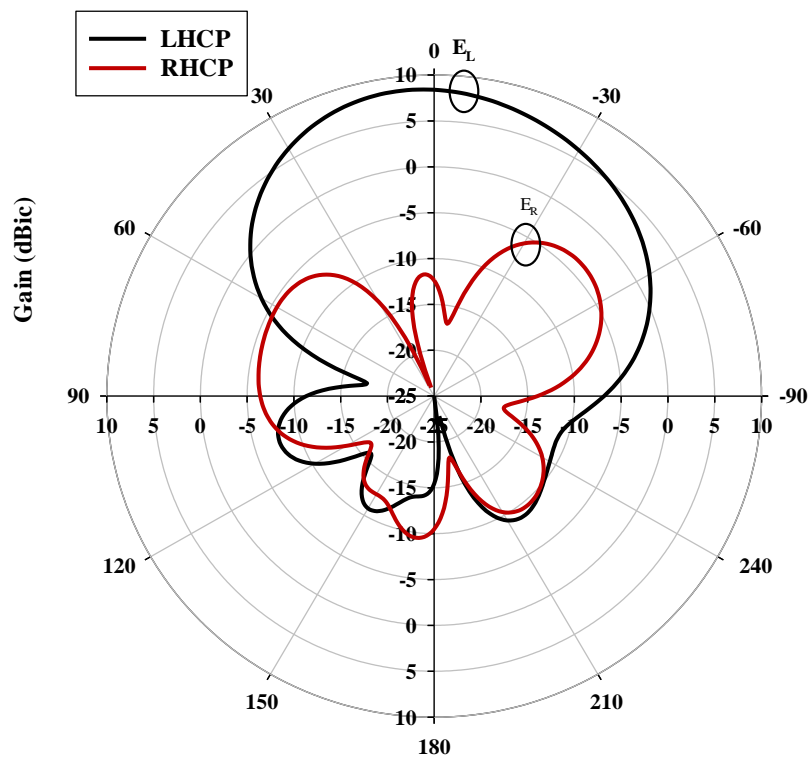


Figure 4.7: Gain of a rectangular DRA with LHCP radiation.



(a)



(b)

Figure 4.8: Radiation patterns of RDRA excited in the TE_{113} mode at 10.8 GHz. a) E- Plane and b) H- Plane.

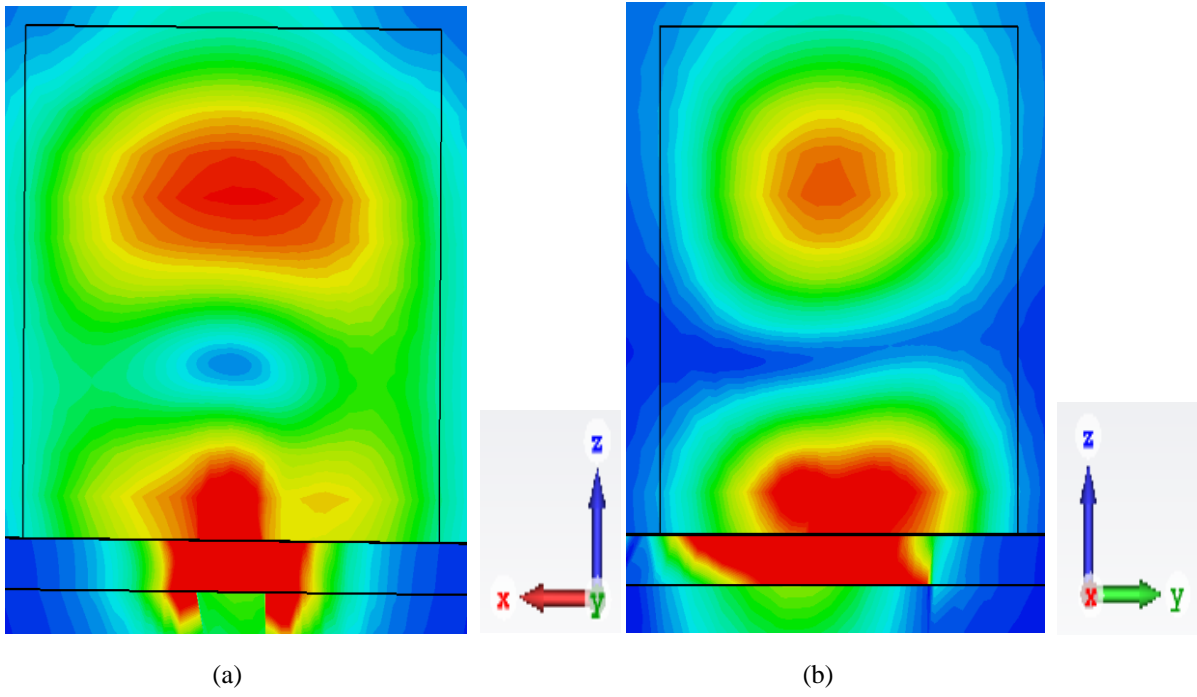


Figure 4.9: The magnetic field for the TE_{113} mode at 10.8 GHz. (a) xz plane (b) yz plane.

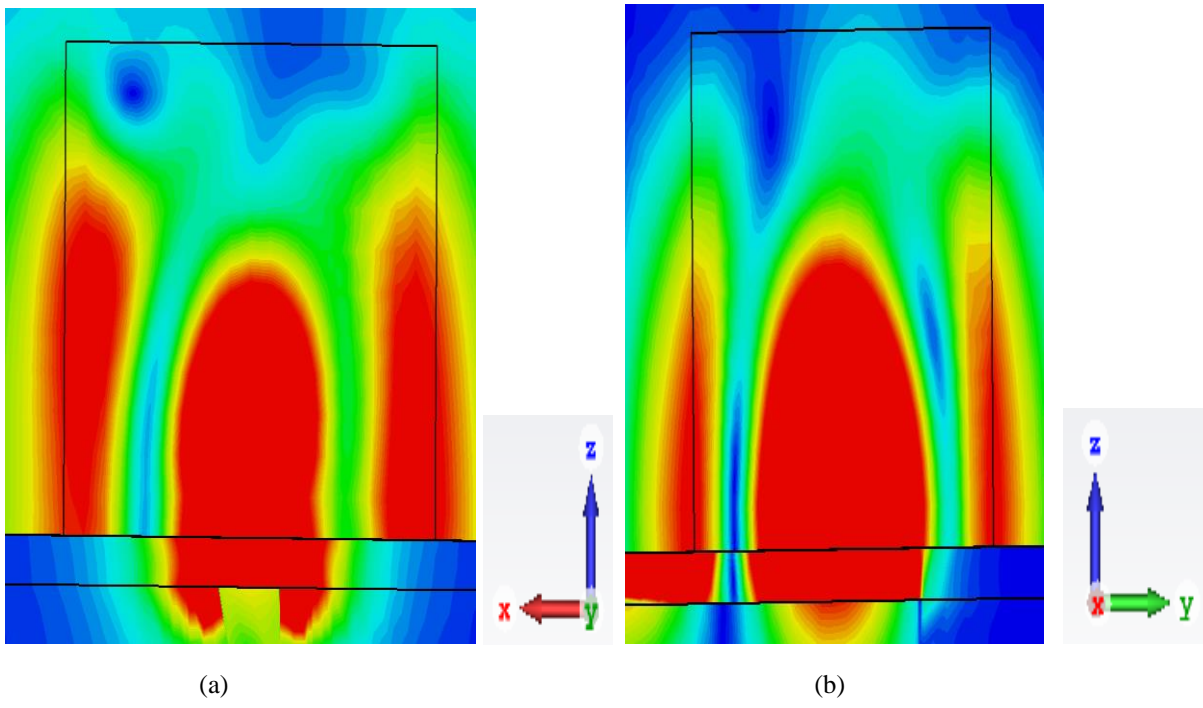


Figure 4.10: The magnetic field for the TE_{321} mode at 13.4 GHz. (a) xz plane (b) yz plane.

4.2.3 Right-hand Circular Polarisation

In the second scenario: the D_3 and D_4 diodes have been forward biased, i.e. In the ON State, and the D_1 and D_2 diodes are reverse biased, i.e. in the OFF state. This means the arm length of the second arm of the cross-slot, S_2 , is 4.9 mm, which is shorter than the first arm, S_1 . In this case, the RHCP wave will be radiated. As expected, the achieved results are similar to those of the left-hand circularly polarised DRA. Figure 4.11 shows the antenna offers a wide $|S_{11}| < -10$ dB bandwidth that extends from 10.15 to 13.67 GHz. A wide AR bandwidth of 15% has been achieved with a maximum gain of 8.2 dBic as presented in Figures 4.12 and 4.13. In addition, Figure 4.14 illustrates the far-field pattern, which confirms the RHCP radiation since E_R is greater than E_L by 20 dB at 10.8 GHz.

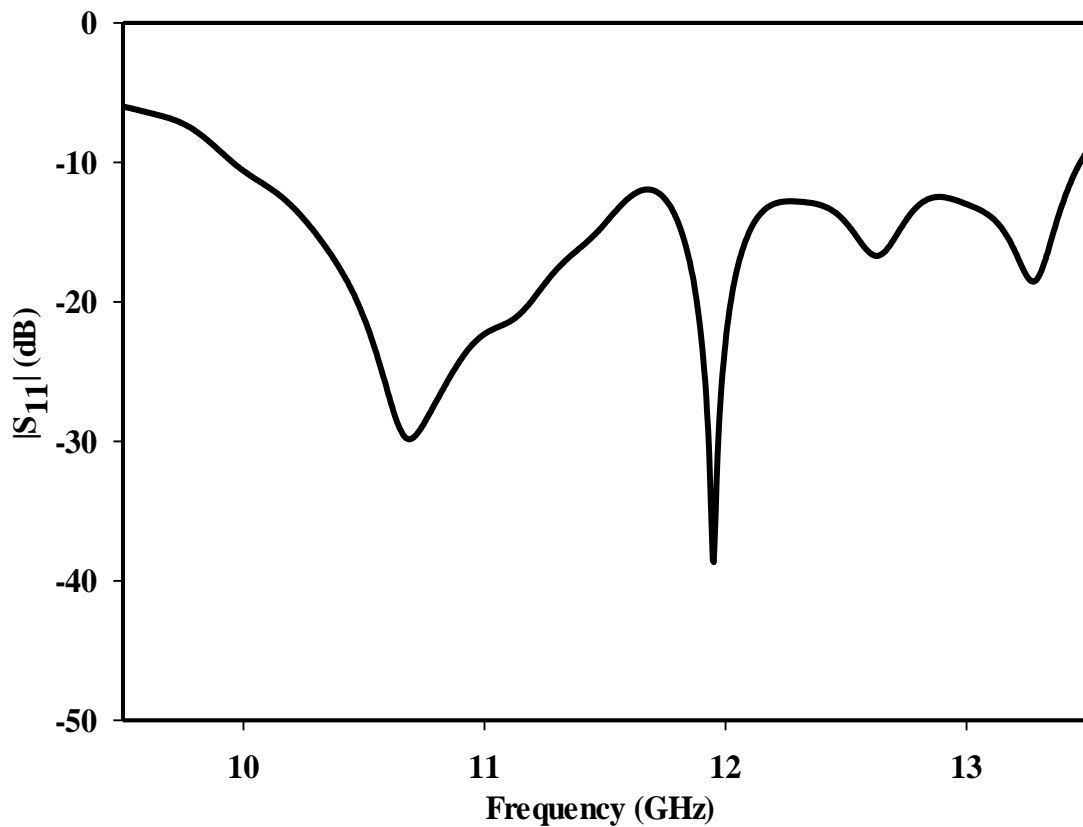


Figure 4.11: Return losses of the circularly polarised rectangular DRA.

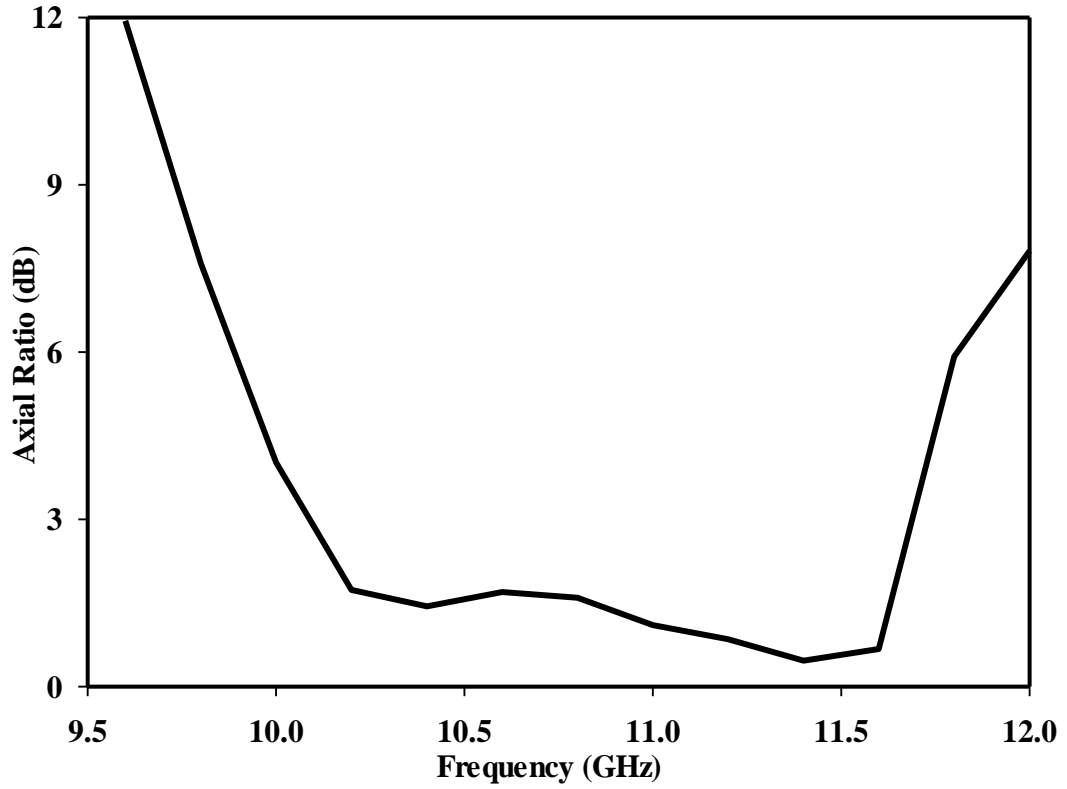


Figure 4.12: Axial ratio for rectangular DRA with LHCP radiation.

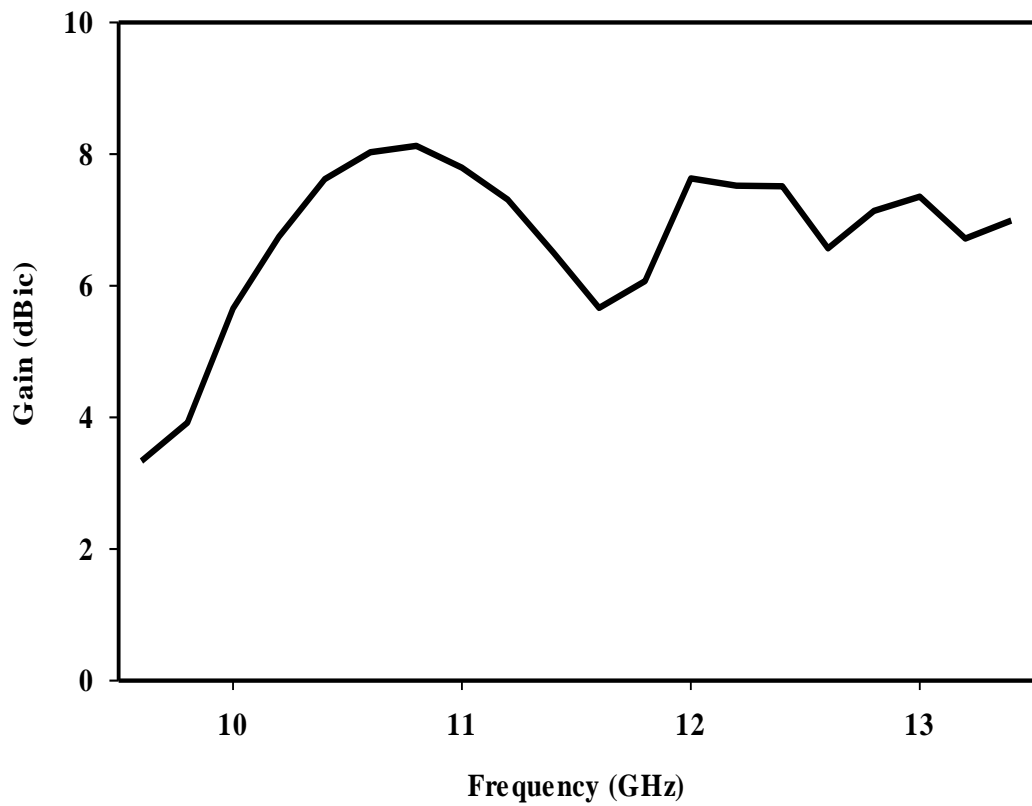
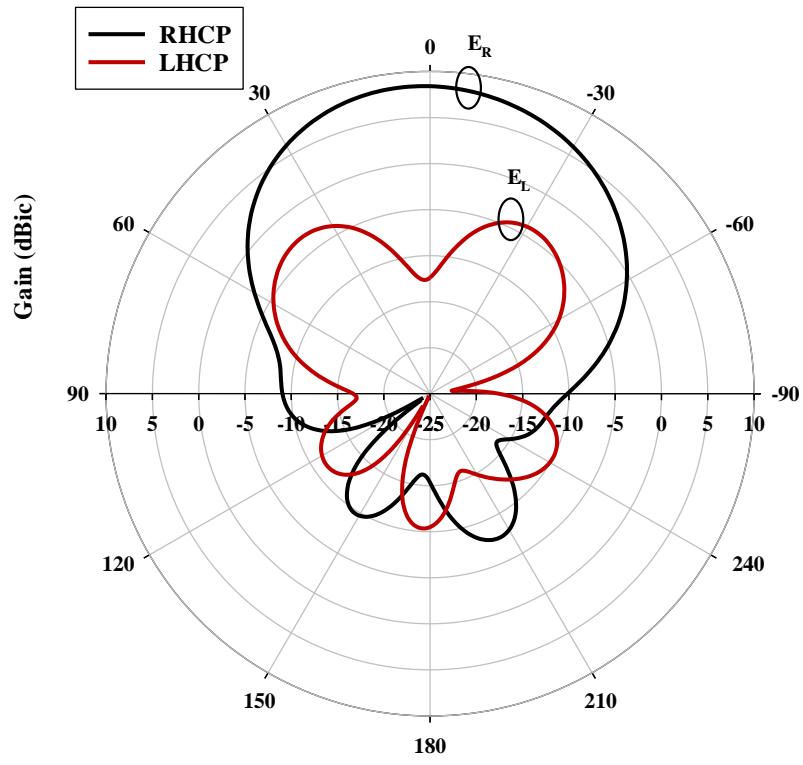
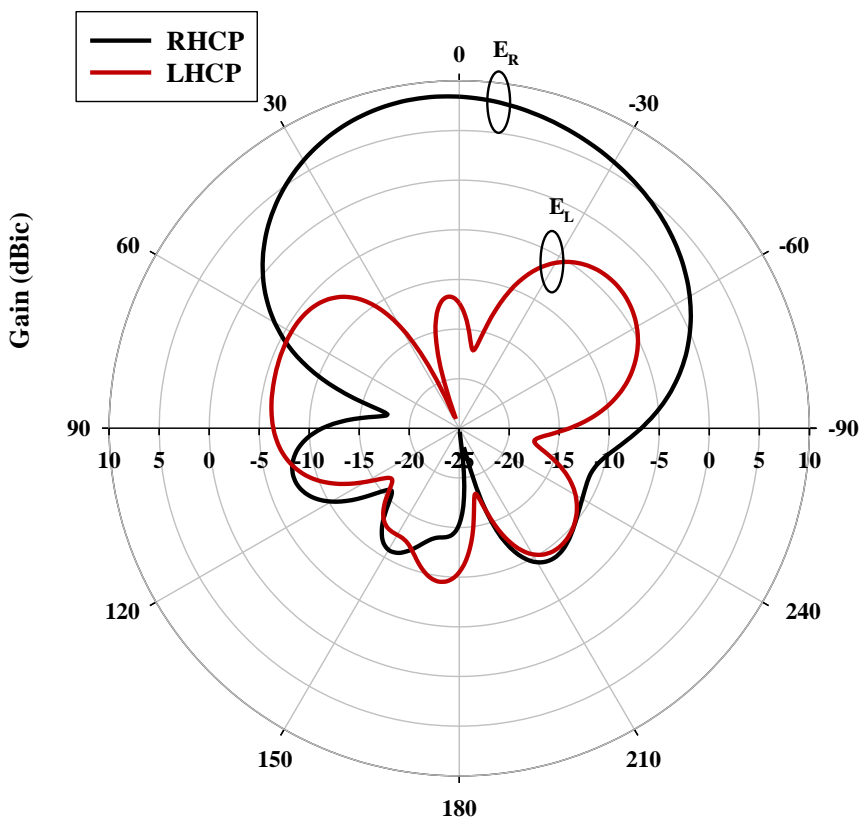


Figure 4.13: Gain for rectangular DRA with RHCP radiation.



(a)



(b)

Figure 4.14: Radiation patterns of RDRA excited in the TE_{113} mode at 10.8 GHz. (a) $\phi = 0^\circ$ (b) $\phi = 90^\circ$.

4.2.4 Linear Polarisation

In the third scenario, all four diodes have not been biased. Therefore, both of the cross-slot arms have an equal length of 6 mm, which results in LP radiation. The achieved impedance bandwidth is ~9.2% as it extends from 10.8 to 11.8 GHz as illustrated in Figure 4.15. The proposed rectangular DR antenna offers a gain of ~ 7.7 dBi as shown in Figure 4.16. Figure 4.17 illustrated a far-field pattern. The magnetic field distribution inside the rectangular DRA is presented in Figure 4.18, where it can be noted that the resonance mode TE_{113} has been excited at 11.2 GHz.

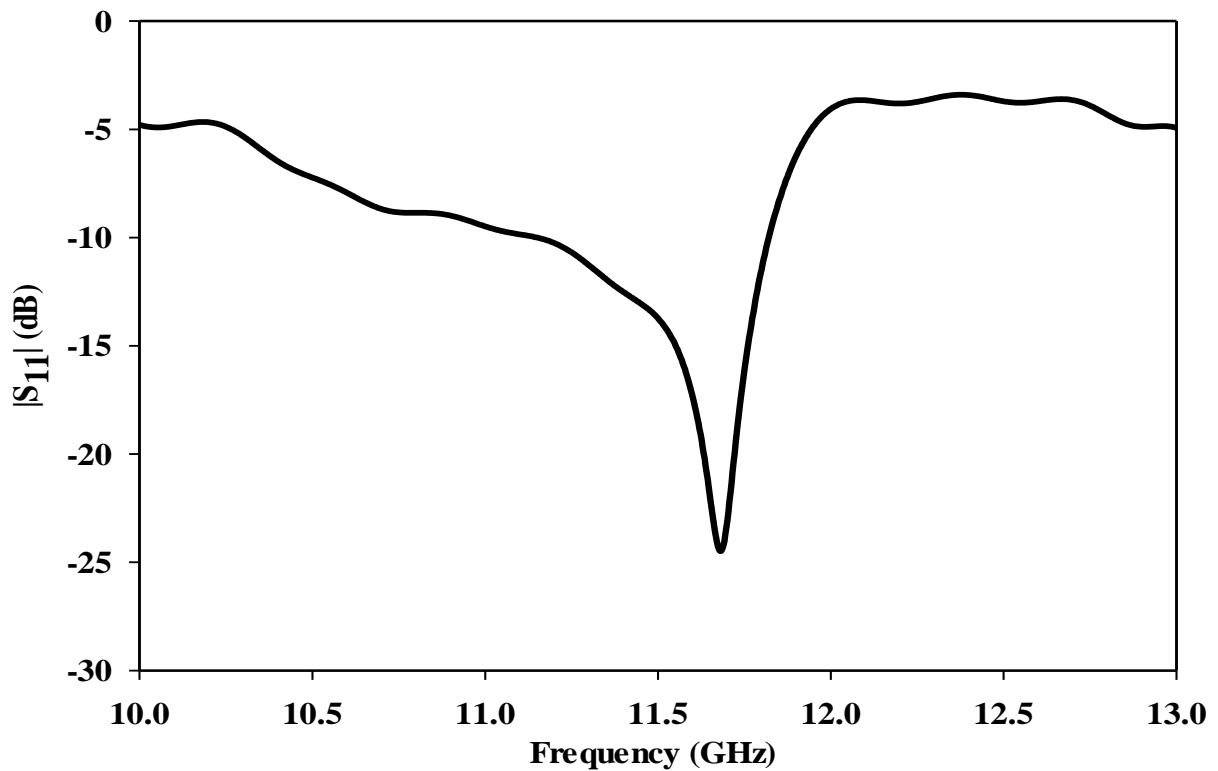


Figure 4.15: The return loss of linearly polarised rectangular DRA.

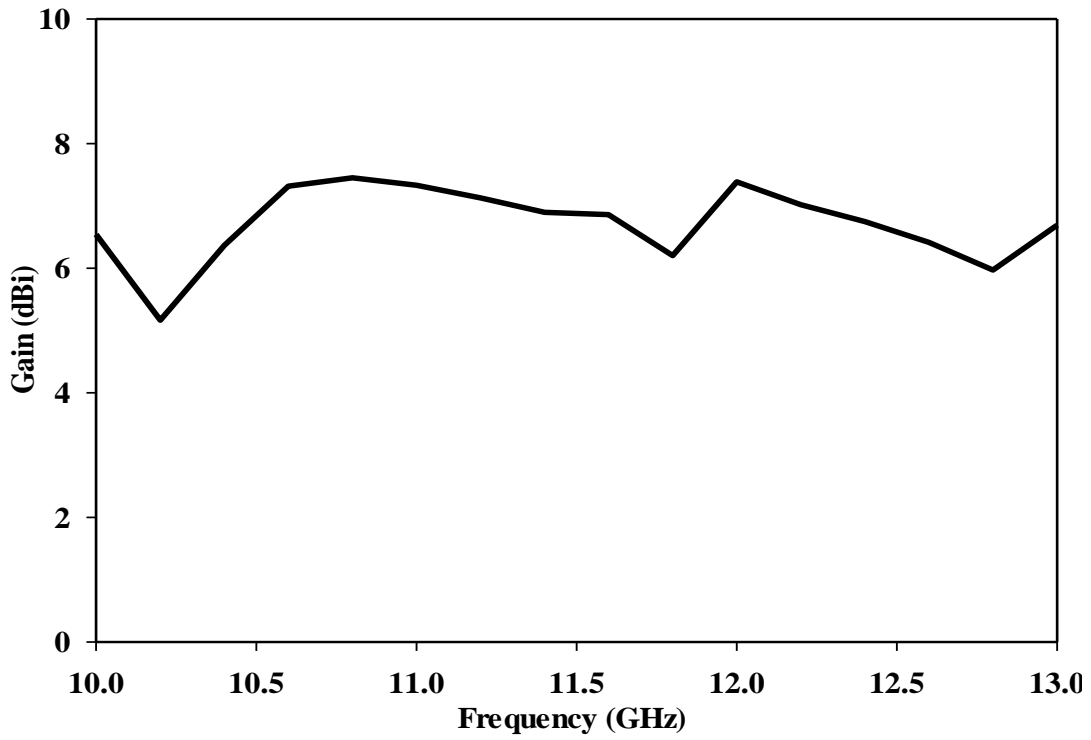


Figure 4.16: Gain of the linearly polarised rectangular DRA.

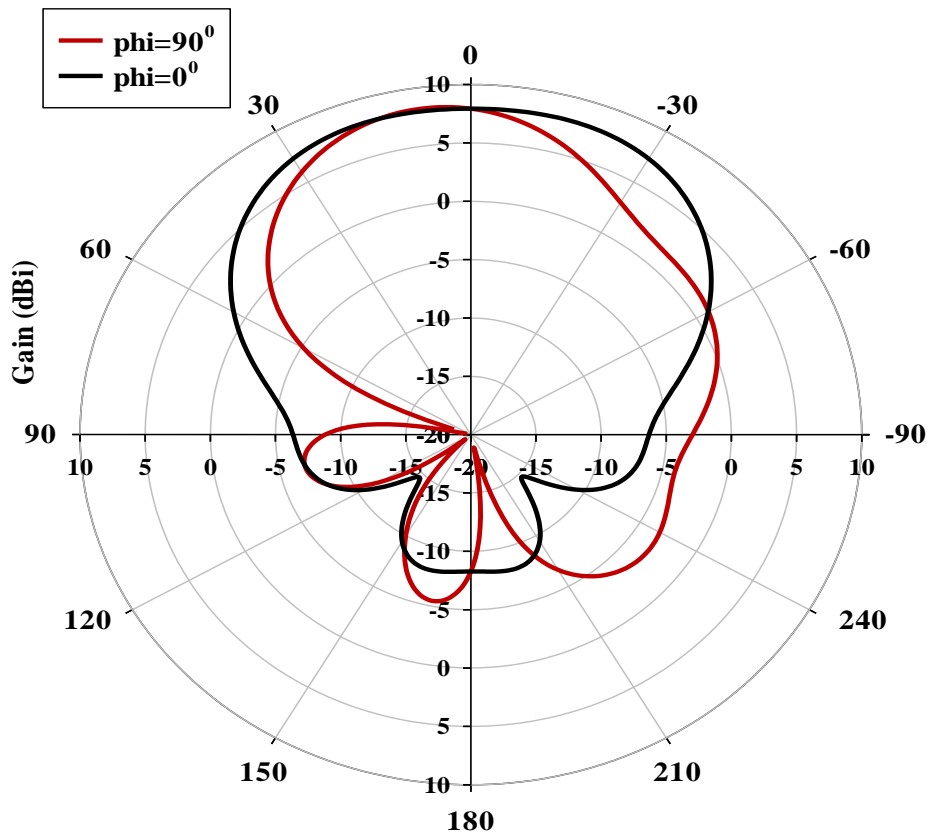


Figure 4.17: Radiation patterns of the linear polarisation rectangular DRA excited in the TE₁₁₃ mode at 11.2 GHz.

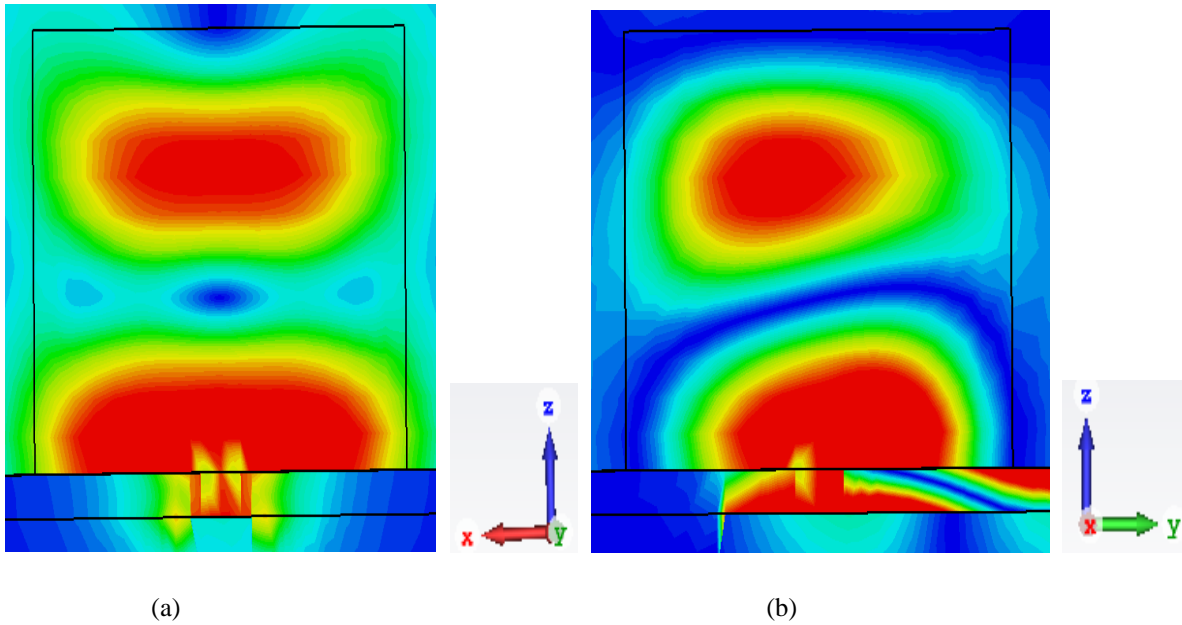


Figure 4.18: The magnetic field for the TE₁₁₃ mode at 11.2 GHz. (a) xz plane (b) yz plane.

Table 4.1 presents a comparison between the proposed DRA and other published reconfigurable polarisation counterparts, where it is clear that the proposed antenna outperforms the published electrical-controlled DRAs in terms of the wider impedance and AR bandwidths as well as higher Gain. This is in addition to a simpler biasing approach that is based on dividing the ground plane into four sections and arranging the diodes connections accordingly.

Table 4-1: Performance comparison proposes a design with another reconfigurable polarisation antenna.

Ref	Antenna Type	Mechanism	No. Of Switches	S ₁₁ Bandwidth	AR Bandwidth	Peak Gain dBic
[89]	MIMO DRA	PIN	4	11.2% LHCP 11.2% RHCP 11% LP	8.7% LHCP 8.7% RHCP	6.4
[94]	Meta-surface	PIN	4	16% LHCP 16% RHCP	13% LHCP 13% RHCP	6
[95]	RDRA	PIN	8	22% LHCP 28% RHCP 21% LP 27% LP	1% LHCP 1% RHCP	5
Propose design	RDRA	PIN	4	30% LHCP 30% RHCP 9.2 % LP	15% LHCP 15% RHCP	8.2

4.3 Square Slot-fed Polarisation Reconfigurable Rectangular DRA

This section introduces an alternative approach for generating circularly polarized (CP) radiation using square slot apertures. This is a demonstration of the feasibility of using this technique to achieve CP radiation in reconfigurable DRAs.

4.3.1 Antenna Configuration.

Another polarisation reconfigurable rectangular DRA is proposed, which has been designed using Alumina with respective dielectric constant and loss tangent of $\epsilon_r=9.9$ and $\tan \delta < 0.002$. The selected length, width, and height of $a= 10$ mm, $b=8.6$ mm and $h=8.8$ mm have been determined by following the procedure described in [23]. As illustrated in Figure 4.19, the DRA has been placed on top of a metal ground plane that is supported by a Rogers RO4350B substrate with respective size and thickness of 50 mm and 0.8 mm and has a dielectric constant and loss tangent of 3.48 and 0.0037, respectively. The ground plane and substrate have identical dimensions.

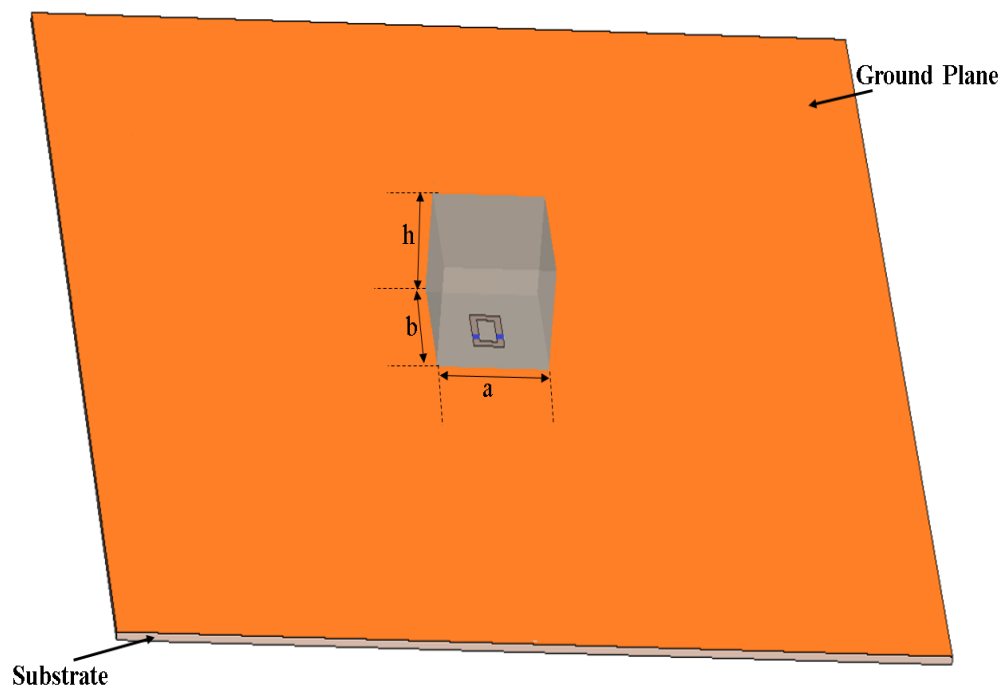
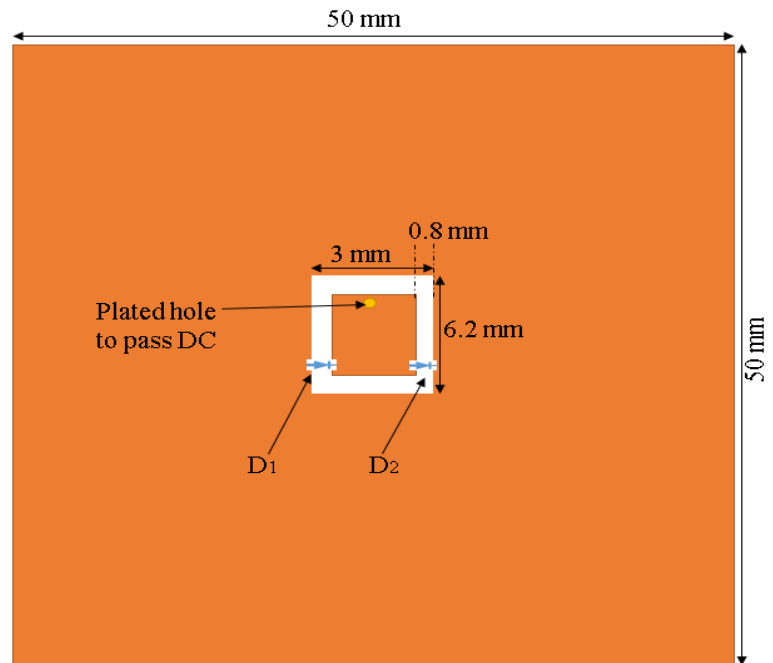


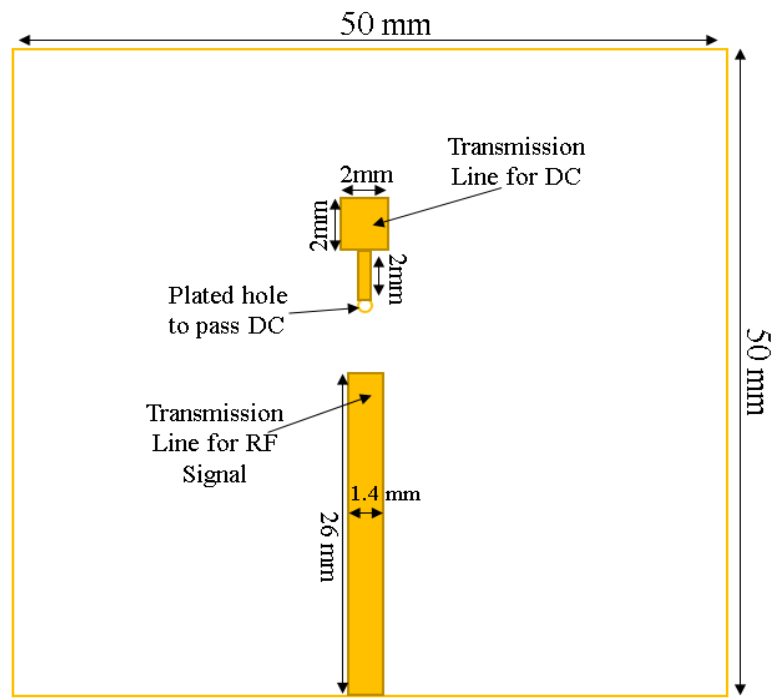
Figure 4.19: Configuration of proposed Rectangular DRA.

A rectangular ring slot has been utilised to excite the DRA with dimensions of $6.2\text{mm} \times 3\text{mm}$ and a slot width of 0.8 mm. It should be noted that CP can only be achieved when a short circuit section is created along the rectangular ring slot. The required polarisation sense can be achieved by creating the short circuit on the long left, or right hand, of the rectangular ring slot.

However, the size and position of the short circuit need to be optimized in order to achieve the CP radiation. In this study, the short circuit has been created by using a forward biased PIN diode to facilitate the polarisation reconfigurability. The dimensions of the used diode are pre-determined from the data sheet and the position has been optimised using CST.



(a)



(b)

Figure 4.20: The geometry of the slot-fed reconfigurable RDRA, (a) Top View, (b) Bottom View.

The ground plane has been cut into two parts inner and outer rectangular ground plane to control the PIN diode biasing as demonstrated in Figure 4.20a. The bottom view of the substrate illustrates a microstrip transmission line for the RF signal and the other line is to pass the DC signal to the inner smaller ground plane section through the plated hole as shown in Figure 4.20b.

Figure 4.21 and 4.22 illustrates the simulated reflection coefficients $|S_{11}|$ and AR for different switch positions; top, middle and bottom of the long side of the feeding slot. Table 4.2 demonstrates that the best AR bandwidth has been achieved when the switch position is located either at the bottom or top of the long side of the rectangular ring slot. The bottom position is 1.8 mm away from the centre of the ground plane, and the top position is also 1.8 mm away from the centre of the ground plane. On the other hand, the widest impedance bandwidth has been achieved when the switch is placed at the bottom of the longest slot side. Although the top and bottom switch locations provide the same AR bandwidth, the impedance bandwidths are different since the position of the switches is different with respect to the feeding microstrip line, which is of less significance for the far field characteristics.

Table 4-2: Different switches positions when D1 is ON and D2 is OFF.

Switch Position	$ S_{11} $ BW%	AR BW%	Gain
Top	9.8%	3.8%	7.2 dBic
Middle	4.2%	null	6.5 dBi
bottom	21.3%	3.9%	6.9 dBic

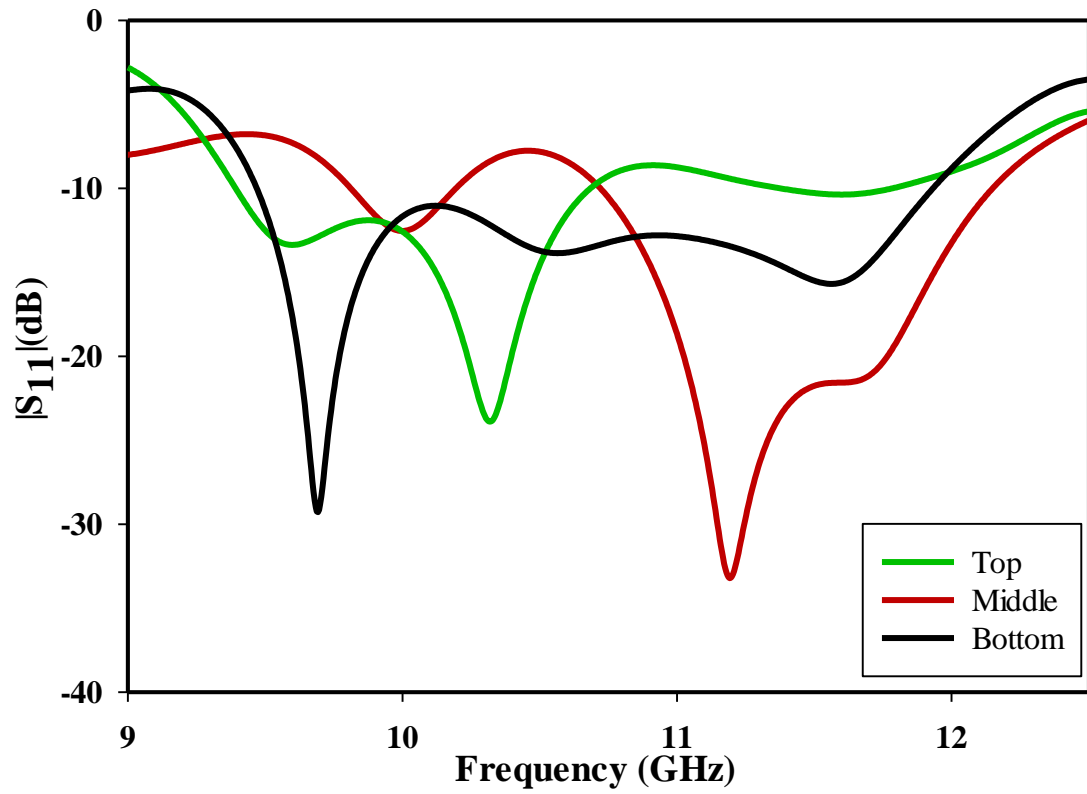


Figure 4.21: Simulated return losses of rectangular DRA for different switch positions.

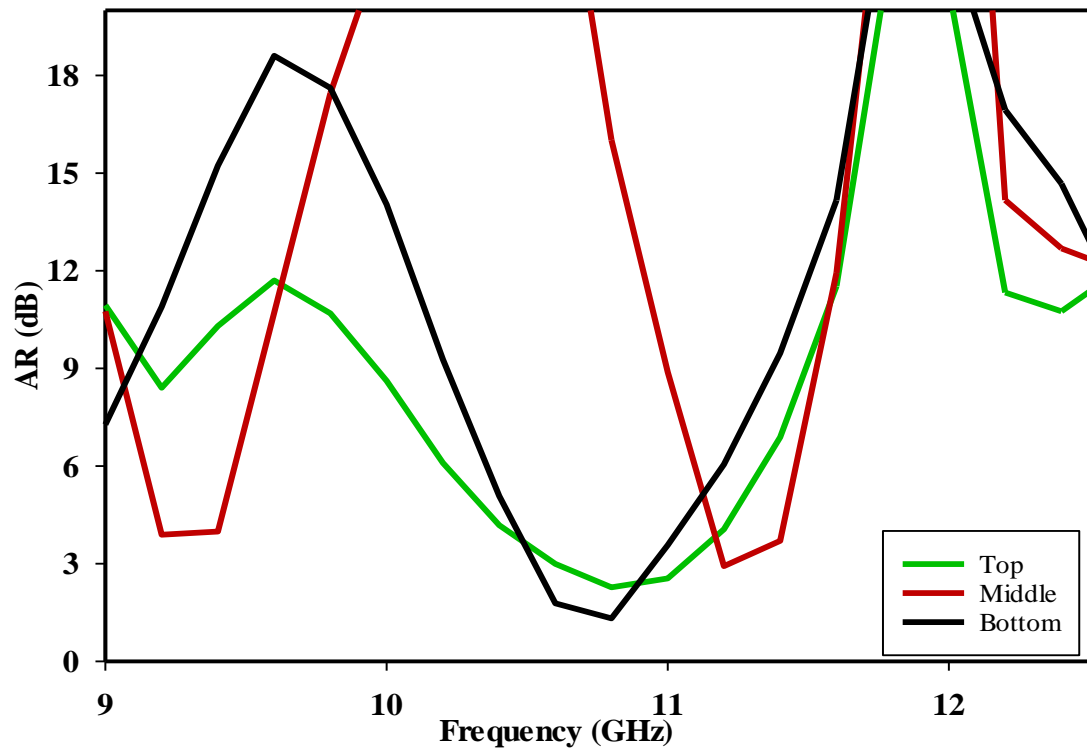
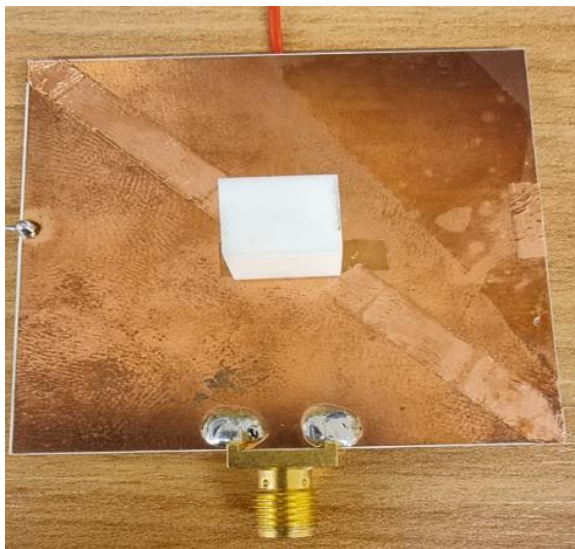


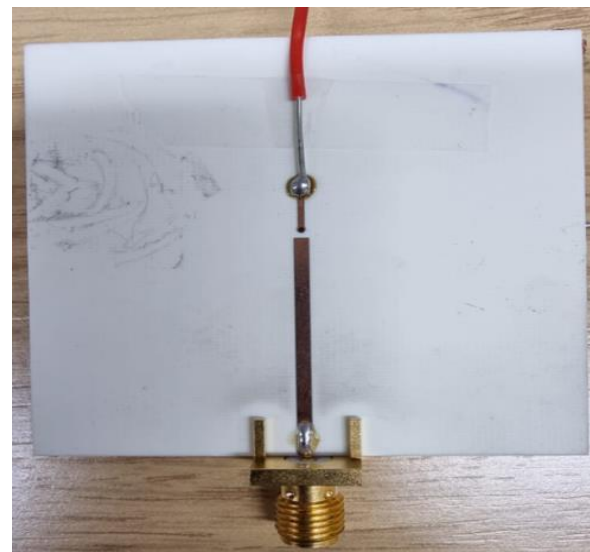
Figure 4.22: Simulated axial ratio for different switch positions.

4.3.2 Experimental Results

Figures 4.23 a) and (b) present the front and back views of the prototype of the rectangular DRA. The feed network has been fabricated at the Wrekin-circuits workshop. The rectangular DRA has been fabricated at T- CERAM Company and bonded to the metallic ground plane using a double-sided adhesive copper tape with a thickness of 0.036 mm. In addition, the PIN diode has dimensions of $1.2\text{mm} \times 0.4\text{mm} \times 0.2\text{ mm}$ for length, width, and height. The diodes have been placed at the long sides of the feeding slot as illustrated in Figure 4.20a and attached to the ground plane using conductive silver paint.



(a)



(b)



(c)

Figure 4.23: Prototype of the proposed antenna: (a) Top View, (b) Bottom View, (c) Rectangular DRA with a groove.

Two biasing wires are connected to the two ground plane sections. The inner smaller section of the ground plane is biased through a plated hole, which passes through the substrate to create the required connection to the DC transmission line at the bottom of the substrate as shown in Figure 4.20b. In addition, a groove has been etched at the lower DRA side with respective depth, length and width of 0.5mm, 8.6mm and 1.5mm as shown in Figure 4.23c. The purpose of this groove is to accommodate the height of PIN diodes so that the DRA can be positioned steadily on the ground plane without creating air gaps in-between. The reflection coefficient, S_{11} , has been measured using a network analyser through a calibrated cable and the radiation patterns have been measured using an anechoic chamber. A space with a wall covered with radiation-absorbing material (RAM) to ensure that all radiation reflected from the measuring antenna is completely absorbed is known as an anechoic chamber. This is done to make sure that any reflected radiation isn't interfering with the measurement being made. As mentioned earlier, three polarisation states have been achieved from the proposed antenna as described in the following sections.

The prototype of the Rectangular DRAs is shown in Figure 4.23. In this section, a polarisation reconfigurable X-band RDRA is proposed that works in three different configurations RHCP, LHCP and LP radiations. To verify the accuracy of the simulation results from the CST MWS, a physical antenna must be built and tested. The reflection coefficient of the antenna can be measured by connecting the antenna to a network analyser, but it is important to ensure that the cable used to make the connection is properly calibrated. It's worth pointing out that measuring specific far-field characteristics of the antenna, such as the axial ratio and gain, is not a straightforward process. The right-hand circularly polarised electric field component (E_R) and the left-hand CP electric field component (E_L) can be computed utilizing the following mathematical expressions [126]. The axial ratio can be determined by utilizing the following mathematical formula.

$$E_R = \frac{1}{\sqrt{2}}(E_H + JE_V) \quad 3.5$$

$$E_L = \frac{1}{\sqrt{2}}(E_H - JE_V) \quad 3.6$$

$$E_H = H_a \cos(H_p) + V_a \sin(V_p) \quad 3.7$$

$$E_V = H_a \sin(H_p) + V_a \cos(V_p) \quad 3.8$$

Where,

E_H and E_V are the electric field components in the azimuthal and elevation directions. H_p and V_p determine the direction of the electric field in the far-field region of the antenna. H_a and V_a are the amplitudes of the horizontal and vertical components of the electric field.

$$AR = \frac{|E_R| + |E_L|}{|E_R| - |E_L|} \quad 3.9$$

The electric field component in the azimuthal direction, denoted by E_H , and the electric field component in the elevation direction, denoted by E_V , can be experimentally determined. To measure E_H , a receiving horn antenna is fixed inside an anechoic chamber and is oriented in one direction at an azimuthal angle of $H = 0^\circ$. The DRA is rotated at various angles of elevation ($V = 0^\circ, 45^\circ, 90^\circ, \text{ and } 360^\circ$), and the received power is measured. The axial ratio, which is represented by the difference in received power, should not exceed 3 dB. The same procedure is repeated for the measurement of E_V with the horn antenna rotated at an azimuthal angle of $H = 90^\circ$.

4.3.3 Left-hand Circular Polarisation

In the first configuration, the first PIN diode, i.e. D_1 in Figure 4.20a, has been biased to be in the ON state while the other PIN diode, D_2 , is reverse biased. The positive DC signal is connected to the positive terminal, P, of D_1 via the outer ground plane section and the negative terminal is connected to the inner rectangular ground plane, which is connected to the common ground as mentioned earlier. The negative, N, terminal of D_2 was connected to the positive DC to be in the OFF State. The analysis of $|S_{11}|$ represents the amount of power reflected from the antenna, which is also called the reflection coefficient. Figure 4.24 shows a comparison between the simulated and measured return loss. As can be seen, the proposed antenna is working x-band with a good impedance matching of more than -10 dB. The Network Analyzer has determined that the measured return loss for the Rectangular DRA is -25 dB, while the simulated return loss is -30 dB. It is evident from the measurement that the return loss is lower when compared to simulated data. It might be due to the noise and multipath effect during the experiment. The reflection coefficient has been simulated and measured as illustrated in Figure 4.24 with a simulated impedance bandwidth of 21.6% that has been achieved over a frequency range of 9.6 to 11.9 GHz compared to a measured bandwidth of 21.4% due to the excitation of the TE_{113} higher order mode at 10.6 GHz. Figure 4.25 presents the axial ratio and gain, where it can be observed that an AR bandwidth of 4% (10.4-10.9GHz). A maximum gain of 6.9 dBic

at 10.6 GHz has been achieved as a result of exciting the aforementioned higher-order resonance mode as illustrated in figure 4.26. A close agreement has been achieved between simulated and measured data. In addition, the far field patterns are illustrated in Figure 4.27, where it is evident that a left-hand CP radiation has been achieved since the E_L component is greater than the E_R counterpart by 15 dBi at 10.6 GHz. Finally, the short magnetic dipoles inside the DRA are depicted in Figure 4.28, where it is evident that the TE_{113} mode has been excited at 10.6 GHz.

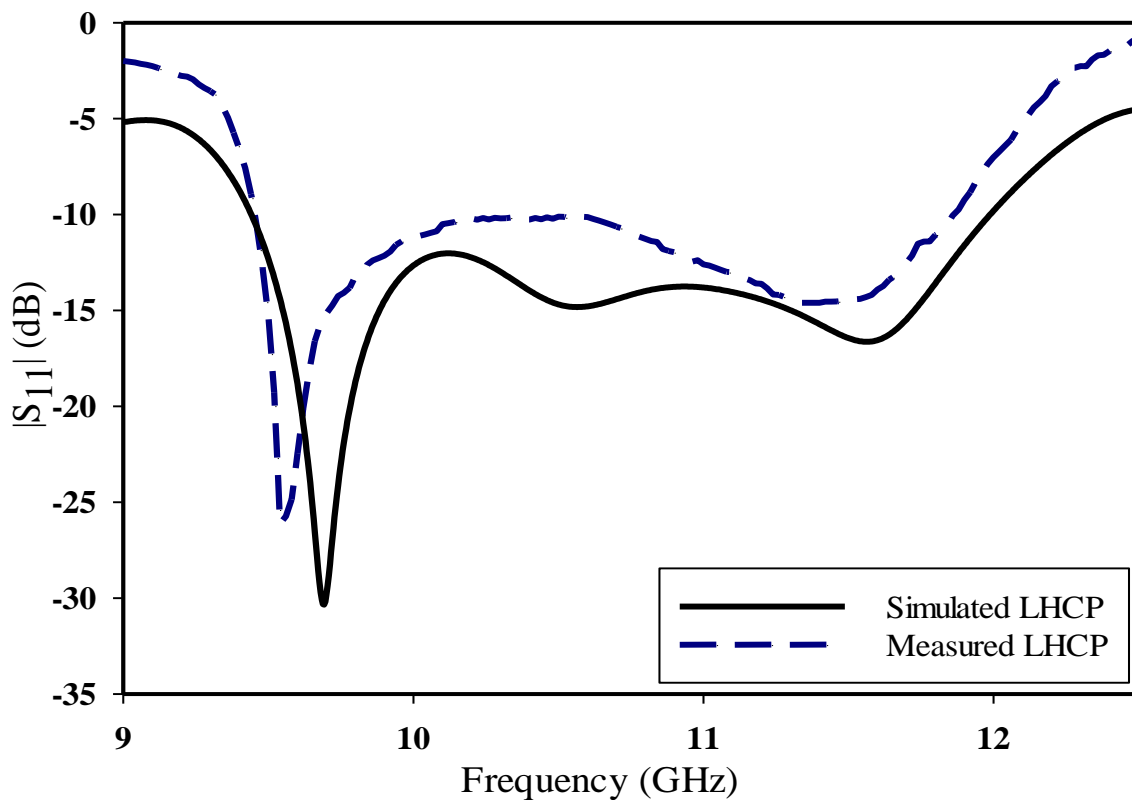


Figure 4.24: Simulated and measured return loss of RDRA.

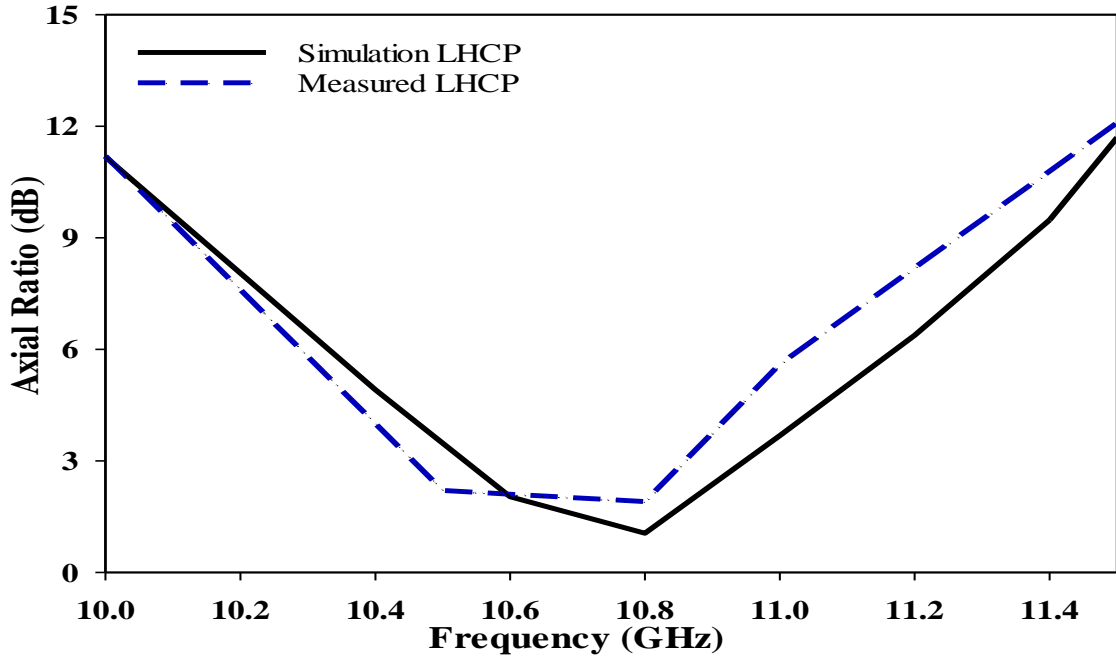


Figure 4.25: Simulated and measured Axial ratio rectangular DRA.

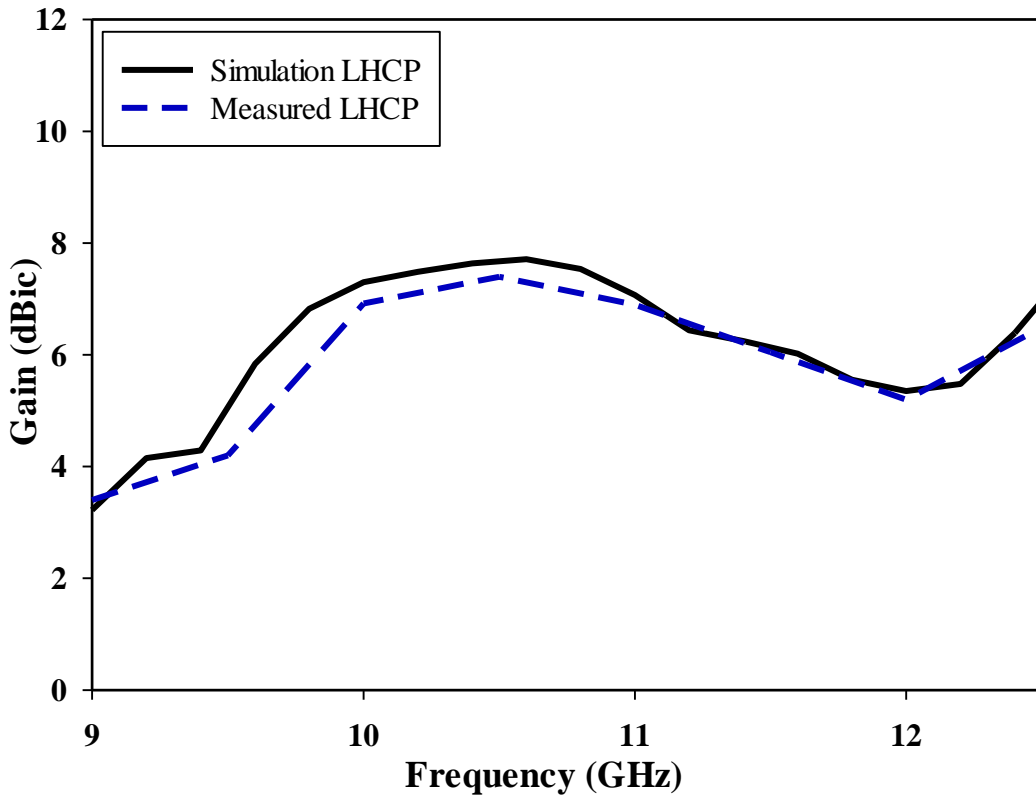
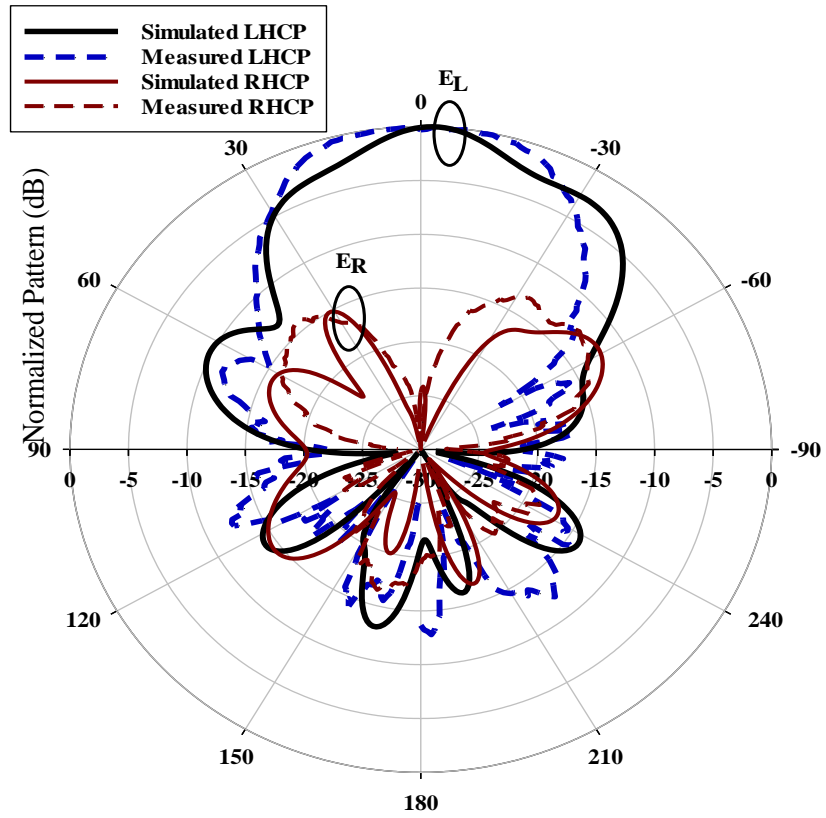
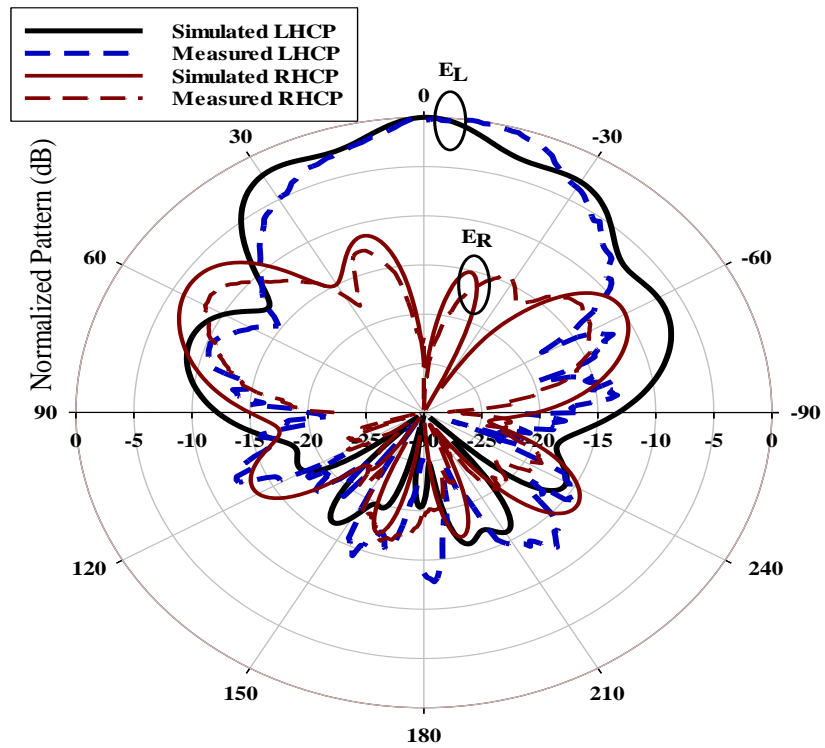


Figure 4.26: Simulated and measured gain for the rectangular DRA.

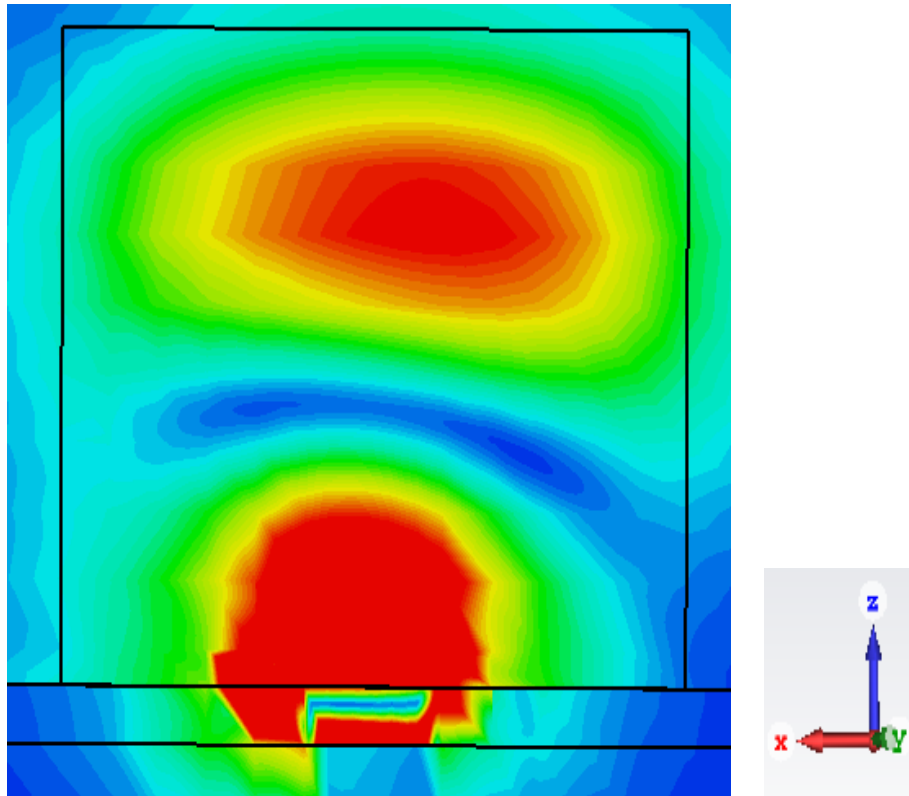


(a)



(b)

Figure 4.27: Simulated and measured normalized radiation patterns for TE₁₁₃ at 10.6 GHz (a) E-plane, (b) H-plane.



(a)

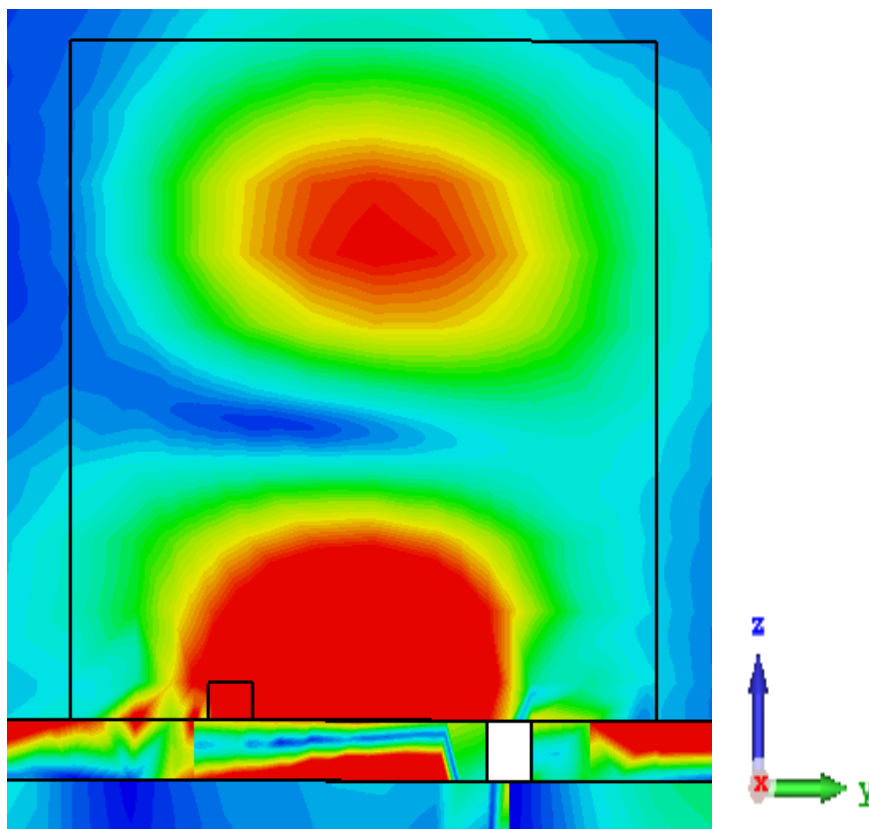


Figure 4.28: The magnetic field for the TE_{113} mode at 10.6 GHz. (a) xz , plane (b) yz plane.

4.3.4 Right-hand Circular Polarisation

In the second scenario, the PIN diode D_1 has been switched to the OFF state and D_2 is switched to the ON State. As a result, the outer ground plane has been connected to the common ground and the inner ground plane section is connected to the positive DC polarity. Therefore, the positive terminal of D_2 is connected via the inner rectangular ground plane and the negative terminal is connected to the outer ground plane. On the other hand, the positive terminal of D_1 is connected to the outer ground plane and the negative terminal is connected to the inner ground plane. Figure 4.29 illustrates the reflection coefficient with a close agreement between the simulated and measured impedance bandwidths of 21.3% and 21.1%, respectively. Once more, good agreement has been achieved between the measured and simulated data for the gain as well as for the axial ratio as illustrated in Figures 4.30 and 4.31. The achieved maximum gain is 6.9 dBic at 10.6 GHz with an AR bandwidth of 4%. Furthermore, the far field patterns are presented in Figure 4.32, where it is evident that a right-hand CP radiation is achieved since the E_R component is greater than the E_L counterpart by 15 dB at 10.6 GHz. In the end, Figure 4.33 shows the short magnetic dipoles within the DRA, and it is clear that the TE_{113} mode has been activated at 10.6 GHz.

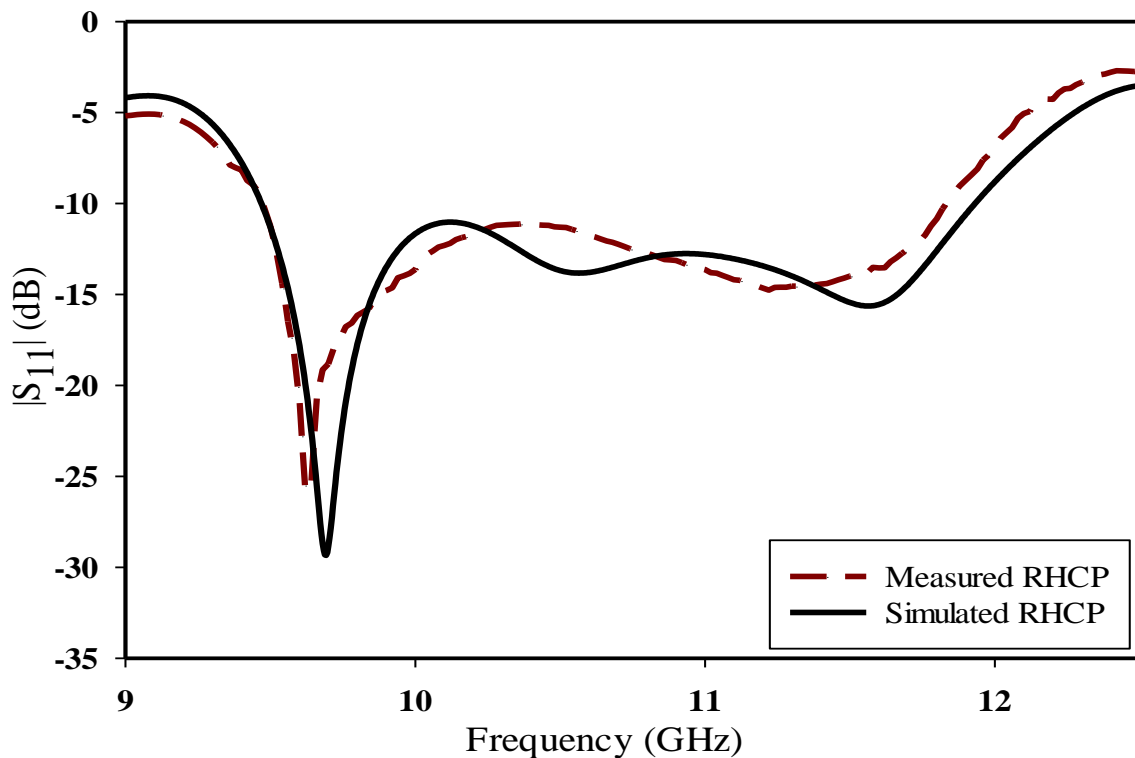


Figure 4.29: Simulated and measured return losses of the rectangular RHCP DRA.

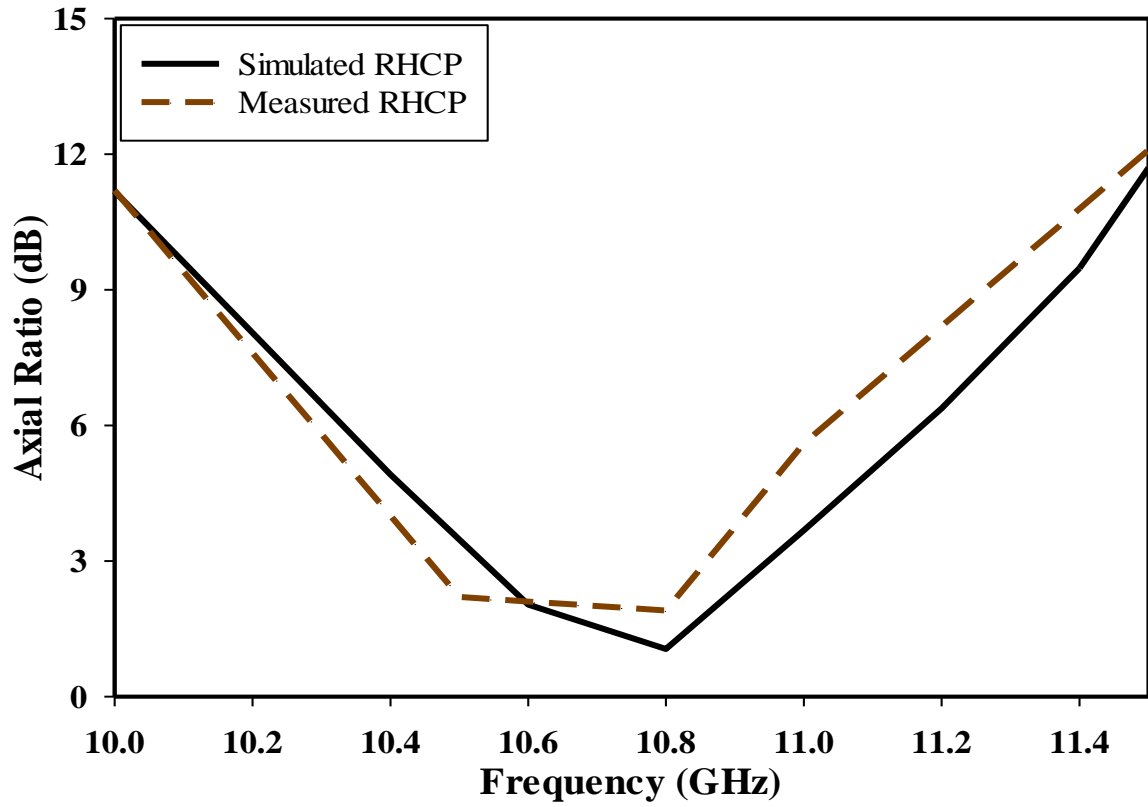


Figure 4.30: Simulated and measured axial ratio for the RHCP RDRA.

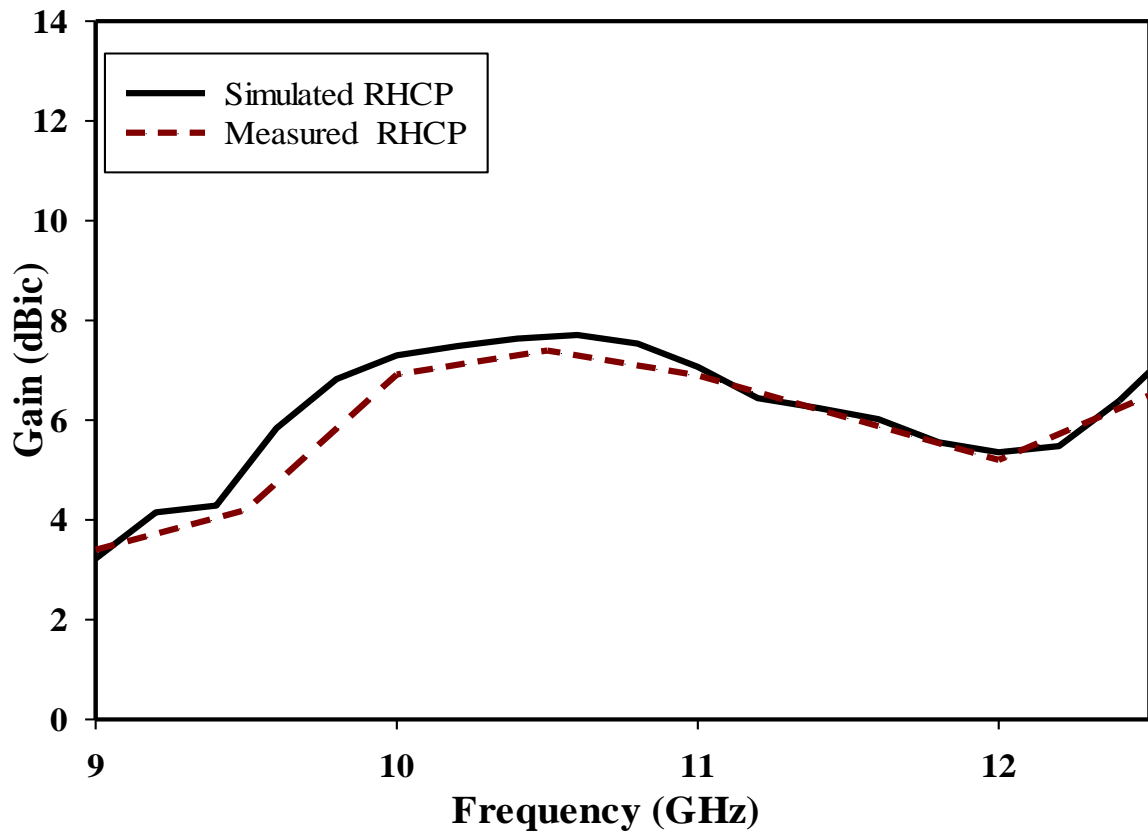


Figure 4.31: Simulated and measured gain for the RHCP RDRA.

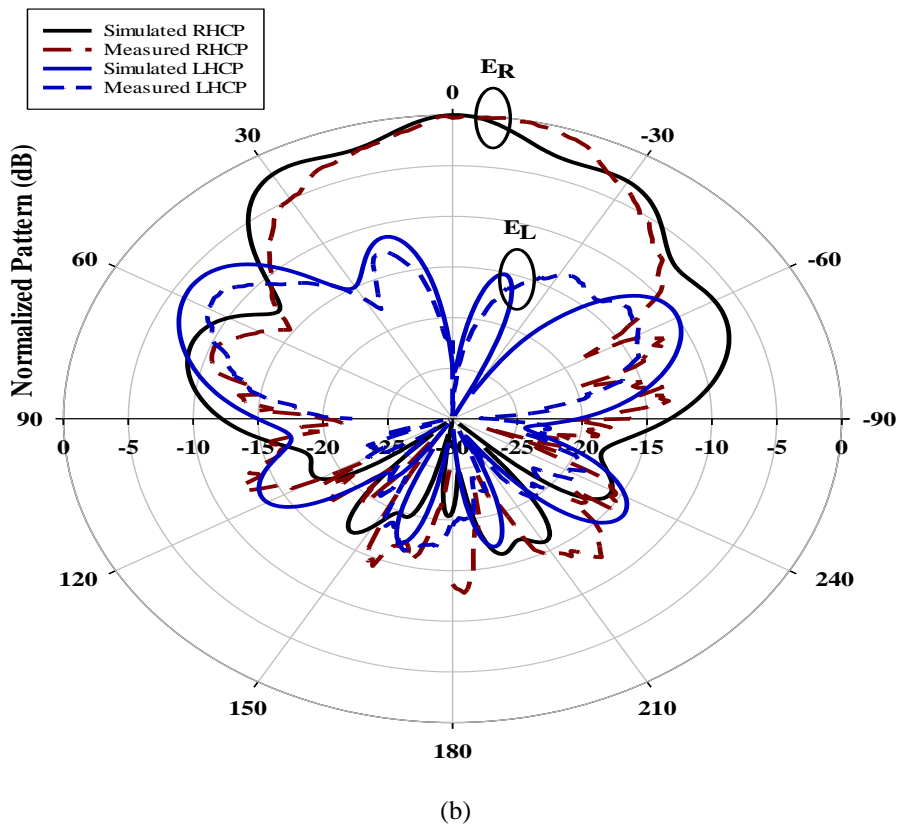
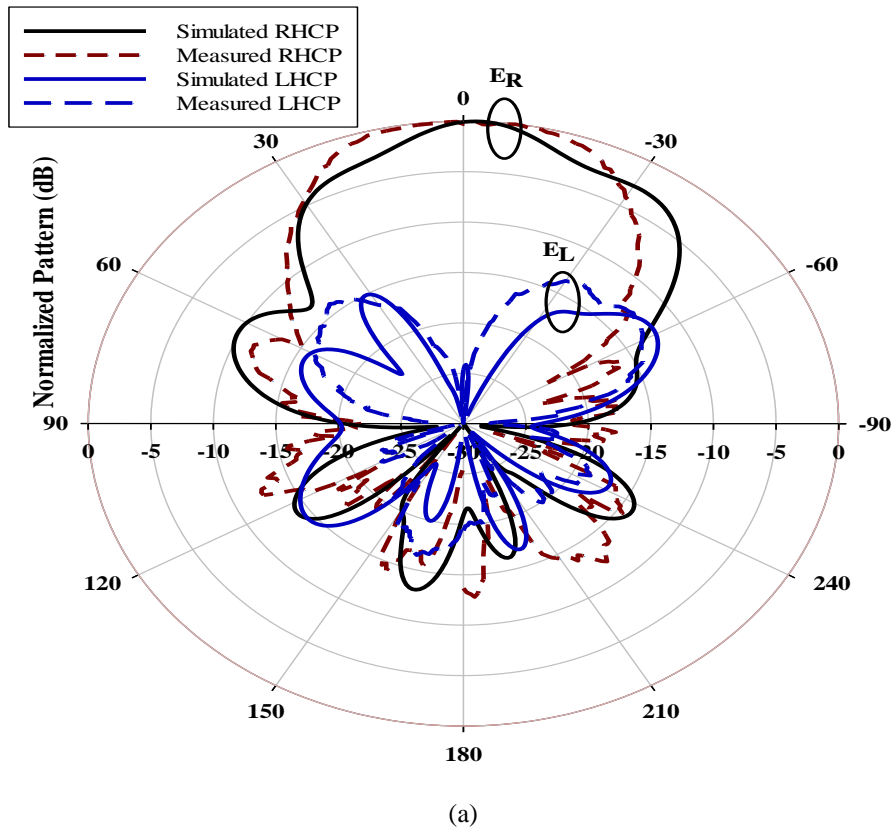
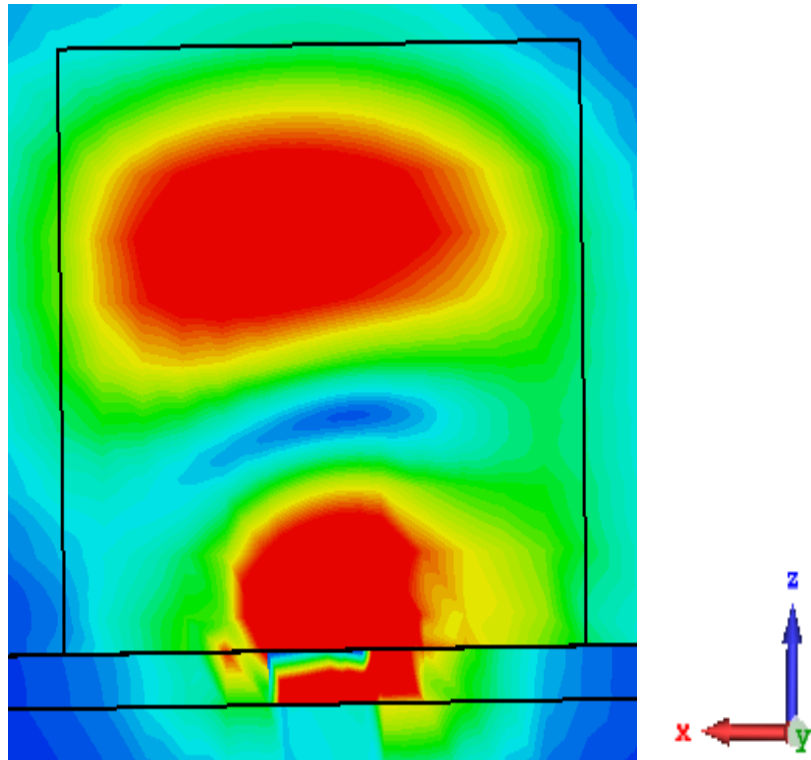
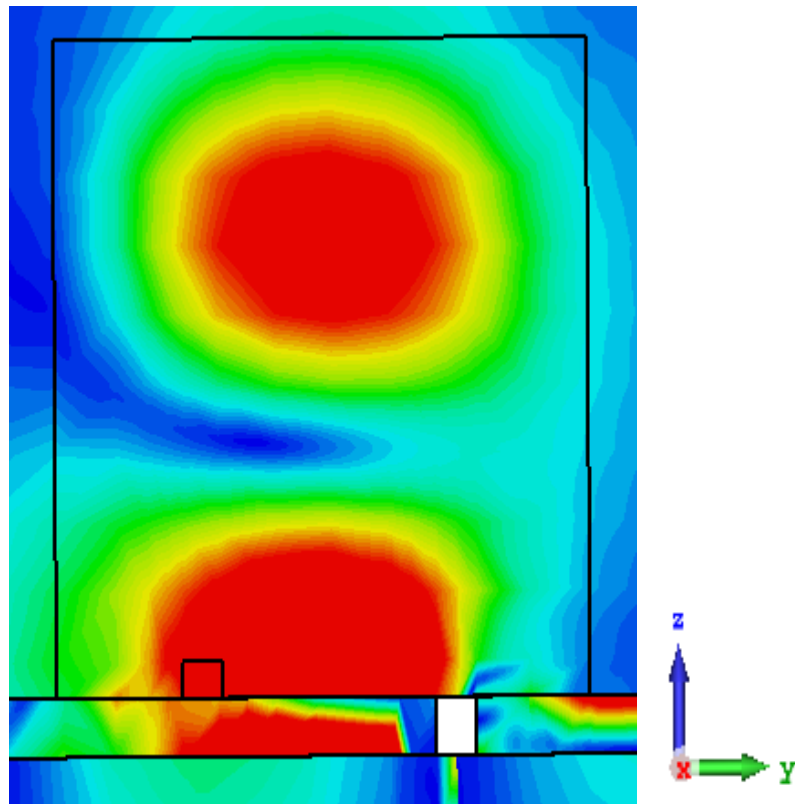


Figure 4.32: Simulated and measured normalized radiation patterns for TE₁₁₃ at 10.8 GHz (a) E-plane, (b) H-plane.



(a)



(b)

Figure 4.33: The magnetic field for the TE_{113} mode at 10.6 GHz (a) xz plane (b) yz plane.

4.3.5 Linear Polarisation

In the third scenario, both of the PIN diodes have not been biased and hence they are switched to the OFF state. Figure 4.34 presents the reflection coefficient with an impedance bandwidth of 3.4% that extends from 10.2 to 10.5 GHz for the simulated and measured data. Figure 4.35 illustrates that the DRA offers a maximum gain of 6.5 dBi at 10.4 GHz with good agreement between simulated and measured data. The far-field patterns at 10.4 GHz are illustrated in Figure 4.36 with a reasonable agreement between measurements and simulations.

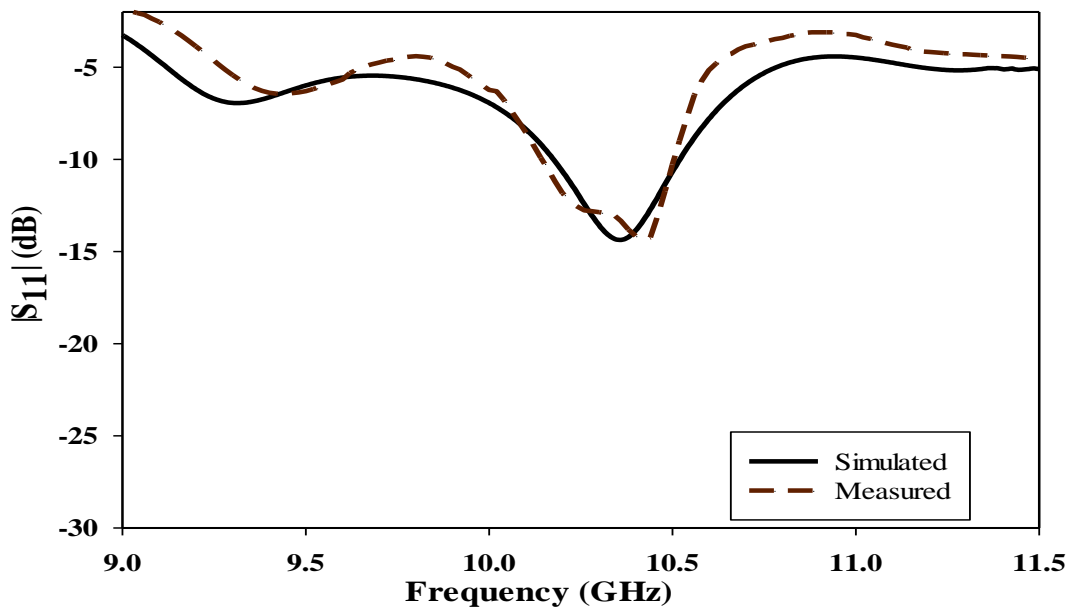


Figure 4.34: Simulated and measured reflection coefficients of linearly polarised RDRA.

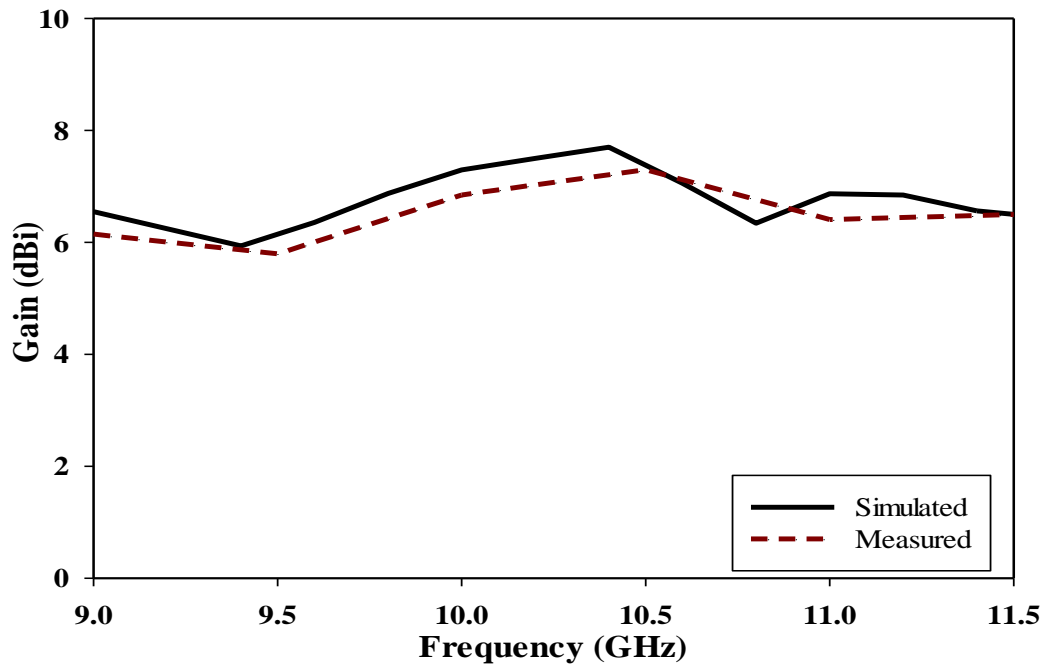
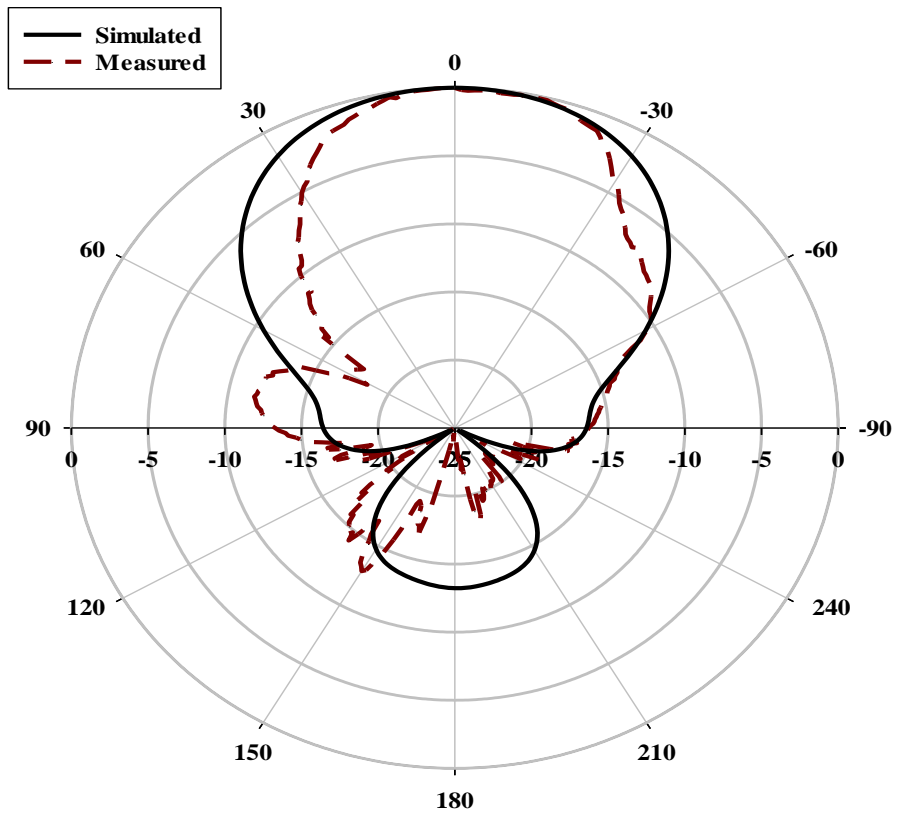
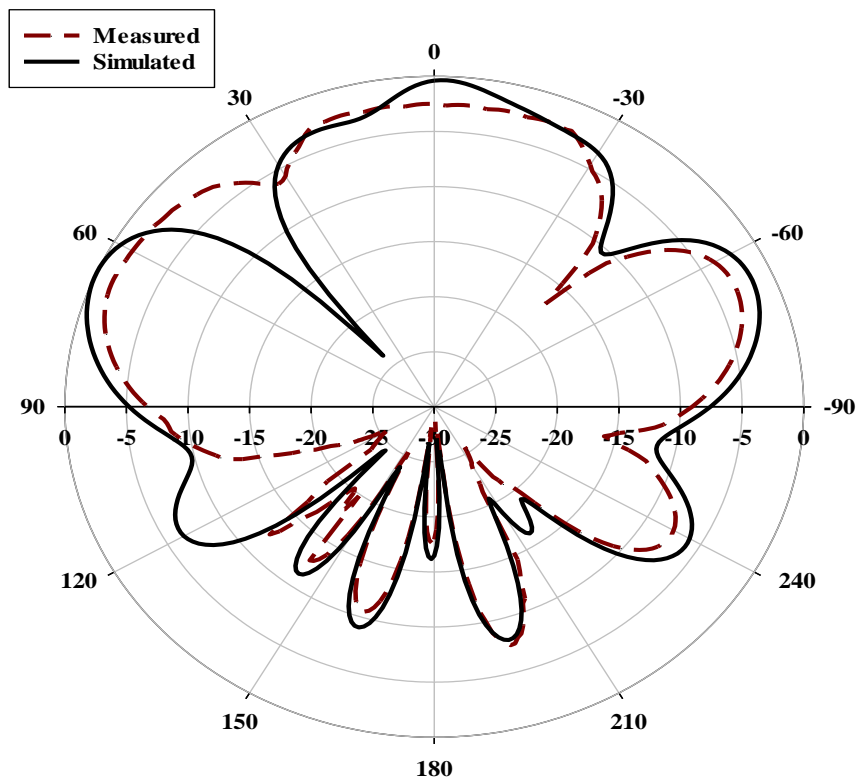


Figure 4.35: Simulated and measured Gain of linearly polarised RDRA.



(a)



(b)

Figure 4.36: Simulated and measured normalized radiation patterns for TE_{113} at 10.4GHz (a) E-plane, (b) H-plane.

4.4 Conclusion

In this Chapter, circularly polarised rectangular DRAs have been studied both theoretically and experimentally. The first design utilized a rectangular DRA, a cross slot, and four PIN diodes to achieve polarisation. An investigation was conducted on a polarisation-reconfigurable rectangular DRA for X-band applications. The proposed antenna can produce LP, LHCP, and RHCP radiation by changing the states of the four PIN diode switches. Simulation results show that the proposed configuration has a wide effective bandwidth of 30% (from 10.15 to 13.67 GHz) for both LHCP and RHCP states, as well as a lower impedance bandwidth of 9.2% for linear polarisation. Additionally, the proposed configuration requires a simple biasing network. The proposed antenna offers potential solutions for X-band applications such as monitoring weather, controlling air traffic, defence tracking, and measuring vehicle speed.

The second design utilizes a rectangular DRA, a rectangular slot, and two PIN diodes to achieve polarisation. By controlling the two PIN diode switches, the antenna is able to produce LP, LHCP, and RHCP radiations. The proposed rectangular DRA has a simple structure that is easy to construct. Simulation results indicate that the LHCP and RHCP radiations have reconfigurable polarisation characteristics with an impedance bandwidth of 21.3%, ranging from 9.6 to 11.9 GHz. In contrast, the LP state has a narrower impedance bandwidth of 3.4%, ranging from 10.2 to 10.5 GHz. Additionally, the proposed antenna has achieved a gain of approximately 6.9 dBic in all polarisations. The simulation and measurement results are in good agreement. The proposed antenna has a compact structure compared to other designs reported in the literature, as well as a simple biasing mechanism, construction, and adjustment. This makes it a potential candidate for numerous applications in wireless communication systems, particularly in relation to polarisation diversity applications.

Chapter 5

Reconfigurable DRA using Photoconductive Switches

5.1 Introduction

Semiconductors have a special property where their electrical conductivity can be altered when exposed to light, a phenomenon known as photoconductivity. Intrinsic silicon, which is pure silicon without any impurities, has a large energy band gap between the conduction and valence bands, resulting in only a limited number of electrons present in the conduction band at room temperature [127]. Upon illumination, photons interact with electrons in the valence band and elevate them to the conduction band, resulting in an increase in the material's conductivity. This increase in carrier concentration leads to a rise in the conductivity of silicon, as well as a decrease in its dielectric constant [69]. As the dielectric loss tangent of silicon rises, it becomes lossier.

The utilization of high-resistivity silicon wafers as switches enables the optical manipulation of antennas. This is accomplished by exposing the silicon to optical radiation, which alters its conductive properties from that of a semiconductor to those similar to a conductor. The photons that subjected to laser illumination possess sufficient energy to excite electrons in the valence band, prompting them to transition to the conduction band and form an electron-hole plasma, leading to an increase in conductivity. Furthermore, the wavelength and power of the optical radiation impact the level of conductivity obtained, necessitating meticulous consideration [128].

Table 5.1 presents the Silicon's physical properties such as the conductivity (σ), the loss tangent ($\tan \delta$), and the relative permittivity (ϵ_r) under different power levels. This phenomenon has been utilised to design a frequency reconfigurable antenna in which the switch is created using photoconductive Silicon, that is illuminated by a laser power set on 212 mW. Such a level of incident powers changes the Silicon properties from $\epsilon_r = 8.88$ and $\sigma = 622$ in the ON state to $\epsilon_r = 11.85$ and $\sigma = 52$ in the OFF state when the laser power is set as 0 mW [69]. It should be noted that the utilisation of photoconductive switches eliminates the need for bulky

DC biasing and associated wires, which eliminates any impact on the antenna's performance. This is most suitable when working with physically smaller antenna such as those operating at the mmWave frequencies.

Table 5-1: Physical Properties of Silicon at 12 GHz [69].

Laser Power (mW)	σ	$\tan\delta$	ϵ_r
0	52	0.58	11.85
50	211	2.56	10.94
120	409	5.5	9.87
212	622	9.29	8.88

5.2 Optically Controlled Frequency-Reconfigurable Rectangular DRA

5.2.1 Antenna Configuration

Figure 5.1 illustrates the proposed frequency reconfigurable DRA, which has been assumed to be made using Alumina with a square cross-section size of 6 mm and height of 8mm, which results in the aspect ratio of 0.75 that facilitates the excitation of a single higher order mode (TE₁₁₃) at 12.7 GHz [116].

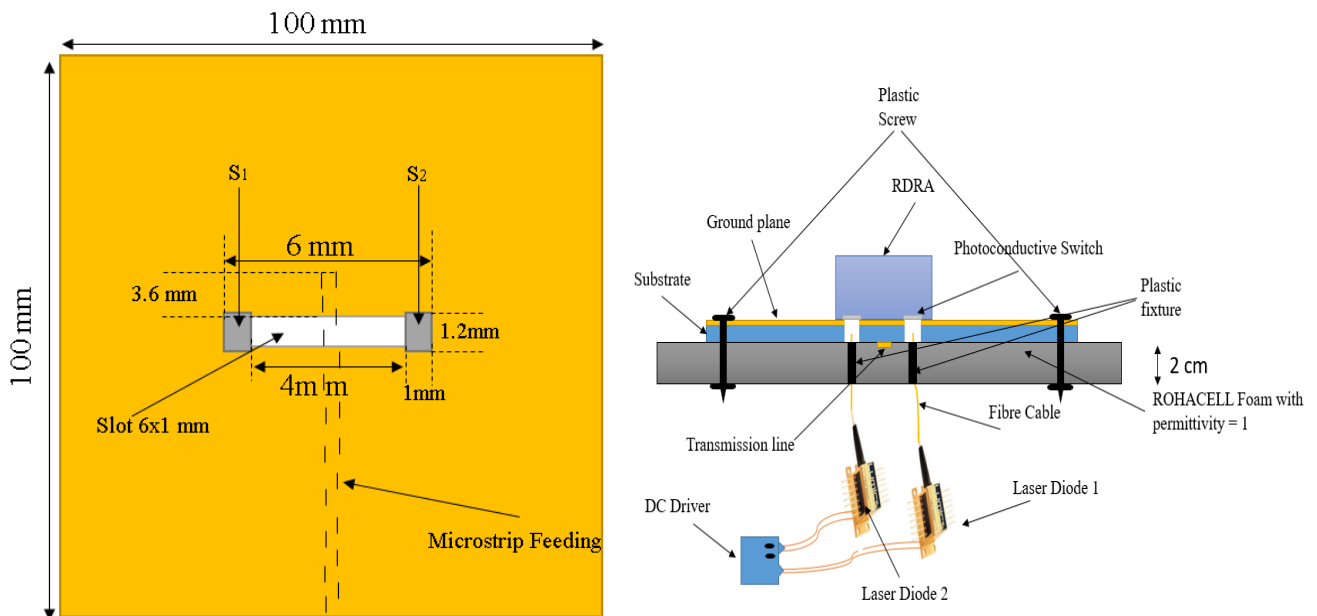


Figure 5.1: Geometry of the optically controlled frequency reconfigurable DRA.

The rectangular DRA has been mounted on a 100 mm^2 ground plane and excited using a microstrip line through an aperture-coupled slot, as shown in Figure 5.1, this method brings the previously mentioned of feeding the aperture by a transmission line that is located below the ground plane. This isolates the radiating structure from unwanted coupling or spurious radiation from the feed [129]. The stub length has been chosen as 3.6 mm for optimum matching. A Roger substrate RO4350B was utilised with a thickness of 0.8 mm, dielectric constant of 3.48 and loss tangent of 0.0037. Additionally, the 6 mm rectangular slot utilises two photoconductive switches S_1 and S_2 that are located near the slot edges. Each photoconductive switch has dimensions of $1 \times 1.2 \text{ mm}^2$ so that when they are both illuminated by laser to be on the ON state and slot length is reduced from 6 to 4 mm. On the other hand, in the absence of the laser beam, both switches will be in the OFF state and hence the slot retains its length of 6 mm. As expected, different slot length excites different resonance modes at different frequencies, and hence frequency reconfigurability can be achieved.

5.2.2 Results and Discussion

Table 5.1 demonstrates the photoconductive switches characteristics under different power levels. It is worth pointing out that the proposed antenna supports a single higher-order operation [116]. Therefore, the excitation of adjacent modes will be avoided. Varying the slot length from 6 to 4 mm results in changing the resonance frequency from 9.5 GHz to 14.5 GHz as shown in Figure 5.2. The simulated return losses of the frequency-reconfigurable DRA are demonstrated in Figure 5.2, using different levels of incident power. It can be noted from these results that in the OFF state when the slot length is 6mm, the DRA resonates at 11 and 13.7 GHz. On the other hand, when the incident power is increased to 212 mW and both photoconductive diodes switch to the ON states, the slot length reduces to 4mm and the DRA resonates at 12.7 GHz.

The antenna operates in the TE_{113} higher-order mode with an impedance bandwidth of 7.6% at 12.7 GHz. The antenna gain is depicted in Figure 5.3 with a maximum of 6.4 dBi at 12.7 GHz when both of the photoconductive switches are ON. The normalized broadside radiation patterns at the TE_{113} mode at a frequency of 12.7 GHz, are shown in Figure 5.4. Figure 4.5 illustrates the magnetic field distribution inside the rectangular DRA, which confirms the excitation of the TE_{113} resonance mode at 12.7 GHz.

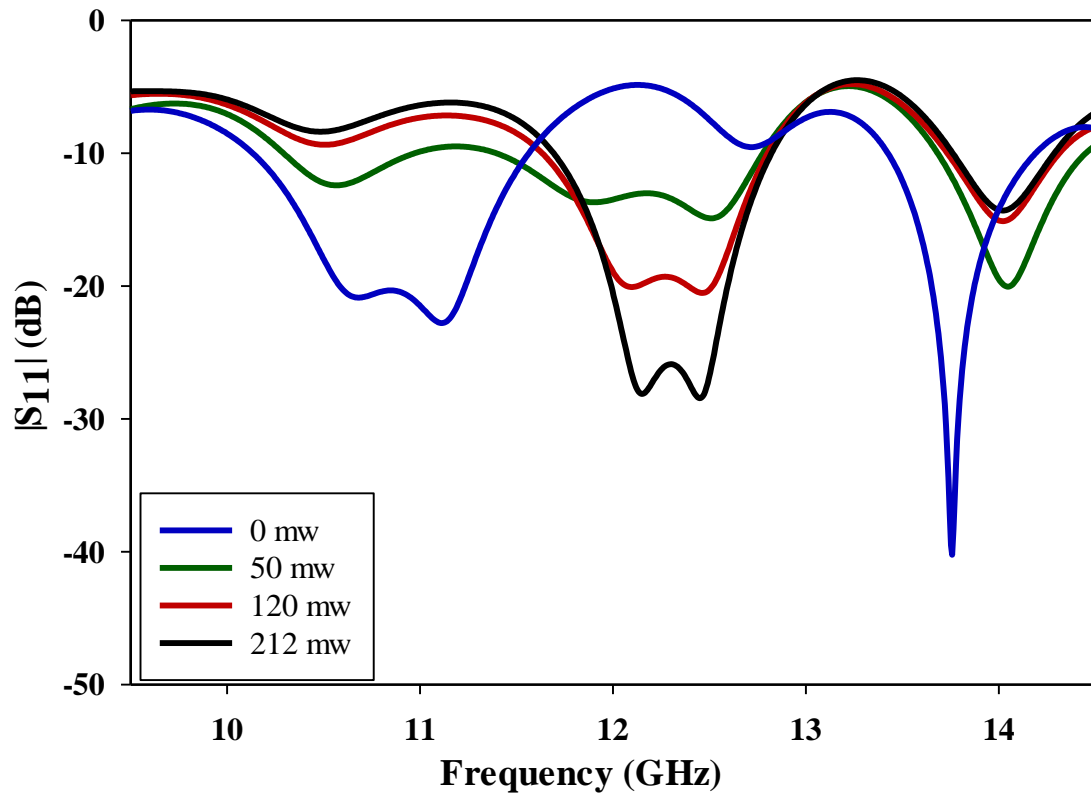


Figure 5.2: Simulated reflection coefficients of RDRA under different illuminating power levels.

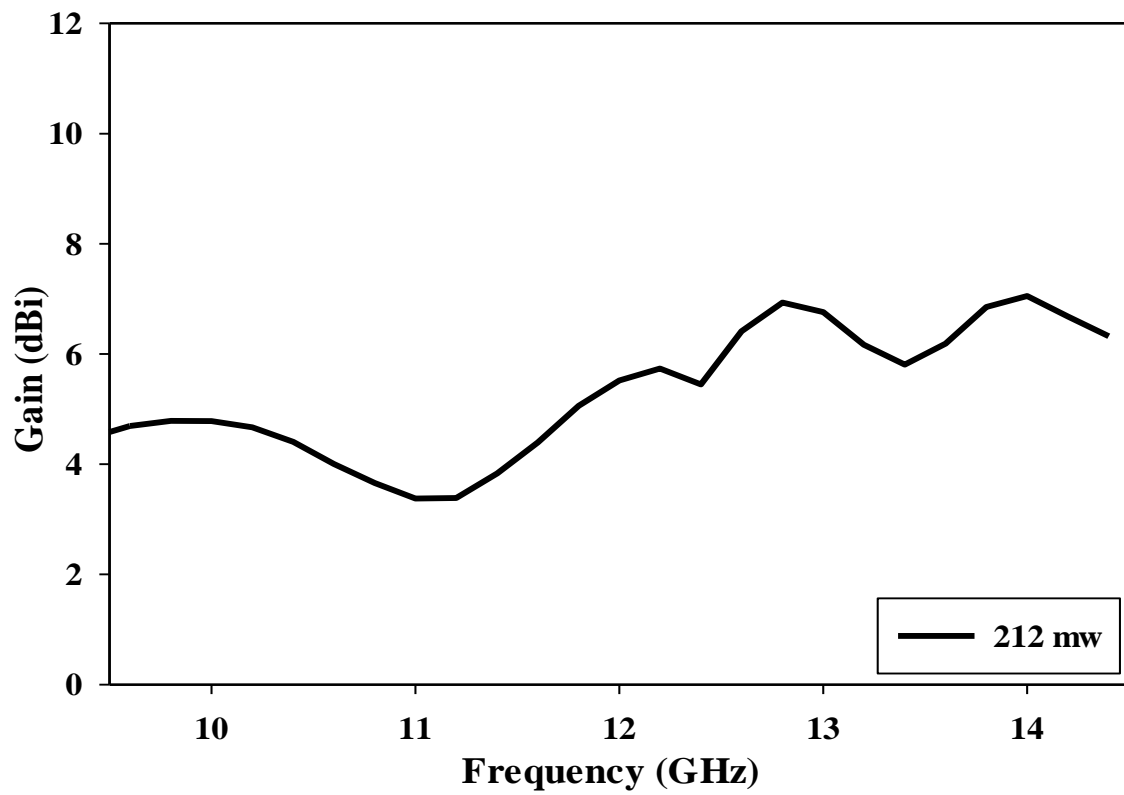


Figure 5.3: Simulated gain as a function of frequency for an incident optical power of 212 mW.

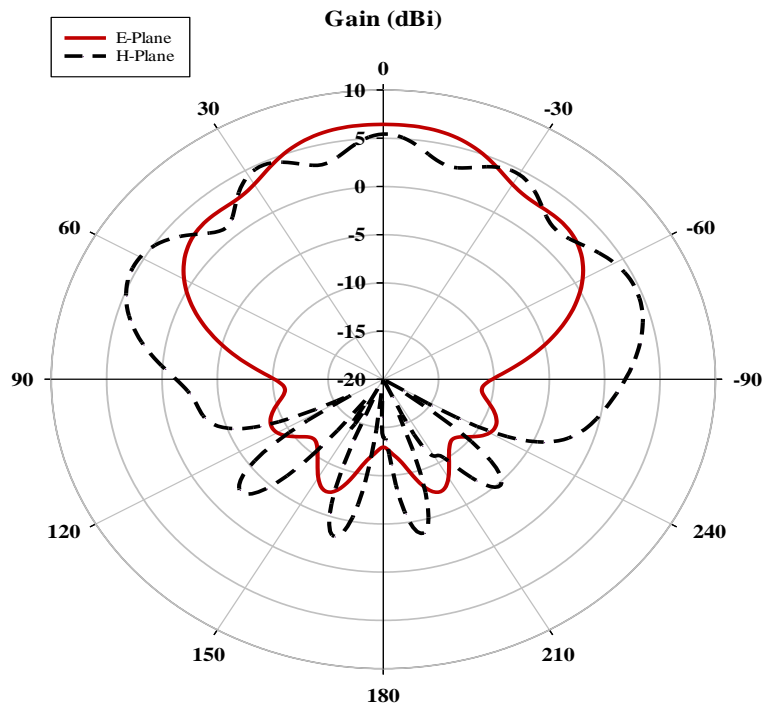


Figure 5.4: The H-plane and E-plane radiation patterns for frequency reconfigurable RDRA at 12.7 GHz with mode TE_{113} When the switches are ON.

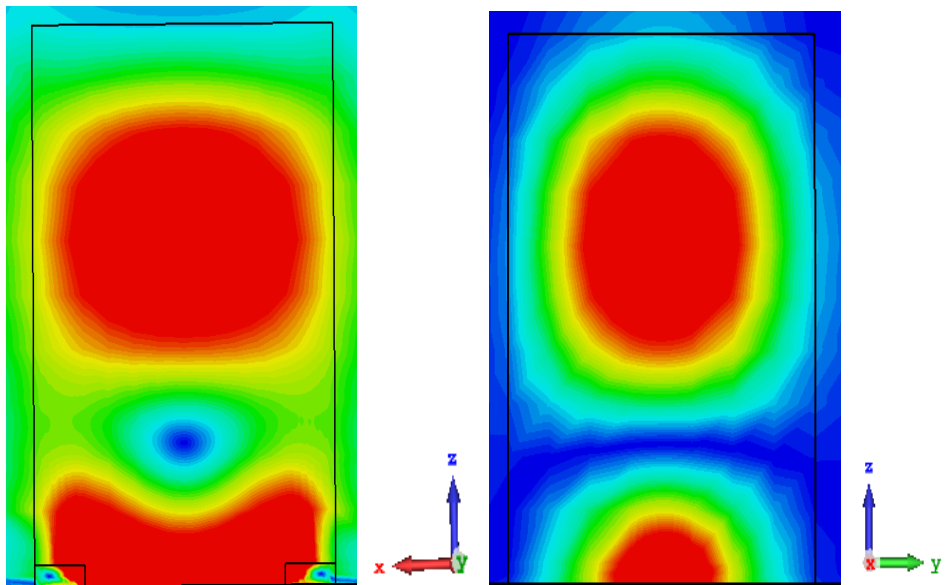


Figure 5.5: Magnetic field distribution inside the DRA for the TE_{113} mode at 12.7 GHz.

In the absence of any laser beam illumination, both photoconductive switches are in the OFF states, where. The antenna operates in dual-bands with respective impedance bandwidths of 13% and 5.6% at 11GHz and 13.7 GHz respectively as demonstrated in Figure 5.6. It should be noted that the wider bandwidth at 11 GHz is expected due to the excitation of the fundamental TE_{111} mode at this frequency. On the hand, a narrow band is achieved at 13.7 GHz

as the higher order mode of TE₁₁₃ has been excited one more. Figure 5.7 demonstrates gain of 6 dBi and 8.3 dBi for the lower and higher-order modes, respectively.

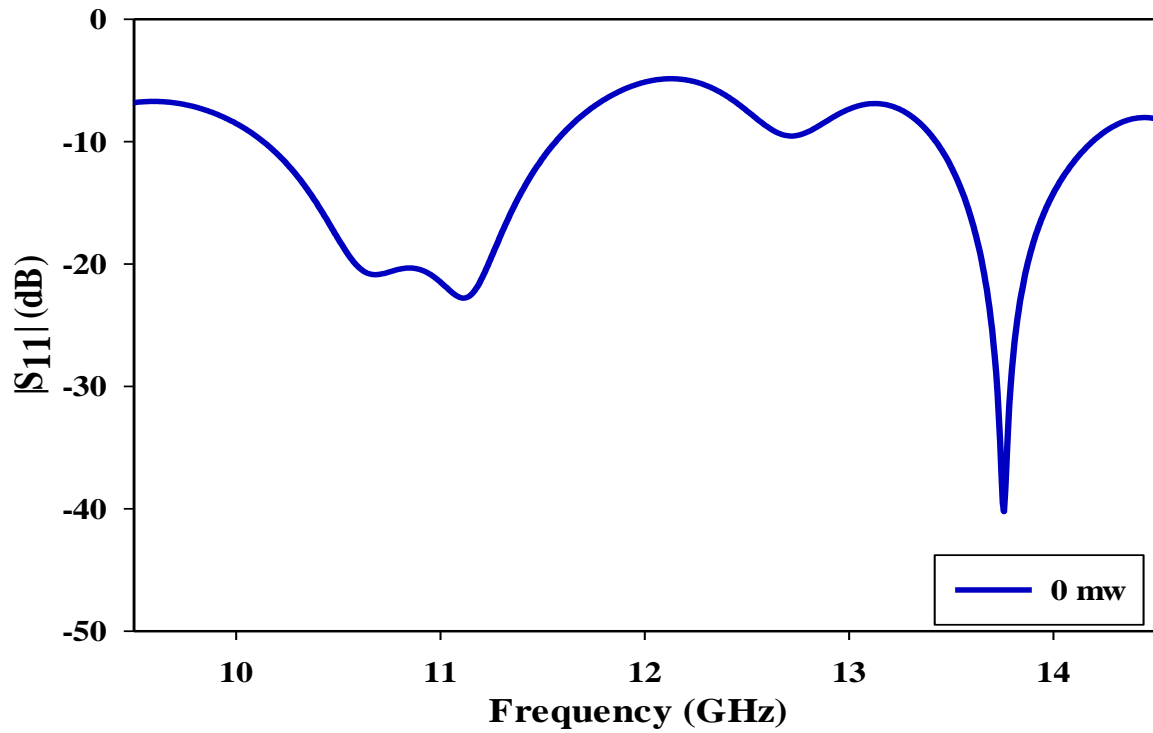


Figure 5.6: Simulated reflection coefficient of frequency reconfigurable RDRA for both 0 mw.

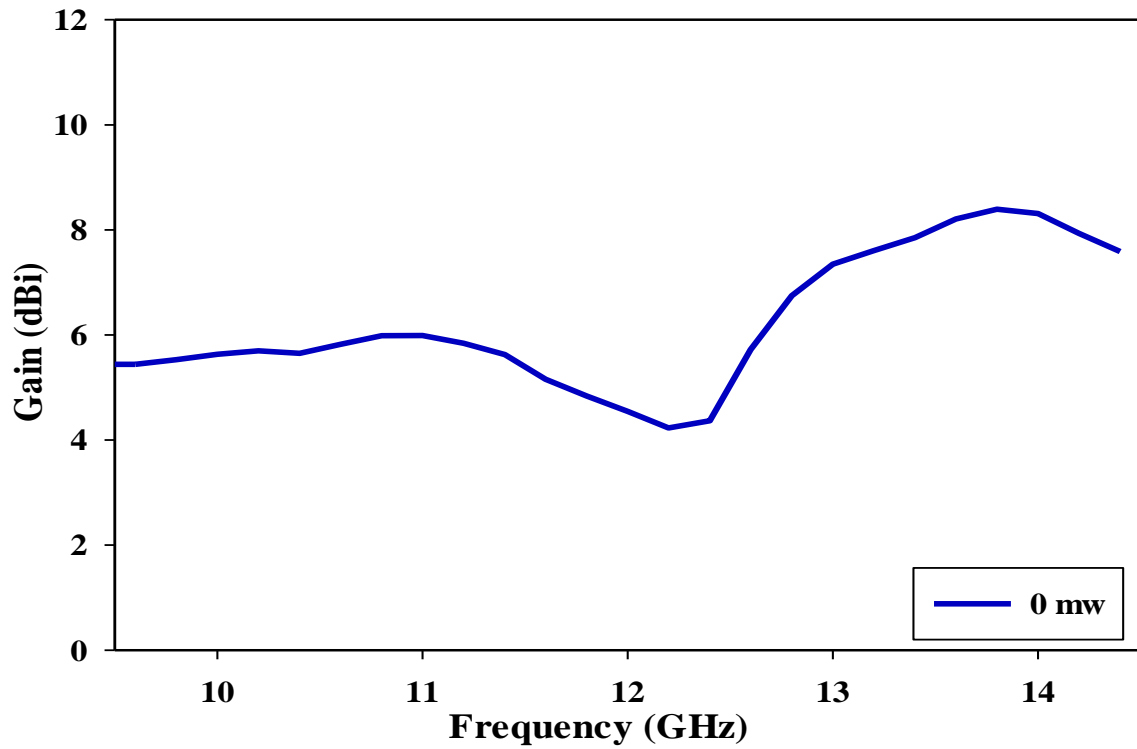


Figure 5.7: Simulated gain as a function of frequency in the absence of the illuminating laser beam.

The radiation patterns of the TE_{111} and TE_{113} modes are demonstrated in Figure 5.8. The magnetic field inside the DRA is illustrated in Figure 5.9 for (a) lower order-mode TE_{111} mode and (b) higher-order mode TE_{113} . In case of switches are ON the single band has been excited. However, the dual-band has been generated when switches are OFF, evident that the resonance modes can be controlled by optimizing the slot length.

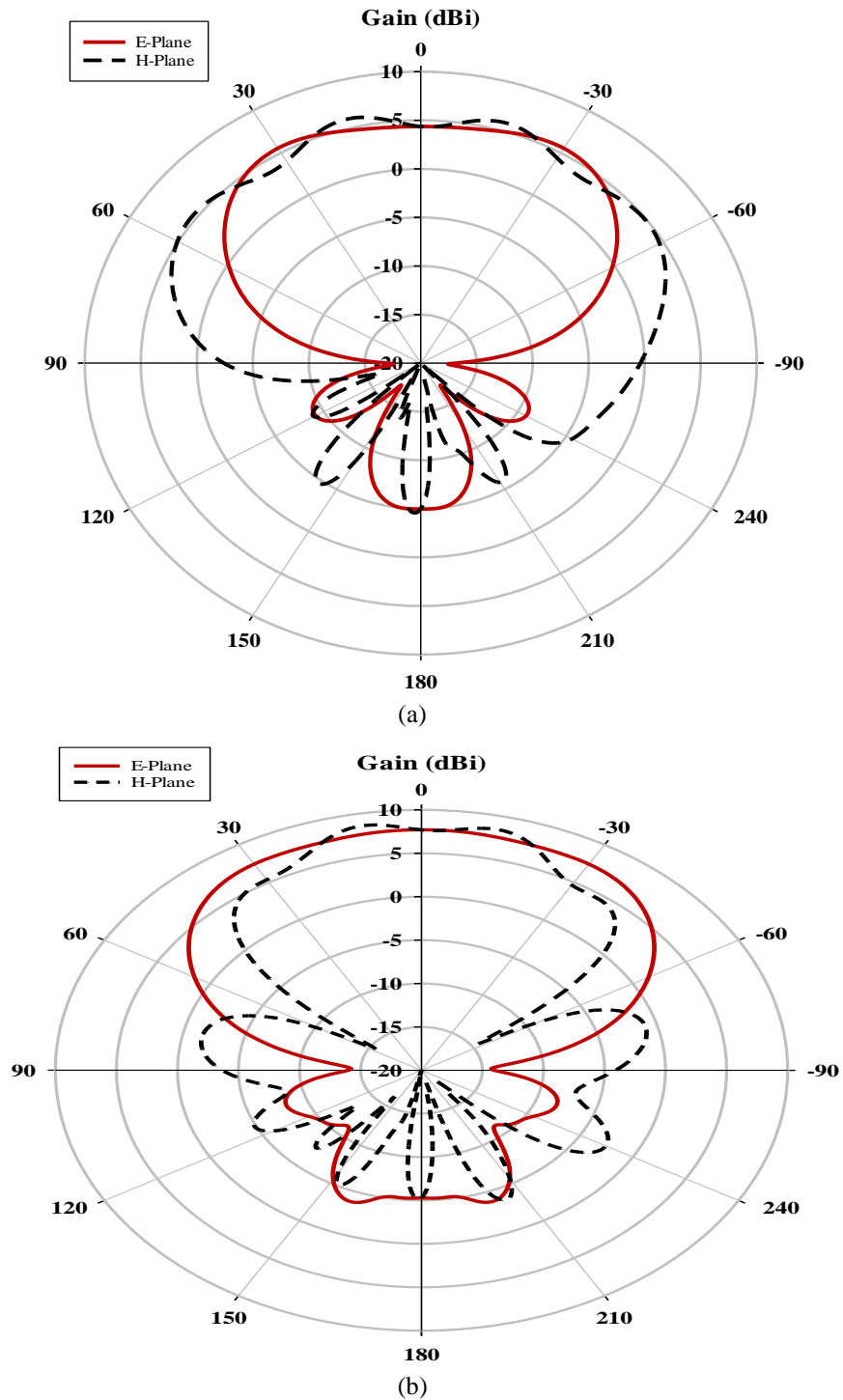


Figure 5.8: The H-plane and E-plane radiation patterns for frequency reconfigurable RDRA for the following modes (a) TE_{111} at 11 GHz and (b) TE_{113} at 13.7 GHz.

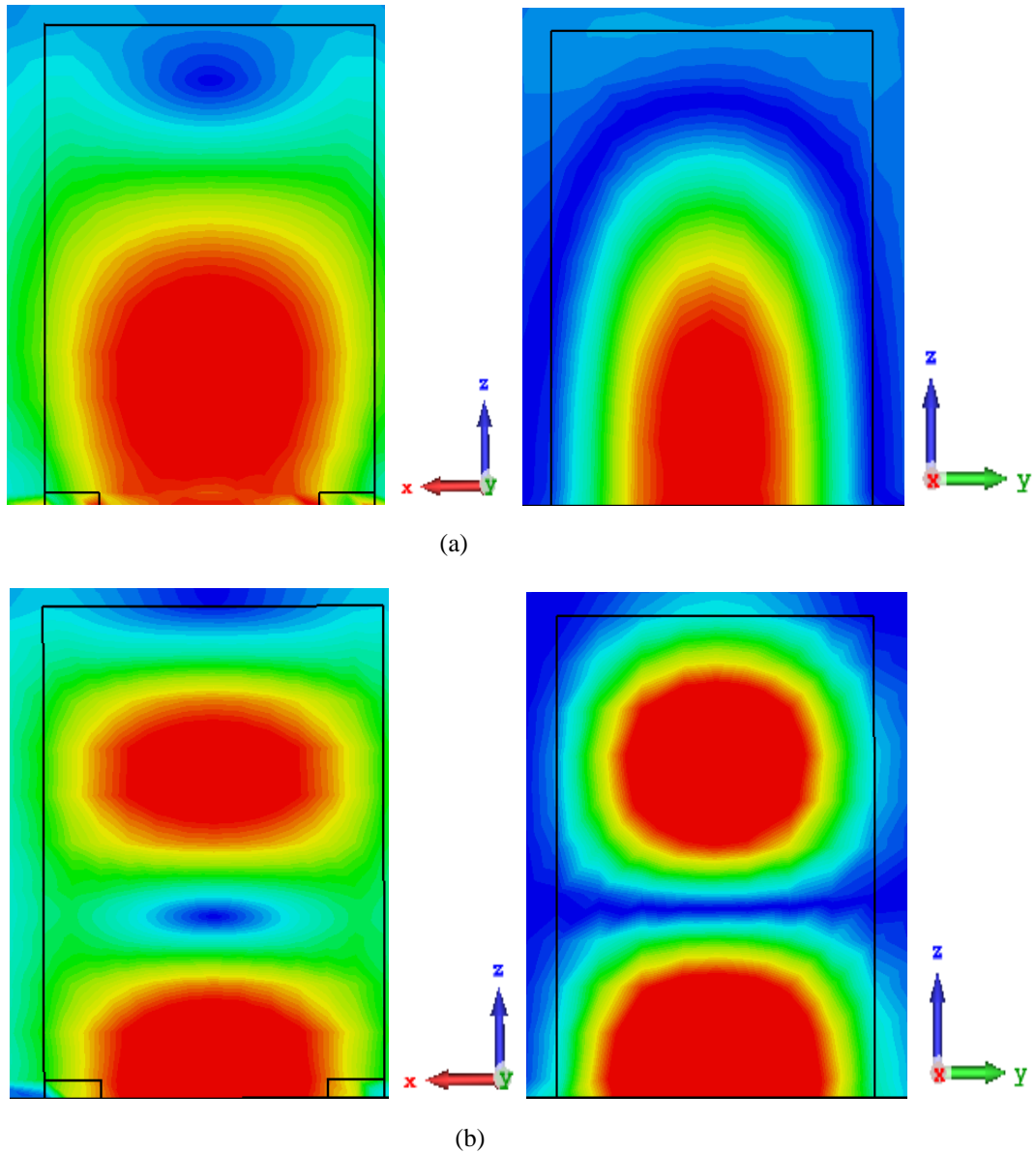


Figure 5.9: Simulated magnetic field for the (a) TE_{111} mode at 11 GHz. (b) TE_{113} at 13.7 GHz.

A third scenario is considered in which one photoconductive switch, S_1 , is illuminated by a power of 212mW, while the other photoconductive switch, S_2 , was not illuminated. This configuration results in the antenna operating in triple-band with an impedance bandwidth of 37.6% (8.26-12.1 GHz), 4.3% (12.2-12.76 GHz) and 4.33% (13.45-14.15 GHz) respectively as illustrated in Figure 5.10. The maximum antenna Gain is 7.6 dB at 13.8 GHz as shown in Figure 5.11. The H-plane and E-plane radiation patterns for frequency reconfigurable rectangular DRA for modes TE_{111} and TE_{113} modes are demonstrated in Figure 5.12. In Figure 5.13 it should be noted that the proposed antenna supports the lower and higher-order modes of TE_{111} at 10 GHz and TE_{113} at 13.8 GHz.

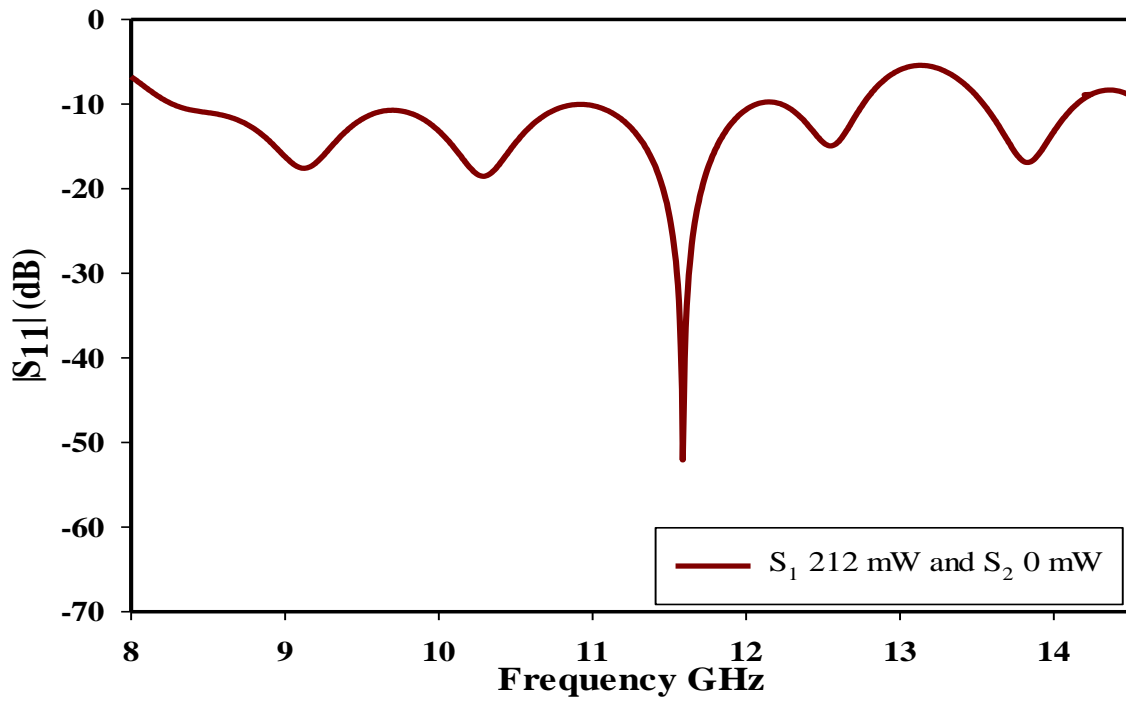


Figure 5.10: Simulated reflection coefficient of frequency reconfigurable RDRA.

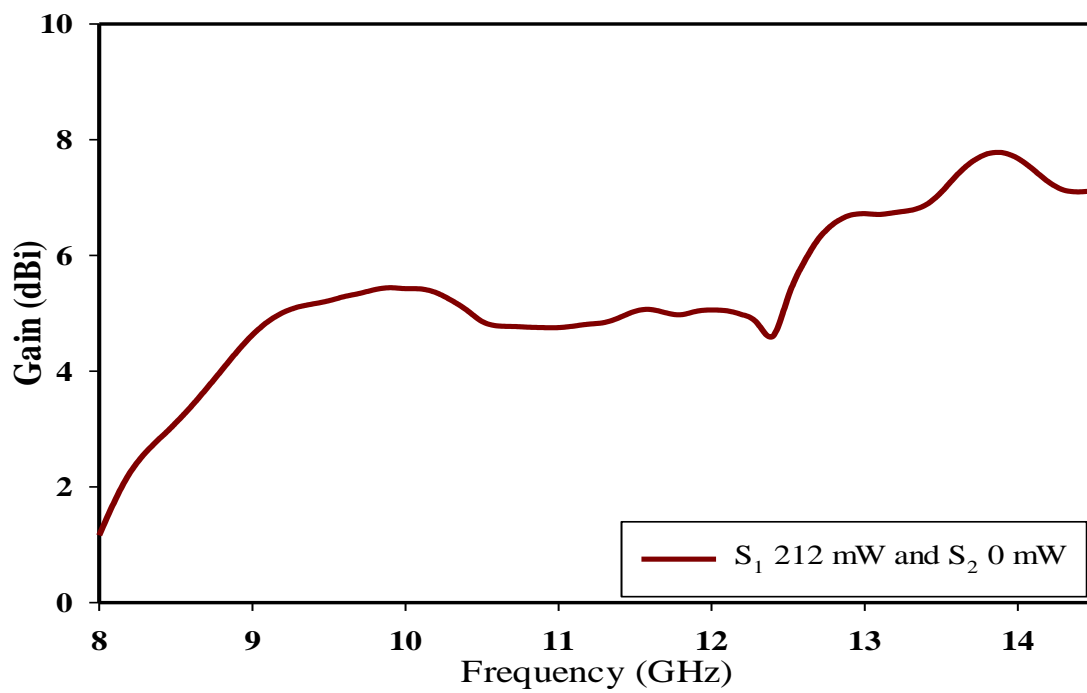
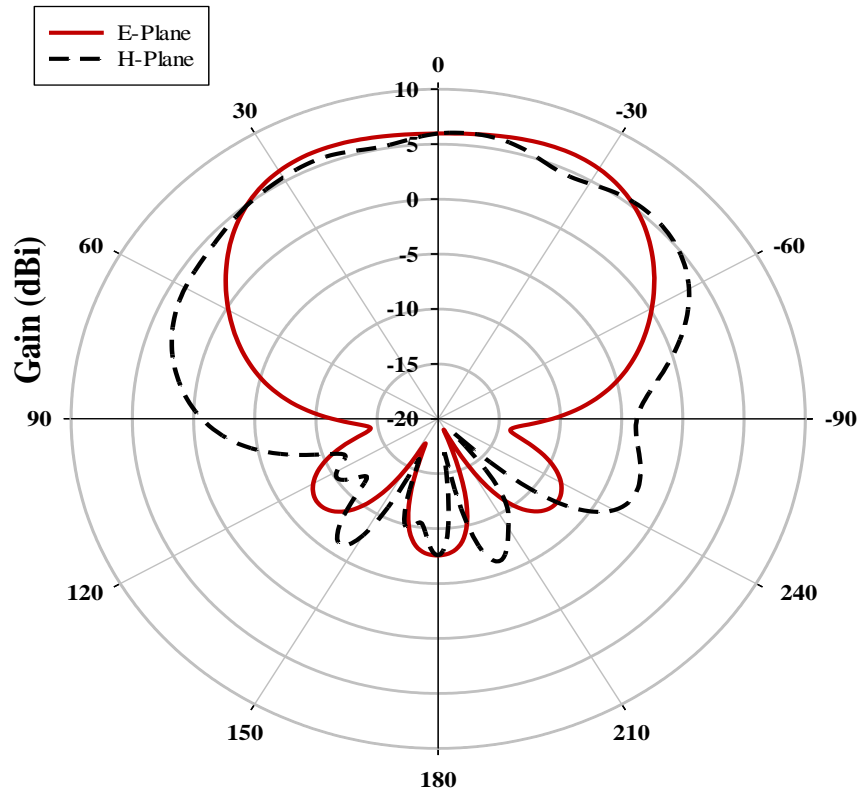
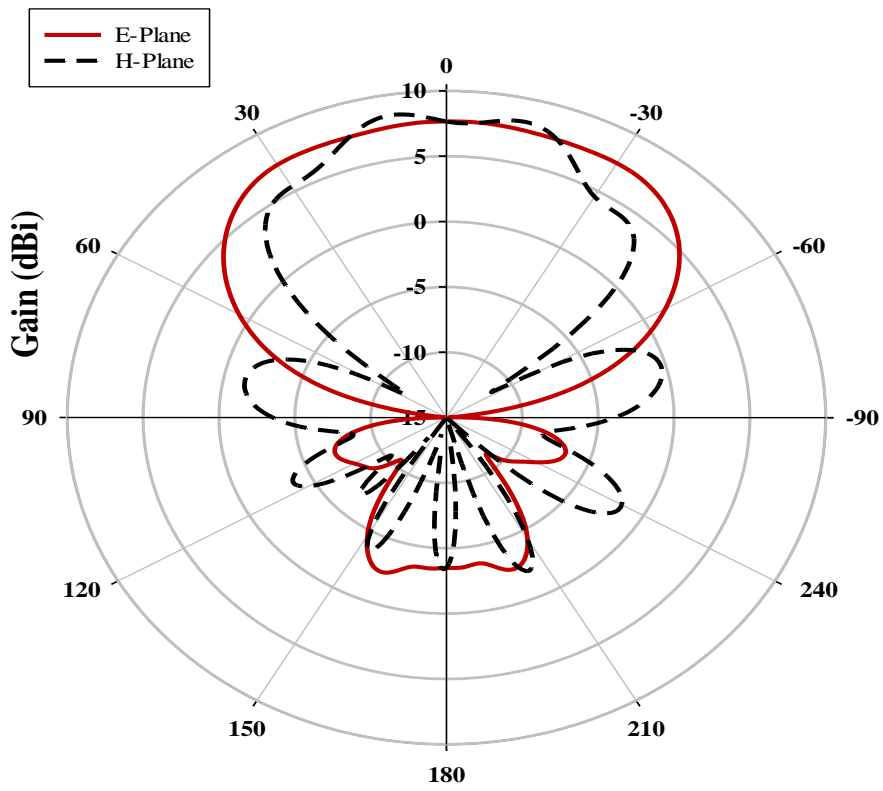


Figure 5.11: Simulated gain as a function of frequency reconfigurable RDRA.

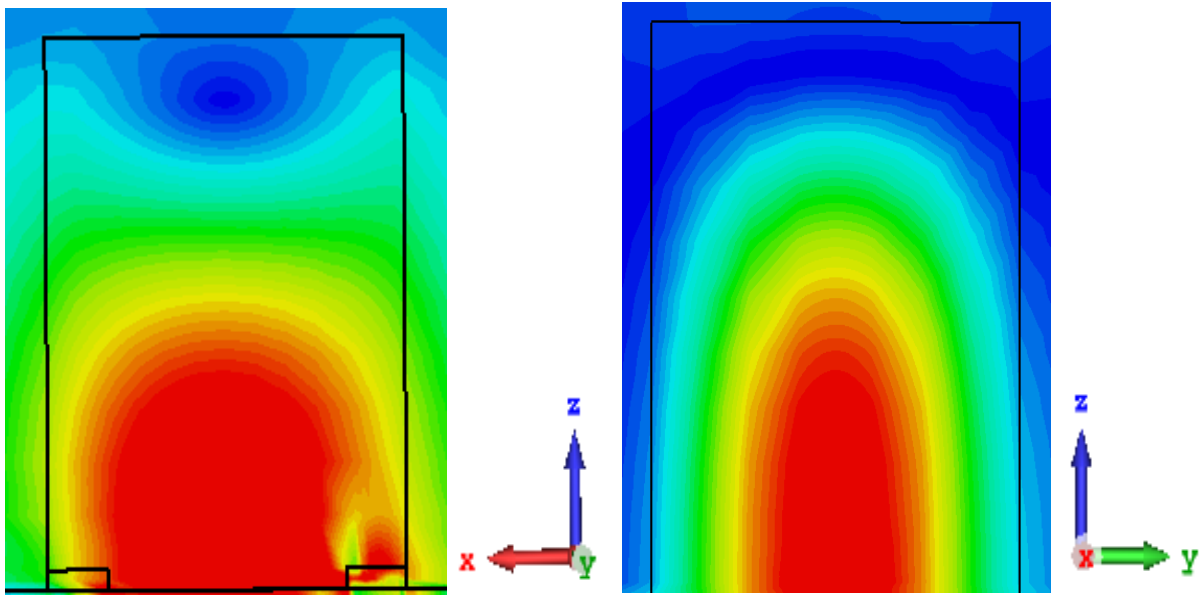


(a)

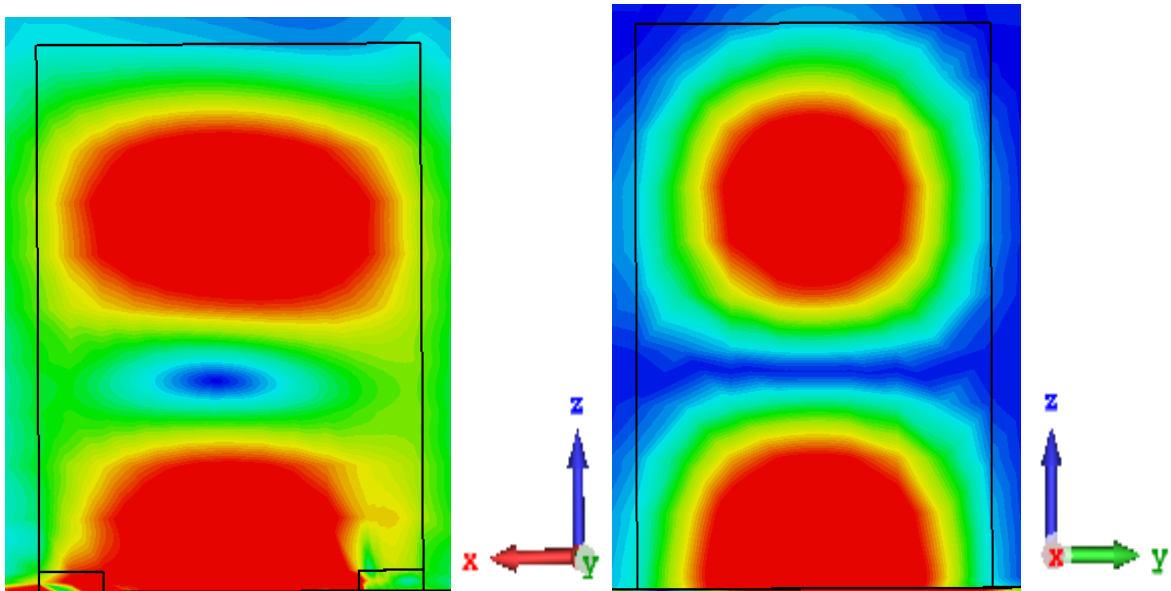


(b)

Figure 5.12: The H-plane and E-plane radiation patterns for frequency reconfigurable RDRA for modes (a) TE_{111} at 10 GHz, (b) TE_{113} at 13.8 GHz.



(a)



(b)

Figure 5.13: Simulated magnetic field for the (a) TE_{111} mode at 10 GHz, (b) TE_{113} at 13.8 GHz.

5.3 Optically Controlled Polarisation Reconfigurable Millimetre-Wave DRA using Photoconductive Switches

The emergence of new technologies like 5G networks and the Internet of Things (IoT) has led to the increased use of mmWave communications. These communications are seen as a solution for the demand for high-speed data transfer, large bandwidth, and small component sizes [130]. However, mmWave communication systems face significant propagation challenges, such as high path loss and shadowing, which can affect their performance [131]. Several approaches have been proposed to address these issues, one of which is the use of reconfigurable frequency antennas. Metallic antennas are unsuitable for millimetre wave frequency bands due to their high conductor and substrate losses. On the other hand, dielectric resonator antennas are well-suited for millimetre-wave systems due to their low profile, low conductor losses, large bandwidth, and high radiation efficiency [132].

5.3.1 Antenna Configuration

An optically controlled polarisation reconfigurable DRA using photoconductive switches has been proposed, where a rectangular ring slot has been utilized to excite the DRA. Two photoconductive switches are placed on the opposite sides of the feeding slot to facilitate polarisation's sense of reconfigurability. A rectangular DRA made of Alumina with a dielectric constant of 9.9 and a loss tangent of $\tan \delta < 0.002$ has been considered. The length, width and height are chosen as $a= 3.23$ mm, $b=4.6$ mm and $h=2.8$ mm as shown in Figure 5.14a. Once more, the antenna is placed on top of a metal ground plane that is backed by a Roger RO4350B substrate with respective size, thickness and a dielectric constant of 35 mm, 0.25 mm, $\epsilon_r=3.48$ in conjunction with a loss tangent of 0.0037. The ground plane has the same dimensions as the substrate. The antenna has been excited using a slot fed that is using a microstrip feeding transmission line. The latter is printed underneath the substrate with a width of $w_t=0.5$ mm.

In order to generate CP radiation, a rectangular ring slot has been employed as illustrated in Figure 5.14b with two gaps that accommodate the photoconductive switches. Each gap's length, width, and height are $0.33 \times 0.4 \times 0.3$ mm. The circular polarisation sense can be controlled by illuminating a single photoconductive switch at a time with a laser beam to achieve either RHCP or LHCP radiation.

Furthermore, in order to allow the laser light to illuminate each of the switches, two holes need to be drilled through the substrate as illustrated in Figure 5.14c. The switch is in the ON state

when the silicon is illuminated by the laser beam and the OFF state in the absence of the laser beam illumination. It is worth pointing out that, the absence of bias lines and easy integrations are the most important advantages of the optical switching option compared with classical approaches. The bias lines cause undesired interference and affect the antenna radiation pattern. The proposed reconfigurable polarisation mm-wave RDRA works in three different polarisation configurations LHCP, RHCP and LP radiations.

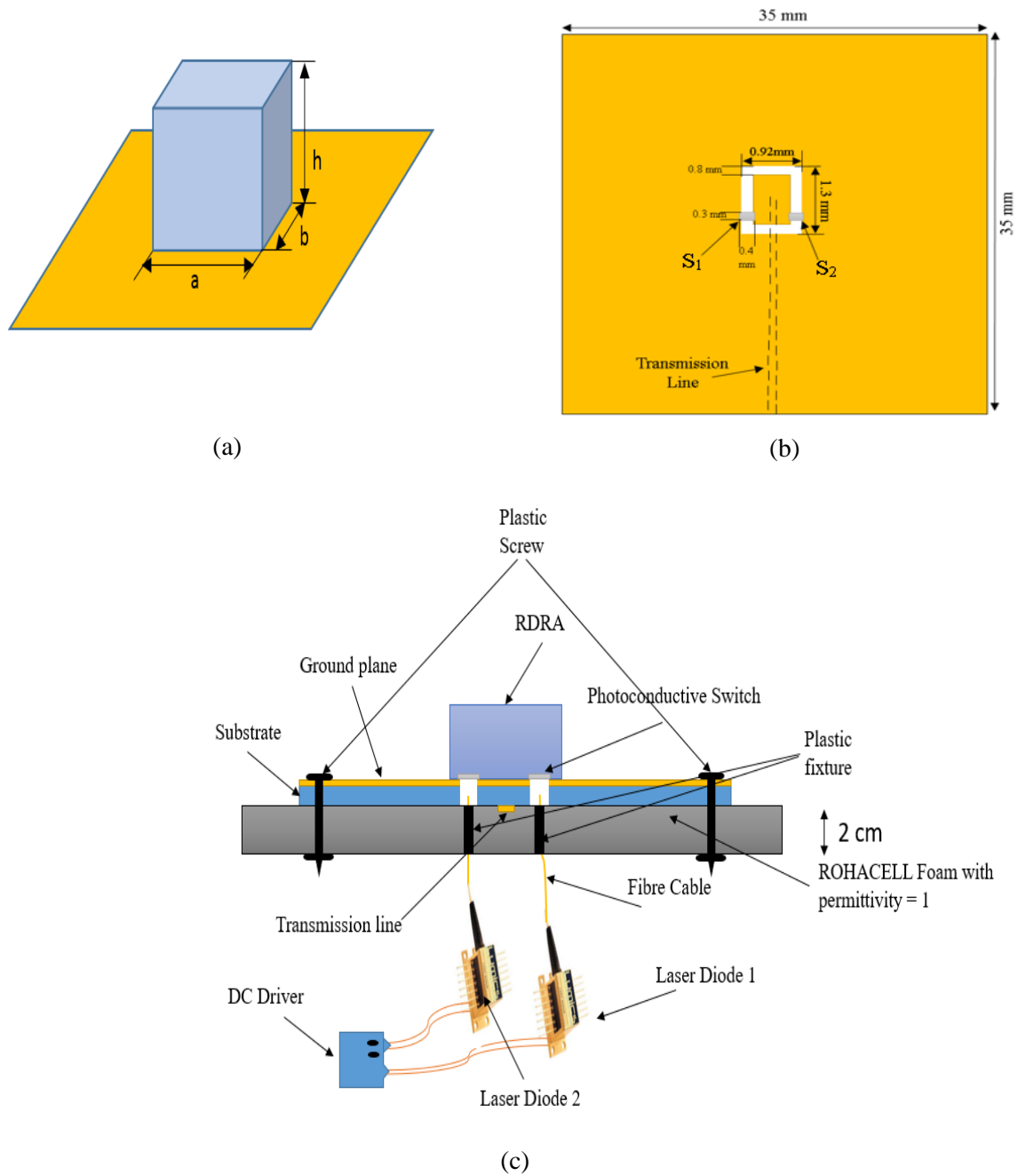


Figure 5.14: The geometry of the polarisation reconfigurable DRA, (a) proposed rectangular DRA, (b) slot feeding (c) complete antenna configuration.

5.3.2 Left-hand Circular Polarisation

In the first configuration, the photoconductive switch (S_2) is assumed to be illuminated by the laser diode 1, i.e. it is in the ON state and the other photoconductive switch (S_1) is in the OFF state. Figure 5.15 illustrates the reflection coefficient with a wide impedance bandwidth of 31.8% that extends from 25 to 34.8 GHz due to the excitation of TE_{113} and TE_{131} modes. The gain and axial ratio are presented in Figure 5.16, where it can be noticed that an AR bandwidth of 11% has been achieved in conjunction with gain of 6.5 dBic due to exciting a higher-order resonance mode.

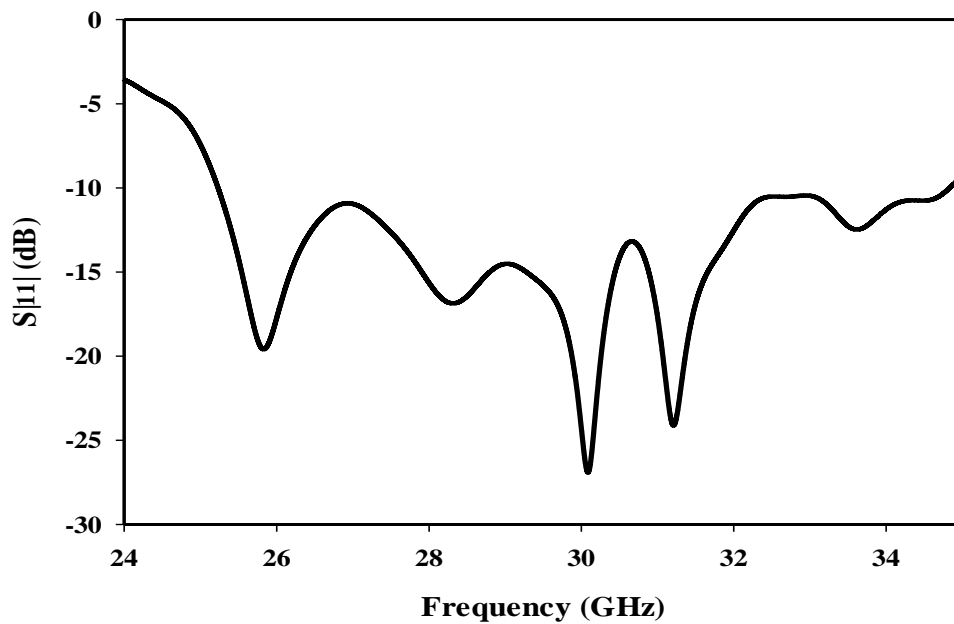


Figure 5.15: Reflection coefficient of the left hand circularly polarised rectangular DRA.

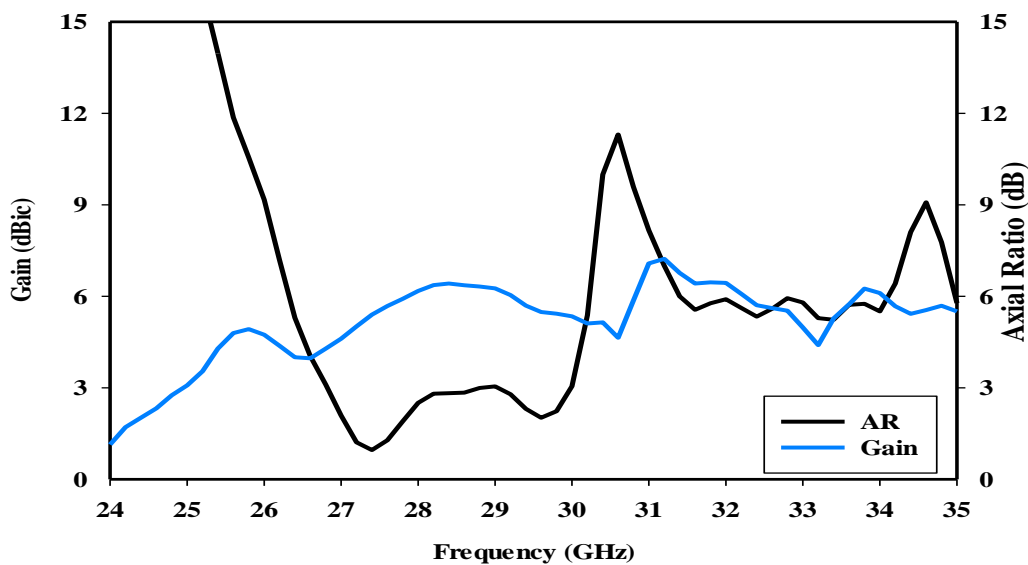
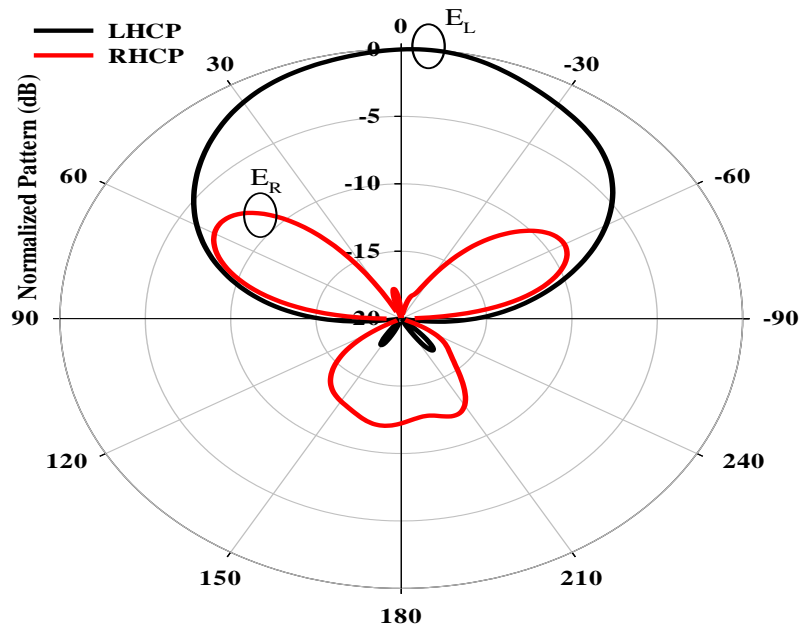
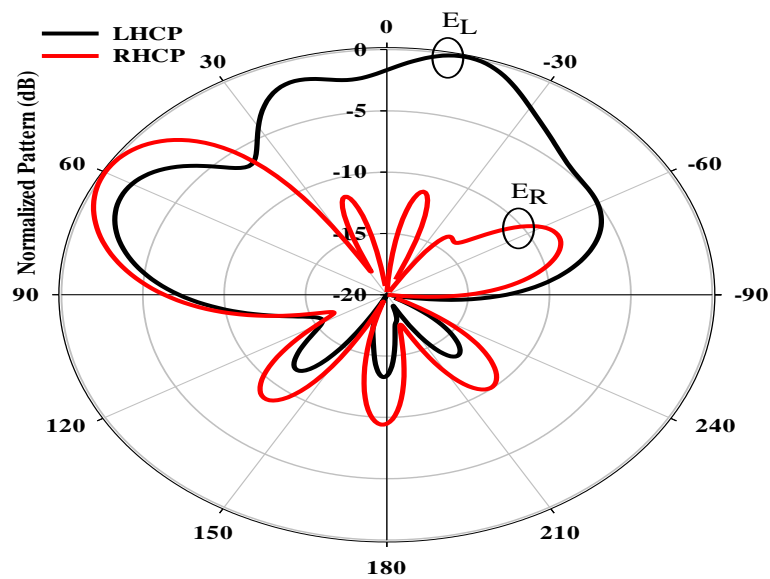


Figure 5.16: Broadside gain and axial ratio for the LHCP RDRA.

The far-field pattern is illustrated in Figure 5.17, where it is evident that a left-hand CP radiation is achieved since the E_L component is greater than the E_R counterpart by 15 dB at 27.5 GHz. It should be noted that the RDRA has been excited in the TE_{113} mode at this frequency. Figure 5.18 shows the far-field radiation pattern at 33.5 GHz. The short magnetic dipoles inside the RDRA are depicted in Figure 5.19, where it is evident that the TE_{113} and TE_{131} modes are excited at 27.5 and 33.5 GHz.



(a)



(b)

Figure 5.17: Radiation patterns of RDRA excited at TE_{113} mode at 27.5 GHz. (a) $\phi = 0^\circ$. (b) $\phi = 90^\circ$.

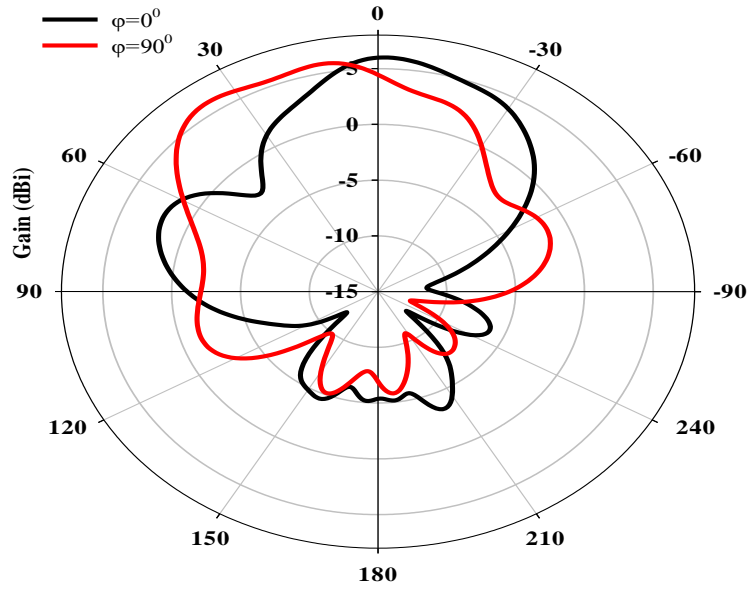


Figure 5.18: Radiation patterns of RDRA excited at TE_{131} mode at 33.5 GHz.

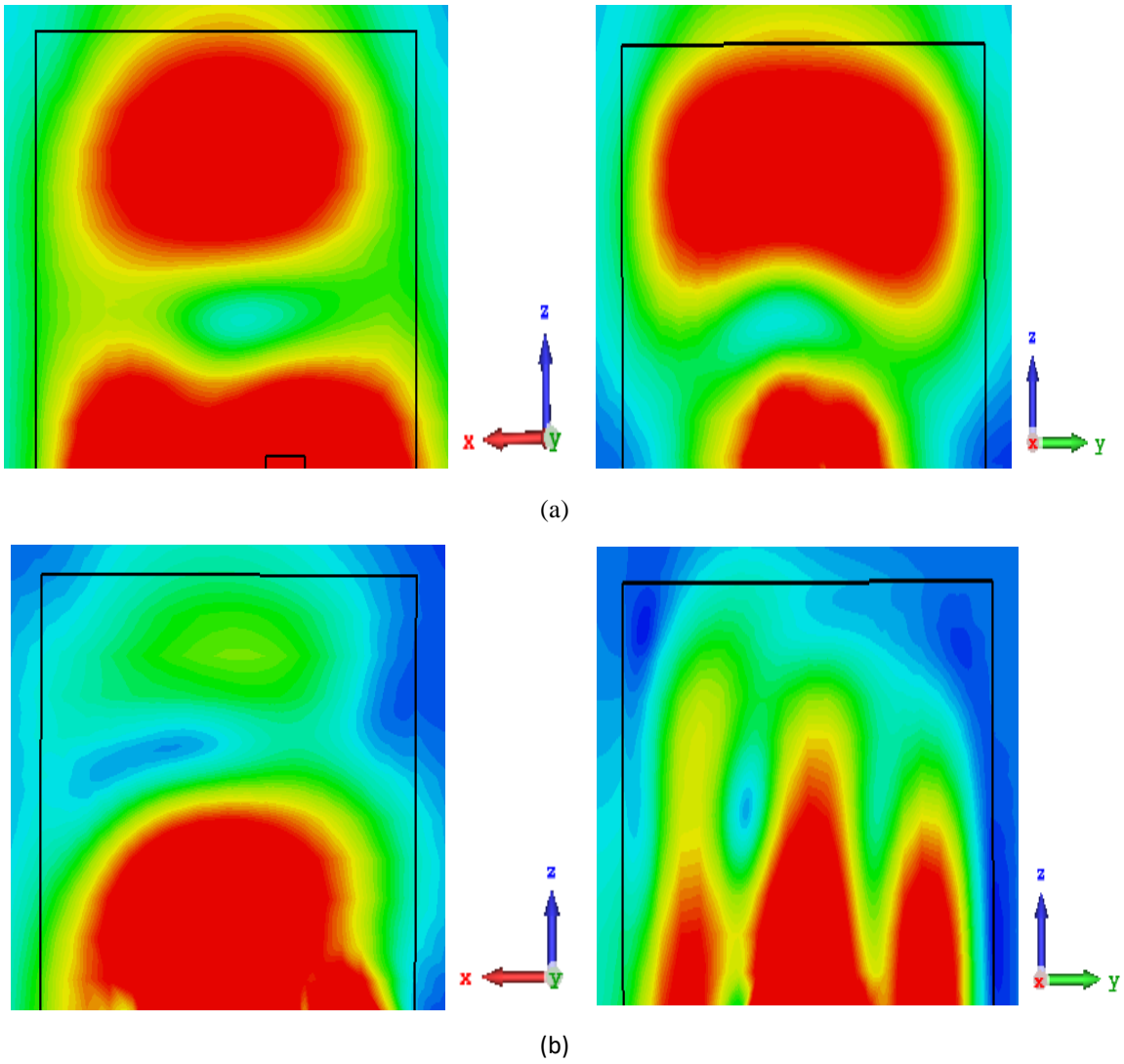


Figure 5.19: The magnetic field distribution for the excited modes (a) TE_{113} at 27.5 GHz. (b) TE_{131} at 33.5 GHz.

5.3.3 Right-hand Circular Polarisation

In the second configuration, the photoconductive switch (S_1) is assumed to be illuminated by the laser beam from laser diode 2, while the other photoconductive switch (S_2) is OFF. As expected, the achieved results are similar to those of the previous section except for the fact that RHCP radiation has been achieved instead. For example, the impedance bandwidth is 31.8% and also extends from 25 to 34.8 GHz. The RHCP axial ratio bandwidth is 11% has been achieved along with a gain of 6.5 dBic as illustrated in Figure 5.20. The far-field pattern is presented in Figure 5.21, which illustrates a right-hand CP radiation since E_R is greater than E_L by 15 dBic at 27.5 GHz. Figure 5.22 shows the antenna far-field pattern at 33.5 GHz.

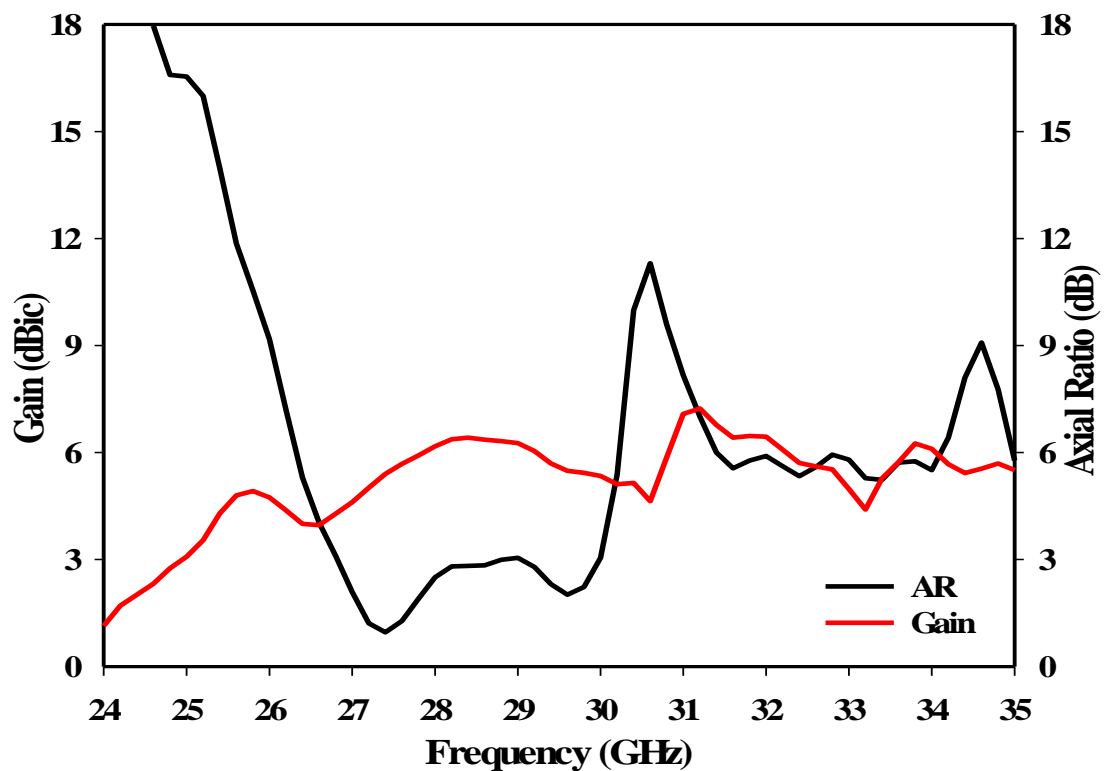
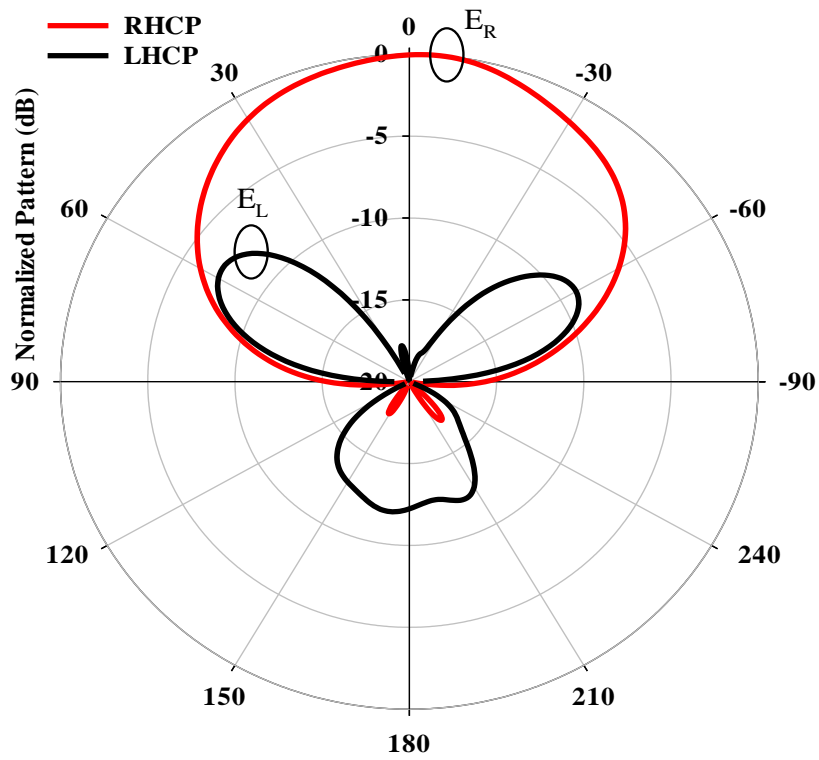
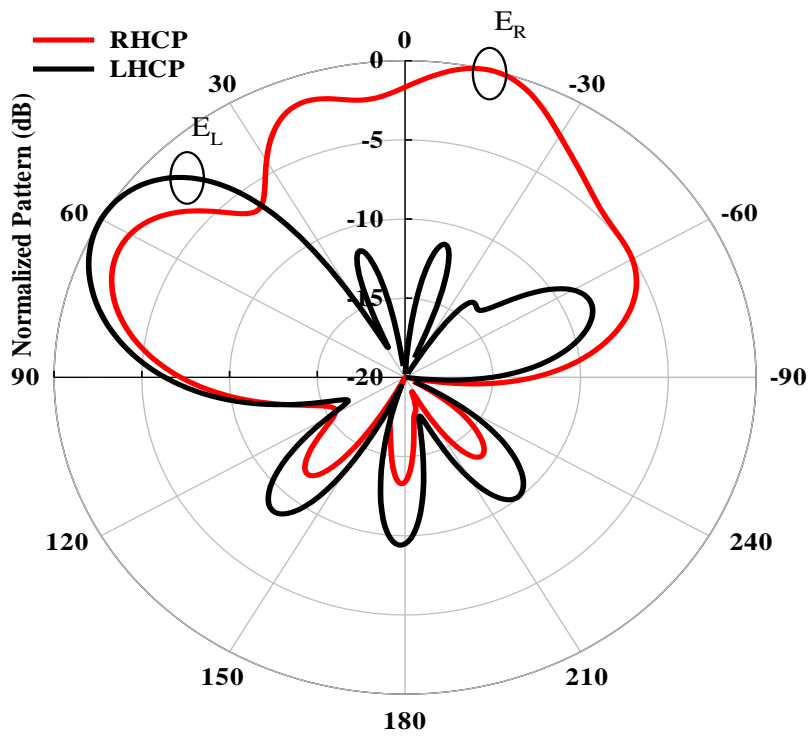


Figure 5.20: Broadside gain and axial ratio for the RHCP RDRA.



(a)



(b)

Figure 5.21: Radiation patterns of RDRA excited (a) $\phi = 90^\circ$. (b) $\phi = 0^\circ$ for mode TE_{113} at 27.5 GHz.

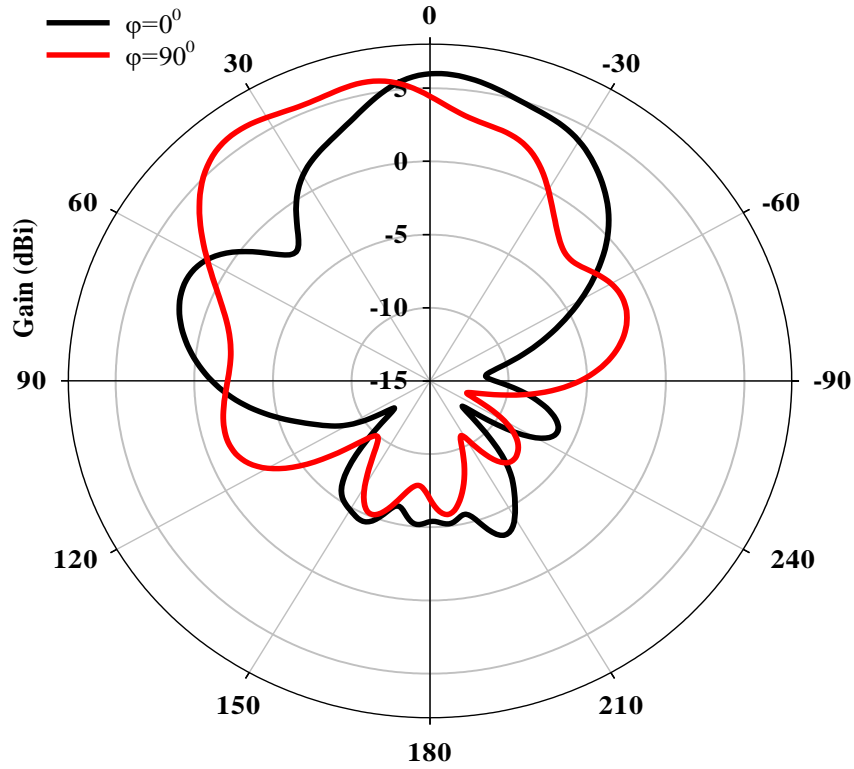


Figure 5.22: Radiation patterns of RDRA excited for mode TE_{131} at 33.5 GHz.

5.3.4 Linear Polarisation

The proposed rectangular DRA can achieve linear polarisation in two cases: when both photoconductive switches are OFF or ON.

Case I: In the third configuration, both of the photoconductive switches are assumed to be in the OFF state. i.e. they have not been illuminated by the laser diodes. Figure 5.23 presents the reflection coefficient with an impedance bandwidth of 9.5% that extends from 29.8 to 32.8 GHz. The rectangular DRA offers a maximum gain of ~ 5 dBi at 31 GHz as illustrated in Figure 5.24. The far-field pattern is presented in Figure 5.25. By studying the magnetic field distribution, it can be noted that the DRA is excited in the TE_{113} mode. The short magnetic dipoles inside the RDRA are depicted in Figure 5.26, where is evident that the TE_{113} mode has been generated at 30.6 GHz.

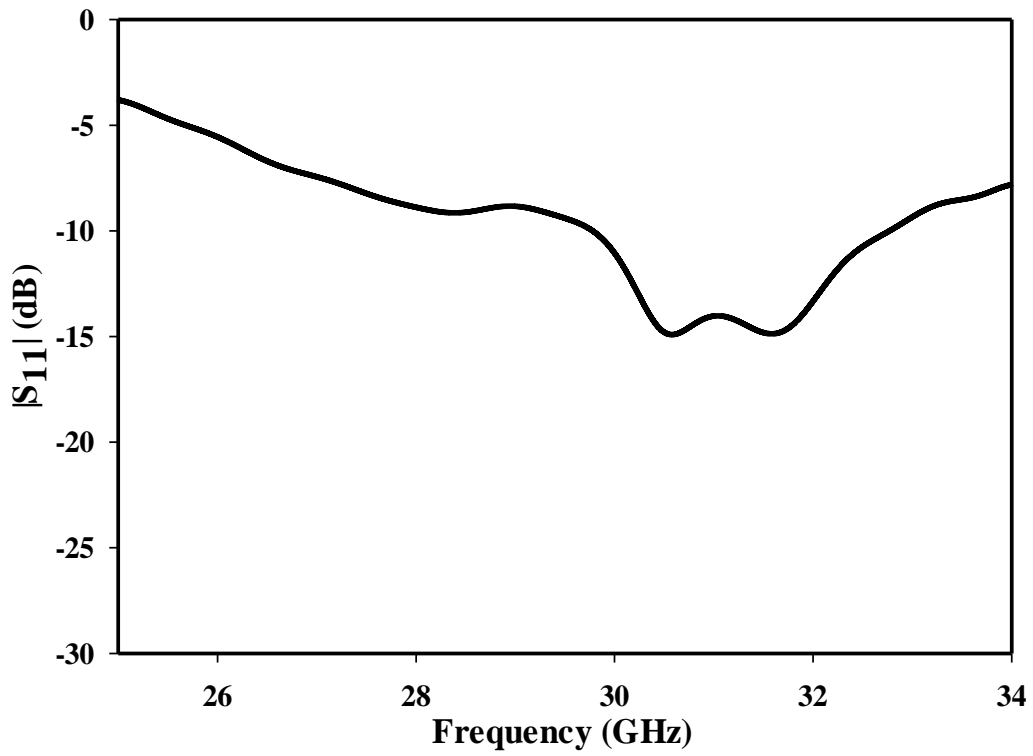


Figure 5.23: Reflection coefficients of linearly polarised rectangular DRA.

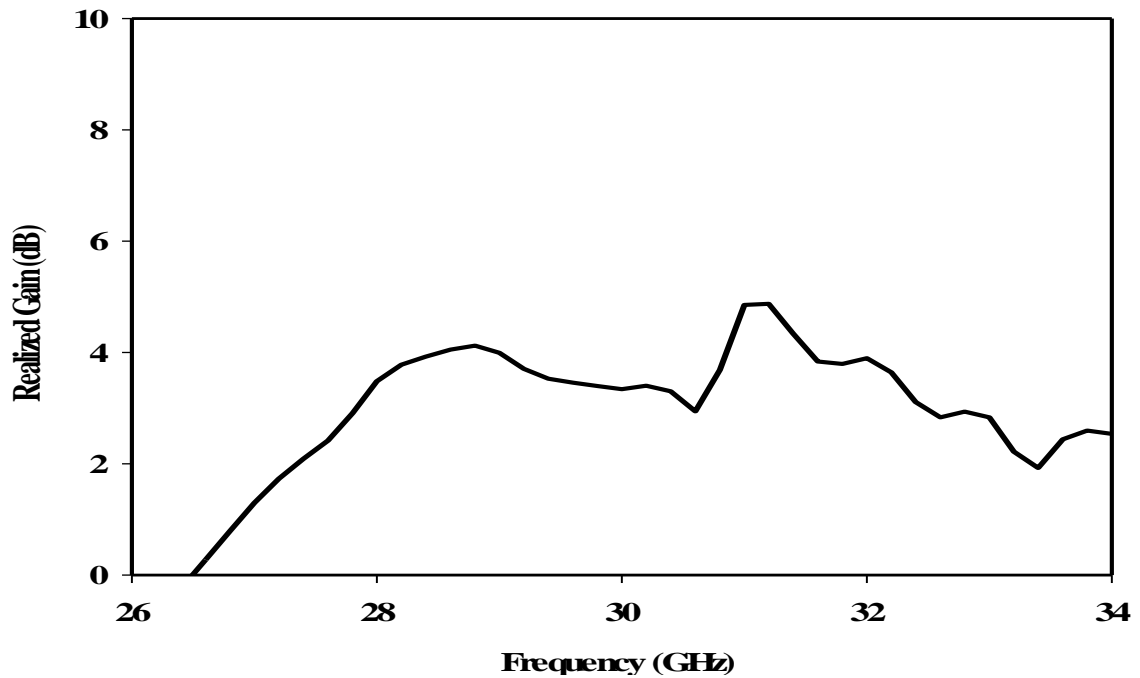


Figure 5.24: Gain of the linearly polarised Rectangular DRA.

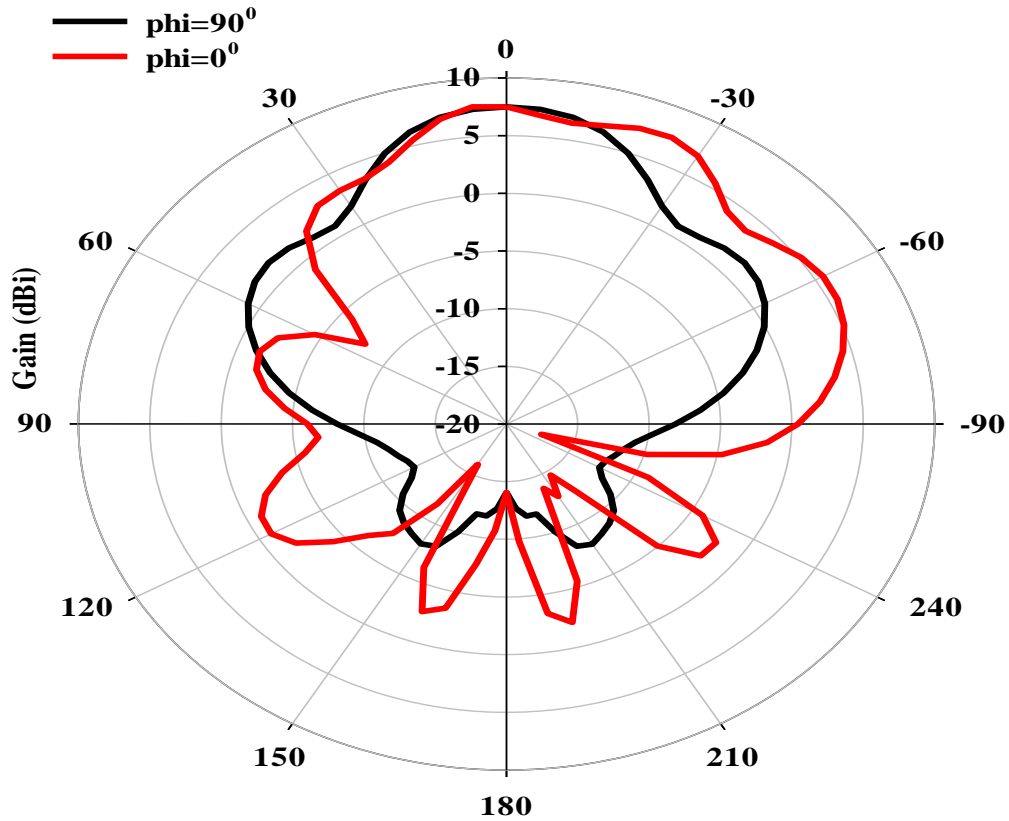


Figure 5.25: Radiation patterns of the LP RDRA antenna excited TE_{113} at 30.6 GHz.

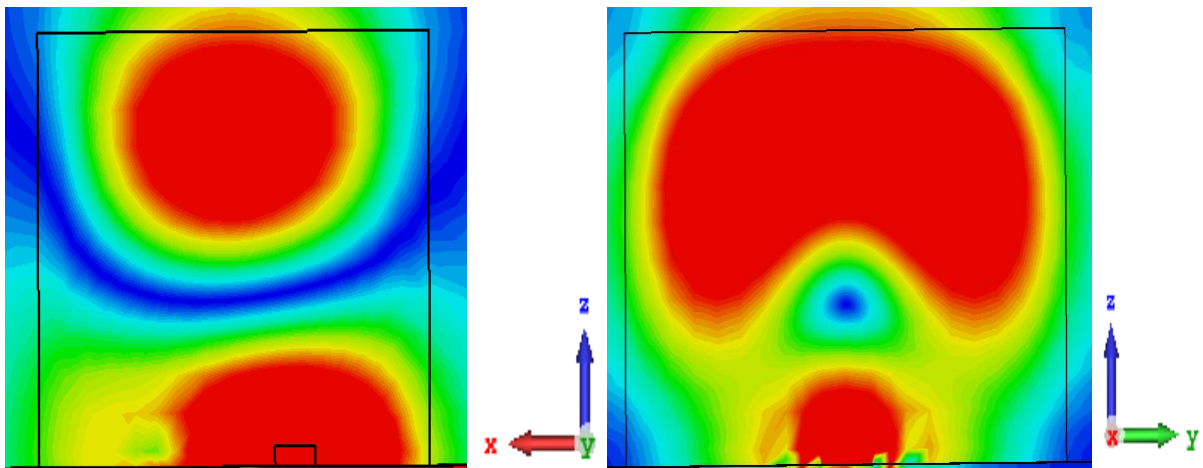


Figure 5.26: The magnetic field distribution inside a rectangular DRA excited TE_{113} mode at 30.6 GHz.

Case II: In the fourth configuration, both of the photoconductive switches are assumed to be in the ON state. i.e. they have been illuminated by the laser diodes. Figure 5.27 presents the reflection coefficient with a dual-band impedance bandwidth of 8.2% (26.48–28.77 GHz) and 20.6% (29.48–36.74 GHz). The DRA offers a gain of ~ 5 dBi as illustrated in Figure 5.28.

The far-field pattern is presented in Figure 5.29. The magnetic fields inside the rectangular DRA are TE₁₁₃ and TE₁₃₁ modes have been generated at 28 and 34GHz.

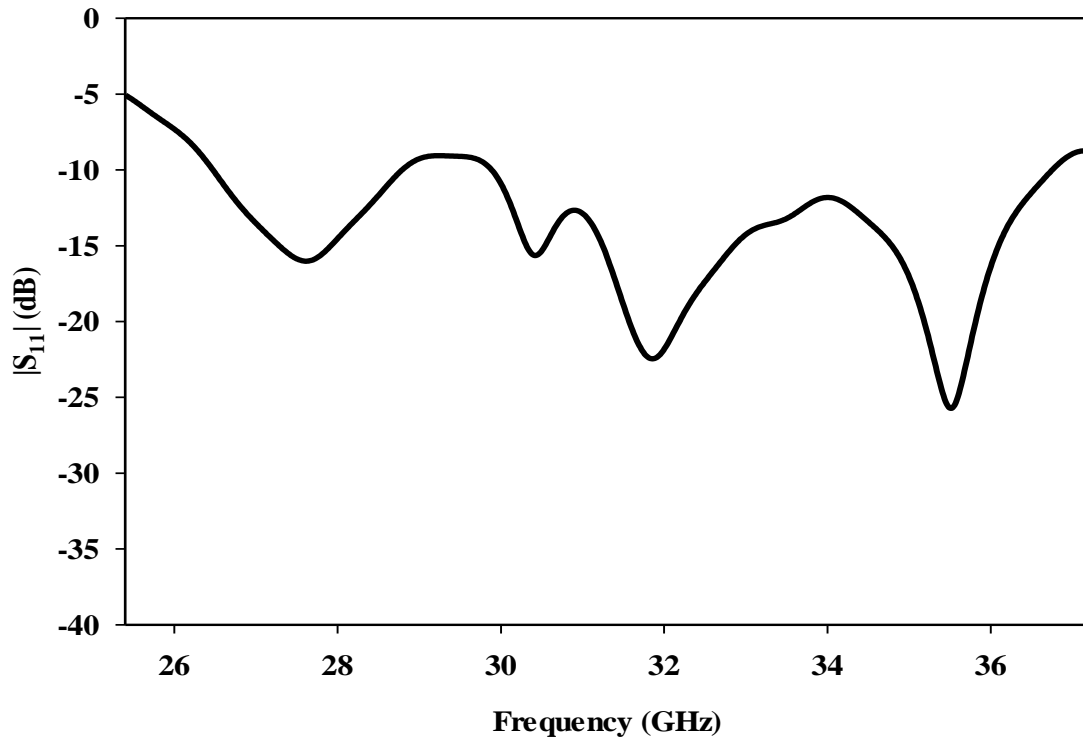


Figure 5.27: Reflection coefficients of linearly polarised rectangular DRA.

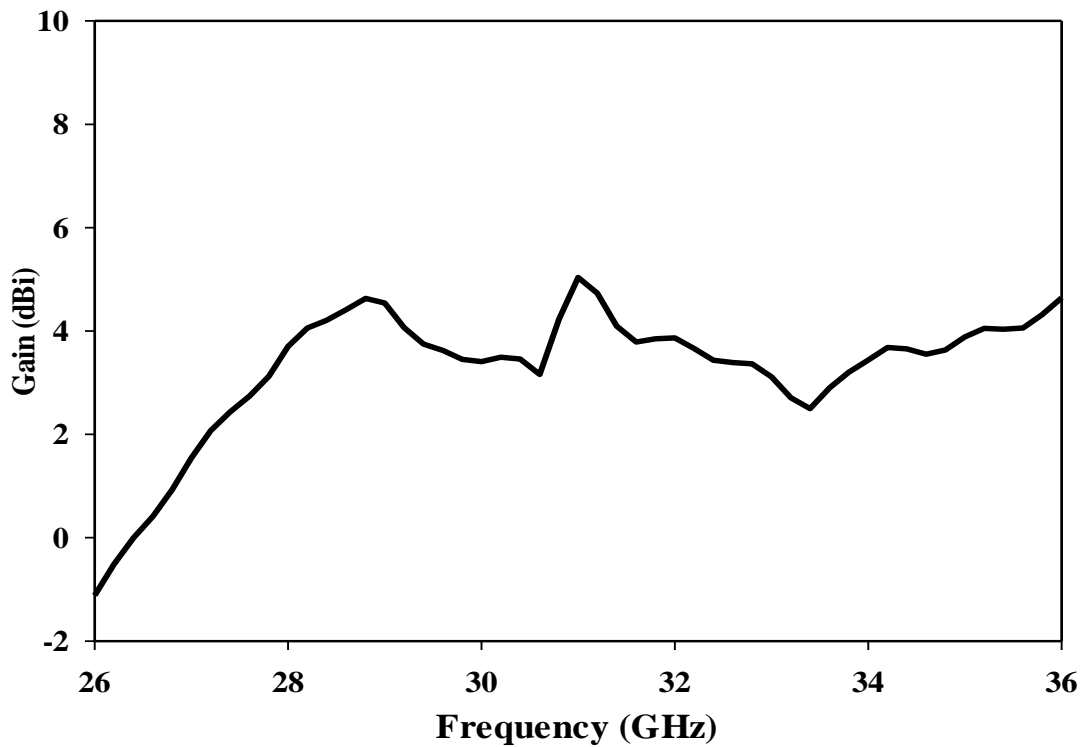
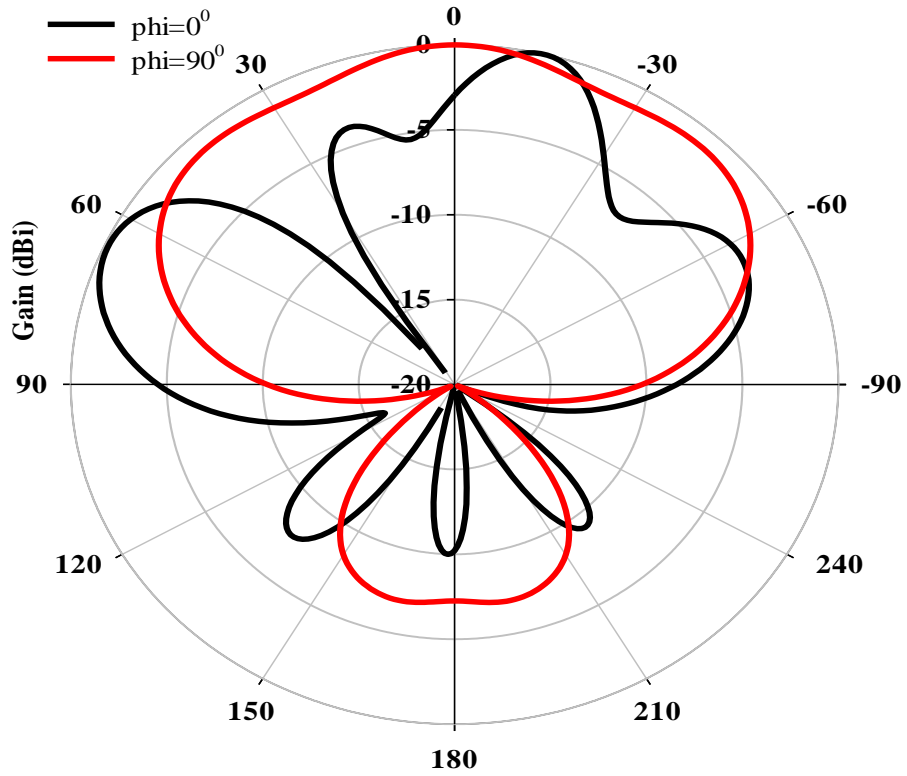
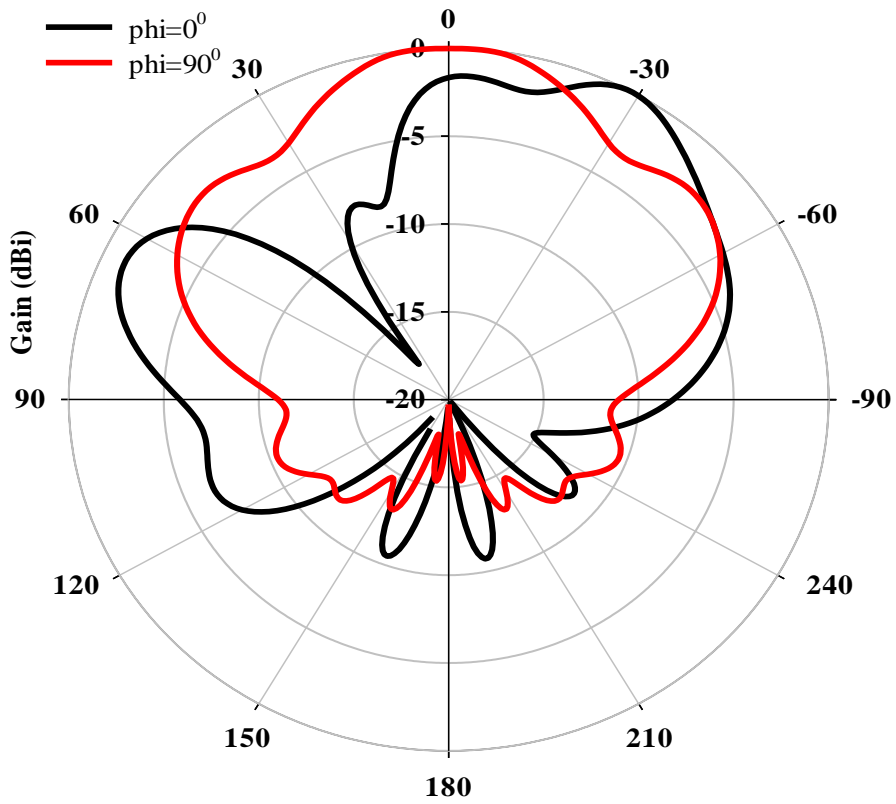


Figure 5.28: Gain of the linearly polarised rectangular DRA operation.



(a)



(b)

Figure 5.29: Radiation patterns of LP RDRA antenna: (a) Excited TE_{113} at 28 GHz. (b) Excited TE_{131} at 34 GHz.

A comprehensive comparison is presented in Tables 5.2 and 5.3, where it is evident that the proposed antenna outperforms the published optically controlled counterparts and offers wider impedance and AR bandwidths. Furthermore, the comparison demonstrated that the proposed antenna has a reduced number of switches, which simplifies the fabrication and reduces the cost. In addition, using the Silicon switches approach to generate CP has not been reported earlier.

Table 5-2: Comparison of Reconfigurable Antennas using Photoconductive Switched to Tune the Frequency and Polarisation.

Reference	Antenna Type	Reconfiguration Type	Frequency Band (GHz)
[40]	patch	Frequency	0.8-1
[76]	patch	Frequency	2.5-5.1
[98]	Arrays antenna	Frequency	28-38
Proposed design	RDRA	Polarisation	24-35

Table 5-3: Comparison of Polarisation Reconfigurable DRAs.

Ref	Antenna Type	Reconfiguration Mechanism	No. Of Switches	S_{11} Bandwidth	AR Bandwidth	Peak Gain (dBic)
[92]	CDRA	PIN	2	12.5% LHCP 14.5% RHCP 3.4% LP	9.7% LHCP 8.5% RHCP	5.6
[91]	CDRA	PIN	8	34.3% LHCP 36.6% RHCP 9.5% LP 6.3% LP	30.4% LHCP 32.9% RHCP	5.58
[95]	RDRA	PIN	8	22% LHCP 28% RHCP 21% LP 27% LP	1% LHCP 1% RHCP	5
Propose design	RDRA	Silicon Switches	2	31.8% LHCP 31.8% RHCP 7.5% & 1.8% LP 8.2% & 20.6% LP	11% LHCP 11% RHCP	7.2

5.4 Conclusion

A simple and novel design for a low-profile reconfigurable DRA has been presented, where a frequency reconfiguration has been achieved for a slot-fed RDRA. Two photoconductive switches have been placed near the edges of the feeding rectangular slot to change its length from 4 to 6 mm. When the two switches are illuminated by the laser beams, the switches will move to the ON state, where the antenna operates in the TE_{113} mode at 12.5 GHz with a gain of 6.8 dBi. However, in the second case, the switches operate in the absence of the laser beams. As a result, the feeding slot is longer and the antenna operates in dual frequency bands at 11 and 13.7 GHz. In addition, the RDRA supports the lower and higher-order resonance modes of TE_{111} and TE_{113} with gains of 6 and 8.5 dBi, respectively. Furthermore, the proposed antenna operates at a wide frequency range of 10-14.2 GHz which means it covers the X and Ku bands.

A polarisation-reconfigurable RDRA antenna has been investigated for mm-wave applications. By controlling the two photoconductive switches, the antenna can provide LP, LHCP, and RHCP radiations. The proposed rectangular DRA has a simple structure and is easy to fabricate. Simulation results demonstrate the polarisation reconfigurable characteristics with a wide impedance bandwidth from 25 to 34.8 GHz with a relative impedance bandwidth of 31.8% for both LHCP and RHCP states compared to 9.5% for a linearly polarised DRA. In addition, all the materials for RDRA and the feed network have been chosen based on the availability of commercial materials. It is worth pointing out that, the proposed antenna can be considered a potential solution for a number of 5G applications such as device-to-device and vehicle-to-vehicle communications.

Chapter 6

Frequency Reconfigurable mmWave Rectangular DRAs

6.1 Introduction

As mentioned in the previous chapter, designing a reconfigurable mmWave antenna is challenging due to the antenna's smaller dimensions and the difficulty of placing PIN diodes in the feeding slot without affecting its performance. In addition, the required incident power level to bias a photoconductive diode switch represents a considerable limitation to utilising these switches. Therefore, an alternative design approach is needed to address this challenge. This Chapter presents simulated and measured results of two mmWave frequency reconfigurable rectangular DRAs. The idea is based on moving the PIN diodes to the lower side of the substrate, which eliminates the need to solder them in the feeding slot and avoids creating a groove in the physically small mmWave DRA. It should be noted that a reconfigurable mmWave DRA has not been reported earlier in the literature.

It is worth pointing out that the rectangular DRA design in Chapter 3 achieved reconfigurability by placing diodes on the long sides of the feeding slot, i.e. the diodes are positioned above the ground plane and underneath the rectangular DRA. As a result, a groove is used to accommodate the height of the PIN diodes to ensure the DRA can be positioned steadily without creating air gaps. In mmWave reconfigurable designs, the size of the rectangular DRA is considerably smaller and creating a groove on the bottom of the ceramic DRA will be too hard and impractical. As an alternative, the PIN diodes will be moved to the opposite side of the substrate to be located on the feeding microstrip line, which offers more flexibility.

The technical specifications of the MA4AGFCP910 diode indicate that its ON state equivalent circuit involves resistance 4.2Ω in series with an inductor that has a maximum of 0.5 nH, while in the OFF state, the diode functions as a 0.02 pF capacitor in parallel with a resistance of 10 k Ω [133]. The Touchstone lumped element in CST can be used to import a file for the ON and OFF states, which includes the values of the equivalent resistance, inductance, and

capacitance for a PIN diode circuit. This allows for the accurate simulation and analysis of the circuit's performance, based on the specific values of the passive elements. Importing the file in this format can also make it easier to change or update the values of the elements, without having to manually input them into the simulation software.

6.2 Frequency reconfigurable single rectangular DRA

6.2.1 Antenna Configuration

A millimetre Wave frequency reconfigurable rectangular DRA that utilizes a single feeding slot is illustrated In Figure 6.1 with dimensions of $a=4\text{mm}$, $b=8\text{mm}$ and $h=4\text{mm}$ as well as a relative permittivity of $\epsilon_r=9.9$. The chosen dimensions are based on the DWM to achieve a DRA that supports at least two resonance modes in the considered frequency range. The proposed DRA was positioned on a Rogers RO4003C substrate The dielectric substrate is characterized by its $30\text{mm} \times 30\text{mm} \times 0.5\text{mm}$ dimensions and 3.38 dielectric constant with a loss tangent of 0.0027. The antenna feed comprises a centrally located slot on the PCB ground plane as illustrated in Figure 6.1. The respective slot length and width have been chosen as 4mm and 0.7mm, which correspond to $0.36\lambda_0$ and $0.063\lambda_0$, respectively, at 27 GHz.

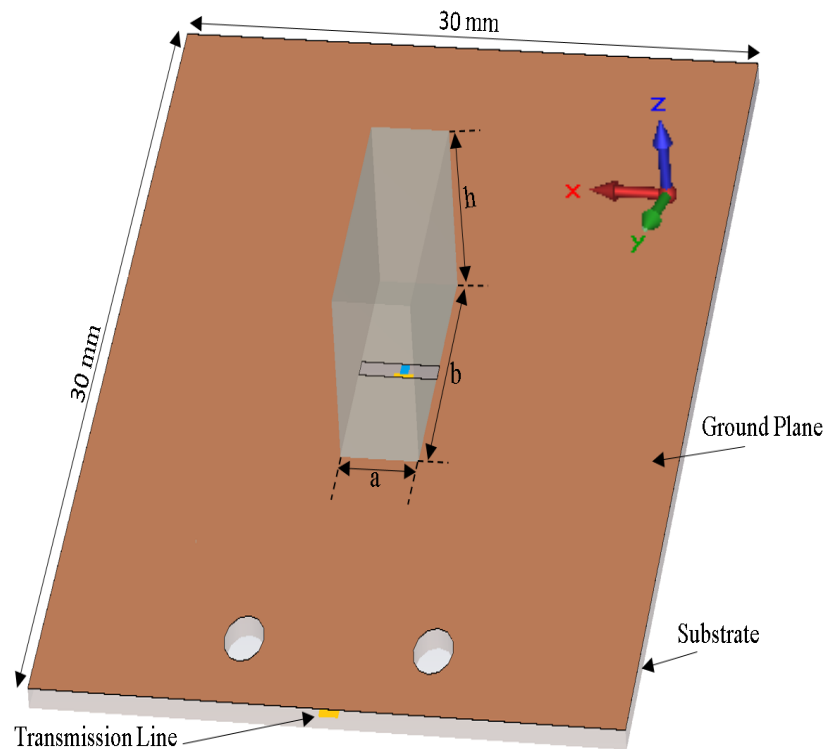


Figure 6.1: Geometry of rectangular DRA.

6.2.2 Parametric study

Figure 6.2 illustrates the bottom view of the proposed rectangular DRA and its feed network, where a microstrip line has been printed on the bottom side of the substrate. To optimize the coupling strength between the DRA and the source, a matching stub can be created by extending the strip transmission line beyond the feeding slot. This matching stub has a length of l_{s1} . In Figure 6.2, there are two holes marked on the PCB for the purpose of securely connecting the connector to the board. These holes align with the screw holes on the connector, which allows for the screws to be inserted and tightened to attach the connector to the PCB firmly. This provides a stable and reliable connection between the two components. The reflection coefficient is illustrated in Figure 6.3 with varying l_{s1} from 0 to 0.75 mm. As can be noted that a considerable coupling has been achieved by employing an optimum stub length of $l_{s1}=0.75\text{mm}$, which corresponds to the excitation of the TE_{131} mode at 22 GHz with an impedance bandwidth of 4.94 % (21.7- 22.8 GHz).

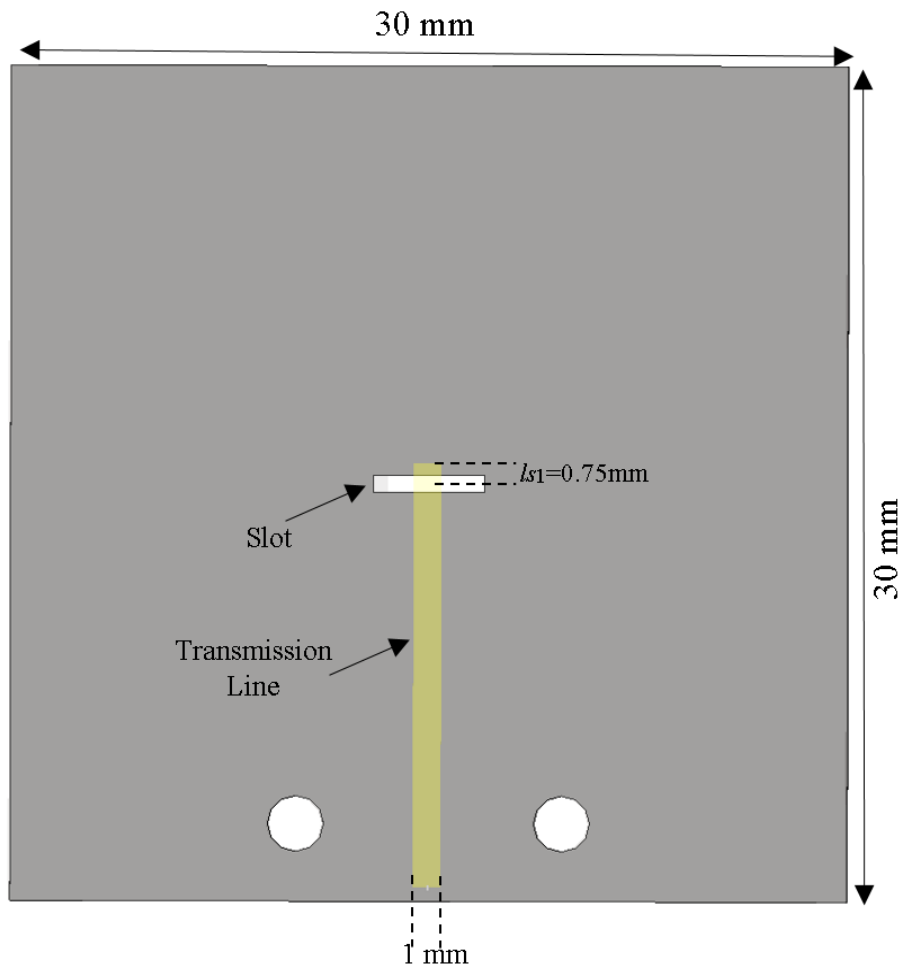


Figure 6.2: A bottom view of the proposed antenna feed network.

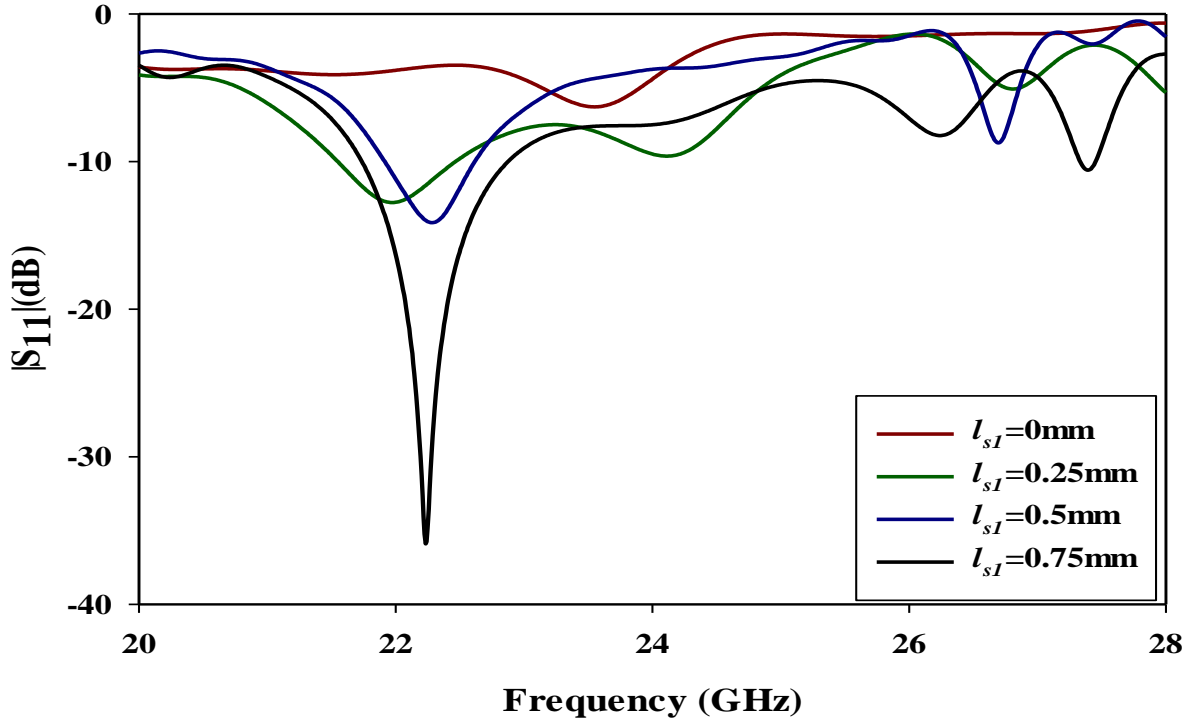


Figure 6.3: Simulated reflection coefficient with different stub lengths.

The optimum position for the PIN diode has been chosen to be at the end of the stub section, i.e. at a distance l_{s1} from the feeding slot's centre. This will facilitate adding another stub section at the end of the PIN diode with a length of l_{s2} . It should be noted that the PIN diode with a length of 0.6 mm. Therefore, the total stub length will vary from l_{s1} when the PIN diode is in the OFF state to $l_{s1} + l_{s2} + 0.6$ in the ON state. The PIN diode biasing has been achieved by connecting a DC source to the board using two microstrip lines with respective lengths and widths of 11 mm and 0.3 mm. The biasing section is illustrated in Figure 6.4, where it can be noted that two biasing strip lines have been utilised at the left- and right-hand sides of the substrate's lower side. The DC-bias circuit was created and improved through simulation.

In order to block the flow of mmWave current along the microstrip biasing lines, two thin bias lines with a width of 0.3 mm are connected at one end to the DC power supply and at the other end to RF chokes. These RF chokes are equipped with inductors that have a value of 30 nH, resulting in an impedance of 5652Ω at 30 GHz. This impedance and 0.3 mm thin bias lines are sufficient to choke any RF signal leakage to the DC bias lines [99, 100]. The biasing lines have been created during the fabrication of the feed network. It should be noted that the utilised model of the diode is MA4AGFCP910 PIN from Macom, which can operate up to 30 GHz. The proposed antenna achieves reconfigurability through two states: OFF and ON. In the OFF state, the positive DC signal is connected to the N terminal of the PIN diode via the right strip line, while the positive terminal is connected to the left strip line that is connected to the

common ground. In contrast, in the ON state, the positive DC signal is connected to the P terminal of the PIN diode via the right strip line, while the negative terminal is connected to the left strip line that is connected to the common ground. Finally, it should be noted that the frequency reconfigurable operation has been achieved by varying the length of the l_{s2} to excite different resonance modes. The reflection coefficient is illustrated in Figure 6.5, with varying l_{s2} values ranging from 0 to 2 mm. As can be seen, a significant coupling effect is achieved by using an optimum stub length of $l_{s2} = 2$ mm. The proposed antenna supports TE_{133} mode at 26.7 GHz. The overall stub length in the ON state is 3.35 mm including two short stub segments with the PIN diode in between.

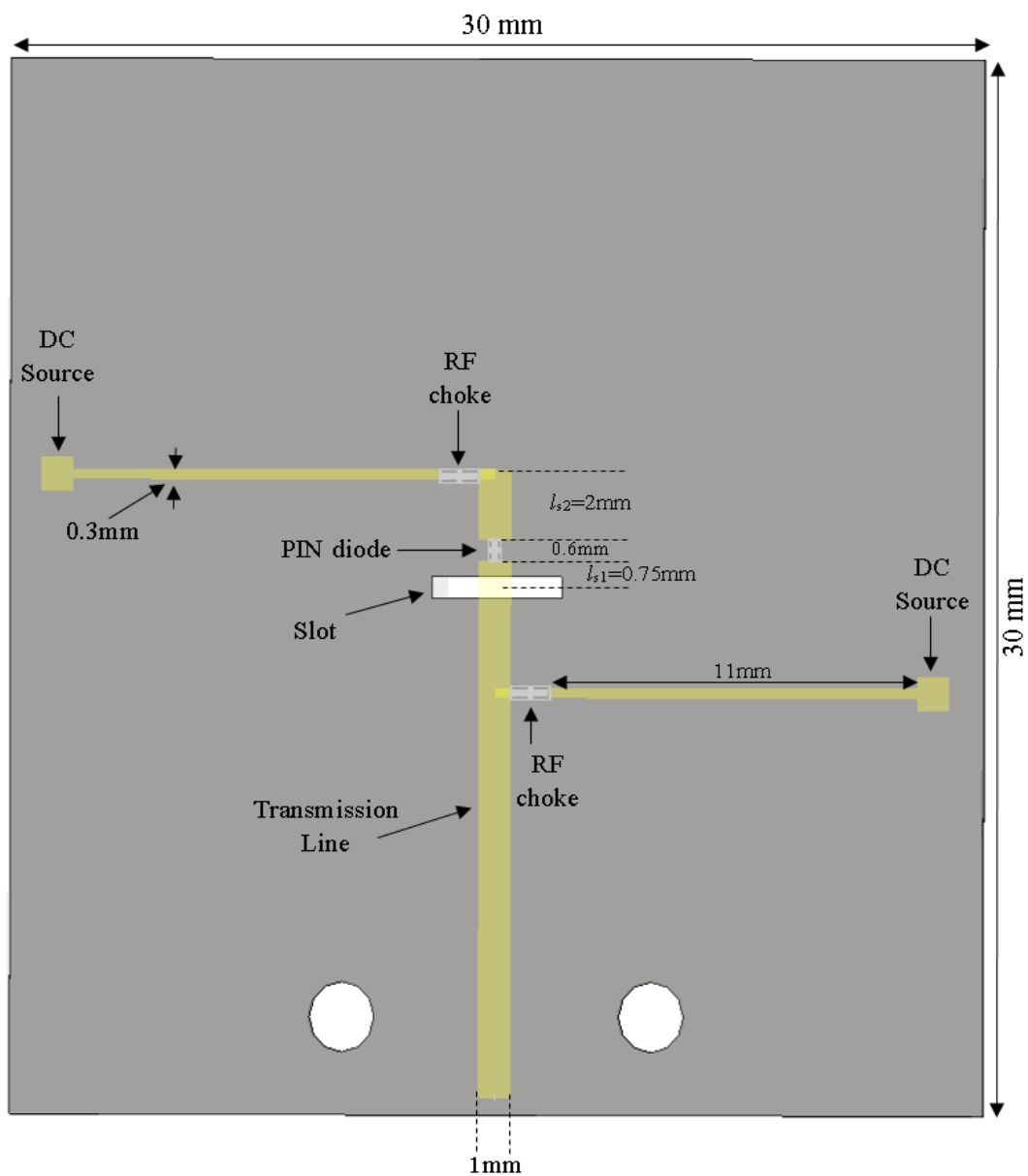


Figure 6.4: A bottom view of the proposed antenna feed network and bias lines.

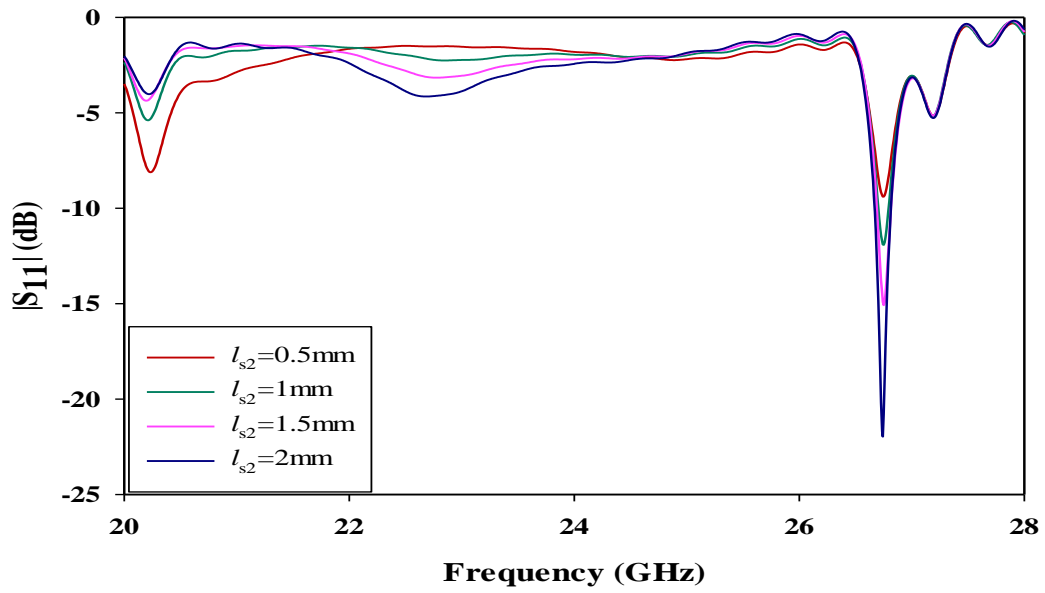


Figure 6.5: Simulated reflection coefficient with different l_{s2} lengths.

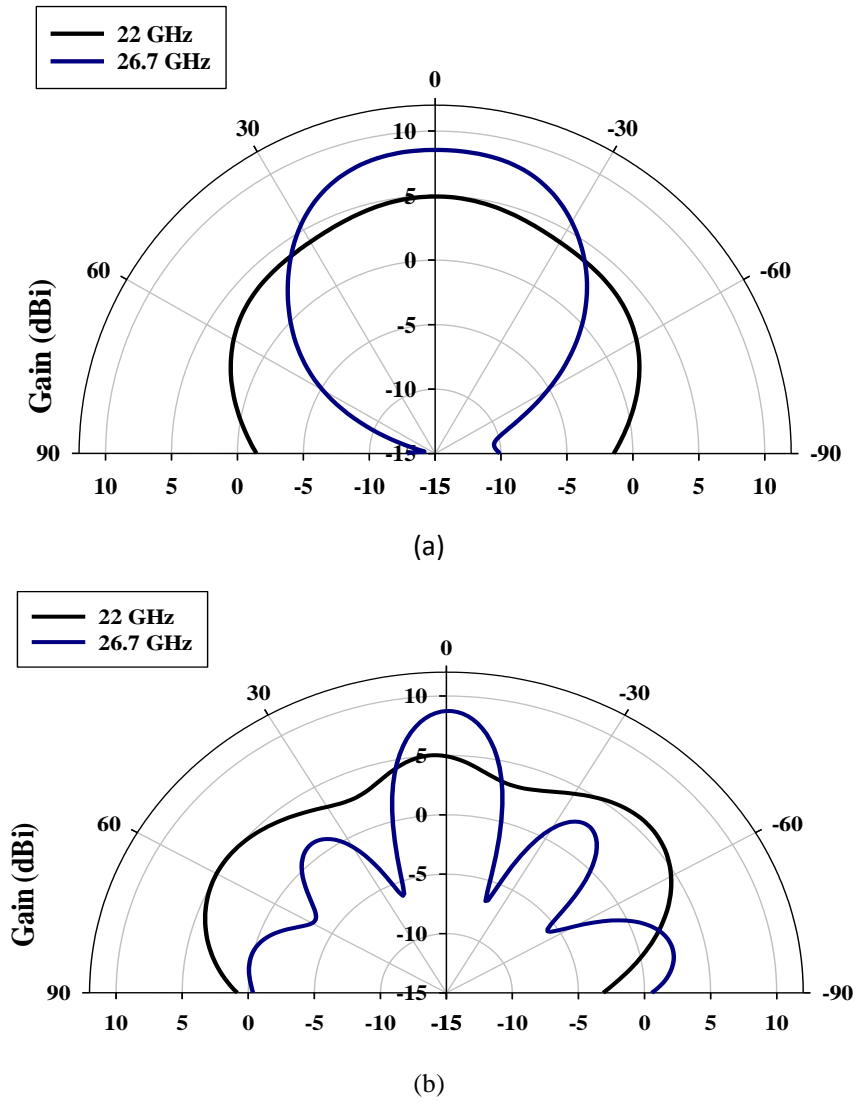


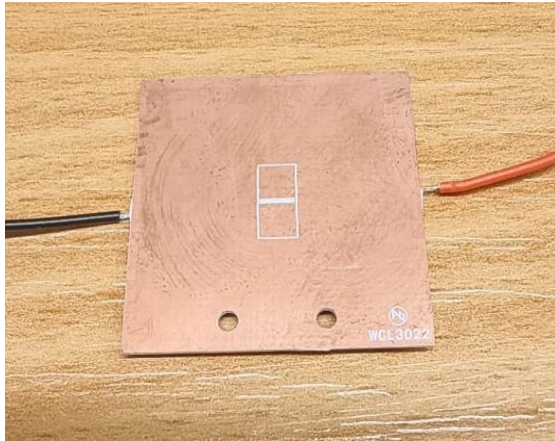
Figure 6.6: Radiation pattern of rectangular DRA at 22 and 26.7 GHz. (a) E-plane. (b) H-plane.

Therefore, the proposed antenna operates in two scenarios, OFF and ON state resulting in a tuning range of $\sim 21.6\%$. The achieved S_{11} bandwidths are 5 % (21.7-22.8GHz) and 0.6% (26.65-26.80GHz) l_{s1} and l_{s2} are chosen as 0.75mm and 2 mm, respectively. The radiation patterns for the excited resonance modes TE_{131} and TE_{133} at 22 and 26.7 GHz are illustrated in Figure 6.6, where it can be observed that broadside radiation has been achieved in both cases with gains of 5 dBi and 8.6 dBi for the 1st and 2nd resonance modes, respectively. The higher gain at 26.7 GHz is expected due to the excitation of a higher order mode.

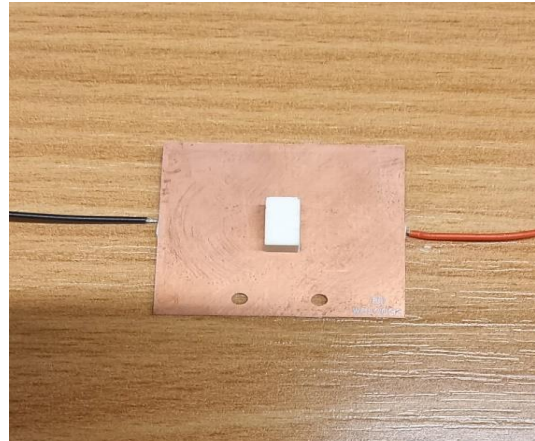
6.2.3 Experimental Results

A prototype of the antenna has been fabricated and placed on top of a ground plane with outlined DRA position using a silkscreen ink to minimise any errors due to the DRA-feed misalignment as illustrated in Figures 6.7 a, b. Bonding between the DRA and feed network has been achieved using short strips of double sided adhesive copper tape in order to remove any potential air gaps in between. The feed network has been fabricated at the Wrekin-circuits workshop, while the DRA has been fabricated at T- CERAM Company. In the x-band designs presented in Chapters 3 and 4, the size of the antenna was sufficiently large to create a groove in the bottom of the rectangular DRA to accommodate the PIN diodes. However, the antenna size is considerably smaller at the mmWave frequency range, making it infeasible to create a groove in a ceramic antenna. In addition, the dimensions of the PIN diode are 0.68 mm \times 0.36 mm \times 0.19 mm, which are too small for easy handling or soldering. Therefore, the PIN diode ends have been attached to the microstrip line using silver paste.

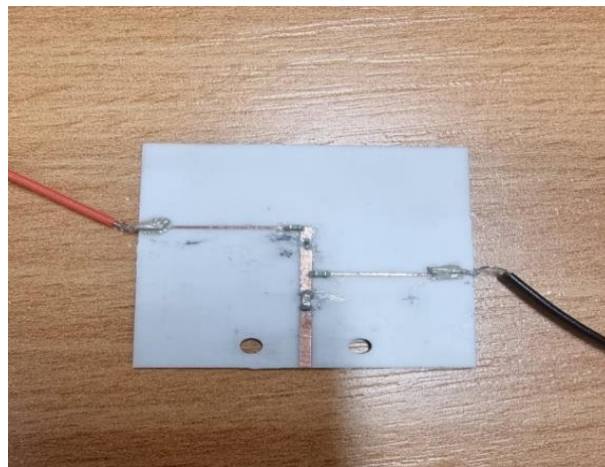
The $|S_{11}|$ was measured using an E5071C vector network analyser connected to a 50 Ω coaxial cable through a 2.92 mm SMA connector to link the coaxial cable to the feeding strip line. The equipment was calibrated using Agilent's 85052D calibration kit. The radiation patterns were measured using the SNF-FIX-1.0 Spherical mmWave Measurement System as shown in Figure 6.8, in which the alignment of the proposed antenna inside the chamber is demonstrated in Figure 6.8a while the mmWave chamber is illustrated in Figure 6.8b. As previously discussed, the proposed antenna achieved frequency reconfigurability by positioning the PIN diode along the microstrip transmission line. This resulted in two scenarios; one where the PIN diode is OFF and another where it is ON.



(a)



(b)



(c)

Figure 6.7: Prototype of mmWave frequency reconfigurable DRA. (a) Feed network with outlined DRA position. (b) Assembled rectangular DRA and feed network. (c) DC bias network.



(a)



(b)

Figure 6.8: Photographs of RDRA. (a) Alignment RDRA. (b) RDRA inside the mmWave Chamber.

6.2.4 OFF state Scenario

In this scenario, the diode will be reverse biased hence the length of the stub is 0.75 mm as illustrated in Figures 6.2 and 6.4. The reflection coefficient is presented in Figure 6.9 with a close agreement between the respective simulated and measured impedance bandwidths of 5.11% (21.73-22.88GHz) and 3.45% (21.6-22.36GHz). From the measurement, it can be seen that the depth of return losses is reduced compared to the simulated counterpart, which may be due to noise and multipath effects during the experiment. The measured and simulated maximum gain is approximately 5 dBi at 22 GHz as illustrated in Figure 6.10.

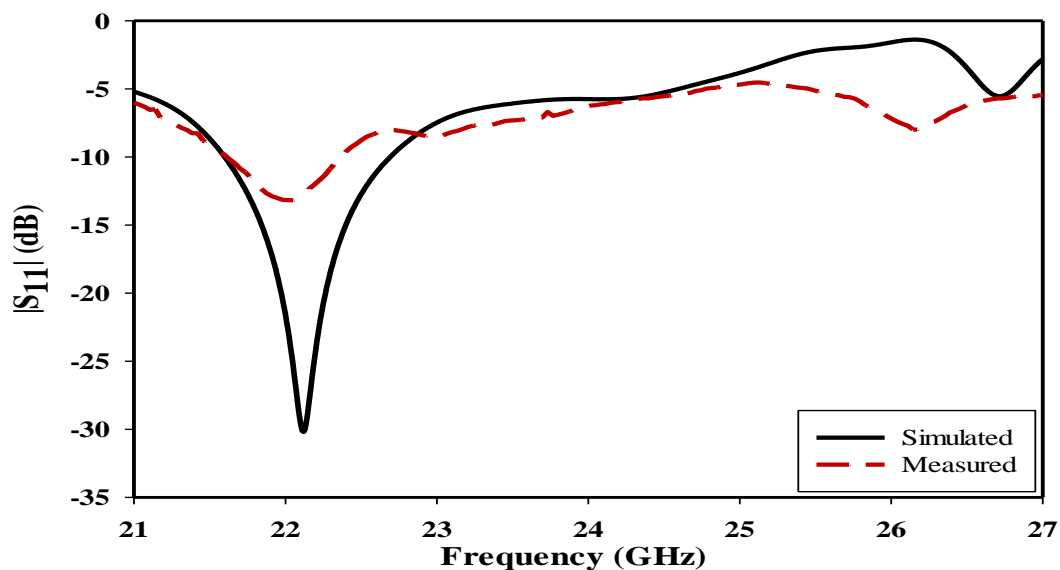


Figure 6.9: Reflection Coefficient of the reconfigurable DRA when a PIN diode is OFF.

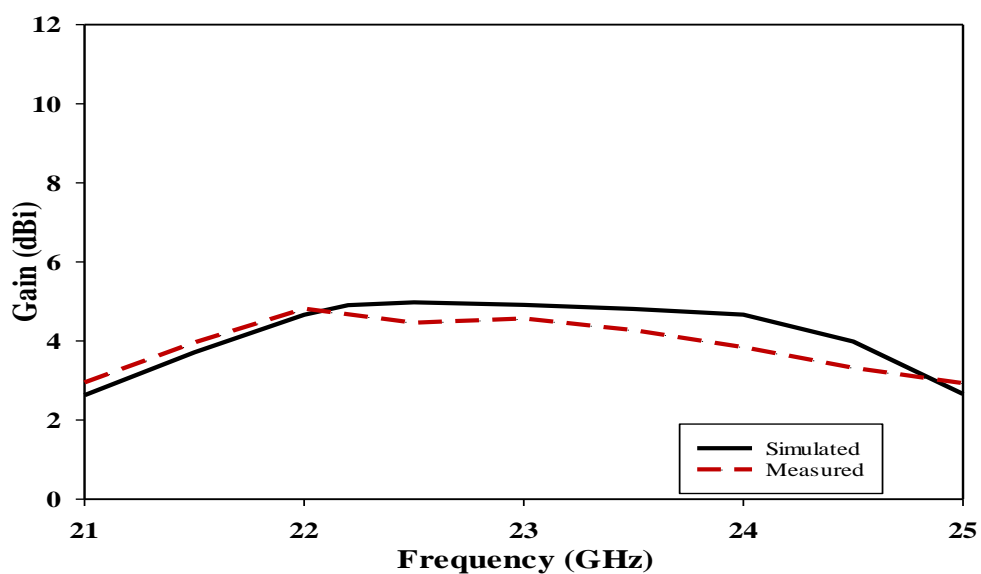


Figure 6.10: Gain of the reconfigurable rectangular DRA for OFF state.

In addition, Figure 6.11 presents the simulated and measured radiation patterns at 22 GHz for the E and H planes with close agreement. The magnetic field distribution inside the rectangular DRA is presented in Figure 6.12, where it can be noticed that the mode TE_{131} has been excited.

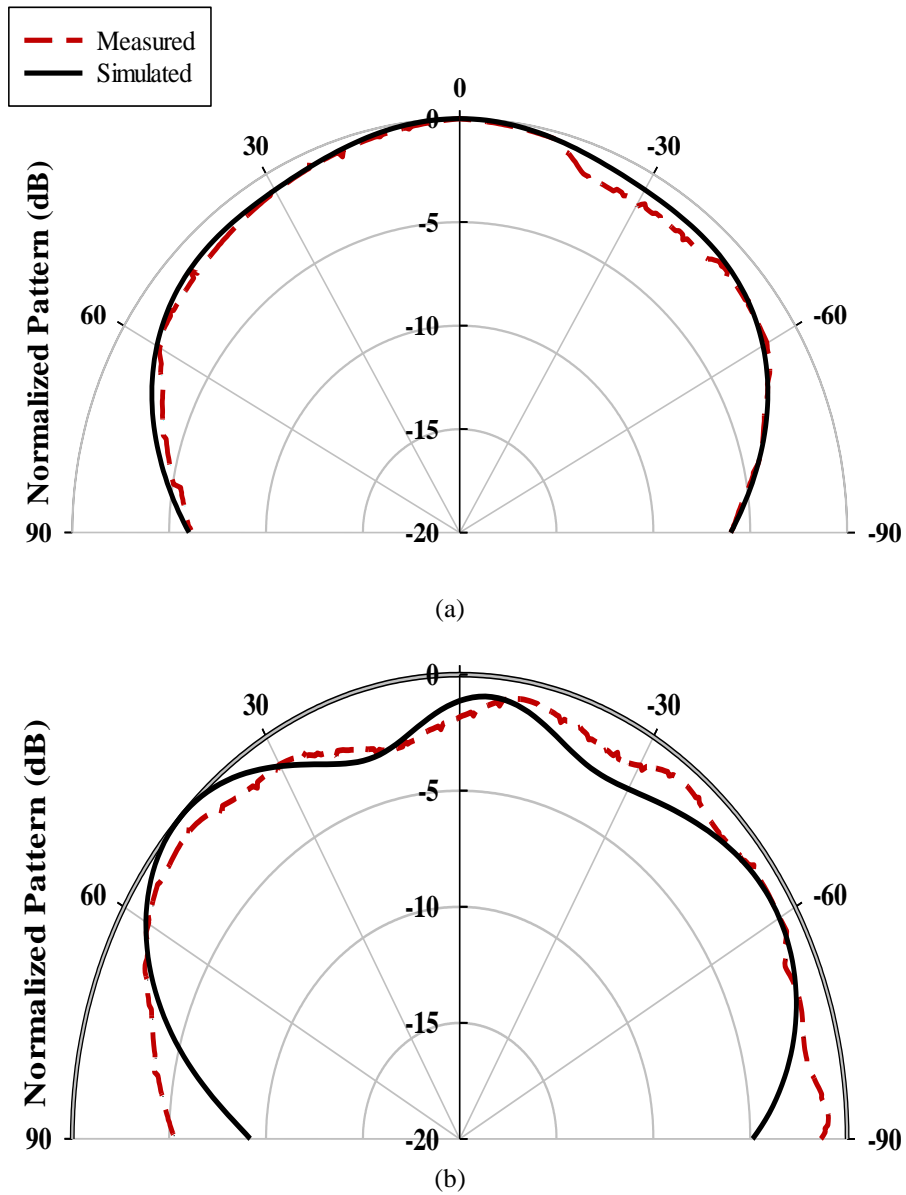


Figure 6.11: Radiation pattern of rectangular DRA at 22 GHz. (a) E-plane. (b) H-plane.

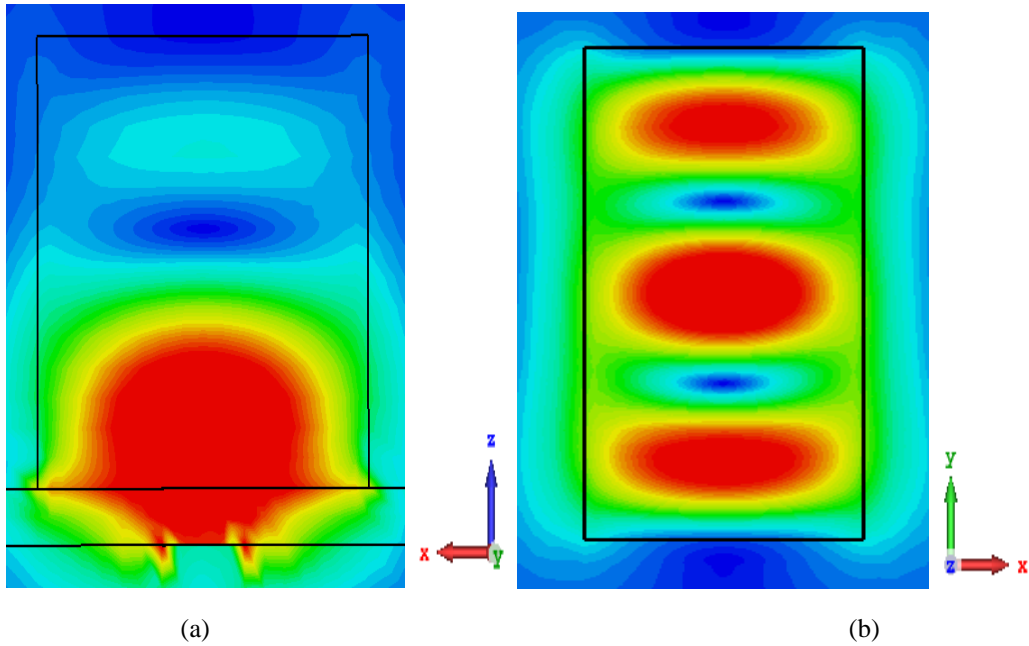


Figure 6.12: Magnetic field of the TE_{131} resonance mode at 22GHz for ON scenario. (a) xz plane (b) xy plane.

6.2.5 ON State Scenario.

In the ON scenario, the PIN diode will be forward biased and as a result, the stub length is increased from 0.75 to 3.35mm as illustrated in Figure 6.4. The proposed rectangular DRA will operate in the TE_{133} higher order resonance mode at 26.7 GHz. Figure 6.13 illustrates the reflection coefficient with respective simulated and measured impedance bandwidths of 0.6% and 2%. It can be noted that the discrepancy between measured and simulated data is more considerable than that in the OFF-state scenario. A possible reason is a fact that the antenna is operating in a higher order mode with a narrower bandwidth, and hence a higher Q factor, which means the impact of any experimental and fabrication error will be more significant. Furthermore, the wider measured impedance bandwidth demonstrates additional losses that have not been considered in the simulations. These losses could be raised from the connections of the PIN diode and capacitor to the feeding microstrip line. The measured and simulated maximum gains of the proposed antenna are approximately 8 and 8.6 dBi, respectively, as shown in Figure 6.14. In addition, Figure 6.15 demonstrates a close agreement between the simulated and measured radiation patterns at 26.7 GHz for the E and H planes. Figure 6.16 illustrates the magnetic field distribution within the rectangular DRA, where it is evident that the TE_{133} resonance mode has been activated.

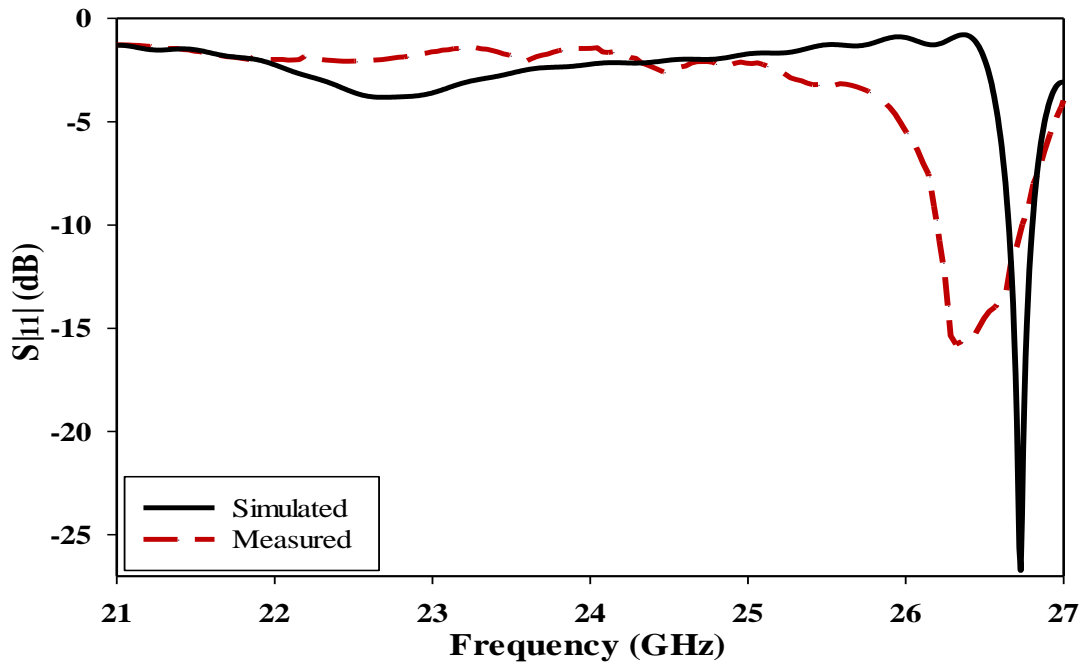


Figure 6.13: Reflection coefficient of the reconfigurable RDRA when a PIN diode is ON.

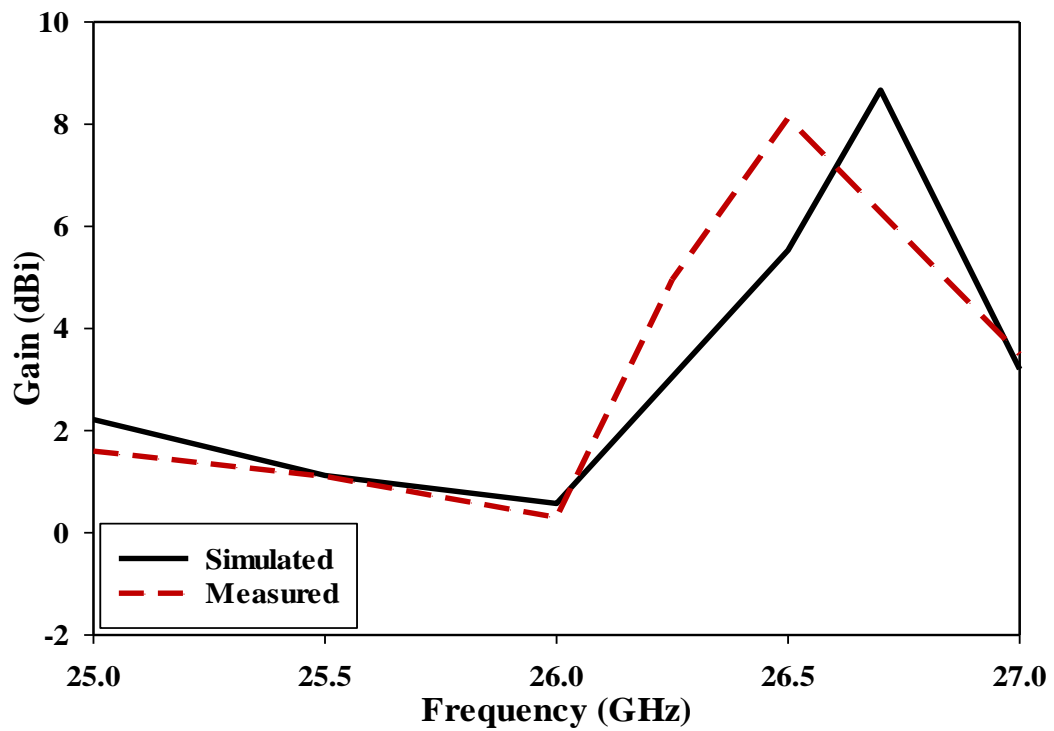


Figure 6.14: The gain of the reconfigurable RDRA when a PIN diode is ON.

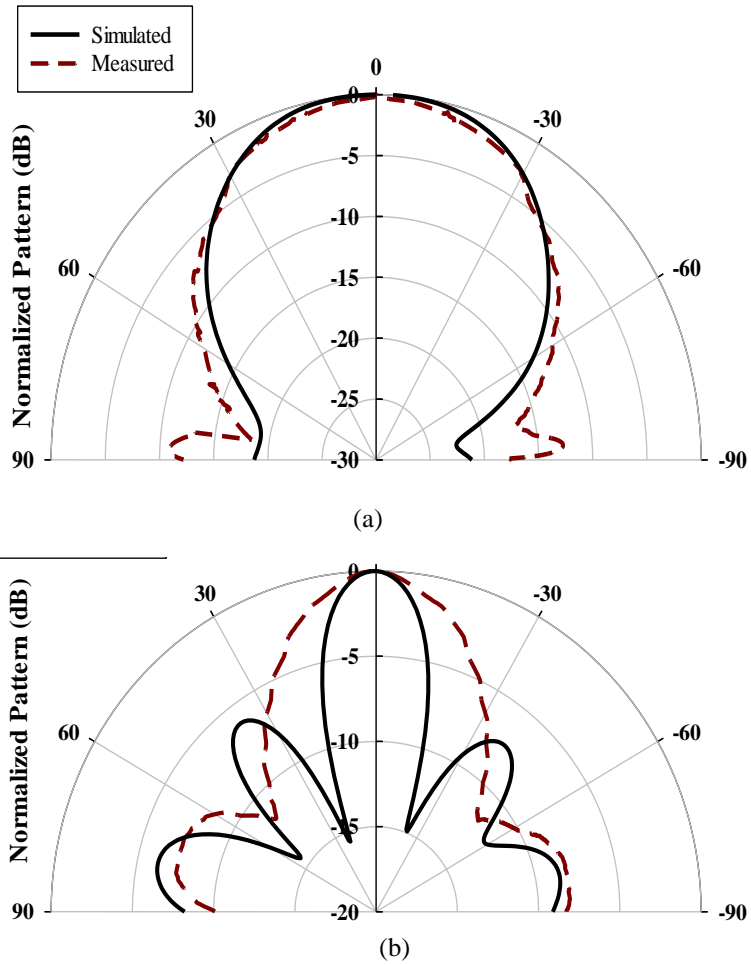


Figure 6.15: Radiation pattern of the reconfigurable RDRA with ON state. (a) E-plane. (b) H-plane.

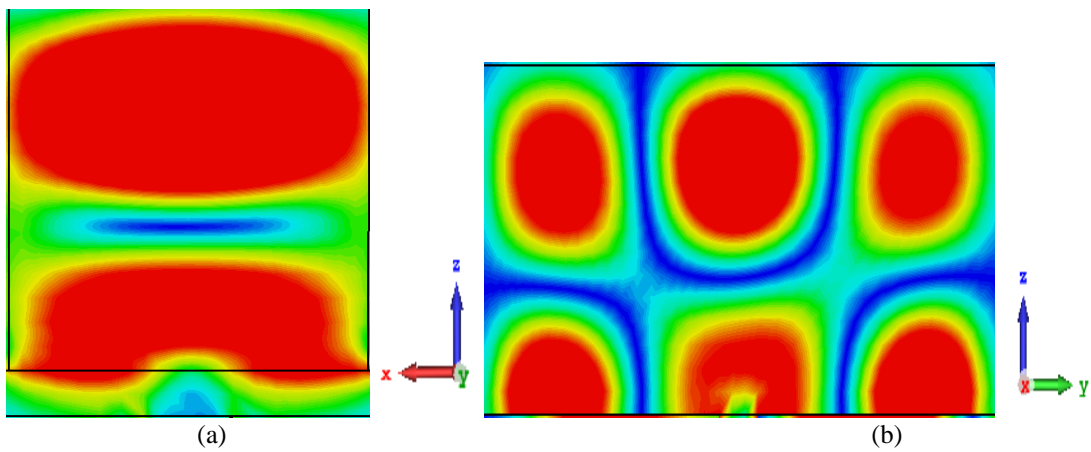


Figure 6.16: Magnetic field of the TE_{133} resonance mode for ON scenario. (a) xz plane (b) yz plane.

6.3 Frequency Reconfigurable DRA Array

6.3.1 Antenna Configuration.

The proposed design uses two elements array with identical dimensions of $a=4\text{mm}$, $b=8\text{mm}$ and $h=4\text{mm}$ and a relative permittivity of $\epsilon_r=9.9$. The feed network consists of a Rogers, RO4003C, and substrate with dimensions of $50\text{mm} \times 30\text{mm} \times 0.5\text{mm}$ and respective dielectric constant and loss tangent of 3.38 and 0.0027. On the top side of the substrate, a copper ground plane has been positioned, and on the lower side, a microstrip transmission line has been printed. The feed network comprises two slots etched on the ground plane with identical lengths and widths of 5.2mm and 1mm. A DC source was connected to the feeding strip line through thin microstrip lines to furnish the necessary biasing voltages for the PIN diode. Additionally, an RF choke was utilized to prevent the mm Wave current from flowing on the biasing line flowing.

6.3.2 Parametric study

An array of two DRA elements is considered next to achieve mmWave reconfigurable frequency operation. Figure 6.17 present the first rectangular DRA with the optimal length of the stub to determine the optimum position of the PIN diode. Figure 6.18 presents the reflection coefficient of the rotated DRA as a function of the stub length l_{s1} . As can be noted, the proposed antenna resonates when the stub length is 0.75 and 2.5 mm. So, the ideal length of the open stub for the first DRA has been chosen to be 2.5 mm, as it provides a wider bandwidth compared to that achieved using a stub length of 0.75 mm. In addition, the excited resonance mode is TE_{311} at 24 GHz with a maximum gain of 5.7 dBi.

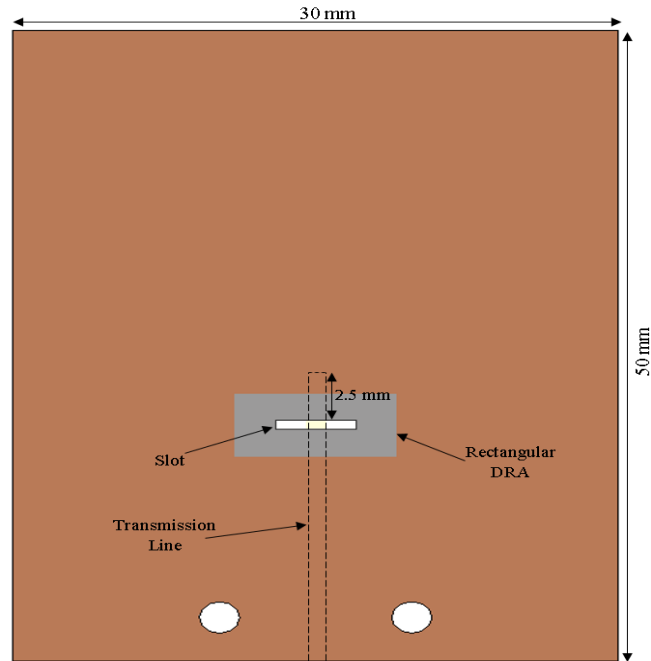


Figure 6.17: Geometry of the reconfigurable DRA.

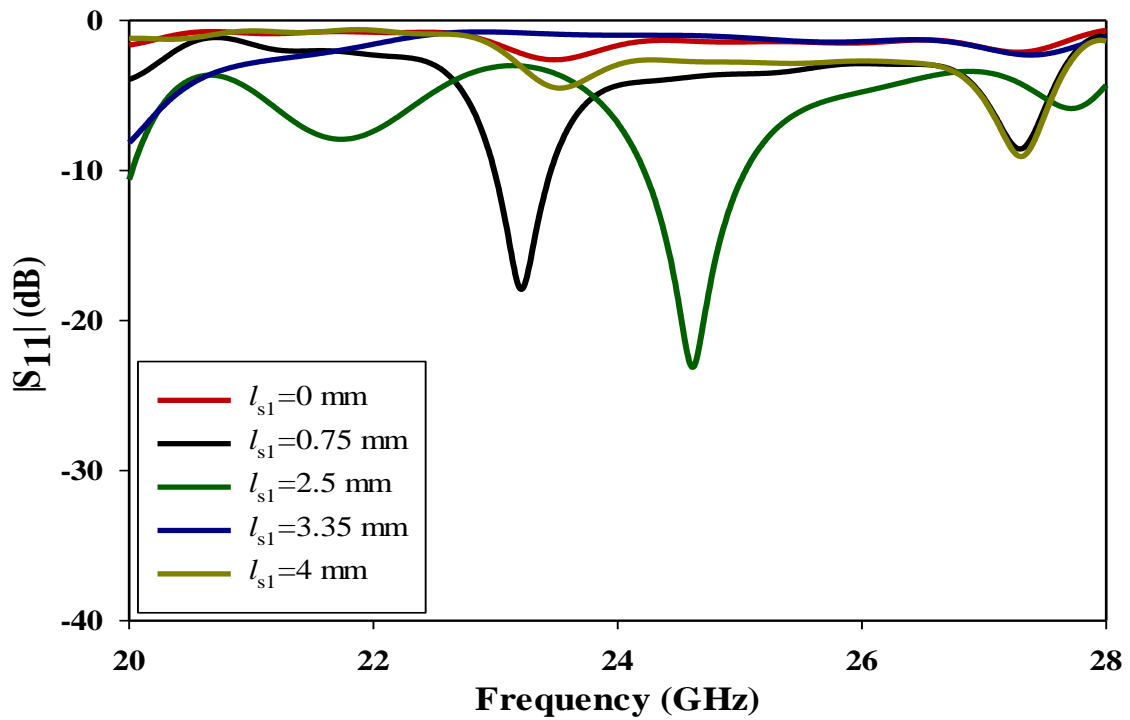


Figure 6.18: Simulated reflection coefficient for the first rectangular DRA with different stub lengths.

The array feed and biasing network are illustrated in Figure 6.19, where it can be observed that the PIN diode is located at the end of the first stub. To maximize the coupling energy fed to the DRAs, two parallel slots have been etched in the ground plane at the centre of the lowest DRA side. On the other side of the substrate, a feeding microstrip line is added. Once more, the PIN diode biasing has been achieved by connecting a DC source to the ground plane using

microstrip lines with respective lengths and widths of 11 mm and 0.3 mm that have been utilised at the left- and right-hand sides of the substrate's lower side. These two biasing lines are connected from one end to the DC power supply and from the other end to the RF chokes. Similar to the previous design, two inductors of 30 nH each have been utilised as RF chokes with 0.3mm bias lines to block any flow of the mmWave current along the microstrip biasing lines. The proposed antenna achieves reconfigurability through two states: OFF and ON. In the OFF state, the positive DC signal is connected to the N terminal of the PIN diode via the right strip line, while the positive terminal is connected to the left strip line that is connected to the common ground. In contrast, in the ON state, the positive DC signal is connected to the P positive terminal of the PIN diode via the right strip line, while the negative terminal is connected to the left strip line that is connected to the common ground. Figure 6.2 depicts the placement of a PIN diode between two slots located beneath the centre of the DRA. When the PIN diode is activated, the proposed antenna functions as an array antenna.

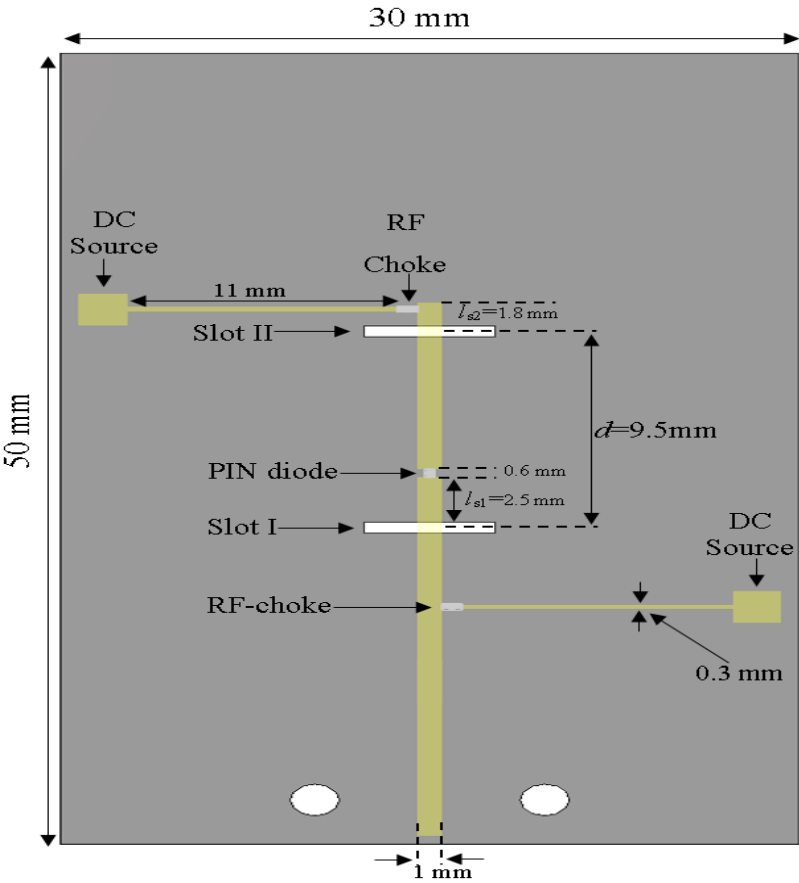


Figure 6.19: Geometry of feed network and biasing lines.

Before adding the second rectangular DRA (RDRA-II), the position of the second DRA needs to be investigated when the PIN diode is ON. The ideal distance, d , between the centres of two

elements is theoretically between $0.5\lambda_0$ and λ_0 . Figure 6.20 illustrates the top view of the geometry of the reconfigurable two elements array with identical dimensions of $a=4\text{mm}$, $b=8\text{mm}$ and $h=4\text{mm}$.

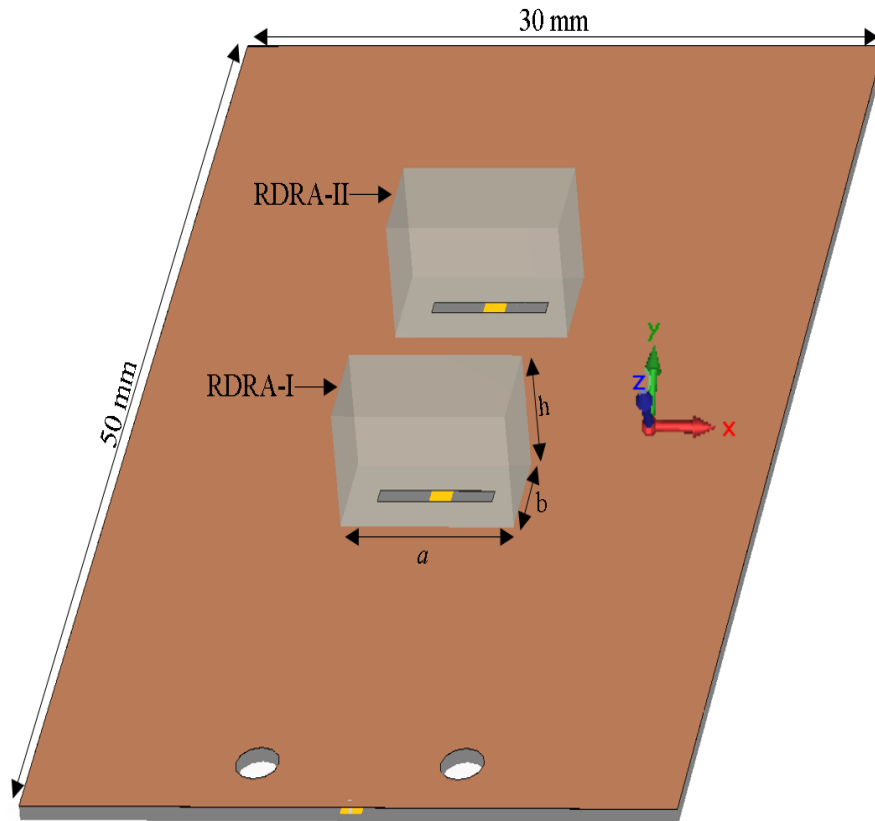


Figure 6.20: Geometry of the reconfigurable DRA array.

To evaluate the antenna's performance, the DRA array was simulated by increasing d from 3.5 mm to 11.5 mm in steps of 2 mm. The reflection coefficient was studied as presented in Figure 6.21, where it can be observed that as d increases from 3.5 mm to 11.5 mm, the achieved impedance bandwidth is 2%, when $d=9.5$ mm, which covers a frequency a range of 29–29.7GHz. The maximum realised gain is 12.5 dBi at 29.3 GHz when $d = 9.5\text{mm}$ as demonstrated in Figure 6.22. Additionally, the results show that when d ranges from 3.5 mm to 11.5 mm, the radiation pattern's side-lobe level is minimized at 9.5 mm, with the beam pointing at 0° , as indicated in Figure 6.23. To enhance the DRA array's anti-interference performance in wireless communication systems, reducing the side-lobe level is crucial. Therefore d has been chosen as 9.5 mm, which corresponds to $0.95\lambda_0$ at 30 GHz. Figure 6.24 shows the reflection coefficient of different values of the length of stub l_{s2} ranging from 0 to 2.4 mm for the 2nd DRA. As can be seen, the proposed antenna resonates at various lengths of l_{s2} . The ideal length of the open stub for the second DRA has been chosen to be 1.8 mm as it

provides a higher gain compared to the other lengths. In addition, the excited resonance mode is TE_{513} at 29.3 GHz, with a gain of 12.5 dBi.

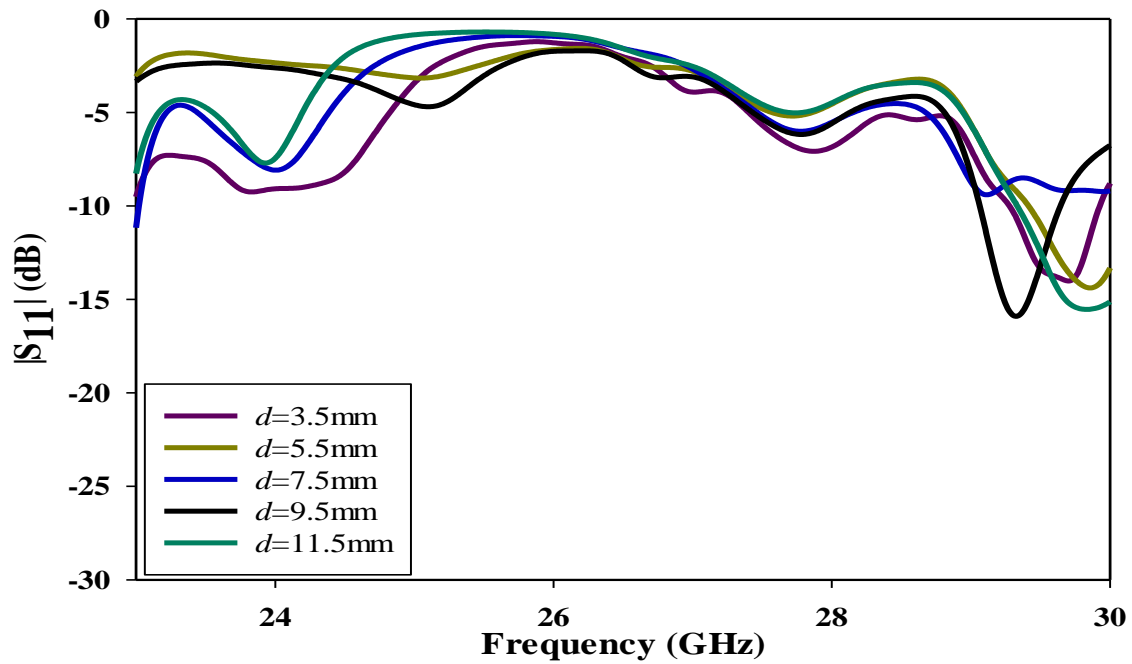


Figure 6.21: Simulated reflection coefficient of rectangular DRAs with different separation distances.

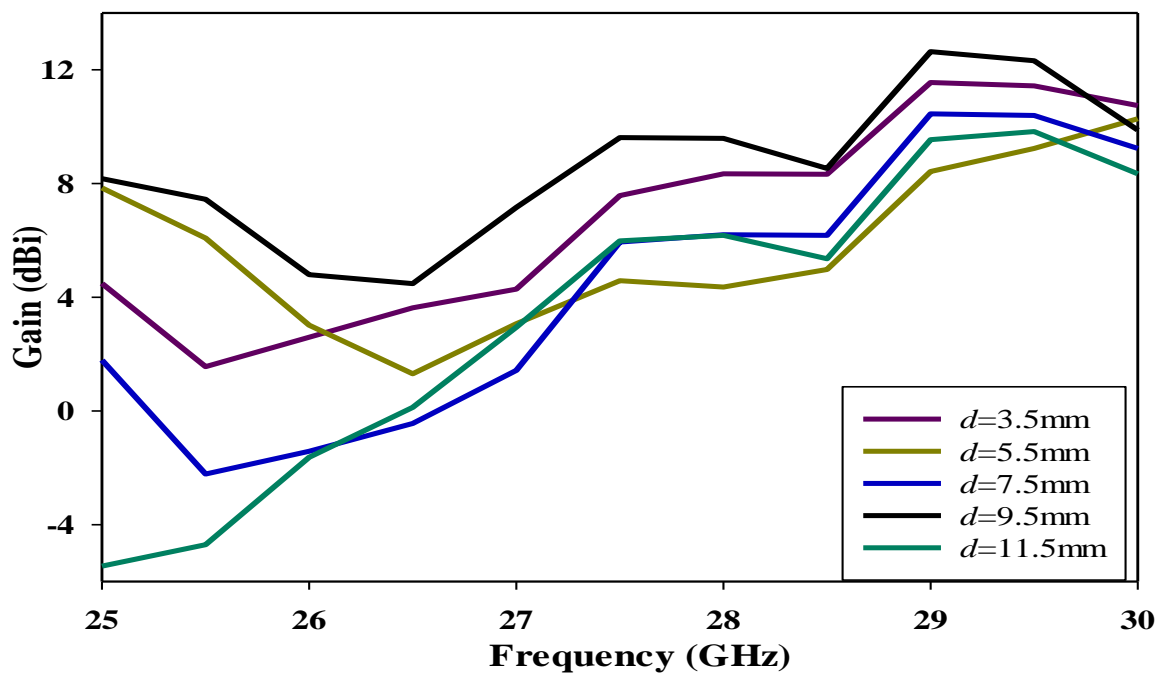
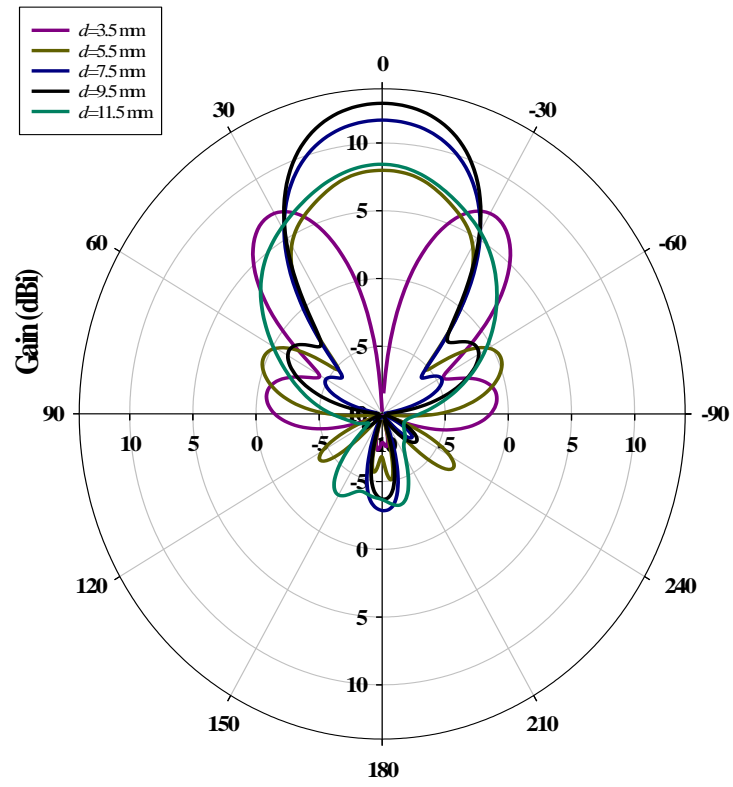
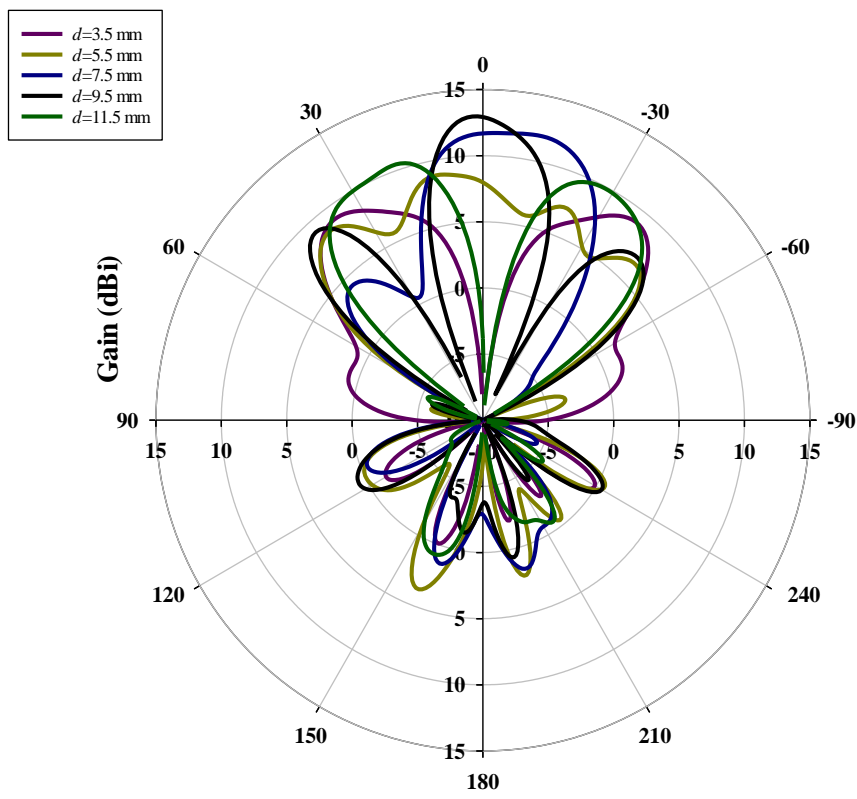


Figure 6.22: Simulated gain of two rectangular DRAs with different separation distances.



(a)



(b)

Figure 6.23: Simulated radiation pattern of the two DRAs configuration when the PIN diode in the ON state for $d= 9.5$ mm. a) E- Plane, b) H- Plane.

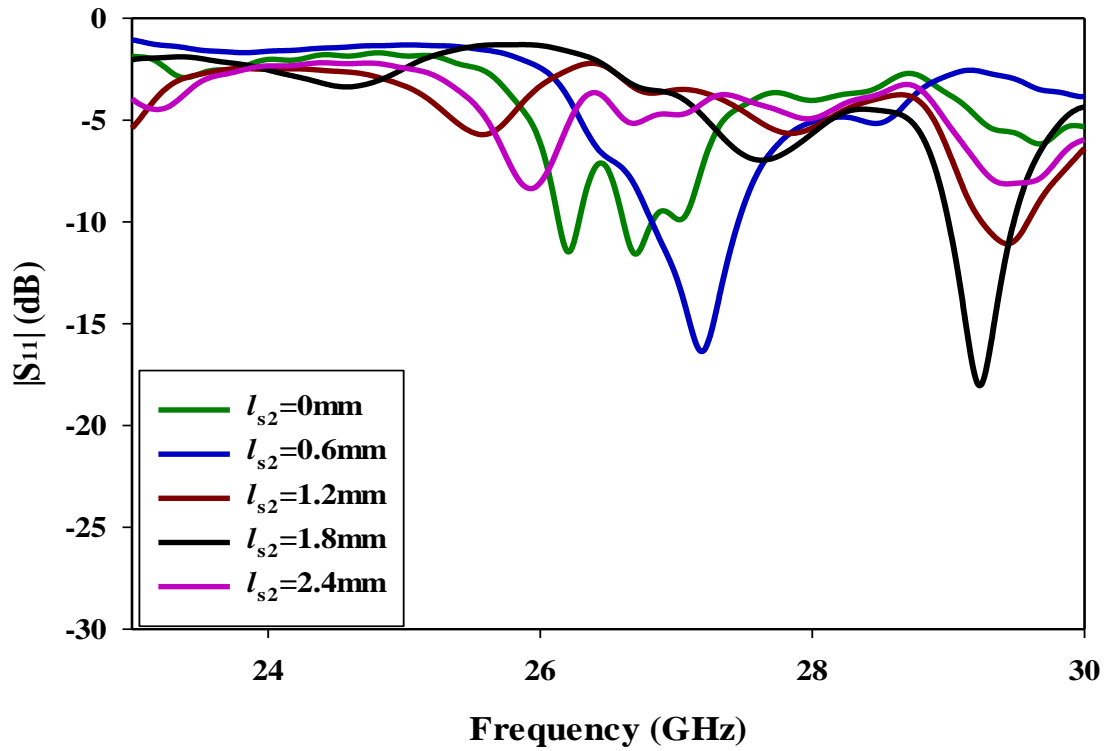


Figure 6.24: Simulated reflection coefficient for the second rectangular DRA with different stub lengths.

6.3.3 Experimental results

The DRAs were fabricated using Alumina, which has a permittivity of 9.9 and a loss tangent of 0.0001. The utilised PCB feed network measuring 30mm×50mm was fabricated at the Wrekin-circuits workshop, while the rectangular DRAs were fabricated by the T-CERAM company.

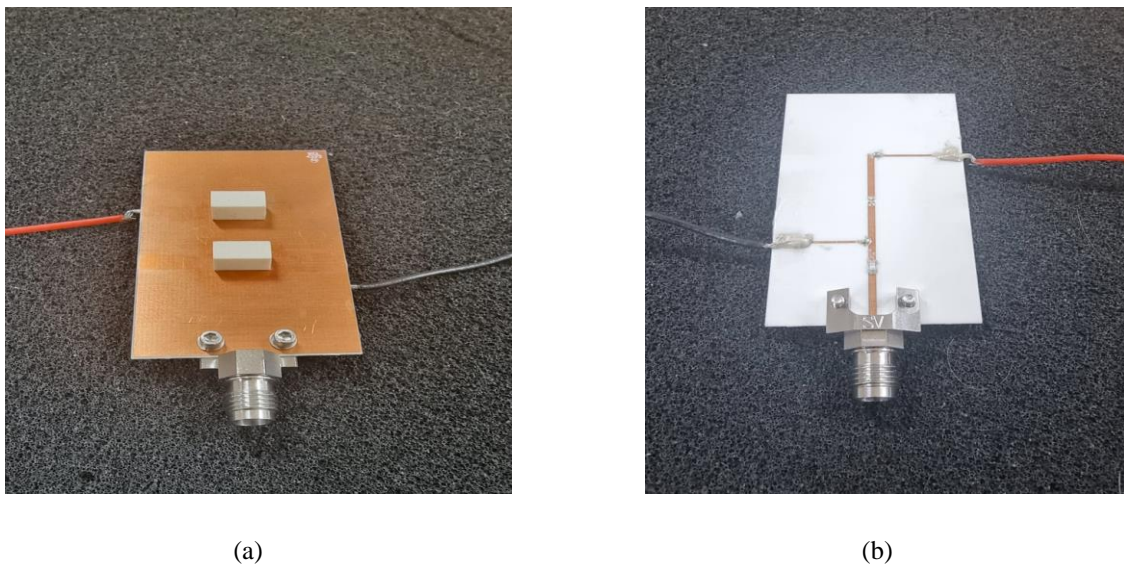


Figure 6.25: Prototype and feed network a) Assembled antenna b) Bottom view.

To eliminate any errors due to misalignment, the DRA positions have been outlined on the ground plane during the fabrication. Bonding between the DRA and the ground plane has been achieved using an extremely thin double-sided adhesive copper tape with a thickness of 0.036 mm. Figure 6.25 illustrates both the top and bottom views of the assembled antenna and feed network.

6.3.4 OFF state scenario

In the first scenario, the PIN diode has been reverse biased to be on the OFF state. Figure 6.26 presents a comparison of the simulated and measured reflection coefficients with a reasonable agreement between them. The simulated and measured impedance bandwidths are 2.3% (24-24.57 GHz) and 2.66% (23.68-24.32 GHz) respectively. The respective simulated measured antenna gains 9.8 dBi at 24 GHz and 9.2 dBi at 24.3 GHz as demonstrated in Figure 6.27. As explained earlier, the first DRA, RDRA-I, operates at 24 GHz which is almost the same as that of two DRAs operating in the OFF-state scenario. Figure 6.28 presents the normalized simulation and measurement of the radiation pattern at 24.3 GHz, with close agreement observed. Figure 6.29 shows the distribution of magnetic fields within the rectangular DRA, where it can be seen that the TE_{311} resonance mode has been excited at 24.3 GHz as identified using the CST simulations and DWM.

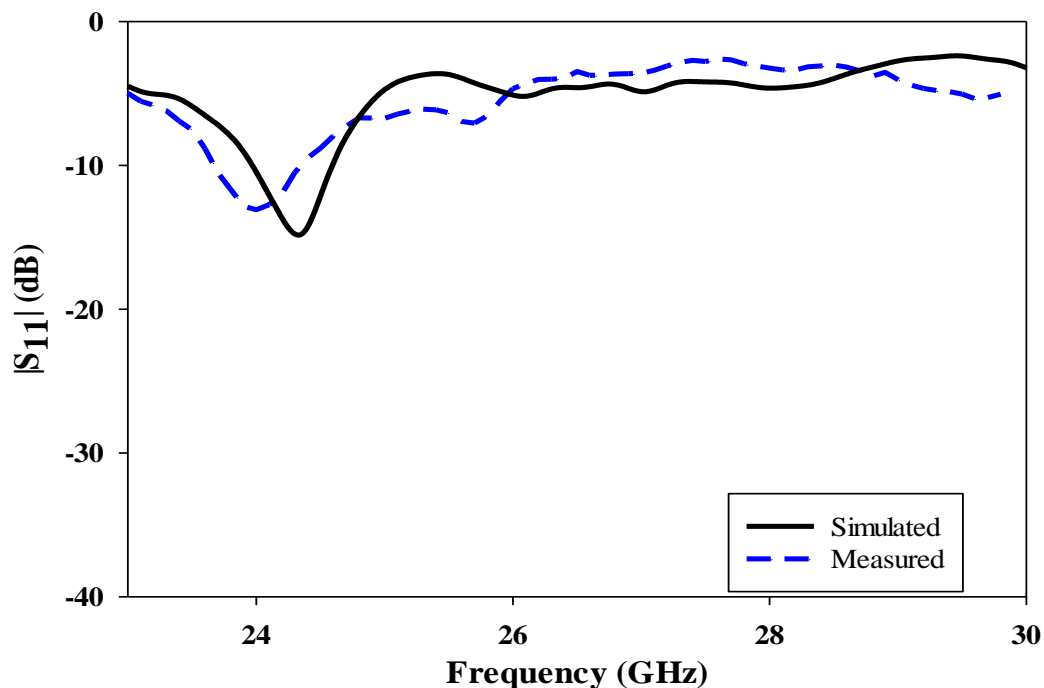


Figure 6.26: Reflection coefficient of two DRAs configurations when a diode is OFF.

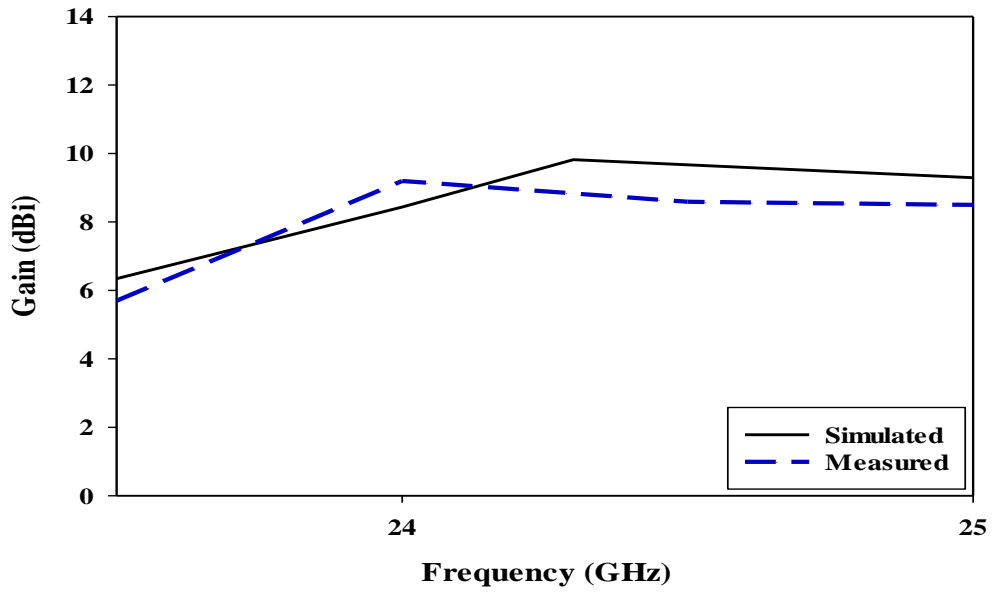


Figure 6.27: Gain of the two DRAs configurations when the diode is in the OFF state.

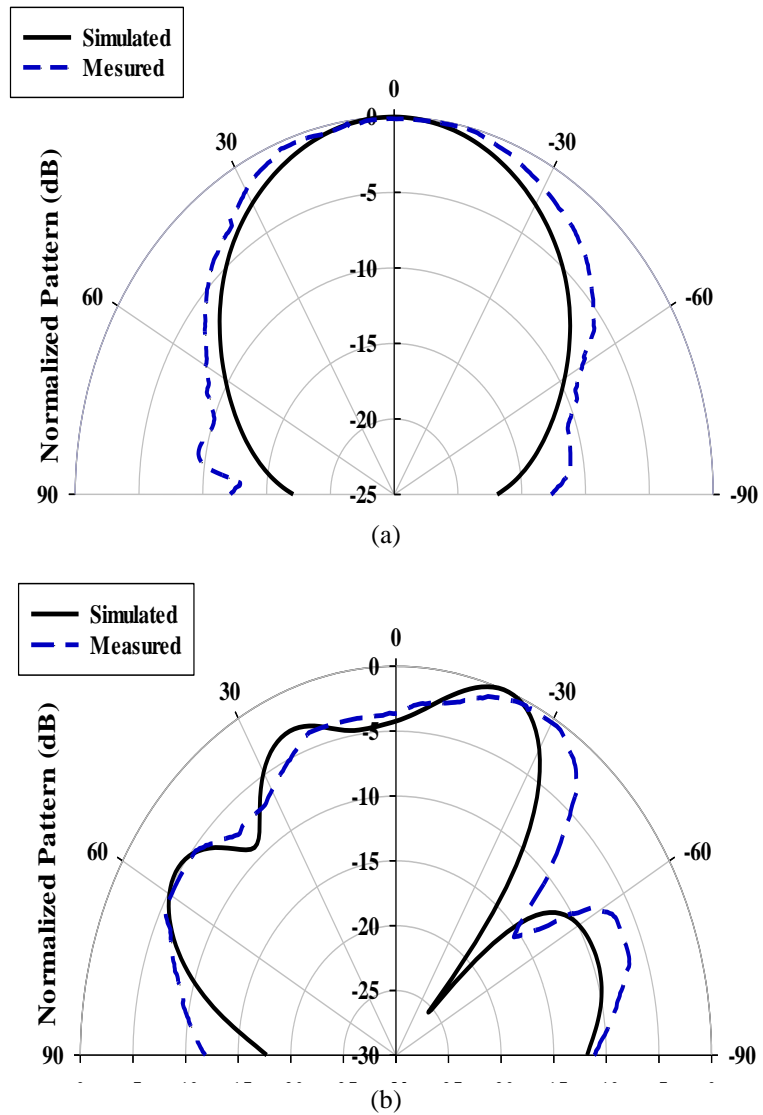


Figure 6.28: Radiation patterns at 24.3 GHz when a PIN diode is OFF. a) E- Plane, b) H- Plane.

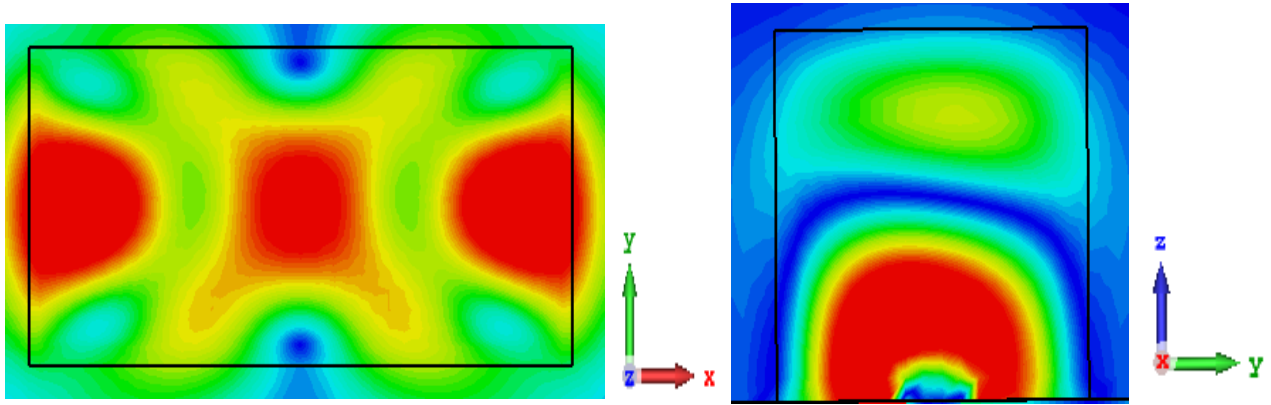


Figure 6.29: Magnetic fields of the TE_{311} resonance modes at 24.3 GHz. (a) xy plane (b) yz plane

6.3.5 ON state scenario

In the second scenario, the state of the PIN diode has been changed to "ON". A matching stub length of 1.75mm has been added under the 2nd DRA. As demonstrated in Figure 6.30, matching has been achieved at 29.3 GHz, where it can be noted that the simulated and measured impedance bandwidths are 2.72% (29 - 29.8 GHz) and 2.9% (28.50 - 29.35 GHz), respectively. Figure 6.31 compares the measured and simulated gains, with close agreement. However, a slight drop in measured gain to 11.8dBi can be observed at 29 GHz compared to a maximum simulated gain of 12.5dBi at 29.3 GHz. The radiation pattern distribution for the TE_{513} resonance modes at 29.3 GHz is depicted in Figure 6.32, with a close agreement observed. Figure 6.33 shows the distribution of magnetic fields inside the rectangular DRA, where it can be seen that the resonance modes have been excited at 29.3 GHz. It should be noted that the same modes and resonance frequencies can be noted for the reconfigurable single DRA and the two DRAs array. This is expected since the supported modes are determined by the dimensions of the DRA element and independent of mutual coupling. However, a stronger mutual coupling may alter the mode's fields inside the DRA and/or excite another mode, which results in impedance matching at a different frequency. Finally, the array configuration has been investigated in the absence of the 2nd DRA, where it has been noted that the proposed antenna operates at 27 GHz.

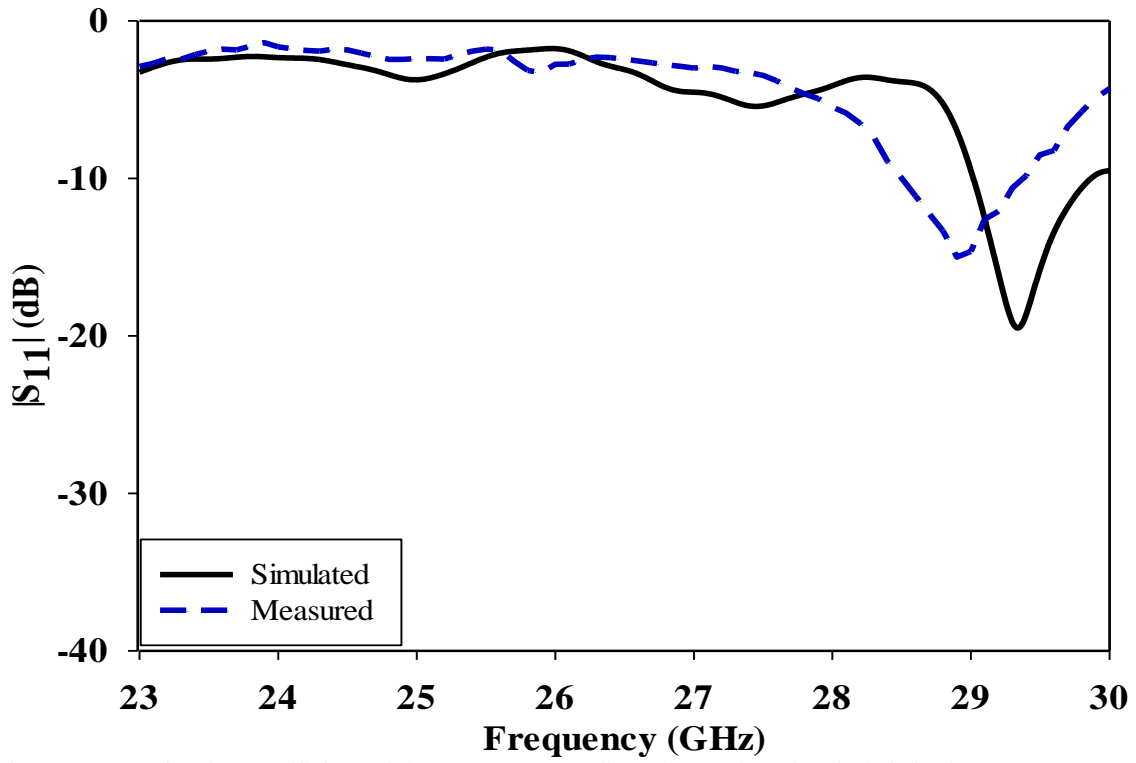


Figure 6.30: Reflection coefficient of the two DRAs configurations when the diode is in the ON state.

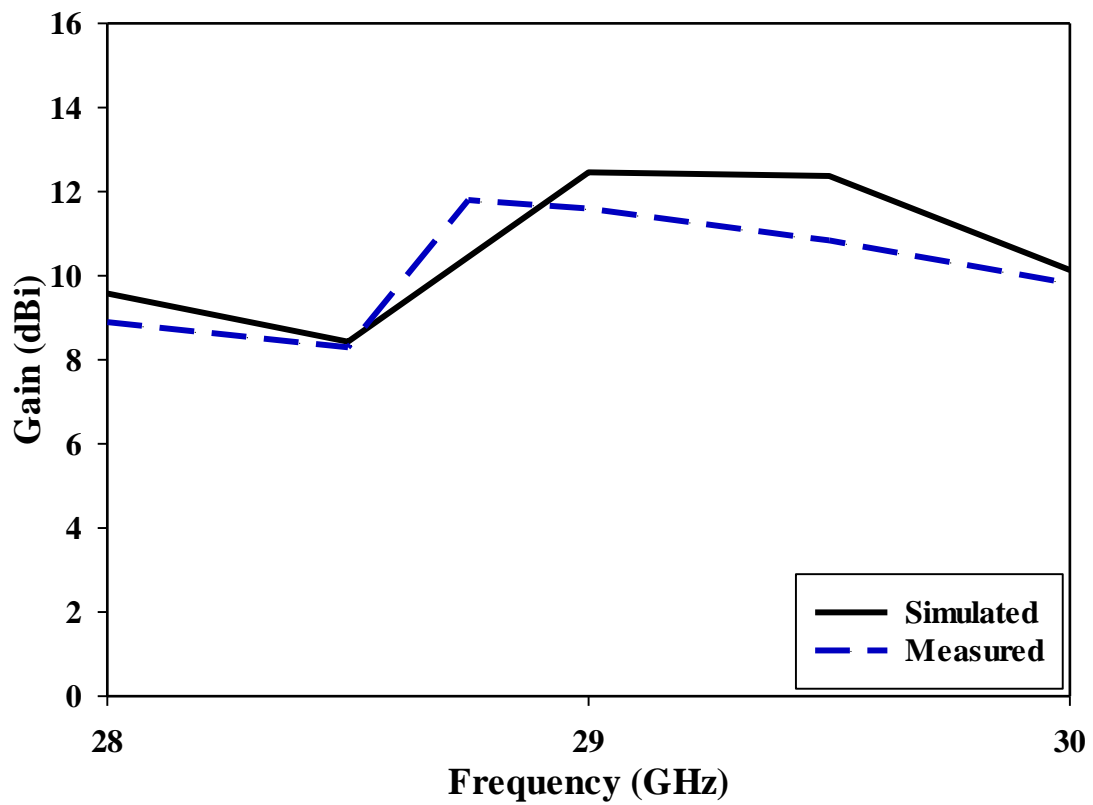


Figure 6.31: Gain of the two DRAs configurations when the diode is in the ON state.

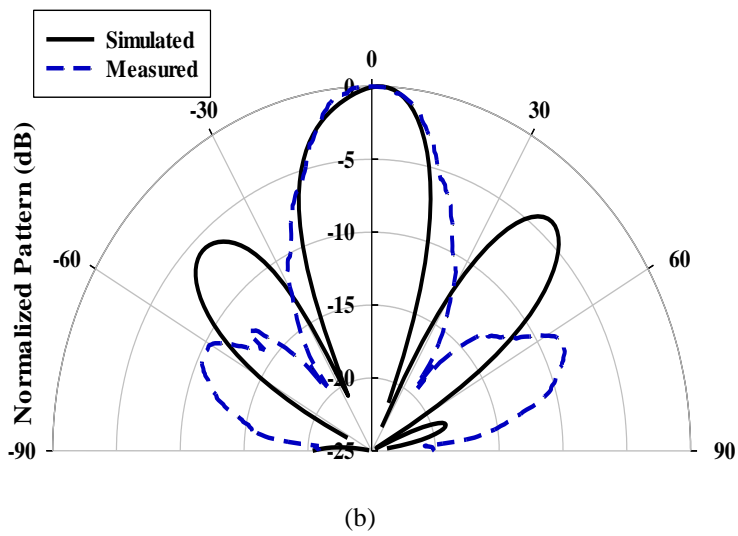
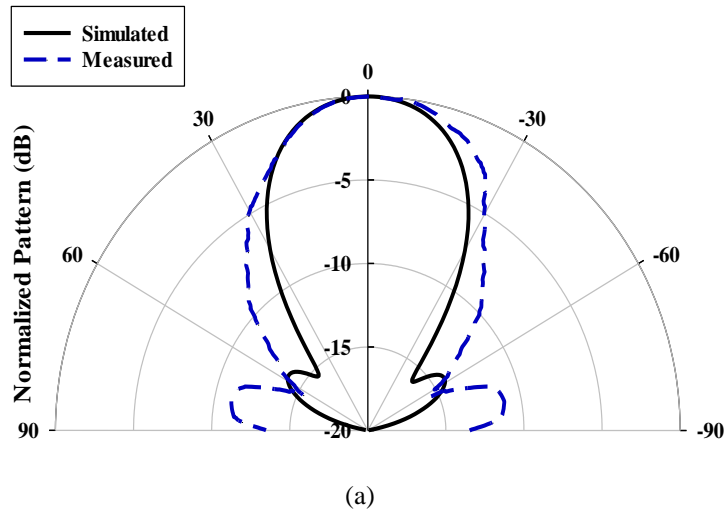


Figure 6.32: Radiation patterns of the two DRAs configurations when the diode is in the ON state at 29.3 GHz. a) E- Plane, b) H- Plane.

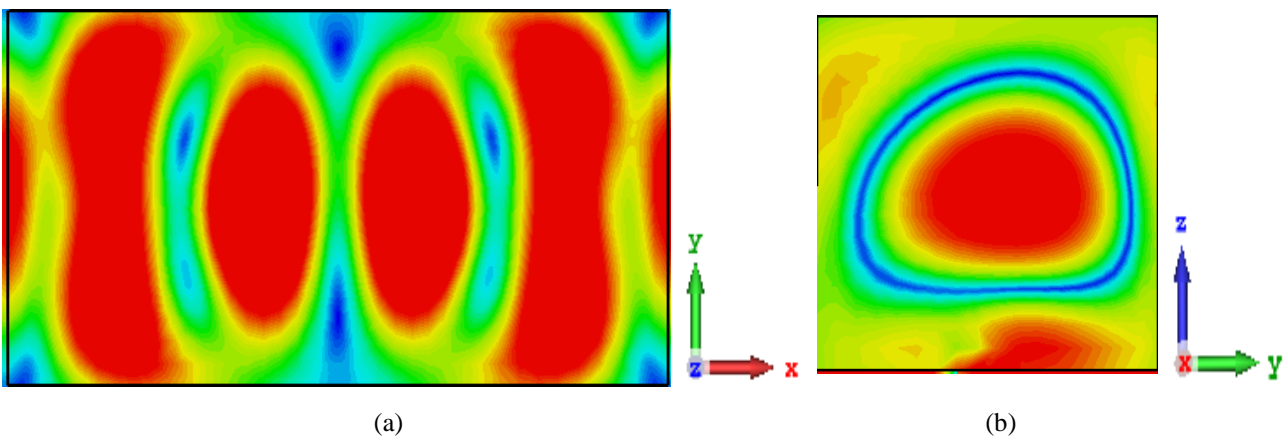


Figure 6.33: Magnetic field distribution of the TE_{513} resonance modes at 29.3 GHz. (a) xy plane (b) yz plane.

Table 6-1 presents a comprehensive comparison between the performances of the proposed reconfigurable frequency mmWave DRA with those other reconfigurable mmWave antennas that were previously reported in the literature. From these results, it can be concluded that the first mmWave reconfigurable frequency rectangular DRA has been demonstrated with performance that is comparable to those of other antenna types albeit with a considerably higher gain and a simpler configuration.

Table 6-1: Comparison of the proposed reconfigurable DRA with previously reported reconfigurable mmWave antenna designs

Ref	Antenna Type	Tuning Tech	Method	Frequency Range (GHz)	Tuning Range (%)	Gain (dBi)
[98]	Slot antenna array	Optical	Photoconductive switch	28 - 38	30.3	9.0
[100]	Slot	Electrical	PIN diode	27.95-28.65	2.47	6.4
[101]	Metasurface	Electrical	Vanadium dioxide	28 - 38	30.3	7.9
This work	Single DRA	Electrical	PIN diode	21.7-26.7	21.11	8
	Two DRAs	Electrical	PIN diode	23.68-29.3	21.21	11.8

6.4 Conclusion

This Chapter examined two designs of reconfigurable mmWave rectangular DRAs both theoretically and experimentally. The first design utilises a single rectangular DRA and a PIN diode to achieve reconfigurability. For a practical design with maximum isolation between the diode and antenna, the PIN diode was placed on the feeding microstrip line, allowing the length of the stub to be altered and the frequency to be tuned from 21.6 to 26.7 GHz, with a tuning range of 21.11%. The rectangular DRA operates in the TE_{131} mode and offers respective impedance bandwidths of 3.45% (21.6-22.36GHz) when the PIN diode is OFF. In another scenario, the PIN diode is ON the proposed antenna operates TE_{133} mode, which offers respective impedance bandwidths of 0.6% (26.6-26.8 GHz) in conjunction with a high gain of up to 8 dBi.

The second design employs two rectangular DRA elements and a single PIN diode to achieve reconfigurability by switching the PIN diode ON and OFF. When the PIN diode is OFF, the RDRA-I operates in resonance mode TE_{311} at 24 GHz, providing an impedance bandwidth of 2.66% (23.68-24.32 GHz) and a maximum gain of 9.2 dBi. On the other hand, when the PIN diode is ON, the RDRA-I and RDRA-II operate in the TE_{513} resonance mode at 29.3 GHz, offering an impedance bandwidth of 2.9% (28.50-29.35 GHz) and a high gain of up to 11.8 dBi. The proposed antenna is a promising solution for applications that require reconfigurable and high-performance antennas at mmWave frequency for 5G and B5G communication systems.

This is the first attempt in realising a reconfigurable mmWave DRA as the reported studies on reconfigurable mmWave antennas were focused on two-dimensional antenna configurations. In addition, the proposed DRA offers a gain that is considerably higher than those reported in the literature for mmWave reconfigurable antennas.

Chapter 7

Conclusions and Future Work

This thesis has successfully realized its set objectives of exploring and implementing various designs of reconfigurable dielectric resonator antennas utilizing different techniques. The initial chapters laid the foundation by introducing the research topic, outlining objectives, and conducting a comprehensive literature review on diverse methods for achieving reconfigurability in DRAs.

Chapter Three addressed the first objective by presenting two designs of reconfigurable rectangular DRAs, achieving frequency and radiation pattern reconfigurability. The first design demonstrated a simple yet effective approach using one slot, a single rectangular DRA, and two switches. The results showed an impressive tuning range of 41.2% over a wide frequency range of 8.78 to 13.34 GHz. The second design, utilizing two PIN diodes and a rectangular ring slot, achieved a tuning range of 14.6% over a frequency range of 8.2 to 9.5 GHz. Experimental measurements validated these results, showcasing the practical feasibility of reconfigurability in frequency and radiation patterns. Chapter Four contributed to the second objective by introducing two circularly polarized rectangular DRA designs, achieving polarization reconfigurability. The first design employed a cross slot and four PIN diodes, demonstrating wide effective bandwidths and axial ratio bandwidths for both LHCP and RHCP states. The configuration exhibited a maximum gain of 8.2 dBic. The second design presented a simple and compact reconfigurable rectangular DRA, demonstrating a gain of approximately 6.9 dBic in all polarizations. The LHCP and RHCP radiations showed reconfigurable polarization characteristics with an impedance bandwidth of 21.3%, while the LP state exhibited a narrower impedance bandwidth of 3.4%. Axial Ratio bandwidth of 4% and a maximum gain of 6.9 dBic at 10.6 GHz were achieved. These results align with the objective of exploring designs with diverse reconfigurability directions.

Chapter Five introduced two novel designs for reconfigurable frequency and circular polarization using photoconductive switches at both X-band and mmWave frequencies. While the first design demonstrated promising simulated results, the absence of experimental measurements emphasizes the need for future experimental validation. The second design, intended for mmWave applications, showcased simulation results with wide impedance

bandwidths and a relative impedance bandwidth of 31.8% for both LHCP and RHCP states compared to 9.5% for a linearly polarized DRA. These designs exemplify the potential of diverse techniques, including photoconductive switches, for achieving reconfigurability. In Chapter Six, two reconfigurable mmWave rectangular DRA were introduced, combining theoretical exploration with experimental validation. The first design featured a single rectangular DRA with a strategically placed PIN diode on the feeding microstrip line, enabling a tuning range of 21.11% from 21.6 to 26.7 GHz. This design exhibited the TE₁₃₁ mode at 22 GHz with a 3.45% impedance bandwidth when the PIN diode is OFF and the TE₁₃₃ mode at 26.7 GHz with a 0.6% impedance bandwidth and a high gain of up to 8 dBi in case the PIN diode is ON. The second design incorporated two rectangular DRA elements and a single PIN diode for reconfigurability. It demonstrated the TE₃₁₁ mode at 24 GHz with a 2.66% impedance bandwidth and a maximum gain of 9.2 dBi in case the PIN diode is OFF, while the TE₅₁₃ mode at 29.3 GHz exhibited a 2.9% impedance bandwidth and a high gain of up to 11.8 dBi in case the PIN diode is ON. These designs, experimentally validated, not only showcased theoretical advancements but also confirmed their practical feasibility. Their potential for reconfigurability and high performance in mmWave DRAs hold significance for future communication systems. The fabricated prototypes in chapters three, four, and six were successfully measured, validating the theoretical analyses and demonstrating the practical feasibility of the proposed designs.

Future Work

This thesis introduces two reconfigurable techniques for achieving electrical (PIN diode) and optical reconfigurability.

- **For electric technique designs utilizing PIN diode switches:**

- The circular polarizer design using a cross slot has undergone theoretical investigation. Further research is needed to transition from X-band to mmWave and experimentally explore the promising results, including wider impedance bandwidth, axial ratio, and significant gain.
- The combined reconfigurable frequency and radiation pattern design merits further investigation, both theoretically and experimentally, especially at mmWave frequencies, as such an approach has not been reported before.
- Reconfigurable two-element DRAs demand more attention due to their substantial degree of freedom. Utilizing reconfigurable arrays allows upcoming wireless networks to attain improved performance while incurring only a fraction of the expenses linked with intricate phased arrays. These arrays provide the potential to dynamically adjust the antenna's radiation pattern, frequency response, and polarization, making them ideal for applications such as 5G communications and radar systems. Consequently, the use of reconfigurable arrays can markedly improve the efficiency and flexibility of wireless systems while simultaneously reducing their complexity and cost.

- **For optical designs employing photoconductive switches:**

This thesis introduces two novel designs for reconfigurable Rectangular Dielectric Resonator Antennas.

- Advancing this optical technique requires conducting experimental investigations to achieve reconfigurable frequency, polarization, and radiation pattern at mmWave frequencies. These experimental studies are crucial, given that no previous studies have reported designs utilizing photoconductive switches. Therefore, further exploration of these novel designs can significantly contribute to the field of reconfigurable antenna design.

Reference

- [1] F. Ferrero, L. Lizzi, R. Staraj, and J.-M. Ribero, "Reconfigurable antenna for future spectrum reallocations in 5G communications," *IEEE Antennas and Wireless Propagation Letters*, vol. 15, pp. 1297-1300, 2015.
- [2] J. C. McDowell, "The low earth orbit satellite population and impacts of the SpaceX Starlink constellation," *The Astrophysical Journal Letters*, vol. 892, no. 2, p. L36, 2020.
- [3] H. Peng, L. Liang, X. Shen, and G. Y. Li, "Vehicular communications: A network layer perspective," *IEEE Transactions on Vehicular Technology*, vol. 68, no. 2, pp. 1064-1078, 2018.
- [4] S. Radavaram and M. Pour, "Wideband radiation reconfigurable microstrip patch antenna loaded with two inverted U-slots," *IEEE Transactions on Antennas and Propagation*, vol. 67, no. 3, pp. 1501-1508, 2018.
- [5] J.-S. Row and Y.-H. Wei, "Wideband reconfigurable crossed-dipole antenna with quad-polarization diversity," *IEEE Transactions on Antennas and Propagation*, vol. 66, no. 4, pp. 2090-2094, 2018.
- [6] H. H. Tran, N. Nguyen-Trong, T. K. Nguyen, and A. M. Abbosh, "Bandwidth enhancement utilizing bias circuit as parasitic elements in a reconfigurable circularly polarized antenna," *IEEE Antennas and Wireless Propagation Letters*, vol. 17, no. 8, pp. 1533-1537, 2018.
- [7] J. Huang and X. Gong, "A wide-band dual-polarized frequency-reconfigurable slot-ring antenna element using a diagonal feeding method for array design," in *2018 IEEE International Symposium on Antennas and Propagation & USNC/URSI National Radio Science Meeting*, 2018, pp. 477-478: IEEE.
- [8] T. Li, M. Shirazi, and X. Gong, "S-band continuously-tunable slot-ring antennas for reconfigurable antenna array applications," in *2016 International Workshop on Antenna Technology (iWAT)*, 2016, pp. 18-19: IEEE.
- [9] M. Borhani, P. Rezaei, and A. Valizade, "Design of a reconfigurable miniaturized microstrip antenna for switchable multiband systems," *IEEE Antennas and Wireless Propagation Letters*, vol. 15, pp. 822-825, 2015.
- [10] J.-F. Tsai and J.-S. Row, "Reconfigurable square-ring microstrip antenna," *IEEE Transactions on Antennas and Propagation*, vol. 61, no. 5, pp. 2857-2860, 2013.
- [11] B. Liu, J. Qiu, and C. Wang, "Polarization and Bandwidth Reconfigurable Rectangular Dielectric Resonator Antenna," in *2020 IEEE International Symposium on Antennas and Propagation and North American Radio Science Meeting*, 2020, pp. 167-168: IEEE.
- [12] X. Liu, K. W. Leung, and N. Yang, "Wideband horizontally polarized omnidirectional cylindrical dielectric resonator antenna for polarization reconfigurable design," *IEEE Transactions on Antennas and Propagation*, vol. 69, no. 11, pp. 7333-7342, 2021.
- [13] W.-J. Sun, W.-W. Yang, L. Guo, W. Qin, and J.-X. Chen, "A circularly polarized dielectric resonator antenna and its reconfigurable design," *IEEE Antennas and Wireless Propagation Letters*, vol. 19, no. 7, pp. 1088-1092, 2020.
- [14] M. Esmaeili and J.-J. Laurin, "Polarization Reconfigurable Slot-Fed Cylindrical Dielectric Resonator Antenna," *Progress In Electromagnetics Research*, vol. 168, pp. 61-71, 2020.
- [15] X. Liu, K. W. Leung, and N. Yang, "A Pattern-Reconfigurable Cylindrical Dielectric Resonator Antenna with Three Switchable Radiation Patterns," *IEEE Transactions on Antennas and Propagation*, 2023.
- [16] J. Ren *et al.*, "Radiation pattern and polarization reconfigurable antenna using dielectric liquid," *IEEE Transactions on Antennas and Propagation*, vol. 68, no. 12, pp. 8174-8179, 2020.

- [17] Z. Chen, H. Wong, and J. Kelly, "A Polarization-Reconfigurable Glass Dielectric Resonator Antenna Using Liquid Metal," *IEEE Transactions on Antennas and Propagation*, vol. 67, no. 5, pp. 3427-3432, 2019.
- [18] S. Long, M. McAllister, and L. Shen, "The resonant cylindrical dielectric cavity antenna," *IEEE Transactions on Antennas and Propagation*, vol. 31, no. 3, pp. 406-412, 1983.
- [19] Q. Lai, G. Almpanis, C. Fumeaux, H. Benedickter, and R. Vahldieck, "Comparison of the radiation efficiency for the dielectric resonator antenna and the microstrip antenna at Ka band," *IEEE Transactions on Antennas and Propagation*, vol. 56, no. 11, pp. 3589-3592, 2008.
- [20] S. Kong, K. M. Shum, C. Yang, L. Gao, and C. H. Chan, "Wide impedance-bandwidth and gain-bandwidth terahertz on-chip antenna with chip-integrated dielectric resonator," *IEEE Transactions on Antennas and Propagation*, vol. 69, no. 8, pp. 4269-4278, 2021.
- [21] N. M. Nor, M. H. Jamaluddin, M. R. Kamarudin, and M. Khalily, "Rectangular dielectric resonator antenna array for 28 GHz applications," *Progress In Electromagnetics Research C*, vol. 63, pp. 53-61, 2016.
- [22] H. A. Malhat, S. H. Zainud-Deen, H. El-Hemaily, H. A. Hamed, and A. A. Ibrahim, "Reconfigurable Circularly Polarized Hemispherical DRA Using Plasmonic Graphene Strips for MIMO Communications," *Plasmonics*, vol. 17, no. 2, pp. 765-774, 2022.
- [23] A. Petosa and S. Thirakoune, "Rectangular dielectric resonator antennas with enhanced gain," *IEEE Transactions on Antennas and Propagation*, vol. 59, no. 4, pp. 1385-1389, 2011.
- [24] S. K. Sahu, T. K. Das, and S. K. Behera, "Design of a Multiband Triangular DRA for C-Band Applications," 2019.
- [25] H. Gharsallah, L. Osman, and L. Latrach, "Study of a Conical DRA Array with Enhanced Bandwidth and Gain for C-Band Applications," in *2018 18th Mediterranean Microwave Symposium (MMS)*, 2018, pp. 51-53: IEEE.
- [26] R. Chair, S. L. S. Yang, A. A. Kishk, K. F. Lee, and K. M. Luk, "Aperture fed wideband circularly polarized rectangular stair shaped dielectric resonator antenna," *IEEE transactions on antennas and propagation*, vol. 54, no. 4, pp. 1350-1352, 2006.
- [27] M. Amin, T. T. Bu, C.-M. Luo, M. A. Basit, and J.-S. Hong, "A bowtie-shaped MIMO dielectric resonator antenna for WLAN applications," *IEICE Electronics Express*, p. 14.20170519, 2017.
- [28] V. Basile *et al.*, "Design and manufacturing of super-shaped dielectric resonator antennas for 5G applications using stereolithography," *IEEE Access*, vol. 8, pp. 82929-82937, 2020.
- [29] S. Trinh-Van, Y. Yang, K.-Y. Lee, and K. C. Hwang, "A wideband circularly polarized antenna with a multiple-circular-sector dielectric resonator," *Sensors*, vol. 16, no. 11, p. 1849, 2016.
- [30] K. S. Ryu and A. A. Kishk, "Ultrawideband dielectric resonator antenna with broadside patterns mounted on a vertical ground plane edge," *IEEE Transactions on Antennas and Propagation*, vol. 58, no. 4, pp. 1047-1053, 2010.
- [31] S. K. Sharma and M. K. Brar, "Aperture-coupled pentagon shape dielectric resonator antennas providing wideband and multiband performance," *Microwave and Optical Technology Letters*, vol. 55, no. 2, pp. 395-400, 2013.
- [32] A. Altaf, J.-W. Jung, Y. Yang, K.-Y. Lee, and K. C. Hwang, "Reconfigurable dual-/triple-band circularly polarized dielectric resonator antenna," *IEEE Antennas and Wireless Propagation Letters*, vol. 19, no. 3, pp. 443-447, 2020.
- [33] C. G. Christodoulou, Y. Tawk, S. A. Lane, and S. R. Erwin, "Reconfigurable antennas for wireless and space applications," *Proceedings of the IEEE*, vol. 100, no. 7, pp. 2250-2261, 2012.
- [34] T. Elkarkraoui, G. Y. Delisle, and N. Hakem, "60 GHz Polarization Reconfigurable DRA Antenna," *Open Journal of Antennas and Propagation*, vol. 4, no. 04, p. 176, 2016.

- [35] R. L. Haupt and M. Lanagan, "Reconfigurable antennas," *IEEE Antennas and Propagation Magazine*, vol. 55, no. 1, pp. 49-61, 2013.
- [36] J. Desjardins, D. McNamara, S. Thirakoune, and A. Petosa, "Electronically frequency-reconfigurable rectangular dielectric resonator antennas," *IEEE Transactions on Antennas and Propagation*, vol. 60, no. 6, pp. 2997-3002, 2012.
- [37] P.-Y. Qin, F. Wei, and Y. J. Guo, "A wideband-to-narrowband tunable antenna using a reconfigurable filter," *IEEE Transactions on Antennas and Propagation*, vol. 63, no. 5, pp. 2282-2285, 2015.
- [38] X.-l. Yang, J.-c. Lin, G. Chen, and F.-l. Kong, "Frequency reconfigurable antenna for wireless communications using GaAs FET switch," *IEEE Antennas and Wireless Propagation Letters*, vol. 14, pp. 807-810, 2014.
- [39] S. Goel and N. Gupta, "Design, optimization and analysis of reconfigurable antenna using RF MEMS switch," *Microsystem Technologies*, vol. 26, no. 9, pp. 2829-2837, 2020.
- [40] S. Pendharker, R. Shevgaonkar, and A. Chandorkar, "Optically controlled frequency-reconfigurable microstrip antenna with low photoconductivity," *IEEE antennas and wireless propagation letters*, vol. 13, pp. 99-102, 2014.
- [41] I. F. da Costa *et al.*, "Photonic downconversion and optically controlled reconfigurable antennas in mm-waves wireless networks," in *2016 Optical Fiber Communications Conference and Exhibition (OFC)*, 2016, pp. 1-3: IEEE.
- [42] I. Da Costa, C. S. Arismar, E. Reis, D. Spadoti, and J. M. Neto, "Optically controlled reconfigurable antenna array based on a slotted circular waveguide," in *2015 9th European Conference on Antennas and Propagation (EuCAP)*, 2015, pp. 1-4: IEEE.
- [43] C. S. Arismar, I. Da Costa, L. Manera, and J. Diniz, "Optically controlled E-antenna for cognitive and adaptive radio over fiber systems," in *2013 IFIP Wireless Days (WD)*, 2013, pp. 1-3: IEEE.
- [44] Y. Tawk, J. Costantine, F. Ayoub, C. Christodoulou, D. Doyle, and S. Lane, "Physically reconfigurable antennas: Concepts and automation," in *2017 IEEE International Symposium on Antennas and Propagation & USNC/URSI National Radio Science Meeting*, 2017, pp. 419-420: IEEE.
- [45] W. Ma, G. Wang, B.-f. Zong, Y. Zhuang, and X. Zhang, "Mechanically reconfigurable antenna based on novel metasurface for frequency tuning-range improvement," in *2016 IEEE International Conference on Microwave and Millimeter Wave Technology (ICMMT)*, 2016, vol. 2, pp. 629-631: IEEE.
- [46] A. Jouade, M. Himdi, A. Chauloux, and F. Colombel, "Mechanically pattern-reconfigurable bended horn antenna for high-power applications," *IEEE Antennas and Wireless Propagation Letters*, vol. 16, pp. 457-460, 2016.
- [47] I. T. McMichael, "A mechanically reconfigurable patch antenna with polarization diversity," *IEEE Antennas and Wireless Propagation Letters*, vol. 17, no. 7, pp. 1186-1189, 2018.
- [48] S. J. Mazlouman, A. Mahanfar, C. Menon, and R. Vaughan, "Mechanically reconfigurable antennas using electro-active polymers (EAPs)," in *2011 Ieee International Symposium on Antennas and Propagation (Apsursi)*, 2011, pp. 742-745: IEEE.
- [49] Z. Chen and H. Wong, "Liquid dielectric resonator antenna with circular polarization reconfigurability," *IEEE Transactions on Antennas and Propagation*, vol. 66, no. 1, pp. 444-449, 2017.
- [50] N. Yang, K. W. Leung, and N. Wu, "Pattern-diversity cylindrical dielectric resonator antenna using fundamental modes of different mode families," *IEEE Transactions on Antennas and Propagation*, vol. 67, no. 11, pp. 6778-6788, 2019.

- [51] Z. Chen and H. Wong, "Wideband glass and liquid cylindrical dielectric resonator antenna for pattern reconfigurable design," *IEEE Transactions on Antennas and Propagation*, vol. 65, no. 5, pp. 2157-2164, 2017.
- [52] A. Iqbal, A. Smida, O. A. Saraereh, Q. H. Alsafasfeh, N. K. Mallat, and B. M. Lee, "Cylindrical dielectric resonator antenna-based sensors for liquid chemical detection," *sensors*, vol. 19, no. 5, p. 1200, 2019.
- [53] H. C. Mohanta, A. Kouzani, and S. K. Mandal, "Reconfigurable antennas and their applications," 2019.
- [54] J.-S. Row and J.-F. Tsai, "Frequency-reconfigurable microstrip patch antennas with circular polarization," *IEEE Antennas and Wireless Propagation Letters*, vol. 13, pp. 1112-1115, 2014.
- [55] M. Jenath Sathikbasha and V. Nagarajan, "Design of multiband frequency reconfigurable antenna with defected ground structure for wireless applications," *Wireless Personal Communications*, vol. 113, pp. 867-892, 2020.
- [56] X. Liu, K. W. Leung, and N. Yang, "Frequency reconfigurable filtering dielectric resonator antenna with harmonics suppression," *IEEE Transactions on Antennas and Propagation*, vol. 69, no. 6, pp. 3224-3233, 2020.
- [57] M. Sun, Z. Zhang, F. Zhang, and A. Chen, "L/S multiband frequency-reconfigurable antenna for satellite applications," *IEEE Antennas and Wireless Propagation Letters*, vol. 18, no. 12, pp. 2617-2621, 2019.
- [58] A. Abdalrazik, A. B. Abdel-Rahman, A. Allam, M. Abo-Zahhad, K. Yoshitomi, and R. K. Pokharel, "Frequency-reconfigurable dielectric resonator antenna using metasurface," *International Journal of Microwave and Wireless Technologies*, pp. 1-7, 2021.
- [59] A. C. Mak, C. R. Rowell, R. D. Murch, and C.-L. Mak, "Reconfigurable multiband antenna designs for wireless communication devices," *IEEE Transactions on Antennas and Propagation*, vol. 55, no. 7, pp. 1919-1928, 2007.
- [60] S. Danesh, S. Rahim, and M. Abedian, "Frequency reconfigurable dielectric resonator antenna for WiMAX/WLAN applications," *Microwave and Optical Technology Letters*, vol. 57, no. 3, pp. 579-582, 2015.
- [61] S. Salman, S. Khamas, and G. Cook, "Slot fed SPIN diode reconfigurable dielectric resonator antenna," in *2014 Loughborough Antennas and Propagation Conference (LAPC)*, 2014, pp. 336-339: IEEE.
- [62] S. Danesh, S. Rahim, M. Abedian, M. Khalily, and M. Hamid, "Frequency-reconfigurable rectangular dielectric resonator antenna," *IEEE antennas and wireless propagation letters*, vol. 12, pp. 1331-1334, 2013.
- [63] S. Danesh, S. Rahim, M. Abedian, and M. Hamid, "A compact frequency-reconfigurable dielectric resonator antenna for LTE/WWAN and WLAN applications," *IEEE Antennas and Wireless Propagation Letters*, vol. 14, pp. 486-489, 2014.
- [64] S. K. Dhakad, U. Dwivedi, and T. Bhandari, "Design and analysis of reconfigurable antenna using PIN diodes for multi band WLAN applications," in *2017 International Conference on Wireless Communications, Signal Processing and Networking (WiSPNET)*, 2017, pp. 1705-1708: IEEE.
- [65] Y. I. Abdurraheem *et al.*, "Design of frequency reconfigurable multiband compact antenna using two PIN diodes for WLAN/WiMAX applications," *IET Microwaves, Antennas & Propagation*, vol. 11, no. 8, pp. 1098-1105, 2017.
- [66] Y. K. Choukiker and S. K. Behera, "Wideband frequency reconfigurable Koch snowflake fractal antenna," *IET Microwaves, Antennas & Propagation*, vol. 11, no. 2, pp. 203-208, 2017.

- [67] P.-J. Liu, D.-S. Zhao, and B.-Z. Wang, "Design of optically controlled microwave switch for reconfigurable antenna systems," in *2007 International Conference on Microwave and Millimeter Wave Technology*, 2007, pp. 1-4: IEEE.
- [68] P. Alizadeh, A. S. Andy, C. Parini, and K. Z. Rajab, "A reconfigurable reflectarray antenna in Ka-band using optically excited silicon," in *2016 10th European Conference on Antennas and Propagation (EuCAP)*, 2016, pp. 1-5: IEEE.
- [69] Y. Tawk, A. R. Albrecht, S. Hemmady, G. Balakrishnan, and C. G. Christodoulou, "Optically pumped frequency reconfigurable antenna design," *IEEE antennas and wireless propagation letters*, vol. 9, pp. 280-283, 2010.
- [70] G. Jin, D. Zhang, and R. Li, "Optically controlled reconfigurable antenna for cognitive radio applications," *Electronics letters*, vol. 47, no. 17, pp. 948-950, 2011.
- [71] Y. Tawk, J. Costantine, S. Barbin, and C. Christodoulou, "Integrating laser diodes in a reconfigurable antenna system," in *2011 SBMO/IEEE MTT-S International Microwave and Optoelectronics Conference (IMOC 2011)*, 2011, pp. 794-796: IEEE.
- [72] S. Junior, A. Cerqueira, I. Feliciano da Costa, L. T. Manera, and J. A. Diniz, "Optically controlled reconfigurable antenna array based on E-shaped elements," *International Journal of Antennas and Propagation*, vol. 2014, 2014.
- [73] E. R. Kusumawati, Y. H. Pramono, and A. Rubiyanto, "Optically Switched Frequency for Reconfigurable Dipole Antenna Using Photodiode Switches," *Telkomnika*, vol. 14, no. 4, p. 1351, 2016.
- [74] C. J. Panagamuwa, A. Chauraya, and J. Vardaxoglou, "Frequency and beam reconfigurable antenna using photoconducting switches," *IEEE Transactions on Antennas and Propagation*, vol. 54, no. 2, pp. 449-454, 2006.
- [75] Y. Tawk, J. Costantine, S. Hemmady, G. Balakrishnan, K. Avery, and C. G. Christodoulou, "Demonstration of a Cognitive Radio Front End Using an Optically Pumped Reconfigurable Antenna System (OPRAS)," *IEEE Transactions on Antennas and Propagation*, vol. 60, no. 2, pp. 1075-1083, 2012.
- [76] A. A. C. Alves, D. H. Spadoti, S. Pinna, A. Bogoni, F. Scotti, and S. A. Cerqueira, "Implementation of an optically-controlled antenna in a dual-band communications system: Systemic characterization with photonic down conversion," presented at the 2017 SBMO/IEEE MTT-S International Microwave and Optoelectronics Conference (IMOC), 2017.
- [77] S.-H. Zheng, X.-Y. Liu, and M. M. Tentzeris, "A novel optically controlled reconfigurable antenna for cognitive radio systems," in *2014 IEEE Antennas and Propagation Society International Symposium (APSURSI)*, 2014, pp. 1246-1247: IEEE.
- [78] M. Abou Al-alaa, H. Elsadek, E. Abdallah, and E. Hashish, "Pattern and frequency reconfigurable monopole disc antenna using PIN diodes and MEMS switches," *Microwave and Optical Technology Letters*, vol. 56, no. 1, pp. 187-195, 2014.
- [79] Y.-H. Ke, L.-L. Yang, and J.-X. Chen, "A pattern-reconfigurable dielectric resonator antenna based on switchable directors," *IEEE Antennas and Wireless Propagation Letters*, vol. 21, no. 3, pp. 536-540, 2021.
- [80] I. Ben Trad, J. M. Floc'h, H. Rmili, and F. Choubani, "A planar reconfigurable radiation pattern dipole antenna with reflectors and directors for wireless communication applications," *International Journal of Antennas and Propagation*, vol. 2014, 2014.
- [81] H. Fayad and P. Record, "Multi-feed dielectric resonator antenna with reconfigurable radiation pattern," *Progress In Electromagnetics Research*, vol. 76, pp. 341-356, 2007.
- [82] B. K. Ahn, H.-W. Jo, J.-S. Yoo, J.-W. Yu, and H. L. Lee, "Pattern reconfigurable high gain spherical dielectric resonator antenna operating on higher order mode," *IEEE Antennas and Wireless Propagation Letters*, vol. 18, no. 1, pp. 128-132, 2018.

- [83] L. Zhong, J.-S. Hong, and H.-C. Zhou, "A novel pattern-reconfigurable cylindrical dielectric resonator antenna with enhanced gain," *IEEE Antennas and Wireless Propagation Letters*, vol. 15, pp. 1253-1256, 2015.
- [84] M. K. Saleem, M. A. Alkanhal, and A. F. Sheta, "Dual strip-excited dielectric resonator antenna with parasitic strips for radiation pattern reconfigurability," *International Journal of Antennas and Propagation*, vol. 2014, 2014.
- [85] M. Kamran Saleem, M. A. S. Alkanhal, and A. F. Sheta, "Switched beam dielectric resonator antenna array with six reconfigurable radiation patterns," *International Journal of RF and Microwave Computer-Aided Engineering*, vol. 26, no. 6, pp. 519-530, 2016.
- [86] B.-J. Liu, J.-H. Qiu, C.-L. Wang, and G.-Q. Li, "Pattern-Reconfigurable Cylindrical Dielectric Resonator Antenna Based on Parasitic Elements," *IEEE Access*, vol. 5, pp. 25584-25590, 2017.
- [87] J.-X. Chen, Y.-H. Ke, L.-L. Yang, and W.-W. Yang, "Pattern-Reconfigurable Dielectric Resonator Antenna with Endfire Beam-Scanning Feature," *IEEE Antennas and Wireless Propagation Letters*, 2022.
- [88] M. Li, Z. Zhang, M.-C. Tang, L. Zhu, and N.-W. Liu, "Bandwidth Enhancement and Size Reduction of a Low-Profile Polarization-Reconfigurable Antenna by Utilizing Multiple Resonances," *IEEE Transactions on Antennas and Propagation*, vol. 70, no. 2, pp. 1517-1522, 2021.
- [89] M. Rezvani, S. Nikmehr, and A. Pourziad, "Reconfigurable Polarization MIMO Dielectric Resonator Antenna," *Progress In Electromagnetics Research M*, vol. 106, pp. 227-237, 2021.
- [90] W.-W. Yang, X.-Y. Dong, W.-J. Sun, and J.-X. Chen, "Polarization Reconfigurable Broadband Dielectric Resonator Antenna With a Lattice Structure," *IEEE Access*, vol. 6, pp. 21212-21219, 2018.
- [91] B.-J. Liu, J.-H. Qiu, C.-H. Wang, W. Li, and G.-Q. Li, "Polarization-reconfigurable cylindrical dielectric resonator antenna excited by dual probe with tunable feed network," *IEEE Access*, vol. 7, pp. 60111-60119, 2019.
- [92] L. Zhong, "A Polarization Reconfigurable Cylindrical Dielectric Resonator Antenna," *Progress In Electromagnetics Research M*, vol. 93, pp. 1-9, 2020.
- [93] A. Iqbal, M. I. Waly, A. Smida, and N. K. Mallat, "Dielectric resonator antenna with reconfigurable polarization states," *IET Microwaves, Antennas & Propagation*, vol. 15, no. 7, pp. 683-690, 2021.
- [94] A. El Yousfi, A. Lamkaddem, K. A. Abdalmalak, and D. Segovia-Vargas, "Broadband Circularly Polarized Reconfigurable Single Layer Metasurface Antenna," in *2022 16th European Conference on Antennas and Propagation (EuCAP)*, 2022, pp. 1-4: IEEE.
- [95] S. Dhar, K. Patra, R. Ghatak, B. Gupta, and D. R. Poddar, "Reconfigurable dielectric resonator antenna with multiple polarisation states," *IET Microwaves, Antennas & Propagation*, vol. 12, no. 6, pp. 895-902, 2017.
- [96] S.-L. Chen, Y. Liu, H. Zhu, D. Chen, and Y. J. Guo, "Millimeter-Wave Cavity-Backed Multi-Linear Polarization Reconfigurable Antenna," *IEEE Transactions on Antennas and Propagation*, vol. 70, no. 4, pp. 2531-2542, 2021.
- [97] W. A. Awan, A. Zaidi, N. Hussain, S. Khalid, and A. Baghdad, "Frequency Reconfigurable patch antenna for millimeter wave applications," in *2019 2nd International Conference on Computing, Mathematics and Engineering Technologies (iCoMET)*, 2019, pp. 1-5: IEEE.
- [98] I. F. da Costa, A. Cerqueira S, D. H. Spadoti, L. G. da Silva, J. A. J. Ribeiro, and S. E. Barbin, "Optically Controlled Reconfigurable Antenna Array for mm-Wave Applications," *IEEE Antennas and Wireless Propagation Letters*, vol. 16, pp. 2142-2145, 2017.

- [99] S. F. Jilani, B. Greinke, Y. Hao, and A. Alomainy, "Flexible millimetre-wave frequency reconfigurable antenna for wearable applications in 5G networks," in *2016 URSI international symposium on electromagnetic theory (EMTS)*, 2016, pp. 846-848: IEEE.
- [100] J. Choi *et al.*, "Frequency-adjustable planar folded slot antenna using fully integrated multithrow function for 5G mobile devices at millimeter-wave spectrum," *IEEE Transactions on Microwave Theory and Techniques*, vol. 68, no. 5, pp. 1872-1881, 2020.
- [101] J. Li, W. Yang, D. Chen, Q. Xue, Q. Wen, and W. Che, "Millimeter-wave frequency reconfigurable antenna using simple VO2-based paired metasurface," *International Journal of RF and Microwave Computer-Aided Engineering*, vol. 32, no. 12, p. e23454, 2022.
- [102] J. Sethares and S. Naumann, "Design of microwave dielectric resonators," *IEEE Transactions on Microwave Theory and Techniques*, vol. 14, no. 1, pp. 2-7, 1966.
- [103] A. Okaya and L. Barash, "The dielectric microwave resonator," *Proceedings of the IRE*, vol. 50, no. 10, pp. 2081-2092, 1962.
- [104] I.K. M. Luk and K. W. Leung, *Dielectric Resonator Antennas* (Research Studies", Press Ltd., Hertfordshire, England, UK). 2003.
- [105] A. Petosa, *Dielectric resonator antenna handbook*. Artech, 2007.
- [106] R. S. Yaduvanshi and H. Parthasarathy, *Rectangular dielectric resonator antennas*. Springer, 2016.
- [107] Y.-D. Zhou, Y.-C. Jiao, Z.-B. Weng, and T. Ni, "A novel single-fed wide dual-band circularly polarized dielectric resonator antenna," *IEEE antennas and wireless propagation letters*, vol. 15, pp. 930-933, 2015.
- [108] A. S. Al-Zoubi, A. A. Kishk, and A. W. Glisson, "Aperture coupled rectangular dielectric resonator antenna array fed by dielectric image guide," *IEEE Transactions on Antennas and Propagation*, vol. 57, no. 8, pp. 2252-2259, 2009.
- [109] M. Zou and J. Pan, "Investigation of resonant modes in wideband hybrid omnidirectional rectangular dielectric resonator antenna," *IEEE Transactions on Antennas and Propagation*, vol. 63, no. 7, pp. 3272-3275, 2015.
- [110] A. P. Kumar, "Higher order mode of a microstripline fed cylindrical dielectric resonator antenna," in *AIP Conference Proceedings*, 2016, vol. 1715, no. 1, p. 020027: AIP Publishing LLC.
- [111] A. Sharma, K. Khare, and S. Shrivastava, "Simple and Enhanced Gain Dielectric Resonator Antenna for ku band Application," *International Journal of Scientific & Engineering Research*, vol. 4, no. 9, pp. 1066-1070, 2013.
- [112] C. A. Balanis, "Fundamental parameters and definitions for antennas," *Modern Antenna Handbook*, pp. 1-56, 2008.
- [113] N. Behdad and K. Sarabandi, "Dual-band reconfigurable antenna with a very wide tunability range," *IEEE Transactions on Antennas and Propagation*, vol. 54, no. 2, pp. 409-416, 2006.
- [114] W. Kang, S. Lee, and K. Kim, "A pattern-reconfigurable antenna using PIN diodes," *Microwave and Optical Technology Letters*, vol. 53, no. 8, pp. 1883-1887, 2011.
- [115] MACOM, "<https://www.macom.com/products/product-detail/MA4SPS402>," 2022.
- [116] Y.-M. Pan, K. W. Leung, and K.-M. Luk, "Design of the millimeter-wave rectangular dielectric resonator antenna using a higher-order mode," *IEEE Transactions on Antennas and Propagation*, vol. 59, no. 8, pp. 2780-2788, 2011.
- [117] MACOM. (S Parameter). <https://www.macom.com/products/product-detail/MA4SPS402>.
- [118] Coilcraft. Accessed: 15-01-2023. Available: <https://www.coilcraft.com/getmedia/54459dcc-b821-4a9d-b91e-0416ea86a9b2/0402hp>
- [119] S. Gregson, J. McCormick, and C. Parini, *Principles of planar near-field antenna measurements*. IET, 2007.

- [120] J. Costantine, Y. Tawk, S. E. Barbin, and C. G. Christodoulou, "Reconfigurable antennas: Design and applications," *Proceedings of the IEEE*, vol. 103, no. 3, pp. 424-437, 2015.
- [121] H. A. Majid, M. K. A. Rahim, M. R. Hamid, and M. F. Ismail, "Frequency and pattern reconfigurable slot antenna," *IEEE transactions on antennas and propagation*, vol. 62, no. 10, pp. 5339-5343, 2014.
- [122] D. Rodrigo and L. Jofre, "Frequency and radiation pattern reconfigurability of a multi-size pixel antenna," *IEEE Transactions on Antennas and Propagation*, vol. 60, no. 5, pp. 2219-2225, 2012.
- [123] Y. P. Selvam *et al.*, "A low-profile frequency-and pattern-reconfigurable antenna," *IEEE Antennas and Wireless Propagation Letters*, vol. 16, pp. 3047-3050, 2017.
- [124] S. N. M. Zainarry, N. Nguyen-Trong, and C. Fumeaux, "A frequency-and pattern-reconfigurable two-element array antenna," *IEEE Antennas and Wireless Propagation Letters*, vol. 17, no. 4, pp. 617-620, 2018.
- [125] M. Studio, "Computer Simulation Technology (CST)," *Online: www.cst.com*, 2015.
- [126] B. Y. Toh, R. Cahill, and V. F. Fusco, "Understanding and measuring circular polarization," *IEEE Transactions on Education*, vol. 46, no. 3, pp. 313-318, 2003.
- [127] I. Da Costa *et al.*, "Optically controlled reconfigurable antenna for 5G future broadband cellular communication networks," *Journal of Microwaves, Optoelectronics and Electromagnetic Applications*, vol. 16, pp. 208-217, 2017.
- [128] C. D. Gamlath, D. M. Benton, and M. J. Cryan, "Microwave properties of an inhomogeneous optically illuminated plasma in a microstrip gap," *IEEE Transactions on Microwave Theory and Techniques*, vol. 63, no. 2, pp. 374-383, 2015.
- [129] A. Petosa, S. Thirakoune, and A. Ittipiboon, "Higher-order modes in rectangular DRAs for gain enhancement," in *2009 13th International Symposium on Antenna Technology and Applied Electromagnetics and the Canadian Radio Science Meeting*, 2009, pp. 1-4: IEEE.
- [130] J. Zhu, Y. Yang, S. Li, S. Liao, and Q. Xue, "Single-ended-fed high-gain LTCC planar aperture antenna for 60 GHz antenna-in-package applications," *IEEE Transactions on Antennas and Propagation*, vol. 67, no. 8, pp. 5154-5162, 2019.
- [131] K. Guan *et al.*, "Channel characterization for intra-wagon communication at 60 and 300 GHz bands," *IEEE transactions on vehicular technology*, vol. 68, no. 6, pp. 5193-5207, 2019.
- [132] J. Mu'ath, T. A. Denidni, and A. R. Sebak, "Millimeter-wave FSS-based dielectric resonator antenna with reconfigurable radiation pattern," in *2014 IEEE Antennas and Propagation Society International Symposium (APSURSI)*, 2014, pp. 1441-1442: IEEE.
- [133] Macom. (2022). <https://www.macom.com/products/product-detail/MA4AGP907>. Available: <https://www.macom.com/products/product-detail/MA4AGP907>